Impedance spectroscopy for in vitro toxicology

PAR

Robert MEISSNER

EPFL

ÉCOLE POLYTECHNIQUE
FÉDÉRALE DE LAUSANNE

Suisse
2013

To my little princess Leïla

Abstract

The impedance of biological material changes with frequency, a phenomenon that has been discovered more than 100 years ago. It is due to the fact that the cell membrane acts as a capacitor which filters out currents at low frequency and lets them pass at high frequency. This fundamental knowledge about biological dielectrics has incompletely been exploited to detect and distinguish toxicity effects on cell cultures, although impedance measurements have been used for long in this field. In this thesis, it was found that low frequency impedance signals are linked to initial stress responses of cells within cell populations when exposed to a toxin whereas high frequency measurements inform about major cell damage as is indicated by intracellular conductivity changes. In addition, when cells gain resistance to a toxin, they experience a higher cell stiffness which is expressed by an increased low frequency impedance. The study of impedance changes as a function of frequency and drug concentrations lead to the creation of an impedimetric concentration-response map which distinguishes cell responses within four concentration ranges without the use of any label. Although being inherently non-specific, this measurement method was shown to report on distinct toxicity effects, an important prerequisite when studying drug action on cancer cells where stimulating and lethal effects need to be distinguished rigorously.

This thesis further encompasses the subject of three-dimensional impedance measurements, i.e. the screening of the entire depth of a three-dimensional tissue culture. Given the success of impedance measurements on cell monolayers, one would expect this development to continue with 3D cultures since the complex structure of *in vivo* tissues is mimicked more closely and, above all, since rapid and inexpensive techniques which are able to probe thick tissue samples are currently inexistent. Nevertheless, few studies have been carried out in this field. Here, the requirements of three-dimensional impedance sensors are discussed and challenged by the fabrication of a corresponding device, involving the development of so-called gel electrodes through a novel 2-step-soft-lithography process. Their specific design allows for the decrease of leak currents, a common problem when performing three-dimensional impedance measurements.

The simultaneous measurement of multiple samples in parallel is an an essential condition when performing high throughput drug toxicity screening. Electrode switch systems are necessary which ultimately lead to setup complexity and signal noises. In this thesis, a method is introduced, enabling the simultaneous implementation of impedance measurements of multiple tissue samples with one electrode pair only. This is simply achieved by exploiting the frequency domain and finally contributed to reducing setup complexity.

Keywords: impedance, toxicity, tissue, cells, frequency, beta-dispersion, 3D, drug resistance, gel electrodes, cell stress

Zusammenfassung

Die Impedanz von biologischem Material ändert sich mit der Frequenz. Dieses Phänomen wurde vor mehr als 100 Jahren entdeckt und ist auf die Zellmembran zurückzuführen, welche elektrische Ströme bei niedrigen Frequenzen filtert und bei höheren passieren lässt. Obwohl Impedanzmessungen schon seit Langem eine wichtige Rolle bei Toxizitätsstudien spielen, konnte dieses fundamentale Wissen über biologische Dielektrika nur geringfügig genutzt werden um toxische Effekte auf Zellen zu messen und zu unterscheiden. In dieser Arbeit wurden Niedrigfrequenzimpedanzen mit anfänglichen Stresssignalen von Zellen als Folge der Behandlung mit toxischen Substanzen korreliert. Hochfrequenzimpedanzen hingegen wurden mit intrazellulären Leitfähigkeitsänderungen in Verbindung gebracht und informieren dadurch über den Zelltod. Darüberhinaus konnte festgestellt werden, dass Medikamentenresistenzen von Zellen eine verstärkte Starrheit verspüren und diese mittels Niedrigfrequenzsignale detektiert werden können. Die Studie von Impedanzänderungen in Abhängigkeit von Frequenz und Wirkstoffkonzentration führte zu der Erstellung einer impedimetrischen Konzentrations-Antwort Karte, welche Zellantworten innerhalb von vier Konzentrationsbereichen ohne zusätzliche Zellmarkierung unterscheidet. Obwohl die Impedanztechnologie eine inhärent unspezifische Messmethode ist, wurde in der Arbeit gezeigt, dass mit dieser Technologie verschiedene Toxizitätseffekte detektiert werden können. Damit erfüllt diese Methode z.B. wichtige Anforderungen an Tests von Krebsmitteln, bei denen zelltödliche von zellstimulierenden Effekten konsequent unterschieden werden muss.

Diese Arbeit befasst sich weiterhin mit drei-dimensionalen Impedanztests von *in vitro* Zellkulturen, bei welchen die gesamte Tiefe eines Gewebes zur Messung beiträgt. Angesichts des Erfolges der Impedanzmethode von 2D Zelleinzelschichten, sollte davon ausgegangen werden, dass diese Entwicklung mit 3D Zellkulturen fortgesetzt wird. Dies wäre nicht nur auf den vermehrten Einsatz von 3D Zellkulturen in der *in vitro* Zellkultur zurückzuführen, sondern vor allem auf die Tatsache, dass aktuell keine andere Methode zur kostengünstigen und schnellen Analyse von Geweben verfügbar ist. Nichtsdestotrotz hat es zu diesem Thema relativ wenige Studien gegeben. In dieser Arbeit wurden Anforderungen an drei-dimensionale Impedanzmessungen diskutiert und ein entsprechender Sensor entwickelt, welcher durch einen 2-Etappen-Soft-Lithographieprozess hergestellten sogenannten Gel-elektroden ausgestattet ist. Das besondere Design dieses Systems verhindert elektrische Leckstellen, ein verbreitetes Problem bei drei-dimensionalen Impedanzmessungen.

Das simultane und parallele Testen von mehreren Proben stellt eine essenzielle Bedingung für Hochdurchsatz Medikamentenuntersuchungen dar. Allerdings involviert eine solche Untersuchung komplizierte Umschaltsysteme, welche auch zu Signalstörungen führen. In dieser Arbeit wurde eine Methode entwickelt, die es unter Zuhilfenahme

der Frequenzdimension erlaubt, die Impedanz von mehreren Proben gleichzeitig mit nur einem Elektrodenpaar zu messen. Dadurch kann das Messsystem nicht nur vereinfacht sondern auch verkleinert werden.

Schlüsselwörter: Impedanz, Toxizität, Gewebe, Zellen, Frequenz, beta-Dispersion, 3D, Medikamentenresistenz, Gel-elektrode, Zellstress

Acknowledgments

I would like to express my greatest gratitude to Professor Philippe Renaud for having excepted me as a PhD student, for his unconditional support and for his continuos trust in my work. He is a brilliant professor from whom I have not only obtained scientific input, but he has also provided me with the necessary time and freedom to develop my skills. It is precisely these aspects which made my PhD simultaneously pleasant and stimulating. I wish to thank Philippe for that.

I would like to thank the jury members Prof. Eric Leclerc, Prof. Andreas Hierlemann, Prof. Nico de Rooij and Prof. Matthias Lutolf for having accepted reviewing my research. I appreciated their constructive feedback. Nanotera (Contract 20NAN1-123593) is acknowledged for the financial support.

I have been lucky working in a group with very pleasant and intelligent people. I have been enjoying this nice work atmosphere and was able to learn so much from my colleagues and friends. I wish to thank the people who have been directly involved in this work: Harsha, for being such a good friend, for having supported me scientifically and morally; Bilge, for being such a loyal and likable person and for having made me discover the world of drug resistance; Pierre, for sharing his thrilling intelligence with me and for being a nice guy at every moment; Anja, for her readiness to collaborate and for her esteem in me; Arnaud for his continuously encouraging support and for his highly competent scientific input.

I equally would like to thank Sophie for her inexhaustible good mood and for always being a very pleasant conversational partner; Ana and Fabien for having organized an unforgettable bachelor's party and for the numerous after-work beers; André M. for being a great motivator and challenger; Guillaume for being a sincerely nice person; Sébastien J. and Mojtaba for always having had an ear for me; Harald for his availability and his scientific help; Jules for the uncountable number of soccer discussions; Sylvie for always being friendly with me; Matteo for the nice soccer matches we played together; Elodie for sharing her large experience in entrepreneurship with me; Sebastian B. for the entertaining lunch breaks and for the nice time we had with lyx, Marc for providing me with the baby-first-aid kit; Jagoda, Diego and Rima for rendering the lunch breaks fun and Gregor who always supported me no matter what, just like a perfect friend.

Not less thanks appertains Nicolas D., Ludovica, Enri, Alessandro, Pietro, Thomas, Songmei, Nina, Lynda, Rodrigo, Georges, Willyan, Faye, David B., David F., Amélie, Baladji, Carolin, Damien, Sébastien M., Vincent D., Umut, Frédérik, Pontus (for his PhD thesis which was a perfect guide), Luis-Mi, Loic, Jonas, Cristina as well as the CMI and the BIOP stuff.

I would like to acknowledge the students who have contributed to this work: Serena, Magalie and André.

Contents

List of publications

Papers included in the thesis

1. R. Meissner, B. Eker, H. Kasi, A. Bertsch, P. Renaud. "Distinguishing drug-induced minor morphological changes from major cellular damage via label-free impedimetric toxicity screening". *Lab Chip*, 11 (14), 2352 - 2361, 2011

2. A. Kunze*, R. Meissner*, S. Brando, and P. Renaud. "Co-pathological connected primary neurons in a microfluidic device for Alzheimer studies. *Biotechnology and Bioengineering*", 108 (9), 2241-2245, 2011 - selected spotlight

3. R. Meissner*, P. Joris*, B. Eker, A. Bertsch, P. Renaud. "Microfluidic-based frequency-multiplexing impedance sensor (FMIS)". *Lab Chip*, 12 (15), 2712 - 2718, 2012

4. B. Eker*, R. Meissner*, A. Bertsch, K. Mehta, P. Renaud. "Label-free recognition of drug resistance via impedimetric screening of breast cancer cells". *PLoS ONE*, 8(3): e57423, 2013

5. P. Joris*, R. Meissner*, H. van Lintel, A. Bertsch, P. Renaud. "On the relationship between tissue structure and dielectric β-dispersion". submitted

6. R. Meissner, B. Eker, A. Bertsch, P. Renaud. "Three-dimensional impedance screening of in vitro cell cultures using gel electrodes". manuscript in preparation

* Equal contribution

Book chapter

1. R. Meissner and P. Renaud. Chaper: "The use of microfluidic-based neuronal cell cultures to study Alzheimer's disease" in Microfluidics for medical applications, *in press*

Related papers, not included in the thesis

1. H. Kasi, R. Meissner, A. Babalian, H. van Lintel, A. Bertsch, and P. Renaud. "Direct localised measurement of electrical resistivity profile in rat and embryonic chick retinas using a microprobe". *Journal of Electrical Bioimpedance*, 1:84-92, 2010

2. J. Park, R. Meissner, O. Ducloux, P. Renaud, F. Hiroyuki. "A calcium ion-selective electrode array for monitoring the activity of HepG2/C3As in a microchannel". accepted at *Sensors & Actuators: B. Chemical*

Conference proceedings

1. A. Kunze, R. Meissner, and P. Renaud. "Neurite guidance through 3D hydrogel layers in a microfluidic environment". *In Proceedings of the 14th International Conference on Miniaturized Systems for Chemistry and Life Sciences (MicroTAS 2010)*, volume 1, pages 187-189, 2010

2. J. Park, R. Meissner, O. Ducoux, H. van Lintel, P. Renaud, and H. Fujita. A Ca2+ ion selective electrode biosensor in microfluidics to monitor hepatocytes activities. *In Proceedings of the 14th International Conference on Miniaturized Systems for Chemistry and Life Sciences (MicroTAS 2010)*, volume 1, pages 247-249, 2010

3. R. Meissner, B. Eker, P. Renaud. "Continuous and label-free toxicity screening of human hepatocytes on chip reveals frequency-dependent impedance profiles". *In Proceedings of the 15th International Conference on Miniaturized Systems for Chemistry and Life Sciences (MicroTAS 2011)*, volume 1, pages 1487-1489, 2011

4. A. Kunze, R. Meissner, S. Brando, and P. Renaud. "Co-pathological states of tau proteins in a 3D micropatterned neural cell culture. *In Proceedings of the 15th International Conference on Miniaturized Systems for Chemistry and Life Sciences (MicroTAS 2011)*, volume 1, pages 696-698, 2011

5. R. Meissner, B. Eker, P. Renaud. "Rapid, label-free distinction of epithelial cancer cells". *NanoBioTech Montreux*, 2011 - awarded with the BioAlps poster prize

List of Figures

List of Tables

Nomenclature

O_2	Oxygen
3D	Three-dimensional
Aβ	Beta-amyloid
AC	Alternating current
AD	Alzheimer's disease
AFM	Atomic force microscopy
AP	Acetaminophen
APP	Amyloid precursor protein
APTES	(3-aminopropyl)-triethoxysilane
BDNF	Brain-derived neurotrophic factor
Bio-MEMS	bio-microelectromechanical systems
BSA	Bovine serum albumin
CCl4	Carbon tetrachloride
CI	Cell index
CI	Confidence interval
CPE	Constant phase element
CYP450	Cytochrome P450
DAPI	4',6-diamidino-2-phenylindole
DC	Direct current
DE	Dispersion element
DIC	Differential interference contrast
DIV	Days in vitro
DMEM	Dulbecco's Modified Eagle's Medium

DMPA	2,2-dimethoxy-2-phenylacetophenone
DMSO	Dimethyl sulfoxide
DOX	Doxorubicin
EC	Entorhinal cortex
ECIS	Electrical cell-substrate sensing
FITC	Fluorescein isothiocyanate
FMIS	Frequency multiplexing impedance sensor
FSM	Frequency seperation method
HF	High frequency
IC50	Half maximal inhibitory concentrations
IDE	Interdigitated electrodes
iPS	Induced pluripotent stem cells
KCl	Potassium chloride
LF	Low frequency
LPE	logarithmic phase element
LSM	Laser scanning microscope
mTG	Microbial transglutaminase
MTT	(3-(4,5-Dimethylthiazol-2-yl)-2,5-diphenyltetrazolium bromide
NFTs	Neurofibrillary tangles
NGF	Nerve growth factor
NOAEL	No observed adverse effect levels
OA	Okadaic acid
PBS	Phosphate buffered saline
PCB	Printed circuit board
PEG-DA	Poly(ethylene) glycol-diacrylate
PMMA	Poly-(methyl-methacrylate)
PRF	Peak resistance frequency

REACH	Registration, Evaluation, Authorisation and Restriction of CHemicals
RPMI	Roswell Park Memorial Institute medium
SEM	Standard error of the mean
TEER	Trans-epithelial electric resistance
TrkB	Tropomyosin-related kinase B
UV	Ultraviolet
WT	Wild-type

List of symbols

Constants

Symbol	Name	Value	Units
ε_0	Dielectric constant of free space	8.8541×10^{-12}	Fm^{-1}
ε_{air}	Dielectric constant of air	1.00058986	-
j	Imaginary number	$\sqrt{-1}$	-
ε_{OHP}	Dielectric constant of the outer Helmholtz plane	12.4	-
d_{OHP}	Helmholtz plane distance	5	Å
π	Pi	3.1416	-

Variables

Symbol	Quantity	Units
A_{cross}	cross-sectional area in the direction of the electric field	$[m^2]$
A_{el}	surface area of an electrode	$[m^2]$
$A_{geometric}$	apparent surface area excluding pores	$[m^2]$
A_{trace}	surface area of the electrode traces	$[m^2]$
A_{true}	true surface area excluding pores	$[m^2]$
A_{wires}	surface area of signal current paths	$[m^2]$
α	CPE exponent	-
α_c	tissue CPE exponent	-
α_{el}	electrode CPE exponent	-
β	CPE magnitude	$[\Omega^{\alpha-1}F^\alpha]$
β_{el}	electrode CPE magnitude	$[\Omega^{\alpha-1}F^\alpha]$
β_c	tissue CPE magnitude	$[\Omega^{\alpha-1}F^\alpha]$
C_β	equivalent β-dispersion capacitance	$[F]$
C_{extra}	extracellular capacitance of a single cell	$[F]$
C_{GC}	Gouy-Chapman capacitance	$[F]$
C_H	Helmholtz capacitance	$[F]$
C_I	Interface capacitance	$[F]$
C_{intra}	intracellular capacitance of a single cell	$[F]$
C_m	equivalent capacitance of a tissue	$[F]$

Symbol	Quantity	Units
C_{mem}	capacitance of the membrane of a single cell	$[F]$
C_n	interface capacitance of the nth electrode-channel segment of a FMIS	$[F]$
C_s	stray capacitance	$[F]$
C_{sol}	solution capacitance	$[F]$
D	total resistance range of a FMIS	-
d_{wires}	distance between signal current paths	$[m]$
E	electric field	$[V/m]$
ε_α	dielectric constant of the alpha dispersion	-
ε_β	dielectric constant of the beta dispersion	-
$\varepsilon_{\gamma/\delta}$	dielectric constant of the gamma/delta dispersion	-
ε_{sol}	dielectric constant of a solution	-
$E_{uniform}$	equivalent electric field for a homogeneous field distribution at the electrode surface	$[V/m]$
f_c	cut-off frequency	$[Hz]$
f_n	cut-off frequency of the nth electrode-channel segment of a FMIS	$[Hz]$
h	distance between the planar electrodes and a top insulating wall	$[m]$
$\triangle f$	difference of cut-off frequencies	$[Hz]$
$\triangle \log R$	logarithmic difference between LF and HF resistance	-
$\triangle R$	total resistance range of a FMIS	-
$\triangle V$	voltage drop	$[V]$
$\triangle V_c$	total cellular volume change	$[m^3]$
I_{ext}	extracellular current within a tissue	$[A]$
Im	imaginary part of the impedance	$[\Omega]$
I_{para}	para-tissue current	$[A]$
J	current density	$[A/m^2]$
k	modulus of K(x)	-
κ	cell constant	$[m^{-1}]$
κ_{2D}	two-dimensional cell constant	-
κ_n	cell constant of the nth electrode-channel segment of a FMIS	$[m^{-1}]$
$K(x)$	complete elliptic integral of the first kind	-
λ	correction factor for κ to account for fringing effects	-
l_{el}	electrode length	$[m]$
l_{trace}	length of the electrode traces and wiring	$[m]$
M	optimization product for a FMIS	-
m	cut-off frequency ratio	-
μ_c	overpotential due to exchange of metal atoms with corresponding ions	$[V]$
μ_d	overpotential due to diffusion of reactants to and from electrode	$[V]$

Symbol	Quantity	Units
μ_r	overpotential due to chemical reactions at the electrode	[V]
μ_t	overpotential due to the charge transfer through double layer	[V]
φ	impedance phase	[°]
φ_{LF}	impedance phase at LF	[°]
φ_{HF}	impedance phase at HF	[°]
P	FMIS sub-sensor bandwidth, plateau length parameter	-
R	resistance	[Ω]
R_0	zero frequency resistance of the β-dispersion	[Ω]
R_∞	infinite frequency resistance of the β-dispersion	[Ω]
R_{bulk}	bulk resistance	[Ω]
R_{CT}	charge transfer resistance	[Ω]
r_d	access channel length	[m]
Re	real part of the impedance	[Ω]
R_{ext}	extracellular resistance of a tissue	[Ω]
R_{extra}	extracellular resistance of a single cell	[Ω]
R_{int}	intracellular resistance of a tissue	[Ω]
R_{intra}	intracellular resistance of a single cell	[Ω]
R_{lead}	wire resistance	[Ω]
R_{medium}	resistance of the cell culture medium	[Ω]
R_{mem}	cell membrane resistance	[Ω]
R_n	solution resistance of the nth electrode-channel segment of a FMIS	[Ω]
R_{para}	para-tissue resistance	[Ω]
R_{spread}	spreading resistance	[Ω]
S	sensitivity	-
s_{el}	electrode spacing	[m]
σ_∞	infinite frequency conductivity of the β-dispersion	[S/m]
σ_{ext}	extracellular conductivity of a tissue	[S/m]
σ_d	distribution width	-
$\sigma_{d,extra}$	distribution width of R_{extra}	-
$\sigma_{d,intra}$	distribution width of R_{intra}	-
$\sigma_{d,mem}$	distribution width of C_{mem}	-
σ_{sol}	solution conductivity	[Sm^{-1}]
σ_{medium}	cell culture medium conductivity	[Sm^{-1}]
S_{LF}	sensitivity at low frequency for cell volume changes	-
S_{HF}	sensitivity at high frequency for intracellular conductivity changes	-
V	applied voltage	[V]
$V_{intercell}$	Intercellular volume	[m^3]
w_{ap}	apparent electrode width	[m]
w_{ch}	microfluidic channel width	[m]
w_{el}	electrode width	[m]
X	reactance	[Ω]

Symbol	Quantity	Units
X_s	Stray capacitance	$[\Omega]$
$|Z|$	impedance magnitude	$[\Omega]$
$z_{1/2}$	measurement depth	$[m]$
$|Z|_{HF}$	impedance magnitude at HF	$[\Omega]$
$|Z|_{LF}$	impedance magnitude at LF	$[\Omega]$
Z_m	total measured impedance	$[\Omega]$
$|Z|_{rel}$	relative difference of impedance magnitude between cell-free and cell spectrum	$[\%]$
Z_{par}	Parasitic impedance	$[\Omega]$
Z_{tissue}	impedance of the tissue	$[\Omega]$
Z_W	Warburg impedance	$[\Omega]$

1. Introduction

A cell is the simplest viable matter that exists within the hierarchy of biological organisation and represents the basic element of all living organisms. The human body is a community of numerous differently specialized cells, which mostly would not be able to survive in isolation. Even if cells ally to higher organizational levels such as tissues and organs, all activities of a living organism remain and take place at the level of a cell, e.g. muscle contraction through myocytes and signal transmission through nerve cells.

To understand the functionality and structure of cells, cell biologists require instruments that are at the same scale, i.e. between 1-100 μm. Although initially being developed for the electronics industry, microtechnology has opened doors to the fabrication of miniature structures that allow manipulating cells precisely. Just as microtechnolgy has enaled the semiconductor industry to be more accurate, efficient and cost-effective, these very same microfabrication techniques can be exploited to render cell analysis more accessible, reliable and high through-put.

Although the domain of bio-microelectromechanical systems (Bio-MEMS) has attracted significant attention in the last years already, this was mostly limited to research purposes whereas the industrialization of such micro-devices is still in the offing.

1.1. Scope

This thesis contributes to the understanding of electrical properties of *in vitro* cell cultures, with a particular view to toxicological studies. Thereby, this work represents an attempt to rendering toxicological laboratory tests more reliable, and by consequence to help decreasing the high number of sacrificed animals in risk assessment of commercialized chemicals. The great potential of impedance spectroscopy for toxicity probing lies in its devoid of sample interfering manipulations (e.g. antibodies), enabling continuous and resource saving implementation of "invisible" toxicity tests. Motivated by the elegance of this technique, the present thesis discusses the implications of toxicity-induced cellular changes and evolutionary adaptation of a cell population on frequency-dependent impedance measurements. It is further described how *in vivo* drug delivery may be mimicked *in vitro* and how impedance screening of three-dimensional cultures is achieved. The design and fabrication of the used micro-devices is therefore presented. A fourth part of this thesis pertains a method that allows multiplexing impedance measurements without using switches.

Finally, an *in vitro* model for the study of disease propagation in Alzheimer's disease was developed as well as a review on microfluidic techniques to study Alzheimer's disease was carried out, however this exceeds the scope of the main text and hence has been included in annex to this thesis.

1.2. Background

1.2.1. Toxicity testing for human safety

Toxicity is generally referred to as the ability of a substance to damage an exposed living organism. One can distinguish between the effect on a whole organism and the effect on a sub-structure of the organism, such as a cell (cytotoxicity) or an organ such as the liver (hepatotoxicity).

Toxicity testing plays an important role in health and environmental fields and is an indispensable tool for risk assessment of products on the market such as drugs, cosmetics, pesticides, food additives or their chemical ingredients. These tests are essential to characterize toxic effects with respect to target organs, dose dependence, relationship to exposure and, when appropriate, potential reversibility . Safety assessment is not a choice but has become an obligation instructed by a wide number of general and specific regulations in several industry domains (European Medicines Agency, 2009). One of the most well-known is REACH (Registration, Evaluation, Authorisation and Restriction of CHemicals), a European Union Regulation that entered into force in June 2007 (European Commission, 2006) and has been described as the most important EU legislation for 20 years (BBC, 2005). REACH aims at making registration mandatory for the currently some 80,000 produced chemicals commercialized worldwide for which toxicity data have partially never been registered as well as for future chemicals (Abbott, 2005).

1.2.2. Cell-based toxicity testing

In pharmaceutical industry clinical trials are required prior to marketing as part of the development process to determine if new drugs are safe and effective in humans. Non-clinical studies are preceding these tests in humans in order to select the best lead chemical and to estimate an initial safe starting dose and dose range (European Medicines Agency, 2009). Non-clinical trials comprehend a wide range of measurement methods whereas tests on animals seem to be both the most important and the most controversial ones. In fact, around one million animals are used every year in Europe in toxicology tests (Abbott, 2005) representing ethical problems as well as enormous costs. More-over, in a large number of cases, animal studies have been proven inadequate for human safety assessment due to species differences (Olson et al., 2000). For example, while all mammals use cytochrome P450[1] (CYP450) to detoxify and eliminate toxic compounds, specific CYP distribution, pathways and rates of reactions vary significantly between rodents and humans (Smith, 1991; Astashkina et al., 2012). Nevertheless, inputs to the risk assessment have traditionally been generated in animal tests as they stand for the closest whole organism alternative to tests in humans, and therefore are required by international regulations (European Medicines Agency, 2009; Opp et al., 2009). All these facts indicate that preclinical evaluation of new drugs is a very important but still controversial task (European Medecines Agency, 2008) that may require rethinking in terms of the significance of animal testing and potential alternatives.

---

[1] Cytochrome P450 is a family of enzymes which facilitates the oxidation of organic substances.

Cell-based assays to predict human toxicity endpoints, may be a key technology towards diminished animal testing in the future. Although the identity, behavior, and survival of a cell depend not only on neighboring cells, but on many molecular pathways and biological processes occurring within the entire organism, it is precisely this complexity of the whole organism as well as the need to use animal models which are problematic when it comes to understanding human and mechanistic toxicity responses (Ward, 2008). Furthermore, based on the assumption that a majority of cancer has environmental causes and that there are more than 80,000 commercialized chemicals, there is neither enough time nor resources for long-lasting whole organism tests. The use of cells for toxicity testing proves promising since, finally, it has a higher physiological relevance with the ability to obtain data directly from cells at various ages and detailed dose-response data directly from human models instead of animals. Moreover, the screening efficiency for potential toxicants may be increased since screens for remediators and for toxicity of mixtures can be easily carried out and sensitive endpoints are conserved across species. Also, through the use of primary cells or stem cell-derived cells, a better translation of findings for comparing studies and thus benchmark criteria for linking *in vitro* to *in vivo* studies are within reach (Liu et al., 2013).

Cell-based toxicity testing already plays an important role thanks to the ease of culture of numerous cell lines, however, it might experience a break-trough in near the future owing to the recent availability of differentiated cells from induced pluripotent stem cells (iPS) (Takahashi and Yamanaka, 2006; Meissner et al., 2007; Okita et al., 2007). The iPS technology enables the unlimited supply and reconstruction of genetically identical tissues, a major advantage over cell lines that possess a rather poor relevance to human biology. Consequently, doors are about to be opened to long term *in vitro* toxicity testing provided that suitable measurement techniques that fulfill requirements such as high throughput, simplicity and cost-effectiveness, but also reliability and repeatability are developed, validated and accepted by industry standards. Therefore, a major difficulty still consists in refining such techniques and more importantly in determining satisfactory morphological or biochemical criteria that characterize early toxicity in culture. Such standards are necessary given the large number of currently employed laboratory techniques, in particular regarding the data acquired through non-invasive and label-free detection of cell toxicity. This is crucial since toxicity testing is an area where a false positive could be accepted but never a false negative.

1.2.3. Impedance monitoring of cells and tissues

The measurement of the electrical properties of biological tissue and cells has attracted significant attention over the last century due to three striking advantages over the majority of conventional techniques: electrical impedance screening is (1) a label-free technique which does not require the use of expensive markers, (2) it is non-destructive meaning that the detection method does not interfere with the cells enabling continuous measurements and (3) it is fully automatable rendering data acquisition and analysis free from human error and thus highly objective. Up-to-date a large number of laboratory devices with focus on impedance measurements have been developed to exploit these advantages

and to study the impedimetric properties of single cells and cell populations *in vitro*; however, as will be shown below, this process has taken more than 100 years and still substantial work is necessary to make this technique exploitable by diverse laboratories as well as by the industry.

It was Rudolf Hoeber in 1911 who first discovered that cells have frequency-dependent electrical properties and that cell membranes may play a big part in that (Höber, 1910). More, rather theoretical work was carried out where this frequency-dependence for cell suspensions and tissues was described (Cole, 1940; Debye, 1929; Fricke, 1924; Cole, 1928). It was further Schwan who founded biomedical engineering as a new discipline by applying the previous technical advances to biological material amongst others to count cells, to measure the electric properties of muscle tissue (Schwan, 1954) and to carry out micro-impedance tomography (Schwan, 1999). He also described that when measuring the dielectric properties of biological material changes with frequency occur in three distinct major steps termed α, β and γ/δ^2 dispersion[3] where the changes originating in the frequency-dependence of the cell membrane (β-dispersion) are most often the ones of interest (figure 1.1) (Schwan, 1994). This fundamental knowledge about biological dielectrics has almost not been exploited to monitor, detect and analyze toxicity effects on cell populations since its discovery.
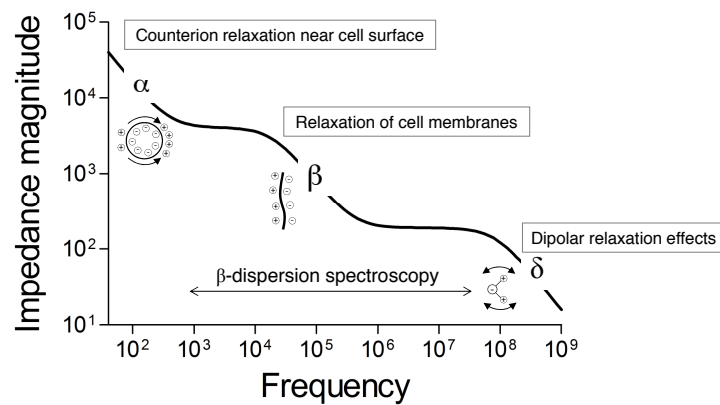
Figure 1.1.: Frequency-dependence of biological tissue. Three distinct dispersions are observed. The term relaxation refers to a decrease in polarization with increasing frequency.

1.2.3.1. *In vitro* monolayer impedance monitoring

First electrical measurements on *in vitro* cell cultures were carried out using the trans-epithelial electric resistance (TEER) technique developed by Ussing and Zerahn (1951).

---

[2] The γ and δ-dispersion concern dipolar relaxation effects of free, unbound water and of protein-bound water respectively. The γ-dispersion occuring at higher frequencies than the δ-dispersion will be ignored hereafter since it is the β-dispersion which is of interest in this thesis.

[3] Dispersion denotes the frequency-dependence according to the relaxation theory where polarization of charges will decrease with increasing frequency because the direction of the applied electric field varies more quickly than the displacement and accumulation of charges (Grimnes and Martinsen, 2008, p.89).

This method exploits the fact that epithelial cells form tight monolayers through inter-cellular junctions (tight and adhesive junctions). The aptitude of a drug to interrupt the permeability of this cell layer is characterized by measuring the trans-epithelial resistance across the cells growing on a permeable filter as depicted in figure 1.2a.

A simplified setup that circumvents the use of a membrane was invented by Giaever and Keese (1984) who cultured cells in a petri dish which was patterned with micro-electrodes (figure 1.2b). It was found that cell attachment and spreading on the electrode results in a strong effect on the measured impedance and that cell movement leads to signal fluctuations. In fact, cells reach the substrate with an almost spherical morphology. The area of closest contact between the basal membrane and the surface is therefore rather small but increases continuously while the cells spread as illustrated in figure 1.2c (Wegener et al., 2000). Interestingly it has been shown that different spreading behaviors (kinetics and amplitude) can be obtained by using different protein coatings. The method was termed electrical cell-substrate sensing (ECIS) and resulted in a considerable amount of studies. Cell motility for example, a common process of mammalian cells within a cell population that normally is observed in tissue culture by time lapse microscopy where resolution is limited by the wavelength of light, has been detected on the scale of nanometers using ECIS (Lo et al., 1993; Giaever and Keese, 1991). Furthermore, cell detachment from the electrode surface has been studied as a parameter for cell toxicity where the temporal evolution of the impedance gives indications about the half-inhibition concentration in response to different toxin concentrations and exposure times (Jahnke et al., 2009; Krinke et al., 2010). Also muscle contraction (Haas et al., 2010), cell migration (Linderholm et al., 2006) and stem cell differentiation (Bagnaninchi and Drummond, 2011) were detected using ECIS, which underlines the impact patterned micro-electrodes already had on cell monitoring and characterization.
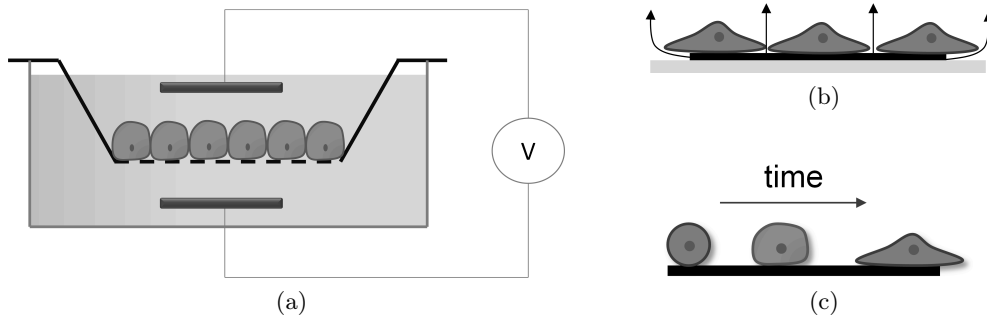
Figure 1.2.: Monolayer impedance monitoring. a) The trans epithelial resistance setup developed by Ussing and Zerahn (1951). b) The ECIS setup developed by Giaever and Keese (1984). c) Time course of cell spreading on a substrate and simultaneous increase of adhesion area

Nevertheless, most of the cell-based impedance studies that have been carried out previously followed-up the impedance magnitude over time at one frequency where the difference between the impedance magnitude profile in the presence and that in the absence of cells is largest. The corresponding impedance magnitude is often referred to as cell index in literature (CI) (Otero-González et al., 2012). In fact, a literature

survey in *pubmed* with the keywords "impedance, cells, toxicity" (20th of January 2013) revealed that 48 out of the most recent 50 publications used single frequency analysis (figure 1.3). Only 2 articles used multi-frequency analysis and both of them were carried out with equivalent circuit fitting, a debatable method as will be discussed more in detail in section 3.6.2. These facts indicate that frequency dependence of biological tissue is a well-known phenomenon; however this has almost not been exploited and rather been neglected when studying toxicity effects on cells.
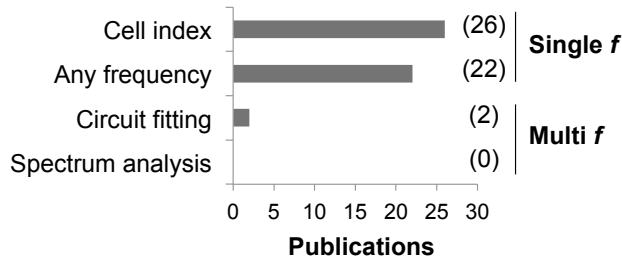
Figure 1.3.: Impedance data analysis methods when studying cell toxicity. The 50 most recent publications (20th of January 2013) from the search engine *pubmed* with the keywords "impedance, toxicity, cells" have been examined.

As already addressed in figure 1.1 and considering a single cell as a shell-covered sphere (Pauly and Schwan, 1959; Gawad, 2004) it is necessary to distinguish cellular events within frequency ranges. At lower frequencies, cells act as insulators due to the capacitive nature of the cell membrane. At higher frequencies, the cell membrane capacitor is short-circuited and intracellular matter has an effect on the impedance. Hence, frequency dependent impedance screening offers plethora of information on intra- and extracellular properties. To date there are no reports on distinguishing toxicity effects on cell populations using frequency-dependent impedance measurements.

1.2.3.2. *In vitro* three-dimensional impedance monitoring

In vivo tissues have a very complex but well-organized three-dimensional structure. In contrast to traditional 2D culture, culturing cells in 3D provides another dimension for external mechanical inputs and for cell adhesion, which affects integrin ligation, cell contraction and associated intracellular signaling (Griffith and Swartz, 2006; Knight et al., 2000; Roskelley, 1994). Moreover, the diffusion of soluble factors changes dramatically compared to 2D cultures. Hence, investigating cells in a 3D environment seems highly promising since the effect of mechanical and chemical stimuli on 3D cultures are mimicked more closely to the ones in the human body.

Several techniques to assess 3D cell cultures exist, however these technologies suffer from either low throughput, low penetration depth, require labeling or are very costly (confocal microscopy, coherence tomography, magnetic resonance imaging). Impedance screening, on the other hand, seems to be an ideal technology owing to its large penetration depth into tissues and its cost-effectiveness. Nevertheless, only few studies have been reported. One of them was presented by Linderholm (2006) who developed a technique
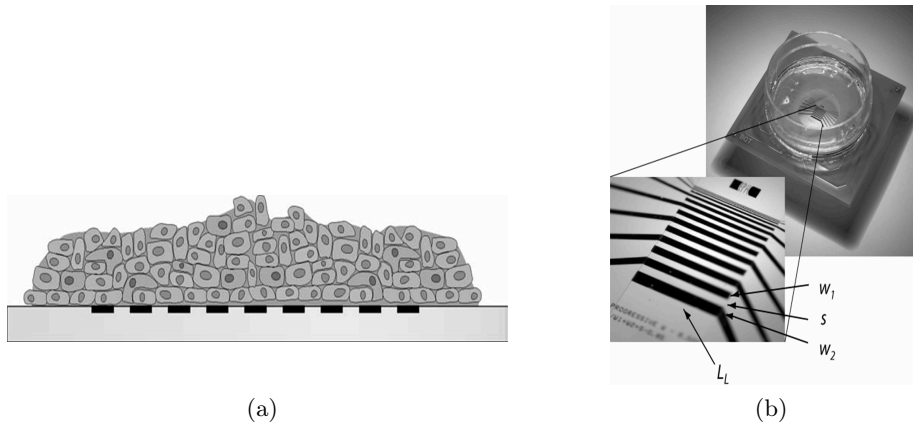
Figure 1.4.: Device for tissue thickness measurements. a) The sensor consists of 16 linear electrodes integrated in a culture dish; b) The device consisted of a glass chip with platinum electrodes bonded to a small circuit board onto which a culture dish was glued. Taken from Linderholm (2006)

for continuous monitoring of the thickness of tissue cultures ranging from 10 to 80μm (figure 1.4a). This was achieved by using multiple electrode pairs at different distances to probe different depths of the overlayed tissue sample (figure 1.4b).

Multicellular spheroids[4] are probably the most classical approach for 3D culture (figure 1.5a) (Friedrich et al., 2009). Dielectric measurements of multicellular aggregates have been conducted previously (Thielecke et al., 2001; Kloss et al., 2008) where a micro-device was adapted to spheroidal shapes (figure 1.5b). An array of 100μm deep square micro-cavities was used for the entrapment of pre-cultured spheroids between gold electrodes. A drawback of this technique remains the imprecise match of spheroid- and micro-cavity size leading to current shunting between the spheroid and the cavity wall and thus lowering the signal sensitivity. Furthermore, single frequency analysis was carried out with no profound information on the relationship between tissue structure or condition and the measured impedance.

While spheroids show several advantages as 3D models such as their well-defined geometry which allows correlating structure with function in a reproducible way, they represent a very dense and low extra-cellular matrix environment. In order to mimic tissues with lower cell density, hydrogels have been employed as a mechanical support for cells, providing 3D architecture (figure 1.5c). Impedimetric characterization of such cultures has been revealed challenging since lower cell densities result in impedances that are barely detectable, above all due to the inverse relationship between intercellular space and resistance ($R \approx 1/A$). Therefore, few experiments have been reported and these were limited to cell growth measurements (Frampton and al., 2007; Lin et al., 2009).

---

[4] Spheroids are large aggregates of cells within the range of several hundreds of micrometers. The mutual contacts between cells and the specific micro-environment allows them to express a tissue-like phenotype.
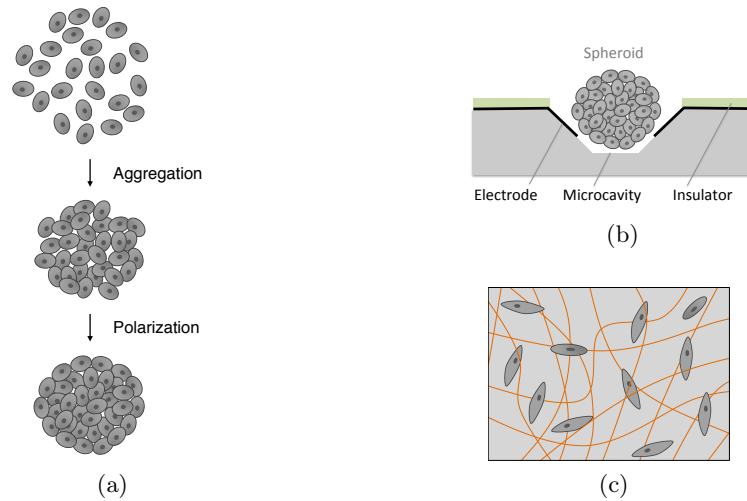
Figure 1.5.: Impedance monitoring of three-dimensional cell cultures. a) Cellular spheroids. Cells aggregate into large (several hundreds of micrometers) spheroids and re-establish mutual contacts and specific microenvironments that allow them to express a tissue-like phenotype (Pampaloni et al., 2007). b) Microcavity chip for capturing and impedance recording multicellular spheroids according to Kloss et al. (2008). c) Hydrogels composed of polymers (orange mesh) provide a 3D environment for culturing cells.

Based on the success of impedance monitoring of monolayers, it seems reasonable to assume that impedance monitoring of three-dimensional cell culture would provide valuable information regarding *in vitro* drug toxicology, however this requires bearing some technological challenges.

1.2.3.3. High accuracy impedance measurements with microfluidic chips

An important technological challenge involves the maintenance of cell viability within a 3D cell culture (in the absence of drug) where some cells are not in direct contact with the nutrient source. To account for cell viability in a complex environment, the human body has capillaries where gasses, nutrients and wastes are continuously exchanged between the blood and tissues by diffusion. Microfluidic chips have been designed previously to mimic such flow conditions *in vitro* where external pumps are connected to the chip by tubes to guarantee a perfusion flow with a specific flow rate. Cells inside the chip are exposed to the flow (figure 1.6a) (Leclerc, 2004) or may be protected from shear stress either by micro-porous microfluidic barriers (figure 1.6b) (Xia et al., 2009; Toh et al., 2007; Zhang et al., 2008) or by culturing the cells within or behind a hydrogel wall (figure 1.6c) (Haessler et al., 2009; Shin et al., 2012). Culturing cells in a hydrogel separated from the perfusion flow represents a configuration close to body tissues given the three-dimensionality and the almost exclusive diffusional transport of nutrients and waste within the cell area. In addition, hydrogels are more compatible with electrodes owing to their electric conductance in contrast to high resistance microfluidic barriers. However, their fabrication combined with impedance sensing is not trivial if mechanical
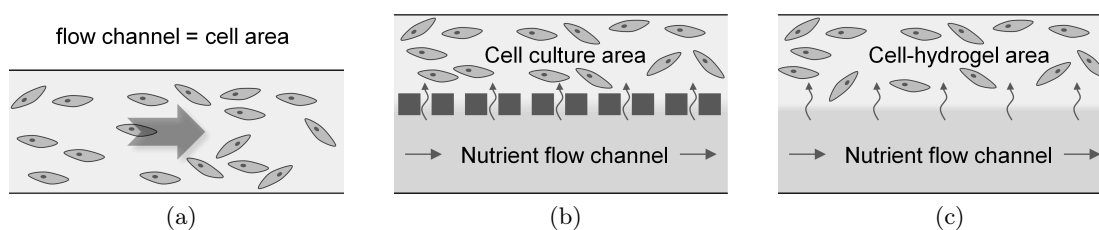
Figure 1.6.: *In vitro* nutrient and waste exchange between cells and a perfusion flow. a) Perfusion flow is in direct contact with the cells and may therefore exert shear stress. b) and c) are configurations where cells are protected from the convective flow: b) Cells are separated from the perfusion flow by microfluidic barriers which have a high fluidic resistance and therefore favor diffusion but hinder convective flow through them. c) Cells are cultured within or behind a hydrogel wall that represents a micro-porous matrix, readily allowing diffusion.

stability and the absence of potential leak currents are to be guaranteed.

In contrast to macro-scale impedance measurements such as tomography, where electrode position, sample geometry and movement artifacts due to breathing greatly degrade signal quality, micro-fabricated systems allow a highly controlled environment. Both the electrode geometry and cell positioning can then be precisely determined, resulting in higher accuracy (Linderholm, 2006). In fact, the electric field lines are required to run in parallel to ensure an equal sensitivity contribution from each part of the tissue to the total impedance. This presupposes parallel electrodes, which are complicated to fabricate. Planar electrodes can be used instead, however, they need to be placed at a certain distance from the tissue sample to damp the non-uniformity of the electric field.

To date there is no device that integrates the impedimetric screening of an entire three-dimensional cell population with continuous perfusion. Such a system is a prerequisite for reliably studying the effect of low doses of drugs on tissue samples, an experimental design that, although it has never been conducted before, would be a highly valuable asset in estimating the relationship between frequency as well as concentrations and enhanced drug responsiveness.

1.3. Research strategy

1.3.1. Problem definition

Given the high costs and time necessary for bringing lead compounds to the market as well as for the matter of human safety, it is of high importance to identify drug-induced toxicity at an early phase. Hence, there is a pressing demand towards the development of rapid and simple laboratory techniques for the investigation of hazardous drug effects. Such *in vitro* techniques are required to mimic the *in vivo* conditions closely in order to provide meaningful results. Furthermore, simple toxicity detection is a prerequisite for achieving high testing throughput.

Currently, several impedimetric screening platforms have been developed, but none of

them enables the screening of three-dimensional cell cultures reliably and under continuous perfusion. Furthermore, the pioneering work of Höber, Cole, Schwan and others that described the frequency-dependence of biological material has remained unexploited when studying drug-induced toxicity on tissues. Although being inherently non-specific, however, impedance spectroscopy allows distinguishing biological effects provided the relationship between impedance measurements and biological phenomena are more comprehensively understood.

1.3.2. Research objective

The objective of this thesis is to contribute to the knowledge of how cellular toxicity and acquired drug resistance can be measured and interpreted based on electrical impedance spectroscopy. More precisely, it investigates whether early drug-induced toxicity can be singled-out from major, irreversible cell injury and thus if impedance screening, a naturally non-specific technique, may be rendered more specific. Also, the impedimetric screening of three-dimensional cell cultures was technologically challenged in terms of design and fabrication of suitable screening platforms.

1.3.3. Thesis structure

This thesis encompasses one theoretical and four experimental chapters. **Chapter 2** comprises a discussion on the theory of impedance measurements of single cells as well as of tissues, together with a description of non-cell-related impedance parameters. General recommendations on the design of planar impedance sensors are provided.

Experimental techniques and methods are partly recurrent throughout the thesis and therefore were summarized in **chapter 3**. A discussion on the analysis of cell-related impedance data is included. Furthermore, the procedural method of all performed numerical simulations is explained.

Impedance measurements on hepatocytes are presented in **chapter 4** and reveal the possibility to distinguish minor toxic effects on cells from major cell injury by choosing different but specific measurement frequencies. It is further discussed how such toxicity distinction is dependent on the cell density.

The acquired resistance of cells to drugs is impedimetrically studied in **chapter 5**. Drug-resistant breast cancer cells were compared with their parental cells regarding their response to doxorubicin, an anti-cancer drug. Distinct impedance changes within four distinct concentration ranges are discussed.

Chapter 6 describes the design and fabrication of a cell culture platform that allows measuring the impedance of the entire thickness of a 3D cell culture (instead of cell-substrate attachment only). The device is partly made of hydrogel that accounts for gentle drug delivery and that acts as virtual "gel electrodes".

A method for screening simultaneously multiple samples with only one electrode pair is presented in **chapter 7**. Instructions for designing such a frequency-multiplexing impedance sensor are provided.

The thesis concludes with a discussion on the significance of impedance technology for toxicology in **chapter 8**. All information that has not been considered vital for the comprehension of the presented results has been placed in the appendix. Moreover, a model, using similar microfluidic technology as was presented in the main part of this thesis, was developed for the study of disease propagation in Alzheimer's disease and is described in appendix E, together with a review of currently available microfluidic-based Alzheimer studies.

2. Bio-impedance theory

Impedance is defined as the opposition of a sample to the flow of an alternating current. The resulting dielectric response of a material to an external electric field is due to the polarization of localized (electronic and atomic polarization) as well as of mobile charges (electronic, atomic, orientational, counter-ion and interfacial polarization) and can be expressed by its permittivity ε and by its conductivity σ. For impedance measurements, a constant current I is applied and the voltage drop $\triangle V$ through the sample is measured. The relation of potential drop to the owing current is defined as impedance Z.

$$Z = \frac{\triangle V}{I} \tag{2.1}$$

Frequency-dependent impedance changes are based on the fact that permittivity contributions of certain relaxation processes[1] that follow the external field at lower frequencies disperse at higher ones. This leads to the conclusion that non-homogeneous samples show characteristic impedance spectra which can consequently be modeled and analyzed as equivalent electric circuits. By this means, biologic material does not represent a perfect dielectric insulator because ion movement outside the biological cell acts as a parallel current path which discharges the ideal cell membrane capacitor. This non-ideal behavior is represented by Z which is a unified term for capacitive and resistive behavior.

$$Z = R + jX = Re + jIm \tag{2.2}$$

R represents the resistive part (real, Re) and X the capacitive part[2] (imaginary, Im) of the biological sample. j is the imaginary number.

2.1. Cell-related impedance parameters and their biological meaning

2.1.1. Single cell impedance

The electric properties of a cell can be described by an equivalent circuit composed of a membrane capacitor C_{mem} with a series intracellular resistance R_{intra} and a parallel extracellular resistance R_{extra} (Isambert, 1998) (figure 2.1a). Accordingly, the current passes around the cell at low frequency (LF) due to the insulating nature of the cell membrane. The value of the corresponding extracellular resistor is characterized by the

---

[1] With increasing frequency, polarization of charges and permittivity will decrease because the direction of the applied electric field varies more quickly than the displacement and accumulation of charges.

[2] Inductive elements do not play a role when measuring the impedance of biological material.

In figure a):

$$C_{extra} = \frac{\varepsilon_{extra}}{\kappa_{extra}}$$

$$R_{extra} = \frac{\kappa_{extra}}{\sigma_{extra}}$$

$$C_{mem} = \frac{\varepsilon_{mem}}{\kappa_{mem}}$$

$$C_{intra} = \frac{\varepsilon_{intra}}{\kappa_{intra}}$$

$$R_{mem} = \frac{\kappa_{mem}}{\sigma_{mem}}$$

$$R_{intra} = \frac{\kappa_{intra}}{\sigma_{intra}}$$

In figure b):

$$R_0 = R_{extra}$$

$$\Delta \log R$$

$$X_{mem} = \frac{1}{j\omega C_{mem}}$$

$$R_\infty = \frac{R_{extra} \cdot R_{intra}}{R_{extra} + R_{intra}}$$

$$f_0 = \frac{1}{\omega R_0 C_m}$$

$$f_\infty = \frac{1}{\omega R_\infty C_m}$$

(a)   (b)
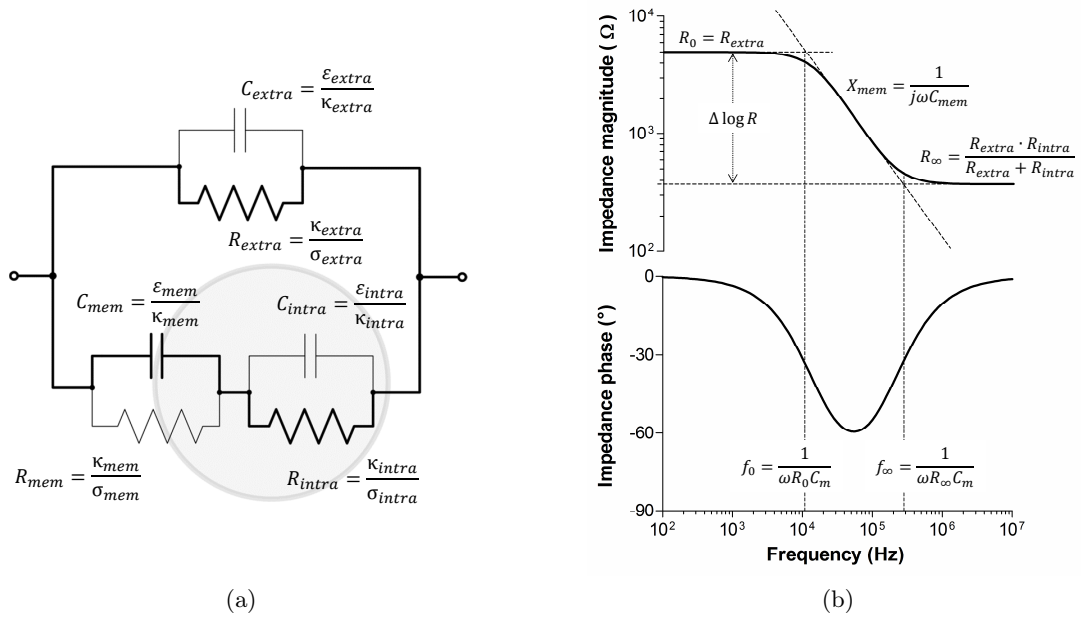
Figure 2.1.: Impedance of a single cell. a) Equivalent circuit model. κ_{ext}, κ_{int} and κ_m are cell constants and represent the volume along the potential gradient that is available to conduct the current outside and inside the cell as well as through the cell membrane respectively. These cell constants consequently depend on cell size, -shape, -orientation, -attachment and on the electrode configuration. The thicker line weight indicates the most often dominating current path within a frequency range of 40Hz-30MHz b) Bode plot of the presented equivalent circuit in a) (weigthed line). f_0 and f_∞ are the cut-off frequencies where the cell membrane reactance X_{mem} equals the zero and infinite frequency resistance R_0 and R_∞ respectively.

conductivity of the extracellular medium as well as by the volume dimensions along the potential gradient that is available to conduct the current (indirectly indicates cell size and cell-substrate binding). By increasing the frequency, the cell membrane capacitor is short-circuited and current passes through the cell. Hence, the high frequency (HF) impedance is determined by the intracellular resistance whereas intermediate frequencies provide information about the membrane capacitor. The value of C_{mem} is determined by the surface area of the cell membrane and scales with the cell size. The thickness of the cell membrane, on the other hand, was described to be constant ($5 - 7nm$) and is therefore ignored when studying relative differences of C_{mem}. The value of the intracellular resistance is a function of the intracellular conductivity as well as of the space available for conducting the current (cell size, number of organelles). The resistor originating from ion channels within the cell membrane R_{mem} is ignored since its resistance is in the $M\Omega$ range and related relative changes are negligible compared to the ones caused by R_{extra} (Borkholder, 1998). In addition, the intra- and extracellular solution may act as a capacitor (C_{extra} and C_{intra}) at very high frequency, however this exceeds the frequency measurement range that was used in this study. Therefore the capacitive properties of conductive solutions are ignored. The corresponding impedance spectrum of the above

described electrical circuit is shown in figure 2.1b.

2.1.2. Cell population impedance

When measuring the impedance of multiple cells within a tissue (figure 2.2a), the impedance spectrum differs from the one hypothesized for a single cell and displays a cell membrane relaxation slope of less than 1 over certain frequency ranges (figure 2.2b-2.2d) (Cole, 1932, see paper V on page 183). This is due to the fact that a tissue is composed of

(a)

(b)   (c)   (d)
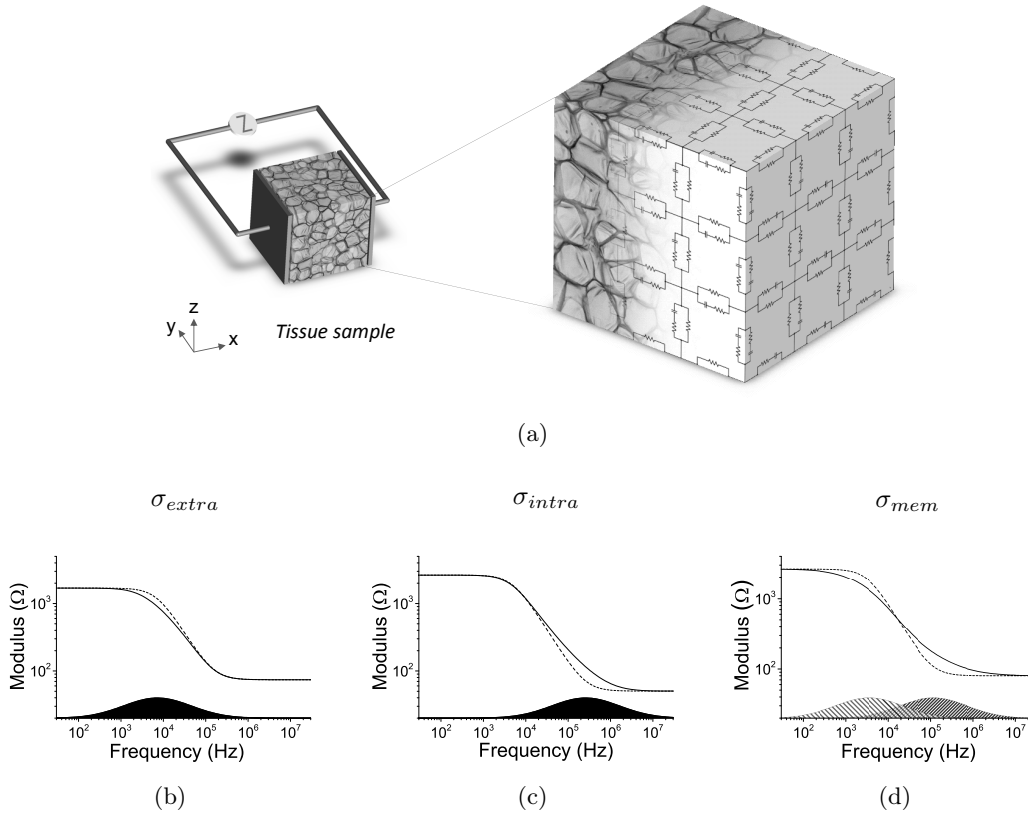
Figure 2.2.: Tissue impedance. a) Simplified equivalent tissue circuit; b), c) and d) show the impedance modulus with a distribution of $\sigma_d = 0.8$ for a) R_{extra}, b) R_{intra} and c) C_{mem}. The resulting curves are compared with the non-distributed curves (dashed line). The distribution curves on the x-axis represent the distribution of cut-off frequencies (f_0, f_∞).

thousands to millions of cells with every single cell being characterized by its specific properties and those of its micro-environment (e.g. distance to neighboring cells, cell size and amount of intracellular organelles). The multitude of cells within a tissue results in a distribution of these properties within a certain range of values, thus ultimately also leading to a distribution of the values of the individual electrical elements of a single cell circuit (R_{extra}, C_{mem}, R_{intra}).

The different elements of a single cell circuit impact distinct parts of the impedance

spectrum. The effect of their distribution within the complex tissue circuit is depicted in figure 2.2b-d. It is noted that each cell in the circuit has two cut-off frequencies ($f_0 = 1/(2\pi R_0 C_{mem})$ and $f_\infty = 1/((2\pi R_\infty C_{mem}))$ where the part of the spectrum at which the impedance is dominated by the membrane capacitance is separated from the parts at which the impedance is dominated by the resistance at zero frequency R_0 (f_0) and by the resistance at infinite frequency R_∞ (f_∞) (these frequencies are precisely defined by the phase being equal to 45°). When all three elements are the same in every cell of the whole tissue circuit, they also have the same cut-off frequencies resulting in an impedance behavior that is equivalent to the one of a single cell circuit (dotted line in figure 2.2b-2.2d). On the contrary, when R_{extra}, R_{intra} and C_{mem} are distributed, this also affects the distribution of f_0 and f_∞, albeit to a different extent: a deviation from the single cell spectrum occurs around f_0 when R_{extra} is distributed (figure 2.2b), around f_∞ when R_{intra} is distributed (figure 2.2c) and around both cut-off frequencies when C_{mem} is distributed (figure 2.2d). In all cases, the transition from resistive to capacitive regime and vice versa is shifted between the single cell circuits. As a consequence, the slope of the impedance modulus $|Z|$ is becoming smaller at these frequencies. Regarding a distribution of C_{mem}, both cut-off frequency distributions overlap if they are wide enough and almost no part of the impedance modulus has a slope of one anymore (figure 2.2d). In a tissue, all three elements are distributed, which leads to a combination of their effects on the impedance spectrum.

Although an element named constant phase element[3] (CPE, equation 2.3) was suggested by Cole (1940);

$$Z_{CPE} = \frac{1}{\beta(j\omega)^\alpha} \tag{2.3}$$

where β is the CPE magnitude, ω is the circular frequency ($\omega = 2\pi f$) and α is the CPE frequency exponent[4]; and used instead of a capacitance for almost a century to describe the particular dispersion behavior of cells in tissues (Halter et al., 2007; Kerner et al., 2002; Meissner et al., 2011), the physical meaning of its parameters (CPE$_c$ exponent α_c and magnitude β_c) has been controversial and for this reason the parameters themselves have been rarely used (Cole and Cole, 1941; Grimnes and Martinsen, 2005; McAdams and Jossinet, 1995). Several studies tried to interpret the α_c as an indicator of tissue heterogeneity in cell sizes and shapes (Ackmann and Seitz, 1984) as well as of heterogeneity in the extracellular space (Ivorra et al., 2005), but no precise explanation has been provided. In fact, the CPE$_c$ assumes a constant phase (of less than 90°) over frequency, which is not correct. In contrast, the distribution of all three circuit elements can be different leading to a frequency-dependent α_c. Therefore, we introduced a general element termed dispersion element (DE, see paper V on page 183) that within the tissue circuit (figure 2.3) perfectly describes the dispersion behavior of every tissue

---

[3] An index "c" is used for "cells" to distinguish the cellular CPE from the electrode/electrolyte CPE indexed by an "el" which will be introduced in section 2.2.1 on page 20.

[4] α and β from the CPE are not to be mixed up with the α- and the β-dispersion. There is no link between the symbols.

as illustrated in figure 2.2a owing to the frequency-dependence of its parameters (equation 2.4). However, this element is theoretical since its parameters cannot be found for
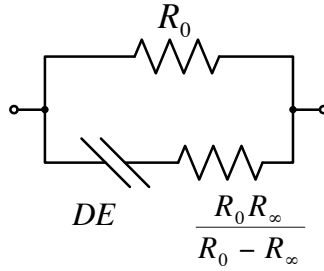
Figure 2.3.: General equivalent tissue circuit that models the complex tissue circuit from figure 2.2a

experimental measurements (see paper V on page 183).

$$Z_{DE} = \frac{1}{\beta(f) \cdot (j\omega)^{\alpha(f)}} \tag{2.4}$$

Different more or less simplified cases of the DE have been considered in the past. Both the capacitance and the CPE are dispersion elements that possess a constant α_c and thus a constant phase over frequency. A new, specific case of the DE was suggested and was termed logarithmic phase element (LPE). It is a more sophisticated element that takes into account (and thus informs about) the distribution weighting of the single cell circuit elements. However, the LPE is not subject of this dissertation and it is referred to paper V on page 183 for more information. Here, the cell membrane relaxation is approximated as a CPE to illustrate the non-linear relaxation behavior of cells within tissues.

Considering an isolated tissue, R_0 from figure 2.3 entirely depends on the tissue structure. However, when the tissue is sourrounded by a conductive solution (e.g. *ex vivo* and *in vitro* tissue culture, liquid layer on isolated organs) a shunting para-tissue current path is created that decreases the sensitivity of the impedance measurement for the trans-tissue impedance (figure 2.4). Therefore, it seems desirable to increase the
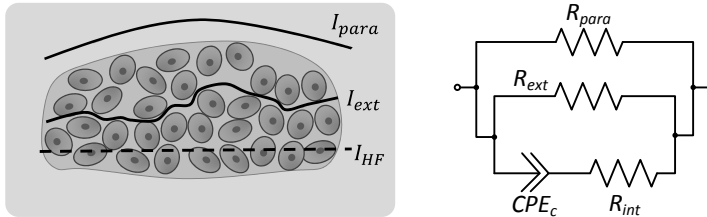
Figure 2.4.: Current paths of a tissue with surrounding solution. Low frequency current flows through the extracellular environment of the tissue (I_{ext}) and through the medium outside the tissue (I_{para}). The para-tissue current decreases the measurement sensitivity for the trans-tissue impedance. The high frequency current (I_{HF}) passes through the cells. The corresponding equivalent circuit is shown.

para-tissue resistance R_{para}. Although the measurement in air is feasible for most plant

tissues that possess evaporation protecting outer skins, this is hardly possible for cell aggregates and *ex vivo* tissues that undergo drying-out. Alternatively, the geometry of the measurement system can be adapted such that the space available for current shunting around the tissue becomes small. This strategy will be employed in chapter 6. Altogether, parameters that are related to the tissue structure itself (e.g. R_{ext}, CPE_c, R_{int}[5]) are distinguished from parameters that concern the measurement system (R_{para}). Uniquely tissue-characterizing parameters such as R_{ext}, R_{int} and $\triangle \log R$ (figure 2.1b) therefore need to be examined with care since R_0 is a function of R_{ext} and R_{para}[6].

2.2. Non-biological measurement parameters

When measuring the impedance of a biological sample, other effects than the ones from the tissue may contribute to the measured total impedance ($Z_{tissue} \neq Z_{measured}$). These additional effects originate from the measurement system and can be represented as electrical components that add up in series or in parallel to the tissue impedance depending on their nature (figure 2.5).
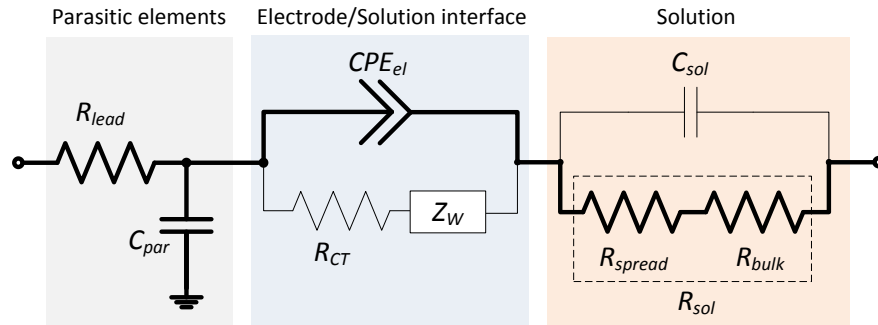
Figure 2.5.: Equivalent electrical circuit of non-biological measurement elements that contribute to the total impedance. R_{lead} is the resistance of the conductor used for wiring, C_{par} is the capacitance between the wiring traces where other traces are grounded for for AC signals, CPE_{el} is the constant phase element (non-ideal capacitor) of the electrical double layer at the electrode/electrolyte interface, R_{CT} is the charge transfer resistance, Z_W is the Warburg impedance, R_{sol} is the ionic solution resistance (composed of the spreading resistance R_{spread} and the bulk resistance R_{bulk}) and C_{sol} is the solution capacitance.

These additional elements are undesirable since they lead to a decreased measurement sensitivity for bio-impedance changes. In theory, the impact of their impedance can be minimized by tuning the multitude of parameters they are dependent on (ionic concentration, type of ions, temperature, geometry of the measurement system, electrode potential, material properties, electrode roughness, impurity adsorption etc.). For biological applications however, most of these parameters are inherently determined by the cell

---

[5] The elements of a tissue circuit are denoted by an abbreviated index (R_{ext}, R_{int}, C_m) in contrast to the ones of a single cell circuit (R_{extra}, R_{intra}, C_{mem}).

[6] Please note that in contrast to a tissue measurement, $R_0 = R_{extra} = R_{para}$ for a single cell measurement and therefore R_0 is determined by the cell and the measurement system simultaneously.

culture medium (specific pH and chemical composition), by the electrode material (noble metals such as platinum and gold are used owing to their high bio-compatibility (Itakura et al., 1989; Linderholm, 2006)) and by the cells themselves that require an incubation temperature of 37°C (for all human and most mammalian cells). Therefore, the measurement system geometry with its corresponding current path and energy dissipation pattern represents the major parameter that may be optimized (figure 2.6).
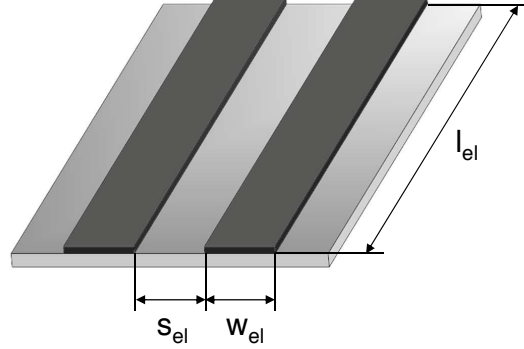
Figure 2.6.: Impression of a planar, rectangular electrode pair showing the electrode width w_{el}, electrode length l_{el} and the inter-electrode space s_{el}. The electrode geometry is the major parameter that may be modified such that the impedance originating from non-cell related system elements (figure 2.5) is minimized.

Table 2.1 overviews the model parameters from figure 2.5 and their dependance on frequency and geometry. A more detailed discussion on how electrode geometry influences the impedance measurement depth and sensitivity of planar electrodes is provided in section 2.3.

Circuit model component	Impedance scaling with frequency and geometry
CPE_{el} magnitude β_{el}	$|Z| \propto 1/A_{true}f$
CPE_{el} exponent α_{el}	$|Z| \propto f^{A_{true}/A_{geometric}}$
R_{CT}	$|Z| \propto 1/A_{true}$
Z_W	$|Z| \propto 1/A_{true}\sqrt{f}$
R_{spread}	$|Z| \propto 1/\sqrt{A_{geometric}}\sqrt{f}$
R_{bulk}	$|Z| \propto s_{el}/A_{cross}$
C_{sol}	$|Z| \propto 1/A_{geometric}f$
C_{par}	$|Z| \propto 1/A_{trace}f$
R_{lead}	$|Z| \propto l_{trace}/A_{trace}$

Table 2.1.: Scaling of theoretically derived model parameters with frequency and surface area (adapted from Kovacs (1994)). A_{true} is the true surface area of a surface including pores. $A_{geometric}$ is the apparent surface area excluding pores ($= w_{el} \cdot l_{el}$). A_{cross} is the cross-sectional area in the direction of the electric field and A_{trace} is the surface area of the electrode traces and wiring. l_{trace} is the length of the wires and electrode traces.

2.2.1. Electrode interface

When a metal is immersed into an ionic solution, a space charge layer builds up at the electrode/electrolyte interface (Kovacs, 1994). This layer is due to chemical reactions where metal atoms go into the solution to form ions and to charge the metal surface. This process reaches an equilibrium with a constant flow of charge across the interface and a net flow of zero. The resulting space charge layer separates the charged electrode from the charged ions and can be distinguished into three separate layers: (1) a hydration sheath of water molecules (inner Helmholtz plane), (2) hydrated cations (outer Helmholtz plane) and (3) a diffuse layer with a decreasing gradient of hydrated cations (figure 2.7a, top). The first two layers have been described by the Helmholtz-Perrin
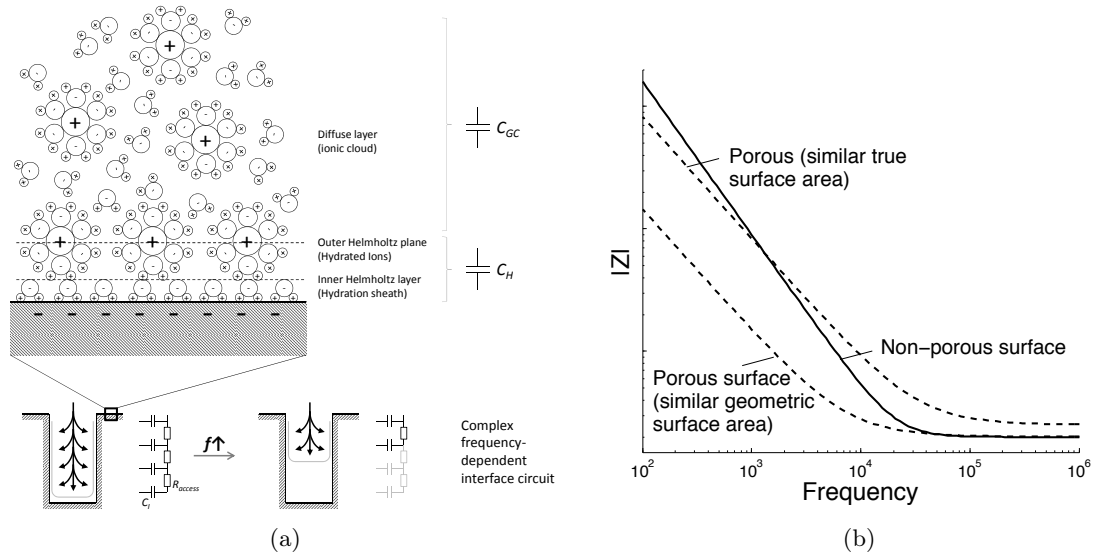
Figure 2.7.: Complex interface capacitance. a) The presence of pores on the metal surface leads to an impedance magnitude slope of less than 45° in contrast to ideally non-porous surfaces. While the true surface area of an electrode takes into account the surface from the pores, the geometric surface is referred to the apparent area (without pores). When kept constant, both cases (similar geometric and similar true surface area) have the same slope, nonetheless their capacitance and bulk resistance values differ. b) Top: Illustration of a space charge layer at the electrode/electrolyte interface that is composed of a layer of oriented water molecules, a layer of fixed hydrated cations and a diffuse layer of free hydrated cations (Kovacs, 1994). Those layers together define the interface capacitance C_I. Adsorbed species are not taken into consideration here. Bottom: The equivalent electrical interface circuit is complex and distributed due to surface roughness with fractal porous structures. In addition, the complex circuit is frequency-dependent since the current flows only through the outer areas of the pore when the frequency is increased (Ivorra et al., 2005).

model where the voltage decreases linearly and the resulting Helmholtz capacitance C_H is voltage-independent. The third layer was described by the Gouy-Chapman model where a diffuse capacitance C_{GC} was considered voltage-dependent. Both layers alone do not fully match with experimental results, but their combination represents a good approximation (Stern model) and gives rise to the interface capacitance C_I according to

equation 2.5. Nevertheless, C_H becomes more important for higher solute concentration and higher applied voltage.

$$\frac{1}{C_I} = \frac{1}{C_H} + \frac{1}{C_{GC}} \tag{2.5}$$

Furthermore, experimental measurements have revealed that the impedance magnitude caused by C_I has a slope of less than 1 in the frequency domain (figure 2.7b). This phenomenon has been explained by the imperfect nature of the metal where surface roughness (De Levie, 1965) and protein deposition (Stieglitz, 2004) lead to a more fractal nature with a distribution of capacitive and resistive properties (figure 2.7a, bottom). Additionally, as frequency increases, the current flows through the outer areas of the pore and that reduces the effective capacitance and resistance resulting in an electrode pore impedance that is frequency-dependent (Ivorra et al., 2005). For these reasons, the complex nature of the electrode/electrolyte interface is best approximated by a constant phase element (CPE_{el}), a circuit element that represents a capacitance with resistive properties.

As was mentioned above, the net flow of the charge through the interface reaches an equilibrium in the absence of an applied voltage V (direct current, DC). By increasing the voltage, the total potential across the interface is pushed away from from its equilibrium value V_0. This potential difference $V - V_0$ is termed overpotential μ and is responsible for the net flow of charge. It gives consequently rise to a charge transfer resistance R_{CT} that adds up in parallel to the interface capacitance. The overpotential is thought to be the sum of different overpotentials (μ_t: charge transfer through the double layer, μ_d: diffusion of reactants to and from electrode, μ_r :due to chemical reactions at the electrode, μ_c: due to exchange of metal atoms with corresponding ions). For low magnitudes of the applied voltage, the electrode will not be greatly perturbed from equilibrium (linear behavior). At high magnitudes however, the charge transfer resistance decreases exponentially with applied potential (non-linear behavior). Under alternating current (AC) conditions, an additional diffusion impedance termed "Warburg" impedance Z_W adds up in series to the charge transfer resistance (Kovacs, 1994). It represents the frequency-dependence of the diffusion effects. Ions cannot follow when the direction of the electric field changes too quickly, resulting in Z_W approaching to zero. Both, R_{CT} and Z_W, are relevant elements that need to be considered when high voltages are applied to the system and when measurements are carried out at low frequencies. In this work however, low voltage was applied ($10mV$, no DC bias) resulting in non-measurable effects of these elements within the screened frequency range ($40Hz - 30MHz$) (see figures 4.5a on page 43, 6.6b on page 70, 7.7 on page 81). Therefore, both circuit components were neglected for equivalent circuit fitting in this thesis.

2.2.2. Electrolyte impedance

When the frequency of the alternating current is increased, the interface capacitance is short-circuited and the sample between the electrodes is probed. The solution conducts the current in the presence of ionic charge carriers and its resistance consequently de-

pends on the ionic concentration, type of ions, temperature, and the geometry of the area in which current is carried. The major problem in calculating R_{sol} is due to the determination of the current flow path since this one is non-uniform in most cases (figure 2.8) (Davey, 1993). The geometrical factor or cell constant κ which accounts for such non-
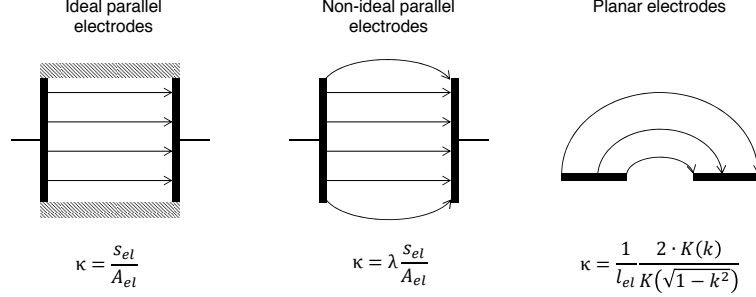
Figure 2.8.: Electric field distribution for parallel and planar electrodes. In the ideal case, current-lines are uniformly distributed. In reality, however, spreading of the current lines occurs. A factor λ is introduced to correct the fringing effect. The field distribution of coplanar electrodes is non-uniform and an analytical solution for the cell constant κ is obtained through conformal transformation (Jacobs et al., 1995). $K(x)$ is the complete elliptic integral of the first kind and k its modulus. An analytical solution of k is given in table 2.2.

uniformity and for the geometry of the electrolyte is determined experimentally for every measurement system (equation 2.6) and an analytical solution may be found through computation using conformal mapping. Table 2.2 provides a summary of equations for several configurations of planar, bipolar electrodes.

Electrode configuration			Cell constant κ	Sub-equation	Ref.
$h > 1.25 \cdot s_{el}$	$s_{el} \approx w_{el}$	coplanar	$\kappa = \frac{1}{l_{el}} \frac{2K(k)}{K\left(\sqrt{1-k^2}\right)}$	$k = \frac{s_{el}}{s_{el}+2w_{el}}$	[1]
		IDE	$\kappa = \frac{1}{l_{el}(n-1)} \frac{2K(k)}{K\left(\sqrt{1-k^2}\right)}$	$k = \sin\left(\frac{\pi}{2} \frac{s_{el}}{s_{el}+2w_{el}}\right)$	[2]
	$s_{el} \gg w_{el}$	coplanar	$\kappa = 2\frac{\ln(4l_{el}/w_{el})}{\pi l_{el}}$	n/a	[3]
$h < 1.25 \cdot s_{el}$	$s_{el} \approx w_{el}$	coplanar	$\kappa = \frac{1}{l_{el}} \frac{4K(k^2)}{K\left(\sqrt{1-k^2}\right)}$	$k =$Eq. 3.48 and 3.41 in [4]	[5]
	$s_{el} \gg w_{el}$	coplanar	$\kappa = \frac{1}{w_{ch}} \left(\frac{s_{el}}{h} + \frac{4ln(2)}{\pi}\right)$	n/a	[6]

Table 2.2.: Cell constants of various planar, bipolar electrode configurations. h is the distance between the planar electrodes and a top insulating wall. An h of more than $1.25 \cdot s_{el}$ corresponds to the case where there is no insulating top wall (Linderholm, 2006, p.72). w_{ch} is the width between two insulating walls in longitudinal direction (along s_{el}) and may equal l_{el} if the electrode reaches over the whole micro-channel; (IDE - interdigitated electrodes); References: [1]: Olthuis et al. (1995); [2]: Van Gerwen et al. (1998); Olthuis et al. (1995); [3]: Kovacs (1994); [4]: Linderholm (2006); [5]: Linderholm (2006, p. 73-78); [6]: appendix B on page 97

The solution resistance is generally composed of a spreading resistance R_{spread} and a series bulk resistance R_{bulk} (figure 2.9). In fact, when the electrode surface area is small compared to the inter-electrode distance (s_{el}), most of the electric energy is dissipated

very close to the electrodes within a zone that is called spreading or constriction zone of the current path. The spreading of the current from the small electrode into a larger electrolyte volume results in a spreading resistance that is determined by the geometrical surface area of the electrode (Franks et al., 2005). The current constriction diminishes from a certain distance of the electrode and the current lines are more uniform. This zone is termed segmental zone and defines the bulk resistance.

(a)   (b)
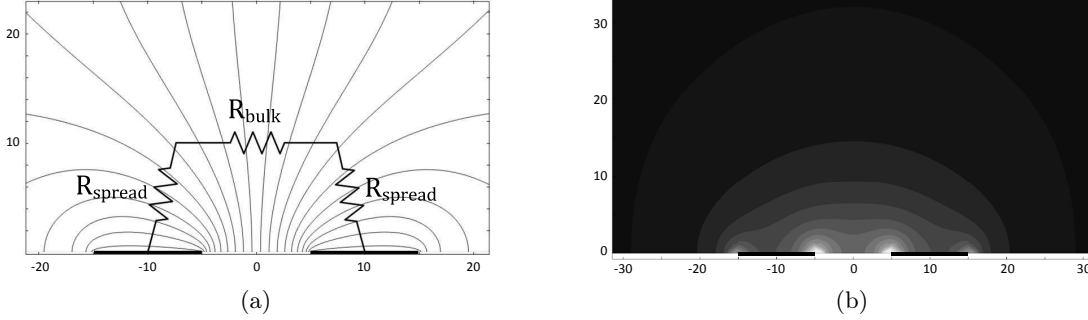
Figure 2.9.: Inhomogeneous solution resistance distribution over distance from planar electrodes. a) Simulated equipotential lines indicate stronger potential drop close to the electrode compared to deeper in the sample. Thus, the solution resistance is distinguished into spreading resistance R_{spread} and bulk resistance R_{bulk}. b) Simulated electric field indicates that energy disspiation is constricted to a zone close to the electrodes.

Although an ionic solution acts as a resistor over a wide frequency range it behaves like a capacitor at very high frequency where the ionic charge carriers cannot follow the direction change of the electric field. Similarly to R_{sol}, the solution capacitance C_{sol} is related to κ (equation 2.6).

$$\kappa = \sigma_{sol} R_{sol} = \frac{R_{sol}}{\rho_{sol}} = \frac{\varepsilon_0 \varepsilon_{sol}}{C_{sol}} \tag{2.6}$$

where σ_{sol} is the conductivity of the solution, ε_0 is the dielectric constant of free space and ε_{sol} is the relative dielectric constant of the solution.

2.2.3. Parasitic elements

Parasitic elements that contribute to the total impedance in this work are those of the wiring resistance R_{lead} and of the parasitic capacitance C_{par} such as the stray capacitance to adjacent signal lines (other capacitances through the substrate and passivation layers may be considered where applicable). Although parasitic elements can be eliminated with apparatus calibration (artificial offset), this does not compensate for the sensitivity loss that is caused by those elements. Therefore, it is recommended to use short and shielded wires and to short-circuit current injection and voltage measurement electrodes as close as possible to the biological sample.

2.3. Geometrical factors of coplanar electrodes

Although planar electrodes display a less uniform electric field distribution compared to parallel electrodes and thus a position-dependent sensitivity pattern, they are widely used in micro-technological devices due to their ease of fabrication and thereby associated low costs. Moreover, the localization of a measurement can be chosen by varying the electrode size, e.g. the detection of single cells requires electrodes of similar sizes. Therefore, planar electrodes assure sensitive and repeatable measurements thanks to simple, standard microfabrication methods.

In this work, coplanar bipolar electrodes have been used to measure the impedance of cell populations. This section discusses how the depth and the sensitivity of an impedance measurement depend on the electrode geometry and how to optimize them by carefully choosing the geometric parameters.

2.3.1. Measurement penetration depth

The impedance measurement depth is defined according to the local energy distribution within the sample and corresponds to the depth below which half of the electric energy is dissipated (Linderholm, 2006). The measurement depth $z_{1/2}$ is given by

$$\iint_{0}^{\infty} \int_{0}^{z_{1/2}} E^2(x,y,z)dxdydz = \frac{1}{2} \iiint_{0}^{\infty} E^2(x,y,z)dxdydz \qquad (2.7)$$

where E is the local electric field. This equation was solved numerically for different electrode spacing s_{el} and widths w_{el} while keeping the electrode length l_{el} constant (figure 2.10a). The penetration depth non-linearly increases for larger values of s_{el} and w_{el}. When normalizing the penetration depth against the sensor size ($w_{el} + s_{el}$), it was found that the measurement depth is small for thin electrodes since the spreading resistance dominates the measurement and most of the energy will be dissipated close to the electrodes (figure 2.10b). When w_{el} is larger than s_{el}, the measurement depth will also be small since most of the current passes between the inner edges of the electrodes. A penetration depth within 10% of the maximum depth regarding the sensor size is therefore obtained when $w_{el} \approx 0.5...3 \times s_{el}$.

In a next step, the measurement depth was numerically solved for different electrode lengths (figure 2.11a). The measurement depth is small for short electrodes since most of the current passes between the bottom and top (longitudinal) edges of the two electrodes. This edge effect becomes negligible when the electrodes are longer, hence the penetration depth saturates. It was found that $z_{1/2}$ was maximal when $l_{el} \gtrsim 9 \cdot s_{el}$ (figure 2.11b). However, larger than this value does not result in a larger measurement depth.

2.3.2. Measurement sensitivity

Although the maximal β-dispersion bandwidth is fundamentally defined by the tissue itself according to $\log(\varepsilon_\alpha/\varepsilon_\delta)$ (where ε_α and ε_δ are the dielectric constants of the α-

(a) (b)
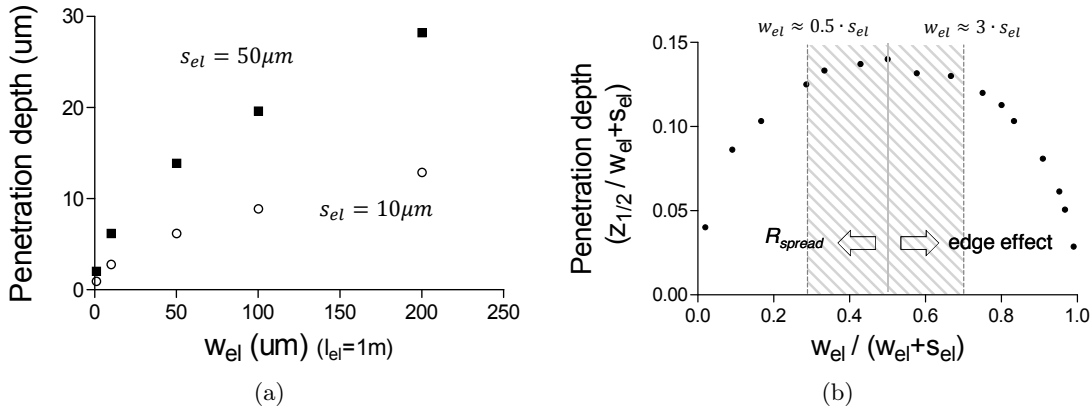
Figure 2.10.: Optimization of fractional sensor width for maximal penetration depth using numerical simulation. a) Penetration depth as a function of w_{el} and s_{el} with $l_{el} = \infty$. b) Size-normalized penetration depth points out an optimal compromise between spreading resistance and edge effects at $w_{el} = s_{el}$. The dashed zone illustrates the $w_{el}/(w_{el} + s_{el})$-range where the depth is within 10% of the maximum penetration depth. The irregularities are due to numerical errors. Details about the numerical simulation are provided in section 3.8 on page 35.

and δ-dispersion respectively), in reality this bandwidth is often smaller. The measured impedance may increase at lower frequencies and decrease at higher ones due to the double layer capacitance at the electrode surface and to the stray capacitance between measurement cables respectively. Both add a frequency-dependent error to the measured solution resistance and lead to a decreased β-dispersion bandwidth as depicted in figure 2.12a. To reduce this error, it is necessary to maximize the corresponding bandwidth within which the tissue measurement sensitivity is always above 0.707 (equals a phase angle of -45°). This optimization requires all three components of the β-dispersion bandwidth to be maximized: 1) the R_{ext}-bandwidth is maximized according to

$$\frac{f_0}{f_{el}} = \frac{C_{el}}{C_\beta} \propto \kappa \cdot A_{el} \tag{2.8}$$

where $f_{el} = 1/2\pi R_0 C_{el}$ and $C_\beta = C_m$.
2) The X_m-bandwidth calculates as follows

$$\frac{f_\infty}{f_0} = \frac{\sigma_\infty}{\sigma_{ext}} \tag{2.9}$$

where σ_{ext} is the extracellular conductivity of a tissue and σ_∞ is the infinite frequency conductivity of the β-dispersion[7].

This bandwidth is normally defined by the tissue sample and should therefore not be affected by a measurement system optimization. However, as was shown in figure 2.4, para-tissue currents can create a leak that results in a decreased $\triangle \log R$.

---

[7] $f_\infty/f_0 = \triangle \log R$ for non-distributed tissues (entirely homogeneous, $\alpha_c = 1$), otherwise $f_\infty/f_0 > \triangle \log R$ with $\alpha_C = \triangle \log R/(f_\infty/f_0)$

(a)

(b)
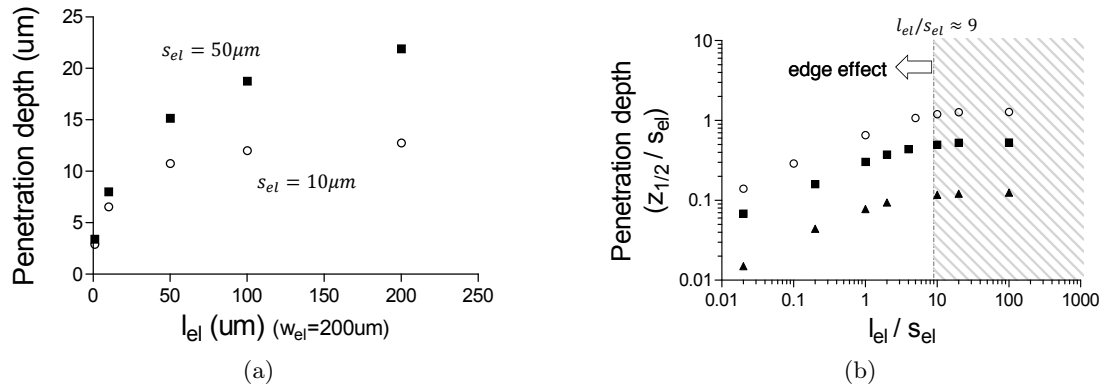
Figure 2.11.: Optimization of fractional sensor length for maximal penetration depth using numerical simulation. a) Penetration depth as a function of l_{el} and s_{el} with $w_{el} = 200\mu m$. b) s_{el}-normalized penetration depth illustrates a maximum depth at a $l_{el}/s_{el} \gtrsim 9$ (circles: $w_{el} = 200\mu m$, $s_{el} = 10\mu m$; squares: $w_{el} = 200\mu m$, $s_{el} = 50\mu m$; triangles: $w_{el} = 10\mu m$, $s_{el} = 50\mu m$). The dashed zone illustrates the length-spacing-ratio range where the depth is within 10% of the maximum penetration depth. The irregularities are due to numerical errors. Details about the numerical simulation are provided in 3.8 on page 35.

3) The R_∞-bandwidth is maximized according to

$$\frac{f_{par}}{f_\infty} = \frac{C_\beta}{C_{par}} \propto \frac{d_{wires}}{\kappa \cdot A_{wires}} \tag{2.10}$$

Finally, it is recommended to first minimize the effect of the stray capacitance $C_{par} \propto A_{wires}/d_{wires}$ where d_{wires} is the distance between signal current paths (cables) and A_{wires} is the surface area of these wires. An elimination of capacitive stray effects can be achieved (1) by employing coaxial cables (shielding) to generally reduce the effect of C_{par} (reduced A_{wires}), (2) by placing the conductors such that the distance between both signal current paths (d_{wires}) is maximal and (3) by compensating for the fixtures with an open calibration. It is noted that the R_∞-bandwidth is maximized up to a certain limit that is defined by the ratio of the δ- and β-dispersion capacitances and thus by $\varepsilon_\beta/\varepsilon_\delta$ (figure 2.12a). This first optimization mostly diminishes the impact of a large cell constant[8] on the R_∞-bandwidth that in turn is needed for a maximization of the R_{ext}-bandwidth. The product of equation 2.8 corresponds to a minimization of f_{el} since $f_0 = \sigma_{ext}/2\pi\varepsilon_\beta$ only depends on inherent tissue properties. This requires w_{el} and s_{el} to be as large as possible. Taking into account the total sensor size ($w_{el} + s_{el}$), a relation of $w_{el} = 1...9 \times s_{el}$ was found to be advantageous (figure 2.12b). When w_{el} is even larger, most of the current passes at the inner edge of the electrodes, thus decreasing the apparent electrode width and resulting in a higher f_{el}. In addition, the minimization of f_{el} does not depend on l_{el} as long as $s_{el} \approx w_{el}$ (table 2.2).

---

[8] The cell constant is constant for all cut-off frequencies as long as the tissue and the electrode dimensions (w_{el}, s_{el}, l_{el}) are much larger than the size of the single cells that compose the tissue. The tissue is then considered as homogeneous.
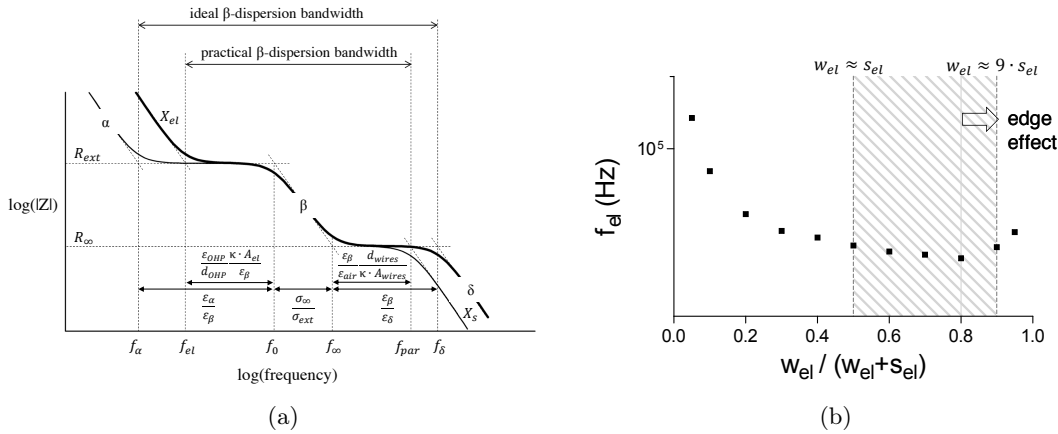
Figure 2.12.: Optimization of measurement bandwidth. a) The maximum β-dispersion bandwidth is defined by the α and δ-dispersions. This maximal bandwidth is decreased by the electrode interface capacitance C_I and the stray capacitance C_{par} between the signal cables (practical β-dispersion bandwidth). This scheme assumes a large tissue and electrode compared to the size of a single cell and thus a constant cell constant κ for all cut-off frequencies. b) f_{el} is plotted against the sensor size normalized electrode width. The dashed area indicates the $w_{el}/s_{el} + s_{el}$-range where f_{el} is within 10% of the minimum value. The irregularities are due to numerical errors. Details about the numerical simulation are provided in section 3.8 on page 35.

2.4. Summary

Cell impedance is not constant with frequency due to the capacitive behavior of the cell membrane. Current flows outside the cell at lower frequencies and through the cell at higher ones. Such frequency-dependence can be exploited to extract information about cell-cell contacts and the cytosol for example. However, the bandwidth within which the tissue impedance is measured sensitively may be decreased by the electrode interface capacitance at lower frequencies and by parasitic stray capacitances at higher ones. Therefore, it is important to optimize the electrode geometry such that the bandwidth is increased. Two general rules should be considered when designing impedance sensors: (1) The total sensor size needs to be identified first ($w_{el} + s_{el}$ and l_{el}). This size may be determined by space restrictions (e.g. within a micro-channel or on an implanting probe) or by the tissue sample itself. In fact, if the electrode is larger than the biological sample, this leads to a decreased X_m-bandwidth and thus to a decreased sensitivity. If the electrode is smaller than the tissue sample, on the other hand, this leads to an increased spreading resistance and again to a decreased sensitivity. Therefore, the sensor is ideally within the size range of the biological sample volume which is measured (e.g. $l_{el} \approx s_{el} \approx 10 - 20 \mu m$ for single cells or $s_{el} = 100 \mu m$ for brain slices). (2) Once the maximum sensor size has been determined (A_{el} and $w_{el} + s_{el}$) the planar bipolar sensor dimensions should be chosen such that $w_{el} = 1...2 \times s_{el}$ and $l_{el} \geq 9 \times s_{el}$ in order to harmonize a maximal penetration depth with a maximum β-dispersion bandwidth.

3. Methods

3.1. Microfabrication

3.1.1. Microfluidic chips

Microfluidic chips were made of polydimethylsiloxane (PDMS) and fabricated by soft-lithography. The fabrication of the mold was carried out using two different methods depending on the critical dimensions. For structures larger than $100\mu m$, a cutter plotter (Robopro CE5000-40-CRP, Graphtec) was used to cut and structure a $120mm$ thick tape that was adhered onto a transparent foil. For structures smaller than $100\mu m$, a silicon wafer with oxidized surface ($1\mu m$) was structured by photolithography (coating and development: EVG150; exposure: Süss MA6) and deep reactive ion etching (Alcatel AMS 200 DSE). The obtained tape or silicon master were then used to mold the PDMS. For this, Silicone elastomer was mixed with curing agent (Sylgard 184, Dow Corning) at a ratio of $10:1$, degassed for $30min$ in a desiccator and cured at $80°C$ for at least $1h$. Holes punched through the PDMS served as injection reservoirs. The PDMS block is further placed on top of a glass slide with micro-fabricated electrodes.

3.1.2. Electrode chips

Platinum was used as electrode material since it is bio-compatible (Itakura et al., 1989) and highly polarizable, thus minimizing faradaic currents and reducing the risk of generation of cytotoxic compounds (Linderholm, 2006). A $20nm$ thick titanium adhesion layer and a $200nm$ thick platinum layer were evaporated in that order and structured on a 4-inch glass substrate using standard photo-lithographic lift-off technique. Electrode edges were rounded up to reduce fringing effects and local current concentration (Kasi et al., 2011).

3.2. Cell culture

HepG2/C3A and MCF-7 cells (wild-type (WT) and resistant to $1µg/ml$ doxorubicin (DOX)) were kindly provided by Prof. Beatrice Desvergne (University of Lausanne) and by Prof. Kapil Mehta (The University of Texas M. D. Anderson Cancer Center, Houston) respectively. All cell lines were maintained at $37°C$ and 5% CO_2 and cultured in $75cm^2$ flasks. MCF-7 cells were incubated in Roswell Park Memorial Institute medium (RPMI) 1640 (Sigma-Aldrich, Switzerland) supplemented with 10% fetal calf serum (Invitrogen, Switzerland), $2mM$ glutamine and antibiotics (100 U/ml penicillin and $100µg/ml$ streptomycin) (Invitrogen, Switzerland). MCF-7 DOX cells were additionally cultured in
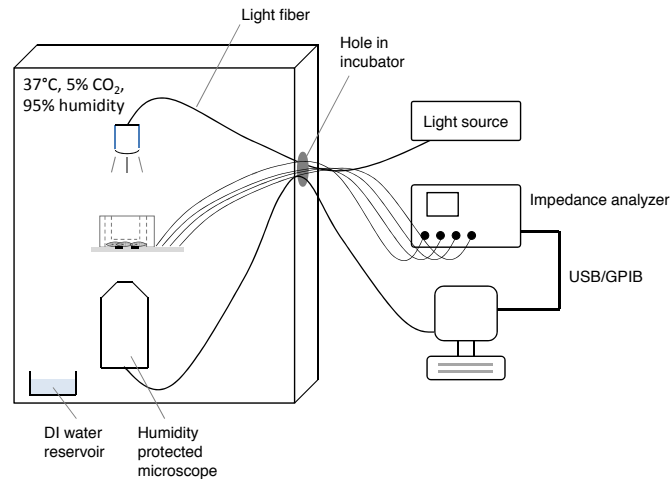
Figure 3.1.: Experimental setup

the presence of 1µg/ml doxorubicin (LC Laboratories, USA) in order to maintain the drug-resistance phenotype. HepG2 cells were incubated in Dulbecco's Modified Eagle's Medium (DMEM) (Invitrogen, Switzerland), containing 10% fetal calf serum (Invitrogen, Switzerland). Medium was changed every three days. Once cell confluency was reached, cells were detached with 0.25% trypsin/EDTA (Invitrogen, Switzerland), counted with a hemacytometer (Sigma-Aldrich, Switzerland) and loaded into the microfluidic chips.

For the microfluidic cell culture, all materials were autoclaved before use except for poly-(methyl-methacrylate) (PMMA) parts that were disinfected with 70% ethanol before use. The glass chip with electrodes and the PDMS chip were surface treated ($50W$, $0.6min$, $0.6bar$) using oxygen plasma (Femto SLS, Diener electronic, Germany). The assembled PDMS and electrode chip were connected to a printed circuit board (PCB) for electrical measurements.

3.3. Experimental setup

The devices were placed into the CO_2 - incubator on top of a microscope with a humidity-protected objective (Precise Eye, Navitar, USA) connected to a C-mount camera (uEye, IDS Imaging, Germany) and an optical light fiber that was attached to a light source outside the incubator. The objective inside the incubator allowed visual follow-up of the microfluidic culture. Tubing was used to connect the inlet of the PDMS chip to the medium reservoir. The tube from the outlet reservoir of the PDMS chip was connected to a syringe pump (NE-300, TSE-Systems, USA). Coaxial cables were used to connect the device to an impedance analyzer (Agilent 4294A, Agilent technologies, USA). A small hole at the back of the incubator connects the inside equipment with the humidity sensitive outside equipment. The impedance analyzer was connected to a PC via a GPIB controller (Universal Serial Bus (USB)-GPIB-HS, National Instruments, USA).

3.4. Immunocytochemistry

For immunocytochemical staining, cultures were fixed with 4% paraformaldehyde in phosphate buffered saline (PBS) (Invitrogen, Switzerland) for $25min$. After washing, cells were dried and stored at $-20°C$ until use. After thawing, HepG2/C3A and MCF-7 cells were treated with 3% bovine serum albumin (BSA)/0.1% Triton X-100 (both Sigma-Aldrich, Switzerland) for $45min$. For tight junction staining, cells were first incubated with the primary antibody monoclonal rabbit-anti-occludin (1:200, Invitrogen, Switzerland) for $90min$ and subsequently with the Cy-2 coupled secondary antibody (1:150, Dianova GmbH, Germany) for $2h$. For actin staining, cells were incubated with fluorescein isothiocyanate (FITC) coupled phalloidin (Sigma-Aldrich, Switzerland) for $2h$. Subsequently, samples were incubated with $0.1µg/ml$ 4',6-diamidino-2-phenylindole (DAPI) in PBS (Sigma-Aldrich, Switzerland) for $30min$. After repeated washing, cells were observed with a confocal laser scanning microscope (LSM 700 inverted, Zeiss, Germany). 3D Images were obtained from z-stack acquisition mode by using the 3D image processor Imaris (Switzerland).

For live/dead staining, cells were washed with PBS and incubated with staining solution of fluorescein-diacetate and propidium iodide (1:1000, Sigma-Aldrich, Switzerland) for 10 min. Samples were examined with a fluorescence microscope (LSM 700 inverted, Zeiss, Germany).

3.5. Cell viability assay

(3-(4,5-Dimethylthiazol-2-yl)-2,5-diphenyltetrazolium bromide (MTT) stock solution was prepared by dissolving $2.5mg$ MTT/ml in PBS without Ca/Mg. Cells were seeded into a 96-well plate and incubated for 2 days. Cell medium was removed and cells were incubated in $200µl$ AP solution ($20mM$) at different times ($2h$, $6h$, $8h$, $24h$). After drug exposure, cytotoxicity was determined by removing the drug solution and adding $200µl$ of fresh medium + $50µl$ of MTT stock solution. Following 3 h incubation at 37°C, MTT-DMEM medium solution was removed and $150µl$ of Dimethyl sulfoxide (DMSO) was added. After shaking well for $30min$, absorbance was analyzed at $590nm$ using a micro-plate reader.

3.6. Impedance spectroscopy

3.6.1. Measurement technique

Impedance spectra were recorded from minimum $40Hz$ to maximum $30MHz$ ($10mV$ amplitude, $0mV$ bias, 100 points per sweep) using the computer-controlled (Matlab, Mathworks) impedance analyzer (Agilent 4294A, Agilent technologies, USA). The software was programmed to carry out a given number of measurements at a given interval.

3.6.2. Impedance data analysis

Three different analysis methods to evaluate recorded impedance data have been used in this work.

1. Equivalent circuit fitting. The impedance spectra have been fitted to the equivalent circuit model from figure 2.5 (without cells; strong line) and figure 2.2a (with cells; with the DE represented by a CPE). Accordingly, cell-dependent circuit components such as R_{ext}, R_{int} and CPE_c (α_c and β_c) were obtained. First, the impedance spectra of the medium without cells were fitted and α_{el}, β_{el} and C_{par} were extracted. By fixing these three system components, the impedance spectra with cells were fitted and R_{ext}, R_{int} β_c and α_c were determined. Equivalent circuit fitting is convenient since it allows attributing values to all elements of a specific circuit model. However, this method carries several drawbacks. There may be different circuit models that result in low fitting error indicating that the extracted values depend on the chosen circuit and therefore are prone to misinterpretation. Furthermore, the used fitting algorithm may also find several non-relevant solutions for the same circuit model. This is especially true for cell cultures at low density where the impedance curves with and without cells are not different enough and the number of fitting cycles is limited. Overall, fitting of impedance data to an equivalent circuit is very useful when characterizing cell cultures at high density (exerting high R_{ext}) since circuit elements can be compared between cell models for example.

2. Maximum cell index. The impedance is followed-up over time at one frequency where the contribution of cells to the magnitude is at its maximum, i.e. where the difference between the impedance magnitude profile in the presence of cells and that in the absence of cells is largest. This frequency corresponds to the one with the highest sensitivity to cellular changes and is determined by finding the maximum relative impedance value according to equation 3.1. The corresponding impedance magnitude is referred to as cell index in literature (Otero-González et al., 2012).

$$CI = max_{i=1,...,n} \left[\frac{|Z|_{cells}\,(f_i) - |Z|_{medium}\,(f_i)}{|Z|_{medium}\,(f_i)} \right] \tag{3.1}$$

where $|Z|_{cells}\,(f_i)$ is the frequency-dependent impedance magnitude in the presence of cells and $|Z|_{medium}\,(f_i)$ the one in the absence of cells. n is the total number of frequency points at which the impedance was measured. Although this method is very sensitive, it neglects the dielectric nature of a cell. In fact, the cell-index frequency not only depends on the membrane relaxation frequency but also on the measurement system (electrode/electrolyte interface capacitance and parasitic capacitance) and therefore it remains unclear what exact circuit element is contributing most to the cell index. This method is suitable for measurements where simply the presence of cells is of interest such as for cell-substrate attachment.

3. Frequency-dependent cell index. This method considers cells as shell-covered spheres where cellular parameters can be distinguished within frequency ranges. This is similar to equivalent circuit fitting, but the analysis is carried out on the raw data and no equivalent electrical model is required. It is simply assumed that the LF magnitude mostly informs about R_{ext} and the HF magnitude mostly about R_{int}. Ideally, LF is

chosen very small and HF very high in order to avoid the impact of the cell membrane capacitor. However, due to the natural imperfection of the measurement system (electrical double layer capacitance at LF and parasitic capacitance at HF), it is necessary to compromise between decreased measurement sensitivity at the extremity frequencies and increased impact of the cell membrane capacitor (figure 3.2). Therefore, LF and HF are chosen such that the influence of C_{el} and C_m as well as of C_m and C_{par} are minimized respectively. In practice, the choice of LF and HF is not trivial since peak resistance
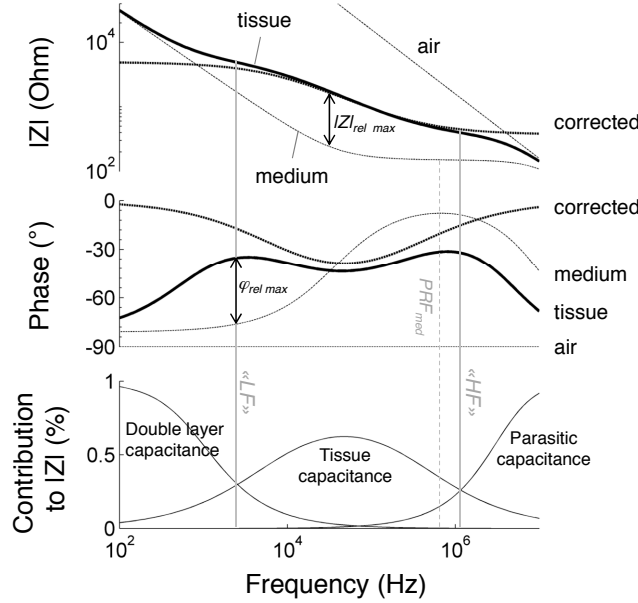
Figure 3.2.: Choice of LF and HF as a function of relative contribution of capacitive components to the measured $|Z|$. The LF and HF impedances are measured at the frequencies where the capacitive contribution from the interface capacitance, the membrane capacitance and the parasitic capacitance are minimal and thus where resistive changes are highly sensitive. The impedance spectrum was simulated according to the equivalent electrical circuit as depicted in figure 2.5 where the solution was replaced by a tissue circuit as shown in figure 2.3 with a DE approximated as a CPE ($\beta_{el} = 10^{-7}\Omega^{\alpha-1}F^{-1}$, $\alpha_{el} = 0.9$, $R_{ext} = 5000\Omega$, $\beta_c = 10^{-7}\Omega^{\alpha-1}F^{-1}$, $\alpha_c = 0.7$, $R_{int} = 400$, $C_{par} = 10^{-10}F$, $R_{medium} = 150\Omega$).

frequencies (PRF[1]) (Mercanzini et al., 2009) for R_0 and R_∞ cannot be identified due to the complex electrode ($\alpha_{el} < 1$) and complex tissue nature ($\alpha_c < 1$) as well as the strong impact of all capacitive components in the system (see figure 4.5a on page 43). Therefore, LF is determined by finding the frequencies where the relative phase change (due to the presence of cells) has its maximum. φ_{LF} is calculated according to equation 3.2.

---

[1] The peak resistance frequency is the frequency of $1/Z = 1/X_1 + 1/(R + X_2)$ where the impedance is most resistive, i.e. the phase angle is closest to 0°. The corresponding impedance magnitude value indicates the value of R. X_1 and X_2 are the reactances of two capacitances (in this case: electrical double layer capacitance at low and the parasitic capacitance at high frequency).

$$\varphi_{LF} = max_{i=1,...,n} \left[\frac{(\varphi_{cells}(f_i) - \varphi_{medium}(f_i))}{\varphi_{medium}(f_i)} \right] \tag{3.2}$$

The impedance magnitude at the maximum relative phase angle frequency has been found to correlate well with the real R_0 and is more sensitive to extracellular changes. R_∞, on the other hand, is extracted at the frequency where the phase angle is closest to 0° after the membrane relaxation (equation 3.3, figure 3.2).

$$\varphi_{HF} = max_{i=1,...,n} \left[\varphi_{cells}(f_i) \right] \tag{3.3}$$

In addition to finding the right measurement frequencies to increase the screening precision, the LF and HF impedance values are corrected by performing calibration measurements. Such impedimetric post-processing allows obtaining values that are closer to the real ones and prevents later misinterpretation of kinetics of biological events. Although the measurement sensitivity remains constant, the corrected values describe more precisely actual biological changes. According to the tissue circuit with a series electrode impedance and a parallel parasitic capacitance, the tissue impedance Z_{tissue} is calculated as follows

$$Z_{tissue}(f) = \frac{Z_m(f) \cdot Z_{par}(f)}{Z_{par}(f) - Z_m(f)} - Z_{el}(f) \tag{3.4}$$

Z_{tissue} is found by correcting the total measured impedance Z_m which is measured with the tissue. The values for the parasitic capacitance Z_{par} are obtained by performing an "open" measurement in air. The values of the interface capacitance $Z_{el}(f) = Z_{medium}(f) - R_{sol}$ are found by subtracting the medium resistance R_{sol} from the measured impedance of cell medium Z_{medium}. R_{sol} corresponds to the impedance magnitude at the PRF (figure 3.2).

3.7. Statistics

Comparison between two, three and more groups was carried out using student's t-test, one-way ANOVA and two-way ANOVA with Bonferroni post-test respectively. The observed importance level (p-value) of the difference between two means was considered significant when $p < 0.05$ (*), very significant when $p < 0.01$ (**) and extremely significant when $p < 0.001$ (***).

In order to evaluate the goodness of a curve fit, the weighted sum of squares (WSS) was calculated based on equation 3.5. The sum of squares was weighted with the experimental impedance magnitudes so that high magnitude values at low frequency have the same weight as low magnitude values at high frequency Macdonald (2005); Dellis (2010).

$$WSS = \sum \frac{((Re, Im)_{model} - (Re, Im)_{observation})^2}{|Z|_{observation}} \tag{3.5}$$

Domain / boundary	Type of condition	Equation
Solution	Current conservation	$\nabla \cdot J = Q_j$ $J = \sigma E + J_e$ $E = -\nabla V$
Bounding box	Electric insulation	$-n \cdot J = 0$
Stimulation electrode	Electric potential	$V = 10 mV$
Ground electrode	Ground	$V = 0$

Table 3.1.: Boundary conditions and equations employed in the simulations operated in DC. J: current density, E: electric field vector, n: normal vector, σ: conductivity, V: voltage

3.8. Numerical simulations

The finite element simulations presented in this work were carried out using Comsol Multiphysics ® 4.3a. Table 3.1 displays the boundary conditions and equations employed in the simulation framework operated in DC. The solution conductivity was set to $1.6 S/m$.

3.8.1. Measurement penetration depth

The sensitivity of an impedance measurement is proportional to the local power dissipation (Linderholm, 2006, p.47). Therefore, the penetration depth of an impedance measurement was defined as the depth below which half the electric energy is dissipated (equation 2.7 on page 24). Regarding a variation of $w_{el}/(w_{el} + s_{el})$, a 2D simulation was carried out by setting l_{el} to $1m$ (considered as infinite). For a variation of l_{el}/s_{el}, a 3D simulation was conducted, keeping w_{el} constant at $1000 \mu m$.

3.8.2. Bandwidth

The computation of the minimal electrode cut-off frequency is based on the following equation:

$$f_{el} = \frac{1}{2\pi R_{sol} C_{el}} \tag{3.6}$$

Note that when the distance between the two electrodes becomes smaller, most of the current passes at the inner edges of the electrodes and only a fraction of the real electrode width contributes to the current flow. Hence, this leads to a decreased electrode double layer capacitance value C_{el}. The corresponding apparent electrode width w_{ap} was determined for each pair of w_{el} and s_{el} as follows

$$\int_{-w_{el}/2}^{+w_{el}/2} E(x)dx = E_{uniform} \cdot w_{el} \tag{3.7}$$

where E is the electric field distribution over the electrode width (at 10nm distance from the electrode for more precision) and where $E_{uniform}$ corresponds to the electric field value for a (hypothetical) homogeneous field distribution at the electrode surface. Once $E_{uniform}$ is known, the apparent electrode width is determined as the width where
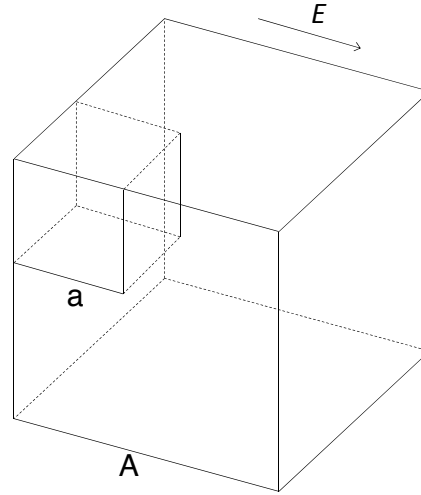
Figure 3.3.: 2-box model for simulating toxicity effects.

$E > 0.5 \cdot E_{uniform}$. Consequently, the electrode region where relatively low current spreads out into the solution compared to the total current flow is neglected. C_{el} is then calculated using w_{ap} in

$$C_H = \varepsilon_0 \varepsilon_{OHP} \frac{A}{d_{OHP}} = \varepsilon_0 \varepsilon_{OHP} \frac{w_{ap} \cdot l_{el}}{d_{OHP}} \tag{3.8}$$

where $\varepsilon_0 = 8.85 \cdot 10^{-12} F/m^2$ is the vacuum permittivity, $\varepsilon_{OHP} = 12.4$ is the relative permittivity of the outer Helmholtz plane with water (Conway et al., 1951), A is the surface area of the electrode, l_{el} is the electrode length and $d_{OHP} = 5\mathring{A}$ is the outer Helmholtz plane distance (Conway et al., 1951).

R_{sol} was obtained according to

$$R_{sol} = \frac{V}{\int_{-\infty}^{\infty} \int_0^{\infty} J(x,y)dxdy} \tag{3.9}$$

where V is the voltage set as $10mV$ and where J is the current density.

3.8.3. Toxicity effect modeling

The model is composed of a first cube which represents the cell medium. A second cube, which represents the cell volume, is placed into the first one (figure 3.3) . Toxicity effects such as cell retraction and cell death are simulated by changing the volume and the the conductivity of the smaller cell cube. The size and conductivity of the larger medium cube remains constant. Considering a side length A of $100\mu m$ for the larger medium cube, the corresponding cell constant equals

$$\kappa = \frac{1}{A} = 10000m^{-1} \tag{3.10}$$

The cell volume fraction or cell density is calculated as follows

$$\text{density} = \frac{a^3}{A^3} \tag{3.11}$$

where a is the side length of the smaller cell cube.
R_0 and R_∞ are obtained as follows

$$R_0 = \rho_{medium} \left(\frac{A - a}{A^2} + \frac{a}{A^2 - a^2} \right) \tag{3.12}$$

$$R_\infty = \rho_{medium} \left(\frac{A - a}{A^2} + \left(\frac{a}{\rho_{intra}} + \frac{A^2 - a^2}{\rho_{medium} a} \right)^{-1} \right) \tag{3.13}$$

ρ_0 and ρ_∞ of a tissue can consequently be obtained by using equation 2.6 on page 23.

4. Distinguishing toxicity effects

4.1. Label-free distinction of minor and major cell damage – the main principle

The analysis of toxic effects on cultured cells is conventionally carried out through colorimetric assays such as the MTT test[1] or through fluorescence-based live/dead stains. These tests are end-point assays and require a considerable amount of material and human resources. Impedance measurements, on the other hand, are simple, inexpensive, non-invasive, real-time and automatable, all being the reason why impedance screening has been used extensively to measure toxic effects on cells (Jahnke et al., 2009; Krinke et al., 2010; Hug, 2003; Cho et al., 2009; Banerjee et al., 2010; Abdelghani, 2002). However, in most cases it is unknown what exact biological phenomenon is associated with the impedance that is measured upon toxin exposure. In former studies, the impedance was recorded over time at a specific frequency where the cellular contribution appeared maximal ($\max(|Z|_{cells} - |Z|_{medium})$, CI). This frequency varies depending on the electrode measurement system, the cell density and the cell model that is used. The impedance associated to this frequency may carry information about the extracellular, membrane or intracellular properties or even a mix of them, depending on the extent to which the membrane capacitor has been short-circuited at the given frequency. Therefore, impedance measurements have remained unexploited regarding the distinction of toxicity-induced morphology changes (cell-substrate unbinding) from cell death (membrane rupture and cell fragmentation), thus rendering this technique unspecific and inadequate to be compared directly with labeling-based viability assays.

Considering a single cell as a shell-covered sphere (Pauly and Schwan, 1959; Gawad, 2004) it is necessary to distinguish cellular events within frequency ranges. At low frequency, cells act as insulators due to the capacitive nature of the cell membrane. At high frequency, the cell membrane capacitor is short-circuited and intracellular matter has an effect on the impedance. Hence, frequency dependent impedance screening offers plethora of information on intra- and extracellular properties. This chapter[2] shows how measurements at different and well-chosen frequencies can provide information on both morphological changes (low frequency) and cell death (high frequency) simultaneously (figure 4.1) without using any label. Consequently, the resulting two distinct signals allow distinguishing minor toxic effects (morphology changes) from major cell damage[3]

---

[1] (3-(4,5-Dimethylthiazol-2-yl)-2,5-diphenyltetrazolium bromide is reduced to purple formazan in living cells

[2] This chapter has been subject to a publication (see paper I on page 143) (Meissner et al., 2011).

[3] A specific definition of the term "cell death" with regard to biochemical mechanisms does not exist. Cell
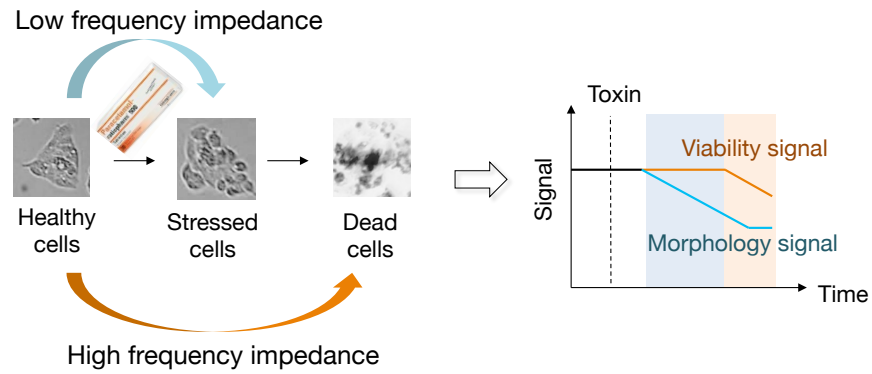
Figure 4.1.: Scheme of how frequency-dependent impedance is associated with biological information when cells are exposed to toxins. The low frequency impedance informs about toxicity-induced minor cellular changes ("sick" cell) and the high frequency impedance about major cell damage (cell death).

(membrane rupture, dysfunction of ion channels), rendering this technique not only very sensitive since early sub-lethal effects can be measured, but also qualitative since two different biological information are obtained.

4.2. Design of a perfusion-based, shear stress-protective micro-system

4.2.1. Microfluidic chip design

A microfluidic chip with filters inducing mechanical trapping and perfusion for liver cell culture was designed (figure 4.2). Hepatocytes are versatile cells having high energy demands. *In vivo*, hepatocytes are located close or in direct contact to the fenestrated sinusoid endothelium providing efficient nutrient and oxygen supply (North-Lewis, 2008). In the here described device, a low hepatocyte-perfusion distance was guaranteed by introducing four relatively thin filters ($100 \times 500\mu m$), separated by $50\mu m$ gaps. The filters were defined by arrays of PDMS pillars ($\varnothing 40\mu m$). The total channel height was $60\mu m$. Cell-filled filters cause high flow resistance, resulting in the perfusion medium to flow between the filters rather than through them. $5\mu m$ spacing between neighboring micro-pillars allowed efficient diffusion and exchange of nutrients and waste. In addition, cells are not directly exposed to the main flow which potentially hinders cell proliferation.

---

death can be classified according to its morphological appearance, enzymological criteria, functional aspects or immunological characteristics (Kroemer, 2009). Since no specific biochemical mechanism of cell death is provided in this study, it will be generally referred to as "major cell injury".
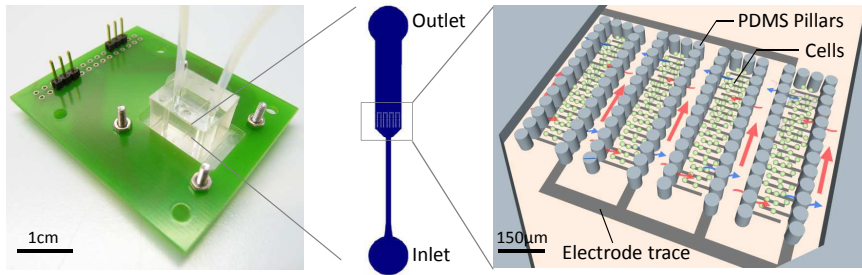
Figure 4.2.: Microfluidic device and electrical interface. a) Photograph of the printed circuit board with polydimethylsiloxane (PDMS) chip. b) Design of the microfluidic channel. c) Schematic of cell culture area involving PDMS pillars for cell immobilization and flow stress protection. The main flow is passing between the filters (large red arrows), and efficient nutrient supply and waste removal is provided by gentle diffusion (curved red and blue arrows). Electrodes are implemented for impedance recording.
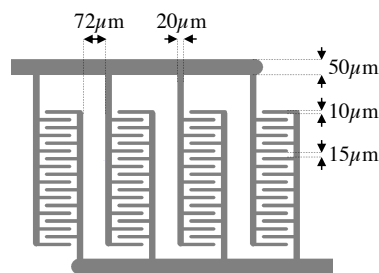
Figure 4.3.: Electrode design. A bipolar interdigitated electrode pair has been adapted to the microfluidic four-filter configuration to maximize electrode surface coverage for high-sensitivity impedance measurement of the cell culture area. A total of 36 electrode fingers are provided for each electrode ($w_{el} = 10$µm, $l_{el} = 100$µm) separated by a gap of 15µm.

4.2.2. Electrode design

Electrodes are implemented in the device for impedance measurements of the hepatic cell population. Interdigitated electrodes (IDE) were designed so that a larger total electrode surface area contributes to higher measurement sensitivity. IDEs were adapted to the microfluidic four-filter configuration such that the sensing area is limited to the region where cells are trapped in filters (figure 4.3). Thus, each electrode trace carries four arms (each 20µm wide) with nine fingers (10µm wide, spaced 15µm apart).

4.3. Results

4.3.1. Impedance changes due to cell growth are frequency-dependent

A microfluidic bio-sensing platform on which the culture and toxicity screening of HepG2 / C3A cells can be performed was developed. The first step involved immobilizing the cells within the four filters as shown in figure 4.4a and figure 4.4c. Cells, injected in the microfluidic device, get trapped within the micro-pillar array with some cells escaping
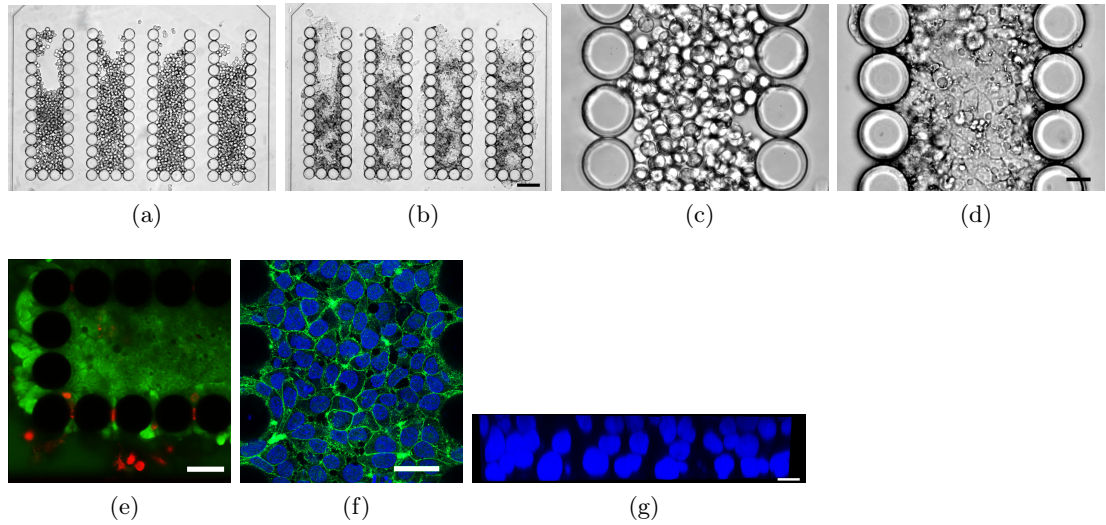
Figure 4.4.: Imaging of cell culture within microfluidic device. a) and c) show nearly full filters after cell loading. b) and d) show cells after 3 days of culture. The high density culture is characterized by direct cell-cell contact and multiple cell layers. (bar=100µm at the top and 20µm at the bottom). e) Viability of cells within filters is shown in green and some cells in perfusion regions undergo cell death (red) due to exposed shear stress (green: fluoresceine-diacetate, red: propidium iodide). f) Immunocytochemical staining of occludin indicates presence of cellular tight junctions (bar= 40µm, green=Cy-2). g) Three cell layers are identified in z-direction (blue: DAPI). (bar= 10µm).

through the gaps between the filters. It was observed that the amount of cells finally immobilized strongly depends on the flow rate during cell loading. Flow rates in the range of $20nl/s$ were the most suitable for an efficient cell loading, resulting in a trapping of up to 90% of the injected cells in the filter.

Cell culture in the microchip was performed for 5 days. Cells attached to the surfaces and to each other during this period (figure 4.4b). This high cell density culture was characterized by close cell-cell contacts (figure 4.4d and figure 4.4f) and multiple cell layers in z-direction (figure 4.4b, dark regions). A confocal image showing the xz-plane in figure 4.4g revealed the presence of three cell layers stacked on top of each other, indicating a 3D cell culture. In addition, as shown in figure 4.4e, despite high cell density, cell viability was maintained within the filters with some dead cells in the perfusion region only.

The hepatic cell population was examined with impedance spectroscopy during the entire cell culture. The impedance spectra as a function of cell culture time are shown in figure 4.5a. An increase of $|Z|$ within a frequency range from $5kHz$ to $3MHz$ was observed. Lower frequencies ($< 5kHz$) are not affected by the growing cell population. The phase angle increased within a frequency window of $1kHz$ to $100kHz$ and decreased at HF. Phase angles obtained at $3MHz$ are much closer to 0° compared to those at lower frequencies, indicating more resistive characteristics at higher frequencies. The largest difference between the impedance magnitude profile in the presence of cells and without
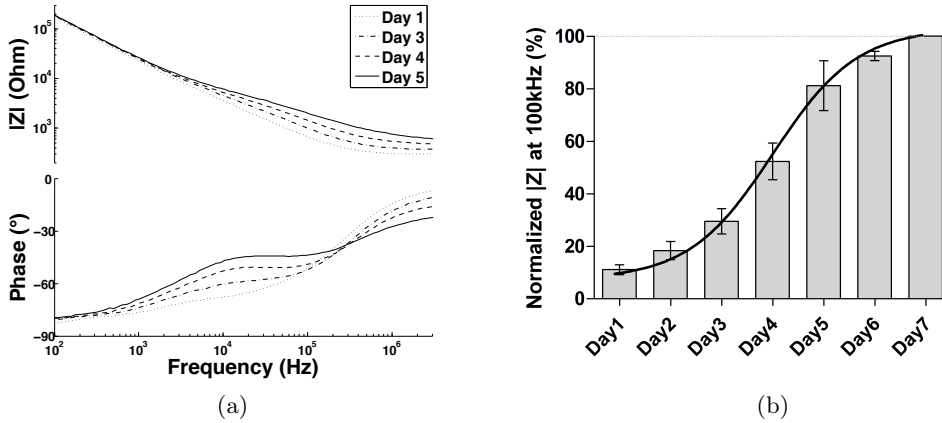
Figure 4.5.: Impedimetric characterization of cell growth. a) Bode plot of spectra recorded on different days of culture. b) Normalized impedance magnitude at 100 kHz for 7 days of culture (n=5). The solid line is a fit of the data.

the cells was observed at $100kHz$. Figure 4.5a shows $|Z|$ at $100kHz$, and the cell growth profile measured by the impedance was confirmed with the cell growth observed under the microscope. A typical growth curve with initial lag phase and exponential growth was obtained by the impedance measurement as seen in figure 4.5b. The stationary phase was reached at the end of seven days once the electrode area was fully covered with cells. Hence, it was shown that impedance changes due to the cell growth are strongly frequency-dependent.

4.3.2. Frequency-Dependent impedance profiles upon drug exposure

The effect of acetaminophen[4] (AP) on the micro-scale culture was studied. In order to analyze AP toxicity-induced effects, LF and HF signals were examined separately. The LF signal provides information about extracellular properties whereas HF signal reflects intracellular characteristics. The phase angle indicates if the system behaves like a resistor ($\rightarrow 0°$) or a capacitor ($\rightarrow$ -90°). LF and HF impedance were chosen as $10kHz$ and $2MHz$ according to the maximum phase change method as described in section 3.6.2 on page 32. As already shown in figure 4.5a, a LF phase angle of -40° ($10kHz$) at high cell density indicated both resistive and capacitive effects.

AP treatment with different concentrations was performed under continuous perfusion exposure. Figure 4.6 shows impedance magnitude changes at $10kHz$ and $3MHz$ for different time points. The long-term impedance magnitude is similar for measurements at $10kHz$ and $3MHz$, but its evolution has different profiles for both frequencies. LF signals drops as early as $2h$ of drug exposure, whereas the HF signal does not change significantly. For AP concentrations above $5mM$, longer exposure results in lower impedance magnitude. Furthermore, increasing concentrations of AP lead to a larger change in

---

[4] Acetaminophen is a widely used analgesic with a well-known severe hepatotoxicity.
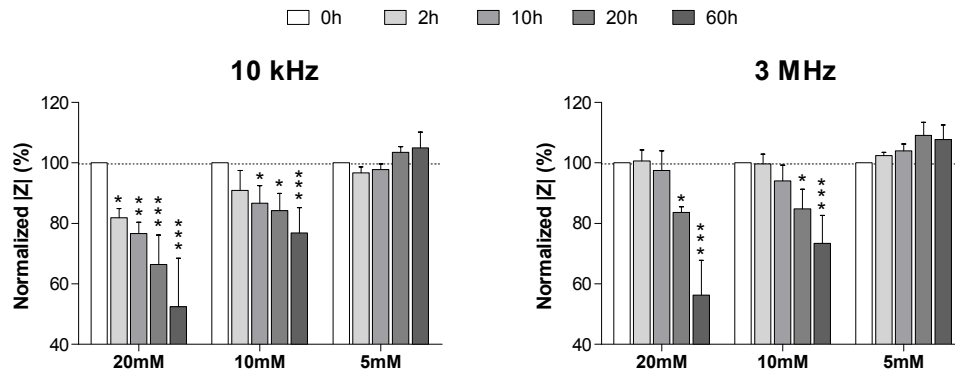
Figure 4.6.: Normalized impedance in the microchip as a function of AP concentration under different drug treatment time. Each value was normalized to their initial ($0h$) value. Impedance magnitude changes (mean $\pm$ CI) at $10kHz$ and $3MHz$ after application of three different concentrations ($5mM$, $10mM$, $20mM$) are shown ($n = 3$). Kinetics of the decrease in $|Z|$ was found to be frequency-dependent. Statistical analysis of each time point was performed compared to the initial value at 0 h (* $p < 0.05$, ** $p < 0.01$, *** $p < 0.001$)

impedance magnitude for treatments of similar durations. The impedance magnitude for an exposure of the cells to a $5mM$ AP concentration follows a different evolution than that for higher concentrations and actually increases with exposure time.

Immunocytochemical staining of actin was performed on cultured cells exposed to a $20mM$ concentration and revealed structural changes as early as $2h$ after AP treatment as shown in figure 4.7a. Non-treated cells exhibit a fiber-like network of actin filaments, providing attachment between cells and the substrate and also neighboring cells. This organizational structure disappeared after $2h$ of AP exposure. Instead, an even distribution of actin was observed in the cells with a slightly higher presence at the cell periphery (figure 4.7a, arrow). Cells that were treated for $24h$ showed heterogeneous dispersion of actin. Also, nuclear fragmentation indicated apoptosis in some cells (figure 4.7a, arrows). The cell viability, on the other hand, decreased significantly after $24h$, and no cell death was observed up to 8 h as shown in figure 4.7b.

4.4. Discussion

It was demonstrated that the presented microfluidic device is a suitable environment for HepG2/C3A cell growth. It was further shown that impedance changes following cell growth and exposure to AP are strongly frequency-dependent. More specifically, different impedance kinetics were observed at LF and HF when the cells are treated with AP. The following sections will discuss why impedance changes are dependent on the frequency and how they relate to biological events.

(a)   (b)
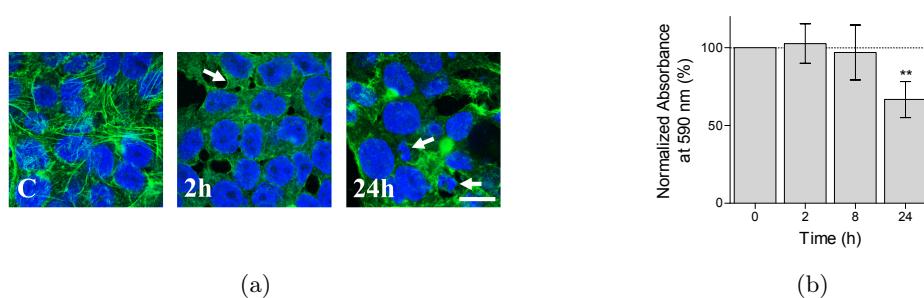
Figure 4.7.: Effect of AP treatment on cell morphology and viability. a) Cytoskeletal changes after AP exposure. Immunocytochemical staining of actin cytoskeleton revealed structural changes as early as $2h$ after $20mM$ AP treatment. C: Actin forms a fiber-like network in the untreated sample. $2h$: Actin is less organized and dispersed throughout the cytoplasm and displays slightly higher fluorescence intensity at the cell periphery (arrow). 24h: Actin is heterogeneously dispersed in the cell. Apoptosis is observed as indicated by arrows. (bar= 10µm, green=phalloidin-FITC, blue=DAPI); b) MTT viability assay. % cell viability vs. time. Mean $\pm$ CI of absorbance at $590nm$ is shown ($n = 4$). Comparison between time point and initial value at 0 h (** p < 0.01).

4.4.1. The microfluidic perfusion culture

A microfluidic device was designed in which cell culture can be performed with continuous perfusion of medium and without shear stress applied on the cells because of the implemented filter design. The experiments showed higher cell viability and cell growth inside the filters than that of outside owing to the protection of cells from the effect of shear stress caused by the direct flow. In addition, sterile conditions can easily be maintained when using a perfusion system (non-loop) and a PDMS microbioreactor. This reduces the need for the use of antibiotics that have potential long term effects on cells (Stieglitz, 2004). The microfluidic cell culture showed very high cell density in the filters with maximum distance of 50µm for diffusion of nutrients as determined by the filter width. These specifications meet *in vivo* conditions since the extracellular matrix constitutes a small portion of the normal liver (about 3 %)(Schmitz, 2007) and tight junctions are important for firm cellular attachment permitting cell-to-cell signaling across communication junctions (North-Lewis, 2008). Although the presented cell culture may not be considered as 3D (due to the absence of extracellular matrix), formation of multilayer stack of cells is still important (Bedossa and Paradis, 2003) since most of the cell surface is in direct contact with adjacent cells. This is not true for standard cell culture in 2D Petri dish, where cells are cultured on a hard surface and with abundant amount of cell medium. Based on cell growth and high cell viability, this device and the culture conditions are considered to be effective for drug cytotoxicity studies, although a complete biochemical analysis (quantification of albumin and CYP450 activity (Prot et al., 2011, 2012; Snouber et al., 2013; Khetani and Bhatia, 2008; Xia et al., 2009)) was not the focus and hence was not conducted in the framework of this study.

4.4.2. Impedimetric characterization of the hepatic cell population

The dielectric properties of HepG2/C3A cells were investigated with the microfludic perfusion system. Although the maximum cellular contribution to the impedance magnitude was observed at around $100kHz$, the phase angle did not change at this frequency but varied significantly at $10kHz$ and $3MHz$. On the one hand, this difference originates in the impedance being dominated by the electrode impedance at LF, thus making the LF impedance magnitude less sensitive to the presence of cells. On the other hand, the extracellular resistance is shorted by the cell membrane capacitor above $10kHz$ as indicated by the phase angle. Hence, if one wants to measure predominantly extracellular events, $10kHz$ appears to be the most sensitive frequency (phase angle is most resistive before membrane relaxation). At $100kHz$ phase angles are constant during the cell culture due to the balance between an increasing extracellular resistance and membrane capacitance. Moreover, intracellular properties can be investigated at HF as mentioned earlier. The impedance at HF increases with the increasing number of cells because intracellular matter is less conductive than the surrounding medium (Gawad, 2004). Nevertheless, the corresponding phase angle decreases due to the increasing tissue capacitance that was observed up to $3MHz$ (figure 4.4a). Thus, these experiments provide information about extracellular, intracellular and cell membrane properties. Such cell specific characteristics can only be distinguished with the interpretation of the impedance spectra with corresponding phase angle profile, thus making phase angle analysis an indispensable tool for understanding cellular phenomena.

The phase-component of the impedance has a typical angle of $-45°$ at $10kHz$ and of $-15°$ at $3MHz$. This indicates a stronger capacitive behavior of the cell population at LF, originating from the electrode and the tissue capacitance. A correction method was introduced to eliminate the effect of the electrode-electrolyte interface and to offer the possibility to theoretically counteract the inherent drawback of bipolar measurement. This technique assumes that electrode characteristics do not change throughout the whole experiment time. Practical alternatives to eliminate the electrode interface contribution are multipolar measurements such as tetra-polar configuration. However, these techniques have a limited practical bandwidth, at least when using micro-electrodes, as described previously (Linderholm, 2006).

4.4.3. Hypothesized correlation between biological events and impedance profiles

4.4.3.1. Sequential two-step toxicity effect

It was observed that impedance changes after AP treatment were time and dose-dependent. Significant changes on the impedance spectra after $2h$ at $10kHz$ confirm that impedance screening is a very sensitive method. When comparing low and high frequency measurements, it was found that $|Z|_{HF}$ decreases later than $|Z|_{LF}$. This shows that different information can be obtained when investigating different frequency ranges as presented in figure 4.8. At LF, cell membranes act as capacitors and block the current flow through the cells. This leads to a high extracellular resistance, considering a densely packed in-
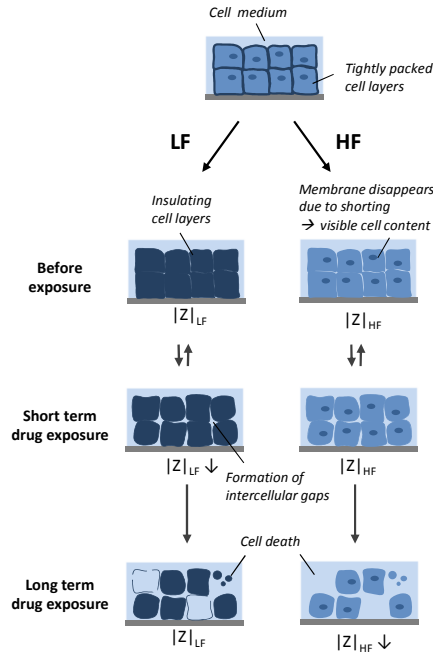
Figure 4.8.: Hypothesized correlation between frequency-dependent impedance changes and cell culture morphology. After short term drug exposure, cell-cell contacts are loosened and the formation of intercellular gaps causes current shunting at low frequency (LF), but no significant impedance change at high frequency (HF) due to their low volume fraction. Cytosol conductivity changes follow cell death after long term drug exposure. This leads to decrease in the impedance at HF.

sulating cell layer. If cell-substrate and cell-cell contacts are loosened and cells start to retract, current shunts through the intercellular space which results in an abrupt resistance drop (due to the inverse relationship between R_{ext} and intercellular space). This phenomenon explains the signal decrease at LF. Such rapid impedance decrease is correlated to cytoskeletal actin changes after AP exposure (figure 4.7a). In cell culture with stiff substrates and dense cell-cell contacts, the actin cytoskeleton tends to organize in stress fibers. AP treatment disrupts this fiber-like organization leading to cell-substrate and cell-cell detachment. Former studies also indicated that AP mediated metabolism can cause the deactivation of the Rho protein which in turn is responsible for the formation of actin stress fibers (Besser and Schwarz, 2007).

In long-term drug exposure, cells start dying either through apoptosis or necrosis (Kon et al., 2007; Pierce et al., 2002) which again leads to signal decrease. This is consistent with the changes observed in the cell morphology inside the microchip such as cell retraction and increase in the intercellular space after $2h$ and cell death after $24h$ AP exposure. On the other hand, at HF, the membrane capacitor is considered shorted and both extracellular and intracellular matter contribute to the measured impedance. Intercellular gaps formed after AP exposure barely contribute to the decrease of HF impedance due to their low volume fraction compared to the large intracellular volume at high cell density.

When cells start dying, ion pumps embedded in the membrane cease functioning and small pores are formed during cell death, leading to exchange of intra- and extracellular matter. Considering continuous perfusion of the cell sample, cell cytosol is replaced by fresh medium, which has two to three times higher conductivity than the cytosol (Gawad, 2004, p.77). The results on HF kinetics indicate that the conductivity change in such large volume contribute to the impedance decrease. Indeed, the measured HF values in figure 4.6 follow the same trend as the profile obtained in the MTT viability test (figure 4.7b) and other reported conventional viability data on HepG2 cells (McHardy et al., 2005; El-Hassan, 2003). The present data strongly suggests that, in combination with high cell density and continuous perfusion flow, HF measurements report serious cell injury, while LF measurements inform about intercellular and morphological phenomena.

In addition, it was measured that $|Z|_{LF}$ was higher at $20h$ and $60h$ than initially when $5mM$ AP was applied. This is due to the continuously growing liver carcinoma cell line used in the experiments. Cell growth is disrupted after AP exposure, and cell cycle reentry occurred after a certain 'adaptation time'. $5mM$ AP concentration was too low to cause serious HepG2 cell population damage within $60h$.

4.4.3.2. Analytical model confirms relationship between biological and impedance changes

Analytical modeling was conducted to further understand the kinetics difference between the LF and the HF signal decrease (see section 3.8 on page 35). For this, cells were placed in the electric field of an electrode pair and two timely shifted biological events were simulated (two-step toxicity): 1) the intercellular space was increased (equivalent to cell retraction); 2) the intracellular conductivity was step-wise adapted to the conductivity of the cell medium. Five observations were made:

1. It was found that the increase of the intercellular space causes the impedance at both frequencies to decrease, but to a different extent (figure 4.9, gray area). The LF signal drop is much more pronounced than the one at HF. This is due to the direct relationship between $|Z|_{LF}$ and R_{ext} on the one hand and to the lesser influence of R_{ext} on $|Z|_{HF}$ owing to C_m shortening on the other.

2. It is noted that linear gap changes result in a non-linear decrease of $|Z|$. This non-linear decay indicates a lesser sensitivity with an increased intercellular distance which is due to the inverse relationship of R_{ext} and intercellular space.

3. The intracellular conductivity change, on the contrary, leads to a more evident signal drop at HF (figure 4.9, orange area). This is explained by the direct relationship between $|Z|_{HF}$ and σ_{intra}.

4. In contrast to the experiments (figure 4.6), the HF signal also decreases slightly when the intercellular space was increased in the simulations (figure 4.9), indicating that $|Z|_{HF}$ is dependent on both σ_{intra} and the extracellular space. This deviation between theory and practice may have different reasons. Biological events were
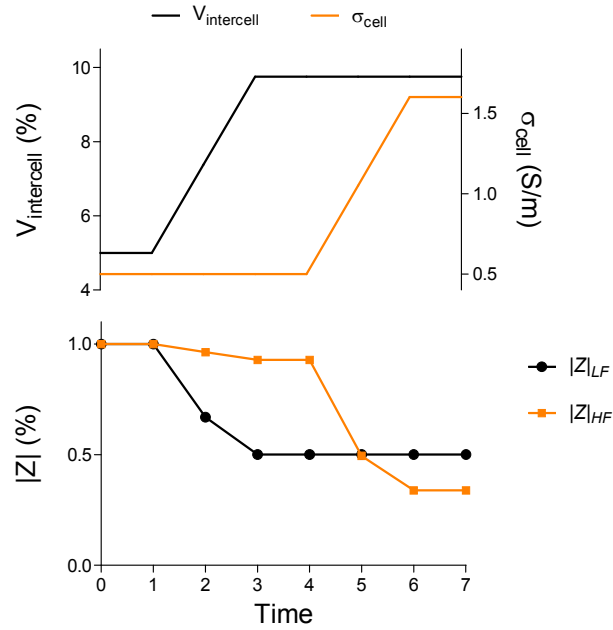
Figure 4.9.: Connection between toxicity-induced biological events and frequency-dependent impedance profiles. The kinetics of biological events such as the creation of intercellular spaces and the intracellular conductivity change determine the frequency-dependent impedance kinetics. Initially, no effect is observed. After a time lag, cells retract and the intercellular space increases (gray area). The LF signal drops dramatically and the HF signal drops slowly. When σ_{intra} from all cells adjusts to σ_{medium} following major cell damage (orange area), the HF signal drops considerably. This calculation was performed at 95% cell density according to section 3.8.3 on page 36.
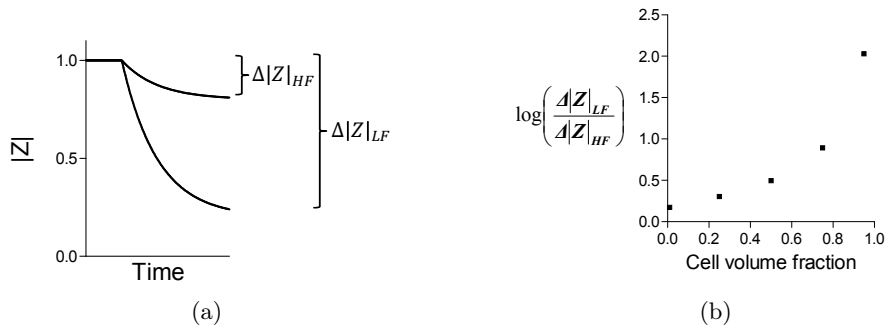
Figure 4.10.: Impact of cell density on the ability to distinguish LF and HF impedance signals following cell retraction. a) Signal decrease at both frequencies following cell retraction is illustrated ($\triangle |Z|_{LF} > \triangle |Z|_{HF}$). b) Difference between LF and HF impedance drops ($\log\left(\triangle |Z|_{LF} / \triangle |Z|_{HF}\right)$) following cell retraction as a function of initial cell density. High cell densities are favorable for distinguishing toxicity effects.
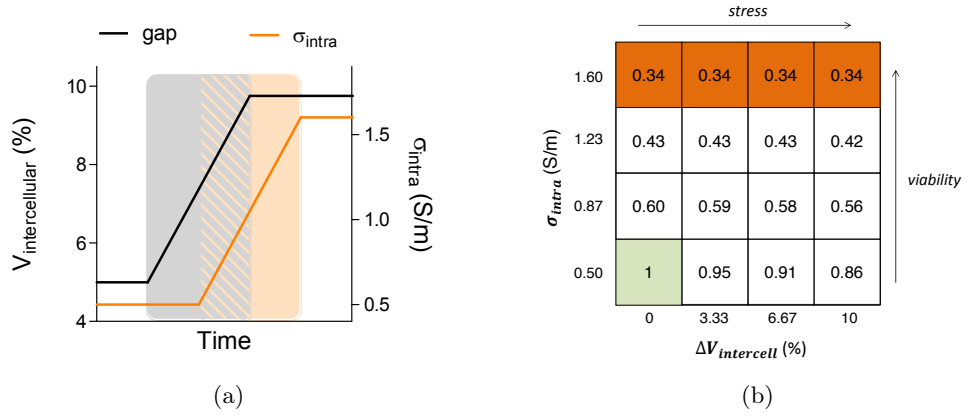
Figure 4.11.: Timely overlap of extracellular space and intracellular conductivity changes. a) Illustration of bio changes overlap. b) Normalized $|Z|_{HF}$ as a function of σ_{intra} and intercellular space change $\triangle V_{intercell}$. The green and the red field represent the healthy and dead cell population respectively. Different paths from the green to the red field are imaginable with different impacts on the impedance value and consequently its sensitivity towards changes of σ_{intra}.

simulated as linear changes to exemplify their effect on the impedance measurements, however in reality their kinetics are likely to be more complex which in turn has a direct impact on the precise kinetics of the LF and HF impedance curves. Also, only two major biological events were considered here, whereas the cellular toxic reaction is presumably more complex (e.g. temporary increase in σ_{intra} might have leveled the signal drop at HF).

5. A study on the difference between LF and HF impedance drops following cell retraction as demonstrated in figure 4.10 pointed out that higher cell densities enable a sharper distinction.

To further understand the impact of both biological events on $|Z|_{HF}$, the effect of their timely overlap was additionally studied. Figure 4.11 shows the normalized impedance as a function of a crosswise variation of σ_{intra} and cell retraction ($\triangle V_{intercell}$) with the green and the red fields representing the healthy ($\sigma_{intra} = 0.5Sm^{-1}$ and $\triangle V_c = 0\%$) and the dead state ($\sigma_{intra} = 1.6Sm^{-1}$) respectively. It was shown that the HF signal is > 2 times more sensitive to σ_{intra} than to intercellular space changes. Furthermore, when both events timely overlap, the measured $|Z|$ is almost entirely determined by σ_{intra}. Nevertheless, the sensitivity of $|Z|_{HF}$ to σ_{intra} decreases with an increasing extracellular spac. However, these observations also indicate that a change in σ_{intra} cannot be fully covered by a change in intercellular space within $|Z|_{HF}$. Therefore the HF signal allows estimating the major health status of a cell population, although it is not an independent parameter for σ_{intra}.
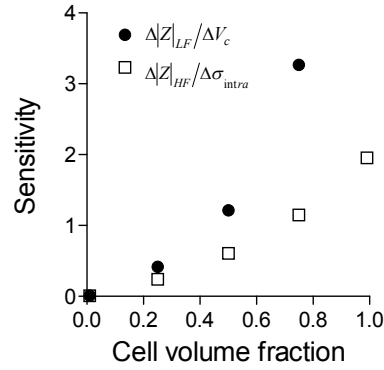
Figure 4.12.: Effect of cell density on the ability to distinguish minor from major cell damage. The measurement sensitivities for 1% change of cell volume (equivalent to cell retraction) and intracellular conductivity were plotted.

4.4.3.3. High cell density for sensitive toxicity distinction

The effect of cell density on the ability to distinguish minor from major cell damage with LF and HF signals was investigated. For this, the relative change of $|Z|$ before and after drug treatment was evaluated as a measure for distinguishing toxicity effects. The relative impedance changes at LF and HF were compared with the relative changes of intercellular distance and intracellular conductivity respectively. The resulting LF and HF sensitivities S_{LF} and S_{HF} are calculated as follows

$$S_{LF} = \frac{\triangle |Z|_{LF}}{\triangle V_c} = \frac{\frac{|Z|_{LF,b} - |Z|_{LF,a}}{|Z|_{LF,a}}}{\frac{V_{intercell,a} - V_{intercell,b}}{V_{intercell,b}}} \tag{4.1}$$

$$S_{HF} = \frac{\triangle |Z|_{HF}}{\triangle \sigma_{intra}} = \frac{\frac{|Z|_{HF,b} - |Z|_{HF,a}}{|Z|_{HF,a}}}{\frac{\sigma_{intra,a} - \sigma_{intra,b}}{\sigma_{intra,b}}} \tag{4.2}$$

where the indexes "b" and "a" are referred to the $|Z|$, $V_{intercell}$ and σ_{intra} before and after drug administration. Figure 4.12 illustrates the sensitivity decrease at LF and HF when the cell density is decreased. The LF and the HF signal show a sensitivity of more than 1 for volume fractions of > 0.5 and > 0.75 respectively and accordingly act as an extracellular space and intracellular conducivity amplifier. All this information indicates that a high cell density culture (confluency) seems to be valuable for the sensitive distinction of minor from major cell damage.

4.4.4. Summary

It was demonstrated that major biological events such as cell retraction and intracellular conductivity lead to frequency-dependent impedance changes. The LF signal is highly sensitive to intercellular space changes. Although the HF signal also changes slightly

with the intercellular volume, the impedance at this frequency is mostly sensitive to intracellular conductivity changes. However, it may be possible to normalize the HF signal using the LF signal resulting in a more independent indicator for σ_{intra} changes. It was further shown that impedance changes do not follow biological changes linearly. This may be considered as a disadvantage when correlating impedance with biological kinetics. On the other hand, this same phenomenon is the reason behind the extremely high sensitivity of impedance measurements for the detection of initial stress and early cellular changes, a major advantage over traditional screening methods.

Overall, the resulting LF and HF signal kinetics correlate with the ones observed in the experiments. Although this model is simplified (ignoring cell-cell junctions) as well as the described toxicity-induced cellular mechanism (intercellular space changes, intracellular conductivity change), it validates the hypothesis as illustrated in figure 4.8 and points out how the two major events that were observed with optical and fluorescence microscopy, alone may justify the observed impedance changes in time.

4.5. Conclusion

In conclusion, a microfluidic-based sensing platform for hepatocyte culture using dielectric screening was presented. It enables direct, continuous, label-free and non-invasive monitoring of the health status of a cell population. It was shown possible to distinguish between morphological changes and severe cell injury within a cell population owing to the combination of high-density culture and the right choice of measurement frequencies using phase angle analysis. More importantly, cellular changes can be sensed long before cellular death, offering a very high sensitive technique over standard expensive and time consuming viability assays.

As a demonstration of drug induced cytotoxicity screening with impedance spectroscopy within a wide frequency range, this study offers a sensitive detection method for cellular behavior during cell culture and drug exposure. Real-time monitoring of cell dependent changes using microfluidics combined with the impedimetric detection of cellular events allow developing new designs of micro-scale cytotoxicity-based sensing systems for different cell types under various physiological conditions. Overall, this system exemplifies the significance of microfluidics and cell dielectric properties to create a miniaturized detection device for cell toxicology studies.

5. Toxicity-resistance screening

5.1. Motivation

The toxicity effect of highly concentrated drugs have implications on a cell's morphology, metabolism and viability. Intermediate concentrations, on the other hand, may impose a pressure on a population of cells since individual cells vary in their sensitivity to the drug. Some tolerate the applied drug concentration while others do not and undergo cell death (natural distribution, see figure 5.1). Hence, a greater fitness and thus a more favorable genotype and phenotype enables a cell to survive the treatment. When a slowly but continuously increasing drug concentration (pressure) is applied, the cell population becomes subject to evolution as a consequence of genetic mutations and the thereupon based selection process. Such acquired drug resistance of cells (bacteria and cancer cells) is a critical issue in clinics and merits particular attention.
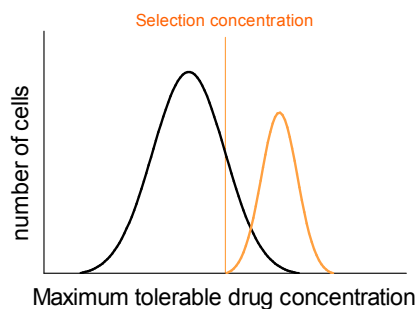
Figure 5.1.: Simplified principle of drug resistance acquisition. Individual cells of a cell population vary in their sensitivity to a drug, giving rise to a normal distribution over the maximum tolerable drug concentration. Intermediate concentrations apply a pressure on the cell population. Only cells with higher concentration tolerance (orange colored part of the distribution) survive and give rise to a more resistant cell population (orange normal distribution curve). The distribution curve of the resistant cell population was drawn smaller due to a decreased population doubling time.

Breast cancer, for example, is one of the most common cancer types and leading causes of female mortality worldwide (Kols, 2002). Chemotherapy is still one of the main treatment methods, causing cell death in breast tumors treated with various anti-cancer drugs. Despite the fact that many tumors initially respond to chemotherapy, cells can gain resistance and they can adapt to survive. Drug resistance often involves the transition of cancer cells from an antiestrogen-sensitive, non-metastatic, hormone dependent phenotype to an antiestrogen-insensitive, metastatic and hormone independent phenotype

(Simstein et al., 2003). Despite the fact that there have been a plethora of studies addressing the mechanism behind drug resistance (Ueda et al., 1987; Kaufmann and Vaux, 2003; Harris and Hochhauser, 1992; Moscow and Dixon, 1993; Tu et al., 1996; Pessina, 1993; Chen et al., 2002), a comprehensive answer to how the transition from drug sensitivity to drug resistance takes place still remains elusive. Hence, a pressing demand has directed preclinical studies towards the development of rapid and simple techniques for the investigation of interactions of cancer cells with drugs at different stages of the disease.

Although cell-based impedance spectroscopy has attracted attention as a tool to characterize drug resistant cells. (Bartholomä et al., 2005), there has been no detailed study that distinguishes cell models of acquired drug resistance without genetic manipulation from their parental cells based on their electrical properties, nor investigation of drug interaction with such cells. Still substantial work needs to be done to demonstrate a comprehensive explanation why dielectric properties of cancer cells change when they gain drug resistance and how drug resistant cells interact with drugs compared to their parental wild type cells. The following chapter[1] addresses these issues and it will be discussed how acquired drug-resistance of MCF-7 breast cancer cells leads to a change in dielectric properties. Moreover, the effect of doxorubicin, one of the most widely used anti-tumor antibiotics, on resistant and wild type cells is investigated.

5.2. Results

5.2.1. MCF-7 DOX and MCF-7 WT cells possesses different extracellular properties

It was investigated weather doxorubicin resistant MCF-7 cells (MCF-7 DOX[2]) can be singled out from their parental cells (MCF-7 WT) based on their dielectric properties. For this, the impedance spectra of MCF-7 WT cells and MCF-7 DOX cells with equal cell density[3] were fitted in the absence of drug. Figure 5.2 shows the values of the fitted circuit components (R_{ext}, R_{int}, β_c) for both wild type and drug resistant cells. Although R_{int}, and β_c showed negligible change when the cells gained resistance to doxorubicin, a significant difference in R_{ext} between these two cell lines was observed. MCF-7 DOX cells exhibited 50% increase in R_{ext} compared to MCF-7 WT cells when both were cultured at confluence on platinum electrodes.

In order to find out the reason behind the increase of R_{ext} when the MCF-7 WT cells gain drug resistance, the nature of MCF-7 cellular tight junctions, adhesive junctions and cytoskeleton structure was investigated by occluding staining, E-cadherine staining

---

[1] This chapter has been subject to a publication (see paper IV on page 169) (Eker and Meissner et al., 2013).

[2] MCF-7 DOX is a sub-clone of MCF-7 WT cells that was selected by continuous exposure to doxorubicin and they are functionally and phenotypically distinct from the parental MCF-7 cells (Devarajan et al., 2002).

[3] 400µl from the cell suspension of $1 million \cdot ml^{-1}$ cell density was injected inside the wells. 400000 cells on each electrode chip were sufficient enough to cover the inside part of the wells ($5095 cells/mm^2$).
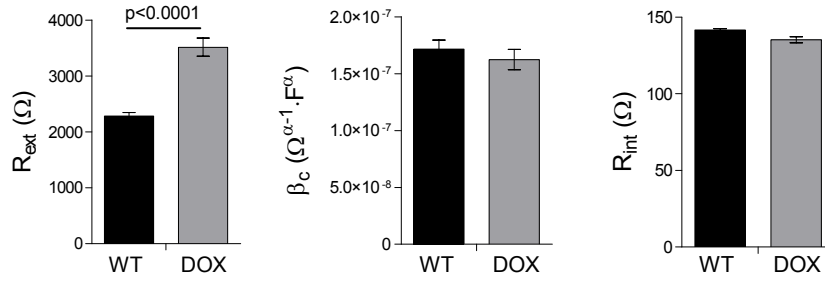
Figure 5.2.: Comparison of the dielectric components of MCF-7 WT and MCF-7 DOX cells (mean ±
SEM). The resistant cells display a significant increase in R_{ext} compared to the wild type
cells. The magnitude β of CPE_c and R_{int} do not show significant alterations when the
cells gain drug resistance. ($n = 35$ for MCF-7 WT and $n = 21$ for MCF-7 DOX cells,
$\kappa = 3660 \pm 50m^{-1}$ and $\sigma_{medium} = 361mS.cm^{-1}$).

and actin labeling respectively (figure 5.3). The presence of cellular tight junctions
and E-cadherin was confirmed for MCF-7 WT cells. Occludin and E-cadherine labeling
was intense and formed a continuous line at the cell contacts. No E-Cadherin could
be identified for MCF-7 DOX cells and tight-junctions were rare. Immunocytochemical
staining of actin cytoskeleton revealed significant structural changes between MCF-7 WT
and MCF-7 DOX cells. Drug resistant cells exhibited a highly dense fiber-like network
of actin filaments while MCF-7 WT cells showed much less labeling for F-actin protein.

5.2.2. MCF-7 DOX and MCF-7 WT cells displayed sharply different response to doxorubicin

The effect of doxorubicin on MCF-7 WT and MCF-7 DOX was studied separately at LF
and HF. First, MCF-7 WT and MCF-7 DOX cells were exposed to a 20µM concentration
of doxorubicin during one day of continuous exposure. Figure 5.4 shows time dependent
impedance magnitude changes at $10kHz$. The impedance response to doxorubicin of both
cell lines is substantially different. While MCF-7 WT cells were severely affected by the
drug at this concentration, MCF-7 DOX cells showed increasing impedance magnitudes
under drug exposure within $24h$. Control experiments showed that both MCF-7 DOX and
MCF-7 WT cells were healthy in the absence of drug and displayed relatively unchanged
impedance profiles within $24h$. In order to make sure the impedance magnitude changes
originate from doxorubicin-induced cellular changes, not from the presence of doxorubicin
in the cell medium itself, the spectra of cell medium with and without drug in the absence
of cells were recorded as a control experiment (data not shown). Only a 5% increase in
the impedance when 20µM doxorubicin was introduced to the cell medium was observed.
This is negligible compared to the observed increase of the impedance in the presence of
cells. In addition, the temporal evolution of $|Z|$ of 20µM doxorubicin in cell medium did
not show any change when there are no cells inside the wells.

Doxorubicin treatment with different concentrations was performed with MCF-7 WT
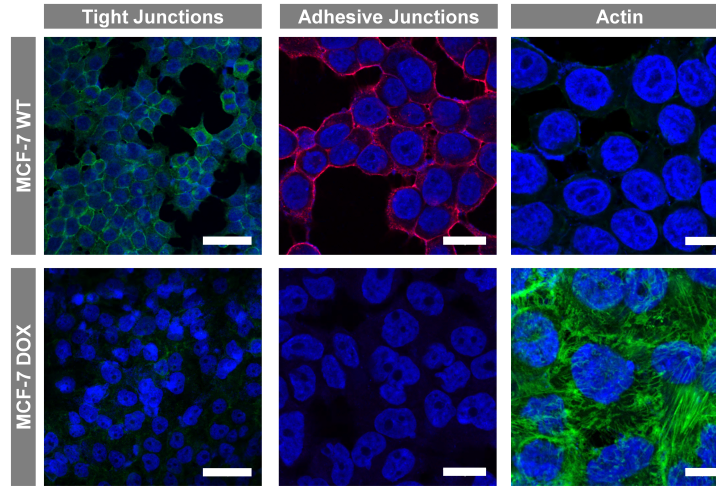
Figure 5.3.: Immunocytochemical staining of cellular tight junctions (green: occludin - Cy-2, blue: DAPI, bar=$50\mu m$), adhesive junctions (Red: E-cadherine - Rhodamine, blue: DAPI, bar=$20\mu m$) and actin (green: Phalloidin-FITC, blue: DAPI, bar=$10\mu m$) for MCF-7 WT and MCF-7 DOX cells. Loss of tight junctions and adhesive junctions is observed upon gaining drug resistance. Drug resistant cells displayed a highly dense fiber-like network of actin filaments compared to MCF-7 WT cells.
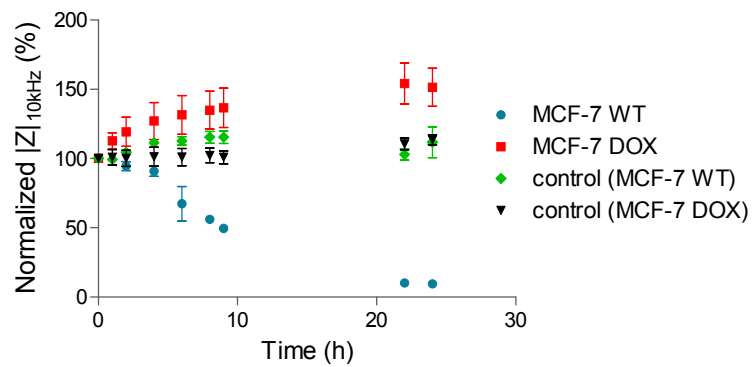
Figure 5.4.: Drug response of MCF-7 WT cells and MCF-7 DOX cells to 20µM doxorubicin at LF ($10kHz$). The impedance drops sharply for MCF-7 WT cells while MCF-7 DOX cells display increasing impedance compared to their control indicating resistance to this drug concentration and demonstrating the substantial differences in the drug response of MCF-7 WT cells and their drug resistant phenotypes.
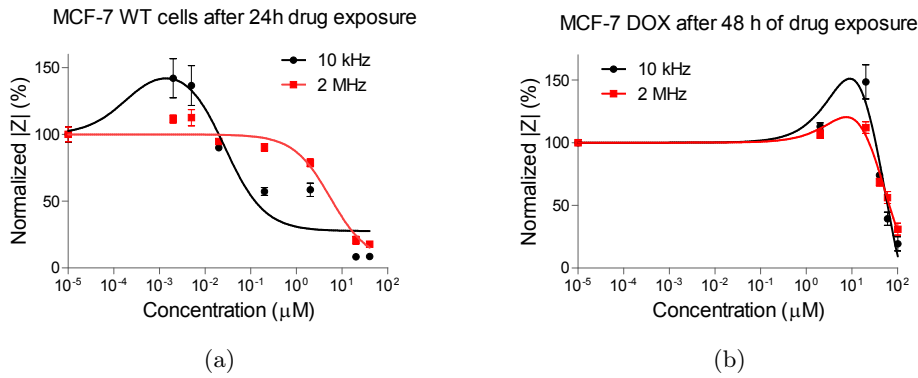
Figure 5.5.: Normalized $|Z|$ vs. different concentrations of doxorubicin at LF ($10kHz$) and HF ($2MHz$) for a) MCF-7 WT: the LF and HF signals exhibit different profiles with respect to different drug concentrations. b) MCF-7 DOX: the LF signal increases at non-lethal drug concentrations while the HF signal exhibited a slight increase. At high drug concentrations such as 40µM and higher, the LF and HF signal displayed similar impedance profiles and dropped sharply. The plots were fitted by nonlinear regression based on the equation for bell-shaped concentration response only for visual presentation.

cells but one day drug exposure was enough to obtain significant cellular changes for highly sensitive MCF-7 WT cells[4]. As seen in figure 5.5a, The LF signal exhibited an increase in the presence of low drug concentrations while the HF signal was unaltered. When cells were exposed to higher drug concentrations, the LF signal reversed its direction and started decreasing after 0.02µM drug intake, while HF signal did not change significantly up to 2µM drug exposures and decreased much later than the LF signal.

On the other hand, since MCF-7 DOX cells are highly resistant; their temporal evolution was monitored during drug exposure for a longer period of time ($48h$). The LF signal showed considerable increase up to 20µM drug exposures while the HF signal displayed a slight increase up to the same drug concentration (figure 5.5b). High concentrations of doxorubicin (from 40µM to 100µM) lead to an impedance drop at both LF and HF, revealing similar kinetics and decreasing sharply at both frequencies.

In addition, concentration-response curves were obtained by plotting $|Z|$ at $2MHz$ after $48h$ of drug exposure vs. different drug concentrations. The half maximal inhibitory concentrations (IC_{50}) for both MCF-7 WT and MCF-7 DOX cells were extracted from the fit to sigmoid concentration-response curves as shown in figure 5.6. IC_{50} values were obtained as 0.4µM and 70µM for wild-type cells and drug resistant cells respectively.

---

[4] Doxorubicin was dissolved in cell medium and added to the cells at different concentrations (from 0.005µM to 40µM for MCF-7 WT and from 2µM to 100µM for MCF-7 DOX).
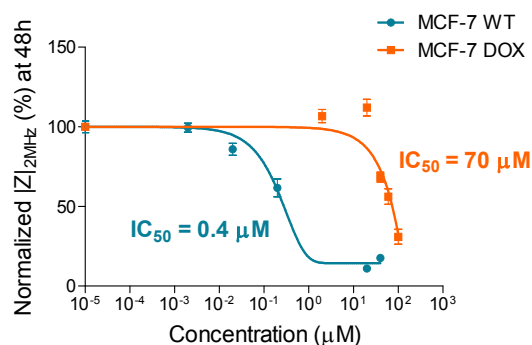
Figure 5.6.: Concentration-response curves are obtained by plotting $|Z|$ at $2MHz$ after exposing the cells to various concentrations of doxorubicin. The data was fitted to a sigmoid model. Based on the resulting fit, IC_{50} values were obtained as 0.4µM and 70µM for MCF-7 WT and MCF-7 DOX respectively.

5.2.3. MCF-7 DOX and MCF-7 WT cells showed remarkable LF impedance increase at nontoxic drug concentrations

MCF-7 DOX cells showed a concentration-dependent impedance increase when they were exposed to drug concentrations between 2µM and 20µM and such impedance increase with respect to the control was more pronounced at LF with very little difference obtained at HF (figure 5.5b and 5.7a). When the drug was replaced with medium after MCF-7 DOX cells were exposed to such concentrations of doxorubicin for $48h$, the impedance signals retrieved back to their initial magnitudes (figure 5.7b). In addition, a step-wise increase of the drug concentration also leads to a step-wise increase of $|Z|$ (figure 5.7c). The subsequent exposure of the resistant cells to first 5µM and then 20µM doxorubicin concentrations (each for $24h$) resulted in a step-wise increase of $|Z|$; finally the signal dropped back to its initial value after incubating the cells in medium for $1h$.

Such an impedance increase at nontoxic drug concentrations was also observed for MCF-7 WT cells (figure 5.5b). MCF-7 WT cells displayed higher impedance when they were exposed to the nonlethal drug concentrations such as 2 and 5nM compared to the same cells in the absence of drug (control). Such an increase was observed only at LF while the HF signal showed negligible change in the presence of non-lethal drug concentrations.

5.3. Discussion

It was demonstrated that impedance spectroscopy is a useful technique that distinguishes drug resistant cells from their parental cells based on their dielectric properties. Breast cancer cells at earlier and later stages of the disease as well as the concentration and time dependent effects of doxorubicin on cell interior and exterior can be screened. It was shown that drug resistant variants exert higher extracellular resistance that can be pinpointed by their impedance profiles. Moreover, it was shown that actin cytoskeletal
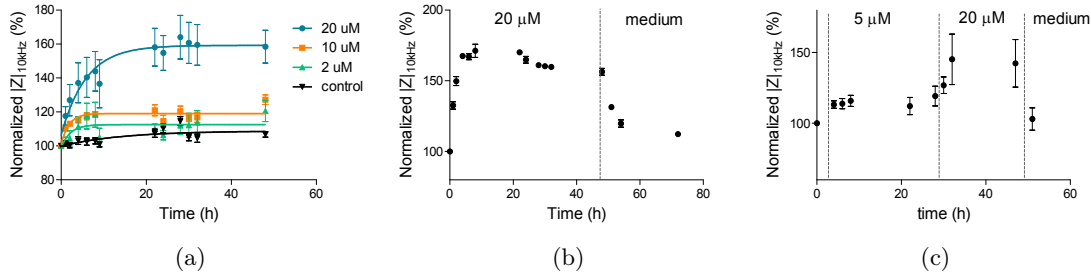
Figure 5.7.: Effect of stimulatory non-toxic drug concentrations on MCF-7 DOX. a) MCF-7 DOX exhibit a concentration dependent increase in impedance magnitudes during drug treatment with nontoxic concentrations. The plot was fitted by nonlinear regression using exponential decay equation only for visual presentation. b) Impedance magnitudes vs. time plots of MCF-7 DOX cells when $20\mu M$ doxorubicin was applied for $48h$ and followed by medium washing for $24h$. This shows that the impedance increase is reversible when the drug is removed. c) Temporal evolution of $|Z|$ when resistant cells were exposed to $5\mu M$ doxorubicin for $24h$, followed by $20\mu M$ drug concentration for $24h$, then medium washing as a last step for $1h$. This shows that the impedance increase can be sequentially added up; once the stress on cells is removed, the initial state of extracellular environment is re-obtained.

remodeling could play an important part in higher extracellular resistant behavior of MCF-7 DOX cells, providing stronger cellular architecture.

5.3.1. Distinction of drug resistant cells with their cell dielectric properties

The dielectric properties of MCF-7 DOX cells and MCF-7 WT cells were investigated. Based on fitting their impedance profiles to the equivalent circuit model, both cell lines exhibited similar R_{int} and β_c indicating that there were no measurable alterations in the electrical properties of the cell membrane and cytosol when MCF-7 cells gain drug resistance. However, drug resistant cells displayed 50% increase in R_{ext}, implying significant changes in the cell morphology and structure upon drug resistance. The finding with R_{ext} is a novel result, however quite unexpected. R_{ext} for drug resistant cells was expected to be lower since loss of tight junctions and absence of E-cadherin in MCF-7 DOX cells (figure 5.3) should have resulted in shunting of the current flow through the intercellular space and thereby lowering the R_{ext}. On the other hand, actin staining shows that MCF-7 DOX cells possessed highly dense F-actin network and had elongated form of actin fibers in cytoplasm up to the cell peripheral region, while MCF-7 WT cells had peripheral actin, which is much less dense in their cellular structure. These results suggest that remodeling of the actin cytoskeleton might probably be the reason behind the higher extracellular resistance when MCF-7 cells become resistant to doxorubicin.

The actin network is a crucial and complex system that provides base and support to retain cell morphology, mechanical structure and function such as cell adhesion, cell migration/motility, cell division, cell exocytosis and endocytosis (Pollard and Cooper, 2009). The extracellular and phenotypical events of a metastatic carcinoma are mainly governed by structural reorganization of actin (Zhao and Guan, 2009; Olson and Sahai,

2009). If the MCF-7 cells use the reorganization of the actin cytoskeleton to become resistant to doxorubicin, then a question may arise about the role of dynamic actin remodeling on transformation of a cancer cell to a drug resistant phenotype. Some studies showed that actin remodeling may play a part in the inactivation of some actin binding proteins such as E-cadherins (Perl et al., 1998; Wheelock et al., 2008) and gelsolin (Rao and Li, 2004) that have tumor-suppressor functions, and activation of actin signaling pathways that leads to malignant phenotypes such as pathways involving Ras (Downward, 2003) and Src (Winograd-Katz et al., 2011) proteins. A recent study showed lower cell stiffness upon disrupting the actin cytoskeleton with an inhibitor of actin polymerization, implying the importance of actin remodeling in drug-mediated cell stiffness modulation and drug resistance (Sharma et al., 2012). However, it is still unclear if such highly dense F-actin network participates in drug efflux by limiting the drug intake by drug resistant cells or if such organization of F-actin filaments participates in drug efficacy through influencing the cell membrane physical properties. In addition, such actin reorganization might be a consequence of drug-induced phenotypic events of a signaling pathway that leads to drug resistance. The exact effect of actin remodeling on the drug resistance remains to be elucidated and was not the focus here.

Overall, the drug resistant cells were distinguished from their parental cells based on their higher extracellular resistance. Such detection of drug resistant cells based on their dielectric properties might allow assessing the stage of the disease by selective recognition of certain phenotypes and designing the optimum personalized treatment based on the disease progress.

5.3.2. MCF-7 DOX display a 175 times higher drug resistance

The drug response of MCF-7 DOX cells was compared with the one of MCF-7 WT cells. It was observed that only strong doxorubicin concentrations such as $40\mu M$ for MCF-7 DOX and higher concentrations could decrease the LF and HF impedance signal within $48h$ (figure 5.5b). MCF-7 WT cells, on the other hand, displayed an impedance decrease from $0.2\mu M$ after $24h$ already (figure 5.5a). This shows that MCF-7 DOX cells are more resistant to doxorubicin.

Based on the concentration response curves of these two cell lines (figure 5.6), MCF-7 DOX cells exhibited a 175 times higher IC_{50} value than that of MCF-7 WT cells, which is consistent with the findings of Chen et al. (2002) who obtained more than 150 times more resistance with MCF-7 DOX cells compared to their parental cells by applying conventional viability assay to the same cell lines (Chen et al., 2002). This shows that impedance screening offers a highly sensitive label-free technique that can assess the effect of the drug on the different phenotypes of the same cell type with high accuracy.

5.3.3. Impedance profiles revealed four distinct drug responses within specific ranges of drug concentrations

As was also shown in chapter 4, HF and LF impedance signals exhibited different kinetics when cells were exposed to drug, revealing different information about cell properties
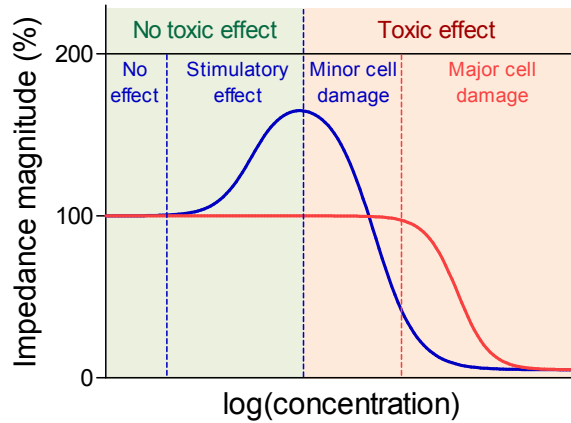
Figure 5.8.: Hypothesized impedimetric concentration-response map. (1) At low nontoxic drug concentrations, the drug has no effect on cells which results in unchanged LF and HF signal. (2) There is a drug concentration range where stimulatory effect takes place and reflects in higher impedance owing to the changes in the cellular structure and cell-cell interaction. (3) At toxic drug concentrations, there are two different circumstances that need to be taken into account. (3) At mild drug concentrations, the drug induces minor morphological changes while cell interior is intact, reflecting in lower LF with HF remaining the same. (4) At high inhibitory concentrations, the LF and HF signal drop sharply due to the substantial morphological changes and major cell damage.

(figure 5.5b). In addition to that, two more distinct responses at LF within specific concentration ranges were observed (figure 5.8). First, the drug has no effect, resulting in unaltered LF and HF signals. Second, at higher nontoxic drug concentrations, an increase in impedance at LF is observed. The cell morphology might adapt itself in a way that cells show stimulatory response upon drug interaction and impede the current more with enhanced cell-substrate contact, resulting in higher impedance at LF while the HF signal remains the same. When the drug is toxic at higher concentrations, there are two circumstances that need to be taken into account. At mild toxic drug concentrations, there might be an intermediate phase where drug induced morphological changes result in lower LF while cell interior is unaffected with no change in HF signal. At higher toxic drug concentrations, the drug might induce substantial changes in the extracellular and intracellular environment, reflecting in a sharp and simultaneous decrease in both LF and HF signal. These findings indicate that impedance spectroscopy not only distinguishes minor morphological changes from major cellular damage based on different kinetics of LF and HF signals, but also provides useful information when applying non toxic drug concentrations, i.e. distinguishing concentrations that induce a stimulatory response from concentrations that result in no measurable effect.

5.3.4. Increased LF impedance at non-toxic drug concentrations

When low doxorubicin concentrations ($2-5nM$ for MCF-7 WT and $2-20\mu M$ for MCF-7 DOX) were added to the cell medium, $|Z|$ showed remarkable increase especially at LF compared to that of cells in the absence of drug (figure 5.5b). The HF signal was relatively unchanged. In addition, there was no impedance change when such drug concentrations were added to the cell medium itself in the absence of cells. These results imply that drug at low and non-toxic concentrations might influence the biophysical and bio-mechanical properties of cells as hypothesized in figure 5.8 and the cellular structure might adapt its organization in a way to fight against the drug by gaining cell stiffness. In fact, while a disease state causes biological and functional changes in cells, it also leads to the significant changes in the morphological properties of cells (Suresh, 2007). Cytoskeletal actin has a crucial role in governing mechanical properties of cells (Satcher and Dewey, 1996; Janmey et al., 1991) and it is prone to dynamic changes during progression of cancer in all forms (Suresh, 2007). Some studies showed increased cell stiffness when normal cells evolve to be cancerous cells (Cross et al., 2008) and some showed reduced cell stiffness upon metastasis using different biomechanical assays (Suresh et al., 2005; Guck et al., 2005). Moreover, it was revealed that chemotherapy drugs such as taxol and cisplatin resulted in an increase in cell stiffness of metastatic cancer cells (Cross et al., 2011) and increased cell stiffness of drug sensitive ovarian cancer cells upon sub-lethal concentrations of cisplatin was shown by using atomic force microscopy (AFM) (Sharma et al., 2012). Here, pronounced and intense changes in the actin cytoskeleton structure and organization were also observed when cells gain resistance . However, cell stiffness might still play a part behind the 50% increase of $|Z|$ in the presence of non-toxic concentrations of doxorubicin, but possibly other factors regarding drug-induced extracellular events might also contribute to such an impedance increase at LF.

In addition, it was shown that the drug-induced impedance increase is concentration-dependent (figure 5.7a) and reversible (figure 5.7b and figure 5.7c). This implies that cells temporarily adapt to the drug either as part of a protection mechanism or due to a direct action of the drug on actin remodeling for example. Furthermore, it may be interesting in future studies investigating weather the time delay to reverse the impedance increase is concentration dependent as well. Such impedance-based information may provide important biochemical kinetics information.

Overall, potential stimulatory drug effects such as cell stiffness of drug resistant cells at nontoxic drug concentrations were measured. These findings confirm that impedance spectroscopy is suitable for detecting and quantifying the increasing cell stiffness of drug sensitive cancer cells upon drug exposure and sensing the alterations of biomechanical properties of cancer cells on the onset of drug resistance.

5.4. Conclusion

In conclusion, it was demonstrated that drug resistant breast cancer cells can be distinguished from their parental cell population based on the differences in their dielectric properties such as R_{ext}. It was also shown that these two cell lines demonstrate a sharply

different impedance response to doxorubicin. Moreover, a reversible increase in the cell stiffness in the presence of nontoxic drug concentrations is implied by the impedimetric measurements, indicating that structural reorganization of F-actin due to the drug could play a significant role on the onset of gaining drug resistance. Such stimulatory response with simultaneous LF and HF analysis enabled the creation of impedimetric concentration response map.

Future investigations may include testing tissue samples from patients and the use of multiple assays running in parallel within an automatic system in order to develop a high-throughput platform that meets the needs of clinical diagnostics and pharmaceutical industry more comprehensively. Cell-based impedimetric sensing opens new avenues in personalized medicine to create new classes of detection devices for drug induced cellular events. Such sensing of cellular phenomena using impedance analysis combined with real-time imaging might represent a useful technique for identification of cancer cells at different stages and their interaction with drug during the progress of the disease. In this context, it may be possible to optimize drug treatment of a patient in chemotherapy.

6. Three-dimensional bio-impedance measurements

6.1. Design and fabrication of a device for 3D impedance measurements

The device from chapter 4 has the advantage of being simple to fabricate, however, it does not allow screening the entire 3D tissue sample. Although multiple layers of cells and thus a three-dimensional culture were present (figure 4.3f), the electrode geometry limited the measurement depth to the first cell layer only (small s_{el}), resulting in a "two-dimensional impedance measurement". In addition, the elliptic current distribution causes the field to be inhomogeneous in z-direction resulting in an inhomogeneous measurement contribution of different tissue depths.

To measure the entire tissue thickness, parallel electric field lines are required, which give rise to a homogeneous current distribution through the sample. This can be achieved by using parallel electrodes, however, these are very difficult to fabricate at the microscale (figure 6.1, left). Therefore, a microfluidic channel with a top insulating wall was employed to guide the electric field lines from the distantly placed planar electrodes towards the tissue sample. This leads to equipotentials on the tissue sample surface, thus resulting in virtual parallel electrodes (figure 6.1, top). A conductive hydrogel is used to separate and keep apart the tissue sample from the planar metal electrodes (figure 6.1, bottom). In addition to being conductive, hydrogels are a porous physical barrier hindering convective flow but allowing the diffusion of small molecules. By consequence, perfusion channels were included on the lateral sides of the hydrogel to account for a constant and gentle supply of nutrients and removal of waste as well as the delivery of drugs for toxicity testing. In summary, the cell culture area is entirely separated from the measurement electrodes as well as from the perfusion area owing to a stable hydrogel scaffold readily allowing diffusion.

6.1.1. Fabrication of hydrogel walls

The fabrication of the device required two silicon masters, one for molding the PDMS casing and a second for molding the hydrogel walls (figure 6.2). First, the PDMS is cured in the oven on top of the first silicon master and holes are thereafter punched to define the inlets and outlets. The structured PDMS chip is then aligned on top of the second silicon master and the liquid hydrogel is injected into the cell area inlet where it fills the empty space between the PDMS and the hydrogel master. This fabrication method was
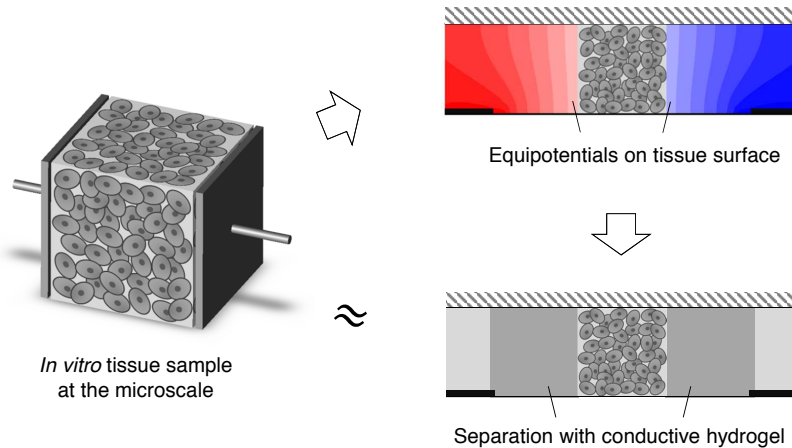
Figure 6.1.: Concept for measuring 3D tissue samples *in vitro* and at the micro-scale. To measure the entire sample thickness, parallel field lines from parallel electrodes are required (left). This can be achieved with distantly placed planar electrodes by guiding the field lines with a top insulating wall (microchannel). Quasi-equipotentials are obtained at the tissue surface (top) and thus parallel field lines. The cells can be separated from the electrodes with a conductive hydrogel that also functions as a permeable wall for nutrient supply from the perfusion channels (bottom).

termed two-step soft-lithography and a detailed process flow is provided in figure A.1 on page 94.

Although three different hydrogels have been tested as conductive spacers, agarose was revealed to be the most suitable one for various reasons as is pointed out in table 6.1. A highly permeable hydrogel is essential for large molecules to diffuse from the perfusion channel to the cell area. Although poly(ethylene) glycol-diacrylate (PEG-DA) was relatively simple to fabricate and reproducible due to its synthetic nature, it has only a small pore size that cannot account for the diffusion of large molecules such as albumin which are necessary for the cells to survive. The fabrication of hydrogel walls made of gelatin was not only much longer ($9h$) compared to PEG-DA and agarose (both $1.5h$), but
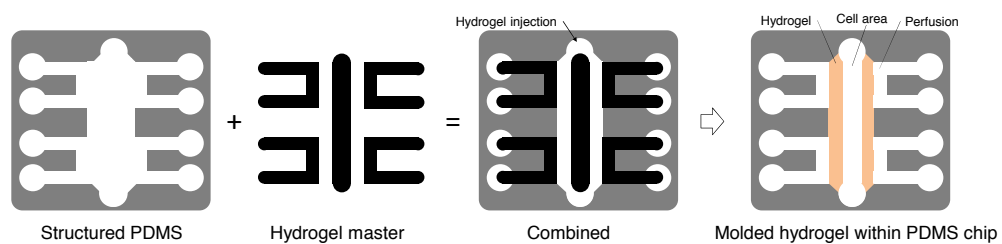
Figure 6.2.: Two-step soft-lithography. The PDMS that was structured with a PDMS master is aligned onto the hydrogel master followed by hydrogel injection in the cell channel inlet. After gelation, the PDMS chip with molded hydrogel is detached from the hydrogel master, cell inlets are freed from the remaining hydrogel and transferred onto a glass chip (e.g. with electrodes).

Hydrogel		Peg-DA	Gelatin	Agarose
Fabrication	Concentration	10%	10%	2%
	Fabrication time	1.5h	9h	1.5h
	Polymerization	UV light exposure	Enzyme cross-linking	Low temperature
Hydrogel properties	Origin	synthetic	natural (collagen)	natural (red algae)
	Adsorption	MW=575: 90% less protein adsorption than glas [1]	strong protein and cell adsorption [4]	no adsorption
	Flouresceine solubility (compared to PBS)	same	higher solubility, leading to osmosis and gel swelling	same
	Mesh size (for comparison: albumin: 14x4x4nm)	4.2nm [2]	9-30nm [5]	200nm [3]
Operator safety issues during fabrication process (according to EC regulations No 1272/2008 CLP)		DMPA: H334 / 400; PEG-DA: H315 / 317 / 318; Octyl-silane: H314	APTES: H302 / 314; Glutaraldehyde: H302 / 314 / 317 / 332 / 334 / 335 / 400, Octyl-silane: H314	Octyl-silane: H314

Table 6.1.: Comparison of physical properties of agarose, PEG-DA and gelatin with regard to their fabrication and utilization as hydrogel walls. References: 1: Shrivastava et al. (2008), 2: Garagorri et al. (2008), 3: Pluen et al. (1999), 4: Liu and Vrana (2009), 5: Yang and Mishra (2007)

the gel itself possessed a higher solubility to small molecules such as fluorescein leading to osmosis and consequently gel swelling. This decreases the stability of the hydrogel which is essential for reliable experiments. In contrast to PEG-DA and agarose, cells interact with gelatin (attachment, digestion), representing a further drawback for the use of gelatin as a stable hydrogel wall material. Besides, working with agarose instead of PEG-DA and gelatin represents less hazards regarding all chemicals used during the fabrication.

6.1.2. Gentle drug delivery through a porous hydrogel

Figure 6.3b shows the fabricated chip with agarose hydrogel walls. The walls are straight, intact and correctly positioned thus validating the two-step soft-lithography protocol. In addition, the shape of the hydrogel remains unaltered when a pressure is applied to the perfusion channel to create a flow. Both, the perfusion culture of MCF-7 cells in 2D and 3D (cells in 0.5% agarose) in the cell area was carried out (figure 6.3c and 6.3d) and displayed a high cell viability. The developed device, therefore, is considered cell culture-friendly with a cell area that is supplied with nutrients under minimal stress conditions, similarily to the conditions found *in vivo*.

To study the diffusion kinetics of the agarose hydrogel walls, a $10\mu M$ solution of fluorescein isothiocyanate-dextran was perfused (figure 6.4a). It was found that the fluorescein concentration in the cell area reaches saturation with a time constant of $10min$. A similar kinetics was observed when the fluorescein was removed through perfusion of pure PBS (figure 6.4b). Considering an experimental time period of more than $24h$, approximate $30min$ time delay until a concentration of 100% is reached represents a negligible time window. In addition, drug delivery to specific tissues in the human body after oral administration never reaches saturation, but rather experiences a fluent transition from concentration increase to decrease. For the matter of precision, the exact applied concentration may be found by calculating the area under curve (AUC) in a control experiment
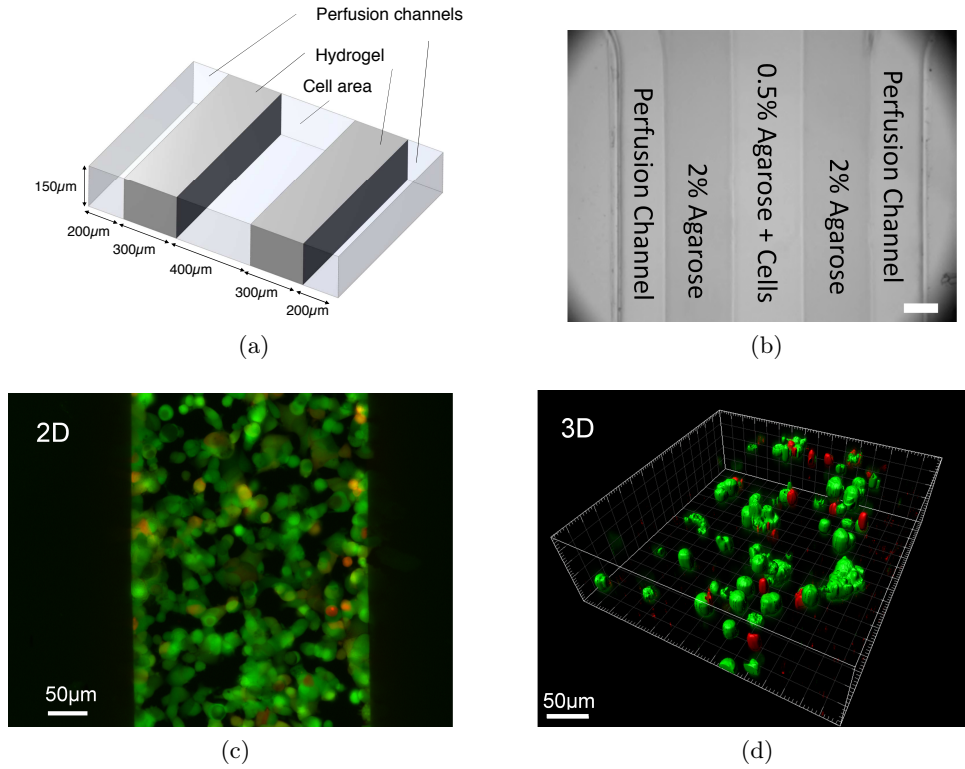
Figure 6.3.: Hydrogel wall-based device. a) Scheme of hydrogel walls that separate the cell area from the perfusion channel; b) Bright field image of fabricated agarose walls; c) & d) Live/dead stain of a 2D and 3D culture of MCF-7 cells one day after cell seeding (green: fluorescein diacetate, red: propidium iodide).
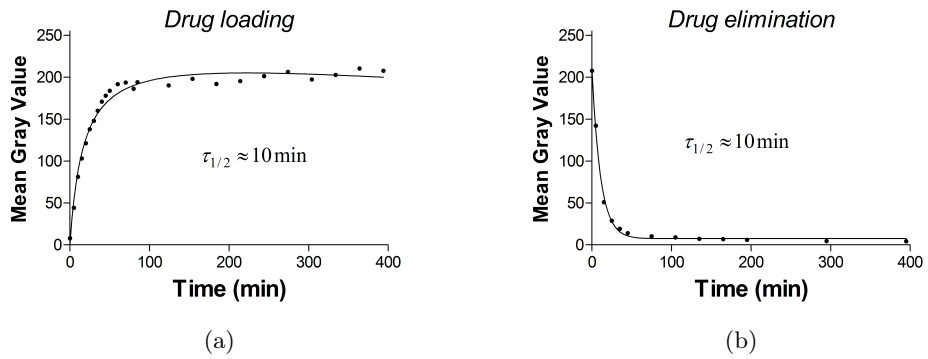
Figure 6.4.: Diffusion kinetics of fluoresceine through the agarose hydrogel walls. a) Fluorescein perfusion indicates a saturation in the cell area with a time constant of $10min$; b) Washing with pure PBS indicates a fluoresceine elimination from the cell area with a time constant of $10min$.

Top view

Side view

(a)

(b)

(c)
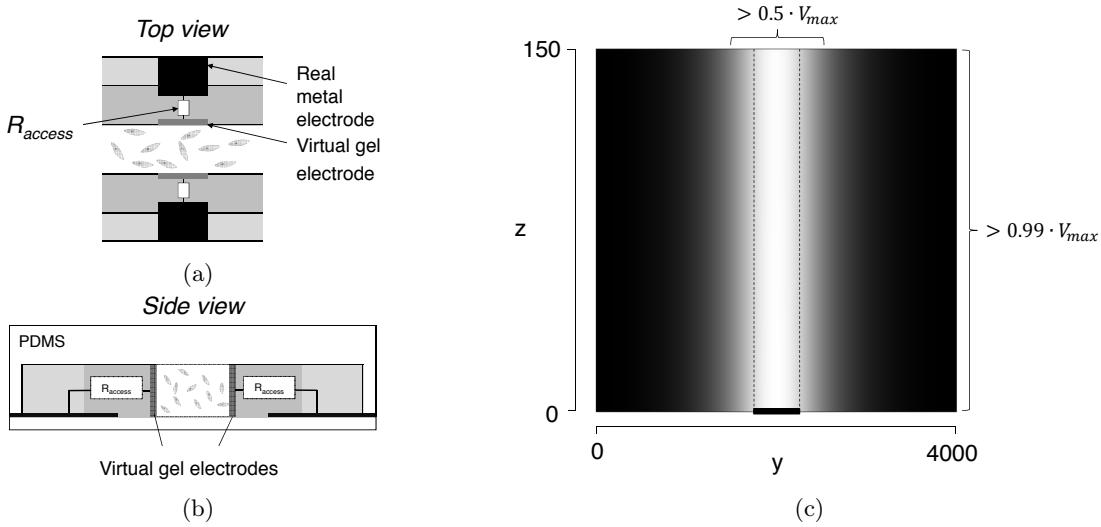
Figure 6.5.: Concept of gel electrodes. a) Top view and b) side view of microfluidicly generated gel electrodes. c) Numerical simulation of the potential on a gel electrode surface. Quasi-equipotentials are obtained in z-direction.

with a fluorescent molecule that has a comparable diffusion coefficient.

6.1.3. Gel electrodes

The goal is to establish a homogenous electric field through the entire tissue thickness. One solution would be the fabrication of three-dimensional electrodes, e.g. by electroplating. This, however, complicates the fabrication dramatically and unnecessarily. Here, relatively large, planar electrodes ($A_{el} = 0.15mm^2$) were used which provide high interfacial capacitance. The current path was defined by the geometry of the PDMS insulating top wall in z-direction that guides the electric field lines and determines the electric field distribution on the tissue sample surface (figure 6.5b). Given the almost entirely homogeneous voltage distribution on the tissue surface in z-direction (figure 6.5c, more than 99% homogeneity in the height), the vertical boundary between the hydrogel and the tissue sample was referred to as "gel electrodes". Nevertheless, such homogeneous distribution of the voltage was not guaranteed in y-direction (figure 6.5c) (1) due to the absence of an electric field line-guiding insulator and (2) due to $s_{el} > l_{el}$ which results in non-homogeneous edge effects (figure 6.5a). However, a uniform field distribution in y-direction was not essential considering that the tissue sample is much longer than the electrodes ($l_{tissue} \gg l_{el}$) and that the voltage drops to 20% of its maximum on the gel electrode surface at $2 \times l_{el}$ already. In conclusion, leakage currents were eliminated owing the newly developed fabrication process that accounts for leakage current reduction with a top and bottom insulating wall and a very long tissue sample and therefore represents a major advancement compared to previous devices (Kloss et al., 2008).

The potentials of the gel electrodes are different from the potentials applied at the

(a)   (b)
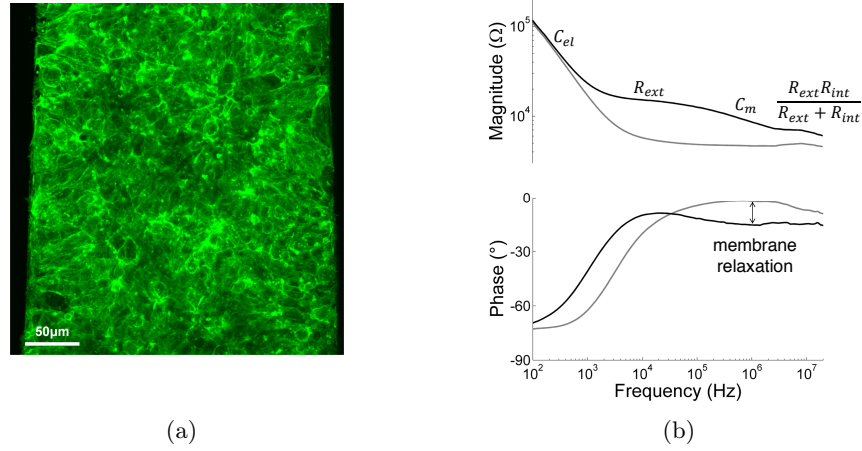
Figure 6.6.: High cell density culture is required for detectable impedance signal. a) Actin staining of a
3D MCF-7 culture indicates a high cell density; b) The corresponding impedance spectrum.

metal surface due to the voltage drop through the hydrogel. The appropriate model for
the "gel electrode" is a vertical but diffuse electrode in y-direction with a known access
resistance R_{access}.

6.1.4. Dielectric properties of the artificial MCF-7 cell tissue

Having fabricated the agarose hydrogel walls which serve as equipotential surfaces (at
least in z-direction), it is examined whether these "gel electrodes" detect the presence of a
3D cell culture. As depicted through an actin staining in figure 6.6a, a large cell density is
necessary to obtain a signal that is three times more resistive than the one in the absence
of cells (figure 6.6b). The parameters that characterize the dielectric properties of the
artificially created MCF-7 tissue were further extracted[1] and compared with the ones
from *ex vivo* tissues (mouse liver, mouse muscle and human blood). These parameters
comprise the low and high frequency reactivities (ρ_0 and ρ_∞), the dielectric constant
(ε_β) at the characteristic frequency of the β-dispersion[2] (see figure 2.12a on page 27) and
the CPE exponent α_c. They are measurement system-independent and therefore allow
their comparison with values from tissues that have a different geometry and that have
been measured with different electrodes [3]. Accordingly, the cell constant of the central
channel is calculated first. It is obtained from a measurement in cell medium using the
ratio between the access resistance R_{access} and the resistance of the central channel R_{ch}

---

[1] The tissue is considered homogenous for this calculation owing to the relatively large tissue dimensions
compared to the ones of a single cell and to the large inter-electrode spacing.

[2] The characteristic frequency is the frequency where $|Z| = \sqrt{R_0 R_\infty}$

[3] Two parallel platinum wires with a cell constant of $1100 m^{-1}$ were used to measure the impedance of
the *ex vivo* tissues ($r_{el} = 150 \mu m$, $s_{el} = 2.54 mm$, $l_{el} = 0.8 mm$)

Cell medium in the central channel:

$R_{access,1}$ R_{ch} $R_{access,2}$

$R_{tot} = 5039 \pm 293\Omega$ (n=11)
$R_{access} = 0.7 \cdot R_{tot}$ (Comsol) = $3582 \pm 244\Omega$ (n=11)
$R_{ch} = 0.3 \cdot R_{tot}$ (Comsol) = $1511 \pm 88\Omega$ (n=11)
→ $\kappa_{ch} = 2419 \pm 140m^{-1}$ (n=11)
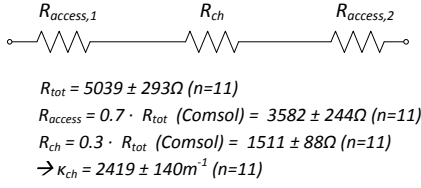
With cells in the central channel:

$\rho_0 = 5.96 \pm 0.19\Omega m$

$R_{access,1}$ $R_{access,2}$

$\varepsilon_c = 7934 \pm 924$ $\dfrac{\rho_\infty - \rho_0}{\rho_\infty \cdot \rho_0} = 1.98 \pm 0.19\Omega m$
$\alpha_m = 0.61 \pm 0.02$
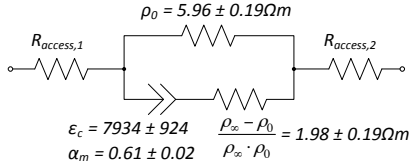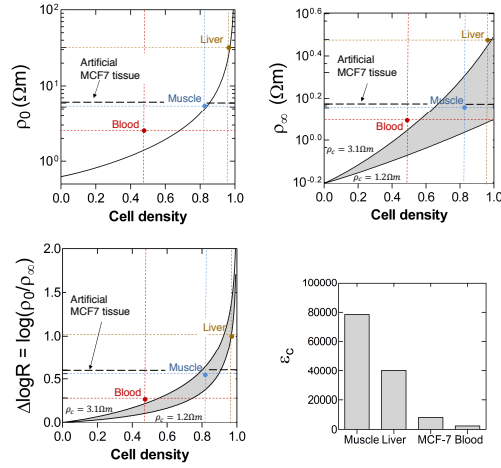
(a)   (b)

Figure 6.7.: Extraction of parameters characterizing the artificial tissue. a) The cell constant of the central channel is needed to calculate the measurement system-independent values of the tissue circuit elements. The tissue is considered homogenous for this calculation owing to the relatively large tissue dimensions compared to the one of a single cell. b) ρ_0, ρ_∞ and $\triangle \log R$ are plotted as a function of cell density. The parallel lines represent measured values and the vertical lines literature values. The area fill is flanked by the calculated curves for $\rho_{int} = 2...5 \times \rho_{med}$ with $\rho_{med} = 0.625\Omega m$. The *ex vivo* measurements are single experiments.

which was found through numerical simulation (figure 6.7a). The corresponding values were then calculated according to equation 2.6 on page 23 and are shown in figure 6.7b. Based on the theoretically determined curves (see section 3.8.3 on page 36), the cell density of the MCF-7 tissue is estimated to be between 0.8 and 0.9. Microscopic images (figure 6.6a) however, suggest an even more dense cell culture. This difference may be due to a weaker cell to cell contact than what is found between hepatocytes in the liver with a large number of intercellular junctions (tight junctions, adhesive junctions). In fact, proteins that are responsible for the adhesion of one cell to another were shown to be absent in this type of cells (figure 5.3), ultimately leading to a mismatch between the cell density and the cell volume fraction which is plotted in figure 6.7b. A further potential explanation for the non-expected relatively low value of the cell density might be a weak adhesion of the cells to the glass (at the bottom) and to the PDMS (at the top), leading to small leak currents. If the case, this can be prevented through surface treatment (e.g. fibronectin or laminin) for stronger cell attachment. Finally, the results indicate a cell population with a similar "dielectric structure" than the one of muscle tissue (provided that no leak currents are present).

Overall, the information about tissue-inherent dielectric properties can be a guidance for tissue engineering by estimating to what extent the *in vitro* recreated tissue resembles the real tissue. For example, cell density and employed cell types or clones may be adapted (which in turn modifies the dielectric constants) until a match is found with a specific *in vivo* tissue.
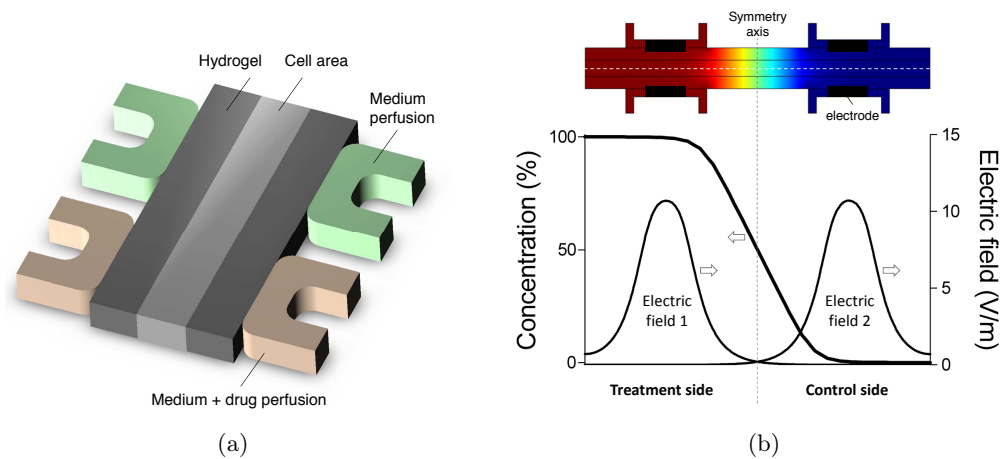
Figure 6.8.: Concept of internal tissue control for toxicity experiments. a) The scheme illustrates the localized toxin perfusion of the tissue sample (red perfusion channels). The part that is perfused with clean medium is used as a control (green perfusion channels); b) Simulation of the established toxin gradient within the device at steady state. Red color indicates 100% and blue 0% concentration. The electric field illustrates the measurement region of both electrode pairs.

6.1.5. Internal tissue control

The device design allows perfusing separate regions of the entire "tissue tube" (cell channel with a high density 3D cell culture) as illustrated by the different perfusion channel colors in figure 6.8a. Such perfusion separation was included (1) to locally treat a specific part of the tissue with a drug and (2) to use another local part of the tissue as a reference or internal control. It is noted that the cells from the treated and the untreated parts share the same history and experience the same culture conditions (apart from the drug treatment) owing to the device symmetry and a common perfusion pumping system. This *in vitro* control measurement concept is referred to as "internal tissue control".

Since reference and treated part are fluidically connected, it is assumed that drug molecules can diffuse from one side to the other. Figure 6.8b illustrates the steady state concentrations along the cell channel. Following the continuous resupply and removal of drug on the treated and control side, a concentration gradient with its center on the symmetry axis is obtained. The treated and the reference side have a concentration of $> 99\%$ and $< 1\%$ respectively, indicating a non-ideal but sufficient control condition. Figure 6.8b also shows the spatial distribution of the electric fields pointing out that the main measurement contributions are limited to the sides where the concentration is either close to 100% (treated) or to 0% (control). In conclusion, treated and non-treated parts of the same tissue are obtained by localized perfusion and the impedance of each region is measured with localized electrodes.

The concept of internal tissue control has been validated in a cell toxicity application where cells were locally treated with $1mM$ SDS. It is shown in figure 6.9a that the
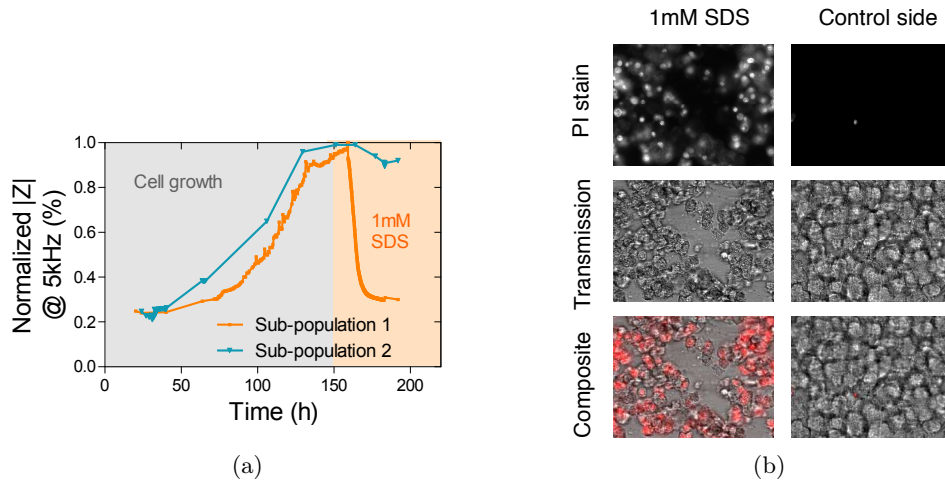
Figure 6.9.: Toxicological validation of internal tissue control. a) Impedance recording over time before and after local treatment with $1mM$ SDS. The untreated side remains highly resistive in contrast to the exposed side; b) Dead stain reveals selective toxin exposure with a large number of dead cells on the treated side.

impedance of the treated part decreased shortly after exposure while the signal of the control population remained more or less constant. This result was compared with a dead staining of the same tissue after the impedance experiment (figure 6.9b). A large number of dead cells and intercellular spaces characterize the treated part of the tissue sample. The control part, on the other hand, displayed almost no dead cell. These results validate the presented *in vitro* method of using distinct parts of the same tissue as testing and reference samples, and additionally points out its advantage of decreasing inter-population variations.

6.2. Conclusion and outlook

Impedance screening is a suitable technique to study toxicity effects on cell cultures since measurement points can be recorded continuously and therefore conclusions about the kinetics of cell injury and recovery can be drawn. However, when investigating three-dimensional cultures, electrodes that are in contact with the tissue result in localized (large inter-electrode spacing) or two-dimensional impedance measurements (small inter-electrode spacing). Also, separating the electrodes from the tissue by the means of a conductive solution generally leads to increased para-tissue currents (see figure 2.4), thus lowering the sensitivity of the measurement for tissue-inherent characteristics.

In this chapter, a strategy to measure the impedance of a three-dimensional cell culture has been presented. For this purpose, a microfluidic chip was designed that allows for the decrease of para-tissue currents on the one hand and for the probing of the entire 3D culture on the other. This was achieved by (1) recessing the electrodes from the tissue, (2) avoiding leak currents owing to the specific design and fabrication process

which involves PDMS and hydrogel molding (2-step soft lithography) and (3) limiting the tissue growth to the central channel through hydrogel walls. This screening platform additionally comprises the possibility to test two distinct parts of the same tissue allowing for the integration of an internal tissue control.

It was found that a confluent cell culture involves a three-fold increase of the impedance and is characterized by a ρ_0 of $5.7\Omega m$ which is comparable to muscle tissue for example with an estimated cell density of $80 - 85\%$ and lower than liver tissue ($\rho_0 = 33\Omega m$) with an approximate cell density of 97%. Further validation is necessary to find out whether this relatively low value at signal saturation (cell confluency) is caused by leaky cell-to-cell contacts and thus by the tissue itself or whether leak currents between the tissue and the top (PDMS) or bottom wall (glass) lead to shunting effects. However, the characterization and comparison of such inherent tissue properties provides additional hints for tissue engineering and merits a more profound study.

The sensitivity of the impedance measurement for the central channel was found to be lowered due to a relatively high voltage drop in the access regions. To counteract this drop, future designs should involve larger electrode surfaces while respecting the design rules established in section 2.3 more rigorously with wider (decreasing R_{access}) and longer (avoiding edge effect) electrodes. Although leading to a stronger impedance signature of the cells, the increase of the tissue width would be compromised by a longer diffusion distance and thus a decreased cell viability.

The design and fabrication of the developed platform has not been valued with experiments involving repeated drug perfusions for example. Given the absence of a computer-controlled switch system that manages multiple platforms in parallel, a statistically relevant investigation would have exceeded the time length of this thesis. However, groundwork has been laid evoking the challenges of three-dimensional impedance screening and providing hints about design rules, material choices, fabrication methods and data analysis.

It is believed that impedance screening of *in vitro* cell cultures has not realized its full potential yet. Being the major advantage of this technique, the continuity of acquiring data points without interfering with the cells offers favorable conditions for long term studies of drug exposures at long term and in repeated patterns and therefore will experience increased attention in near future.

7. Multiplexing toxicity measurements

7.1. Simultaneous measurement of multiple samples with only one electrode

Many cell-based assays rely on the impedance as a cell status indicator for drug response and toxicity (Meissner et al., 2011; Hug, 2003; Kloss et al., 2008; Tarantola et al., 2010; Stolwijk et al., 2011). A great variety of applications have also been demonstrated with small biological components such as proteins (Cornell et al., 1997; Chuang et al., 2011), antibodies (Steude et al., 2011; Rickert et al., 1996) and nucleic acids (Souteyrand et al., 1997; van Grinsven et al., 2011). In all these cases, one electrode pair is used to screen one specific sample only. The automatized measurement of the dielectric properties of various samples results in a multitude of electrodes, each of them additionally connected to a common multiplexing switch that is controlled by multiplexing software. These setups are not only complex, but also add noise to the recorded biological signals.

Similarly, impedance spectroscopy has been used for biomedical purposes where micro-probes are implanted in a tissue *in vivo* to measure their resistivity at different sites (Kasi et al., 2011; Mercanzini et al., 2009; Tijero et al., 2009) To access these sites, the micro-probe had to be either displaced within the tissue leading to cellular damage, or be equipped with an array of separate micro-electrodes along the probe. Separate electrodes require corresponding electrode traces that are placed in parallel on the shaft. This increases the size of the entire micro probe and potentially leads to tissue damage and inflammatory reaction. Thus, there is a great need for very small devices that are, nevertheless, equipped with a multitude of spatially dispersed sensors.
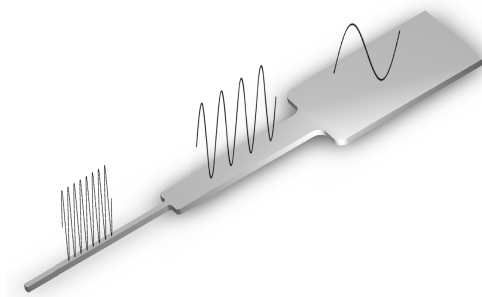
Figure 7.1.: Simplified illustration of a frequency multiplexing impedance sensor (FMIS). The sensor is able to measure multiple signals simultaneously by exploiting the frequency dimension and different local electrode geometries.
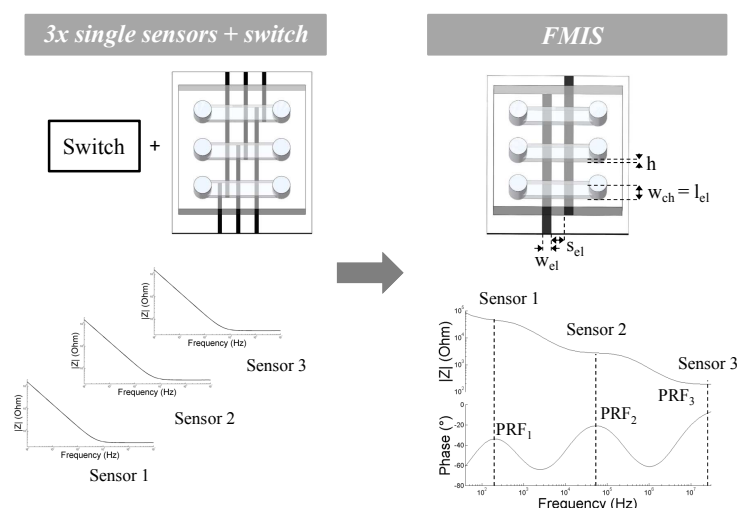
Figure 7.2.: Concept of microfluidic-based frequency multiplexing. Left: Standard measurements of three samples in different channels with three electrode pairs and a switch system. Right: The same measurements using one single frequency-multiplexing impedance sensor (FMIS)

This chapter[1] describes the development of a frequency multiplexing impedance sensor (FMIS) as simplified in figure 7.1. The FMIS technology allows for the screening of multiple sites or channels with one single electrode pair only. A theoretical model for designing a FMIS was developed and devices with up to three sub-sensors were fabricated. Subsequently, the functionality of a FMIS system that records two signals simultaneously is demonstrated. Cell-based toxicity screening is tested and demonstrates the impact that the FMIS technology might have in future applications.

7.2. Concept of microfluidic-based frequency multiplexing

7.2.1. The main principle

The purpose of this device is to screen the bulk resistance in multiple microfluidic channels with a single electrode pair (figure 7.2). Instead of using individual sensors that are accessed through a switch, a "switch-free" simultaneous recording with one FMIS is aimed. This can be achieved by connecting a single electrode pair to different parallelized channels. All channels with their embedded electrode segment define one "sub-sensor" respectively. Due to different geometries of the electrode segments, each sub-sensor has a specific PRF where the sample resistance from the corresponding micro channel can be probed. Accordingly, the impedimetric information is obtained by choosing the corresponding measurement frequency. In conclusion, frequency-dependent current pathways are created where the interface capacitors act as gates.

---

[1] This chapter has been subject to a publication (see paper III on page 161) (Meissner et al., 2012).
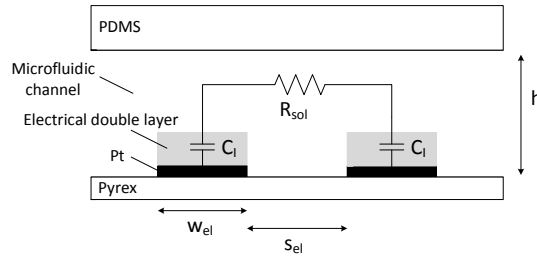
Figure 7.3.: Cross-section of the planar bipolar sensor with corresponding equivalent circuit and dimension parameters

7.2.2. Modeling a sub-sensor

Hereafter, the equivalent circuit model of a sub-sensor is discussed more in detail. As was already mentioned in section 2.2.1 on page 20, an electrical double layer is built up at the electrode–electrolyte interface when an electrode is in contact with a solution. This double layer can be modeled as a capacitor (C_I) and adds up in series to the solution resistance (R_{sol}). The cross-section of the sensor that was used in this study is illustrated in figure 7.3.

The electrical double layer capacitance can be calculated with the simple mathematical Helmholtz–Perrin model ($V < 50mV$) (Kovacs, 1994):

$$C_H = \frac{1}{2}\varepsilon_0\varepsilon_{OHP}\frac{A_{el}}{d_{OHP}} = \frac{1}{2}\varepsilon_0\varepsilon_{OHP}\frac{w_{el} \cdot l_{el}}{d_{OHP}} \tag{7.1}$$

where $\varepsilon_0 = 8.85 \cdot 10^{-12} F/m^2$ is the vacuum permittivity, $\varepsilon_{OHP} = 12.4^2$ is the relative permittivity of water (Conway et al., 1951), A_{el} is the surface area of the electrode, w_{el} is the width of the electrode, l_{el} is the electrode length (= channel width w_{ch}) and $d_{OHP} = 5\mathring{A}$ is the outer Helmholtz plane distance (Conway et al., 1951). The capacitance is divided by 2 to account for both measurement electrodes (in series). It has been described earlier that the double layer capacitance is potential dependent (Kovacs, 1994) (Gouy–Chapman capacitance). For simplicity, the effect of voltage-dependent space charge was not considered because its effect on the sensor design optimization is negligible.

The cell constant can be calculated according to equation 2.6 on page 23 and depends on the shape of the sample and the electrodes. Two cases have been employed in this study (see table 2.2 on page 22 for comparison). For the case where large electrodes are spaced far from each other, the cell constant calculates as follows (Braschler, 2009) (a derivation is provided in appendix B)

$$\kappa = \frac{1}{w_{ch}}\left(\frac{s_{el}}{h} + \frac{4ln(2)}{\pi}\right) \tag{7.2}$$

---

[2] The relative permittivity at an outer helmholtz distance of $5\mathring{A}$ corresponds to 24.8 (and $\varepsilon_r = 0$ at $d_{OHP} = 0\mathring{A}$) according to Conway et al. (1951). An average value of 12.4 for the entire electrical double layer was used in this study. This is valid because of the linear relationship between d and ε_r.
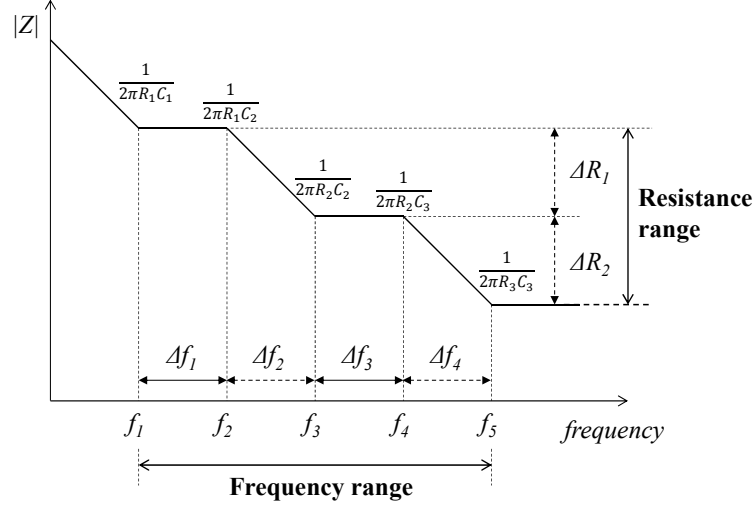
Figure 7.4.: Simplified impedance magnitude-frequency spectrum according to a triple sensor. All cut-off frequencies necessary for the optimization process are shown. C_n is the double layer capacitance and R_n is the bulk resistance of the nth electrode-channel segment.

where s_{el} is the inter-electrode spacing, w_{ch} is the channel width and h is the channel height. The first term can be interpreted as the resistance through the channel and the second term as the series resistance due to the curving of the field lines down towards the metal electrode. For the case where small electrodes are placed in proximity, the cell constant calculates as follows (Olthuis et al., 1995)

$$\kappa = \frac{1}{l_{el}} \frac{K(k)}{K\left(\sqrt{1-k^2}\right)} \tag{7.3}$$

where $K(k)$ is the complete elliptic integral of the first kind and $k = s_{el}/(s_{el} + 2w_{el})$.

7.2.3. Optimization of frequency-multiplexing

For the FMIS, several sub-sensors characterized by different geometries are connected in parallel. In order to perform reliable impedance measurements in the different channels, a number of parameters need to be optimized. Two factors influencing the measurement sensitivity have to be taken into account. First, the PRF of the different sub-sensors needs to be well-defined and well-separated for good identification of all sensor-specific measurement frequencies. Second, the total resistance range needs to be maximal in order to avoid cross-talk between the sensors and to guarantee a large resistance measurement window ($\triangle R$). It is obvious, however, that these two conditions are guaranteed by separating the different cut-off frequencies. This process is named the frequency separation method (FSM). All relevant frequencies for the FSM are illustrated in figure 7.4.

As a specific case, all the following considerations apply to a triple-sensor (a similar reasoning is valid for any number of sensors). A maximal separation of the PRFs re-
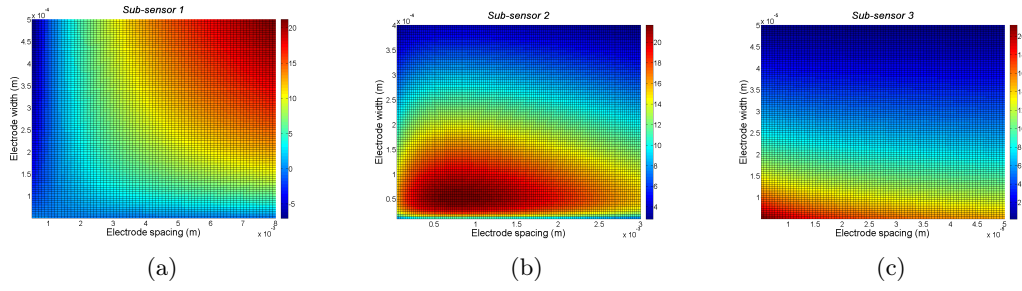
Figure 7.5.: Simulation of M as a function of w_{el} and s_{el}. (a) Sub-sensor 1 indicates a large M with larger values for $w_{el,1}$ and $s_{el,1}$, (b) Sub-sensor 2 indicates an optimum of M at $w_{el,2} \approx 50\mu m$ and $s_{el,2} \approx 1000\mu m$; (c) Sub-sensor 3 maximizes M for small values of $w_{el,3}$ and $s_{el,3}$. All simulations were carried out with the fabrication values ($w_{el,1} = 500\mu m$, $w_{el,2} = 51\mu m$, $w_{el,3} = 5\mu m$, $s_{el,1} = 8000\mu m$, $s_{el,2} = 1150\mu m$, $s_{el,3} = 5\mu m$,)

quires the differences of all cut-off frequencies ($\triangle f_{1-4}$) to be as large as possible. This is guaranteed by maximizing the product of all the $\triangle f$. This product is further referred to as M:

$$
\begin{aligned}
M &= (\triangle f_1 \cdot \triangle f_3) \cdot (\triangle f_2 \cdot \triangle f_4) = P \cdot D \\
&= \left(log\left(\frac{f_2}{f_1}\right) \cdot log\left(\frac{f_4}{f_3}\right) \right) \cdot \left(log\left(\frac{f_3}{f_2}\right) \cdot log\left(\frac{f_5}{f_4}\right) \right)
\end{aligned}
\tag{7.4}
$$

where $\triangle f_n = log(f_{n+1}/f_n)$ is defined as the cut-off frequency difference, P as the plateau length parameter and $D = \triangle R_1 \cdot \triangle R_2$ as the total resistance range. In figure 7.4 the different cut-off frequencies are given by $f_c = 1/(2\pi R_{sol}C_H)$. Consequently, the maximization of M has implications on all the experimental parameters from equation 7.1-7.3. It becomes nevertheless apparent that only w_{el} and s_{el} are relevant for the optimization process since l_{el} is canceled out (if kept the same for all channels) and ρ cannot differ in cell culture applications. Finally, M can be simplified as

$$
M = log\left(\frac{w_{el,1}}{w_{el,2}}\right) \cdot log\left(\frac{w_{el,1}}{w_{el,2}}\right) \cdot log\left(\frac{\kappa_1}{\kappa_2}\right) \cdot log\left(\frac{\kappa_2}{\kappa_3}\right)
\tag{7.5}
$$

where κ is calculated according to the electrode size by using one of the equations from table 2.2 on page 22. M was simulated for all three sensors as a function of w_{el} and s_{el} as shown in figure 7.5. According to figure 7.5a, both electrode spacing and width have to be as large as possible for sub-sensor 1. In this case, the main size limitations are given by the available space on chip and by the lowest AC measurement frequency. Similarly, according to figure 7.5c, the geometrical dimensions have to be as small as possible for sub-sensor 3, the main limitation being now given by the microfabrication process. Once the dimensions of sub-sensors 1 and 3 are set, the electrode spacing and width of sub-sensor 2 can be optimized by maximizing the function M (figure 7.5b).

Note that the dimensions of sub-sensors 1 and 3 determine respectively the lowest
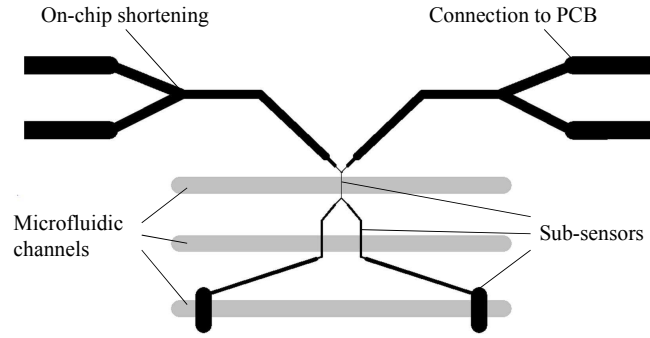
Figure 7.6.: Electrode (black) and channel (gray) design. The bipolar electrode pair is characterized by three sub-regions that differ in electrode width and spacing. Three microfluidic channels are implemented to create a sample separation aligned onto the three sub-sensors. Four PCB connection pads are used since the shortening of the current injection and the voltage pick-up electrodes is done on-chip (higher sensitivity).

and highest cut-off frequencies of the FMIS, and consequently its total frequency range ($= f_1/f_5$) and total resistance range ($= R_3/R_1$). The optimization of the dimensions of sub-sensor 2 determines the other cut-off frequencies such that they are distributed as equally as possible over the total frequency range, especially $P_1 = P_2$ ($\triangle f_1 = \triangle f_3$) and $D_1 = D_2$ ($\triangle f_2 = \triangle f_4$). Moreover, the total resistance range D can be further increased by introducing interdigitated electrodes, simultaneously decreasing the plateau lengths (P). A model was developed that provides the number of interdigitated electrode fingers for a desired resistance range (see appendix C for detailed information).

7.3. FMIS sensor design

7.3.1. Electrode design

The electrode dimensions were based on the simulations presented in figure 7.5. Large $s_{el,1}$ and $w_{el,1}$ ($8000\mu m$ and $500\mu m$) were chosen as indicated by figure 7.5a. The parameters of the third sensor, $s_{el,3}$ and $w_{el,3}$, were chosen small (both $5\mu m$). In the case of the triple sensor, the additional parameters $s_{el,2}$ and $w_{el,2}$ were chosen according to the resulting optimum as demonstrated in figure 7.5b ($w_{el,2} = 51\mu m$ and $s_{el,2} = 1150\mu m$). The FMIS is shown in figure 7.6 (double sensor: only the upper and lower channel was used; triple sensor: all channels).

7.3.2. Microfluidic chip design

A microfluidic chip made of PDMS was used to separate the sensing areas. Two (double sensor) or three (triple sensor) microfluidic channels were embedded, all with a channel width of w_{ch} (l_{el}) $= 500\mu m$ and a channel height of $h = 120\mu m$. The channel height was defined by the fabrication process (thickness of the structured tape that was used for PDMS molding).

Parameters	Calculated	Experimental
R_1	$82\ k\Omega$	$104\ k\Omega$
R_2	$1.2\ k\Omega$	$1.5\ k\Omega$
C_1	$27.4nF$	$28.4nF$
C_2	$0.35nF$	$0.29nF$
f_1	$70Hz$	$40Hz$
f_2	$5.6kHz$	$5.6kHz$
f_3	$383kHz$	$357kHz$
κ_1	$139 \cdot 10^3 m^{-1}$	$169 \cdot 10^3 m^{-1}$
κ_2	$2026 m^{-1}$	$2156 m^{-1}$
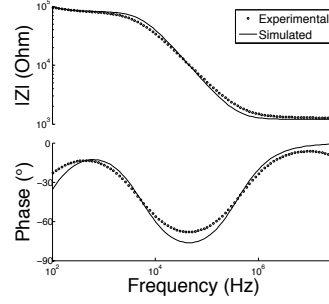
Figure 7.7.: Simulated and experimental impedance data of double sensor. left: Table with theoretical and experimental values for equivalent circuit parameters. Calculated data was obtained by equations 7.1-7.3. Experimental data was extracted through equivalent circuit fitting (mean, n=5). right: Simulated and experimental impedance spectrum

7.3.3. FMIS testing method

The microfluidic channels were filled with different concentrations of PBS (phosphate buffered saline) ($0.125\times$, $0.25\times$, $0.5\times$, $1\times$, $2\times$). First, only one channel was filled with liquid while the other ones contained air (mono sensor). Second, all channels were filled with PBS and the concentration was varied crosswise (double/triple sensor). The solution resistances were obtained through fitting of the recorded impedance spectra to the equivalent circuit. For sensitivity determination (ρ_{meas}/ρ_{real}), the measured resistivity ρ_{meas} was obtained by dividing the mean resistance by the average experimental cell constant. The resistivity of the different solutions ρ_{real} ($= \rho_{sol}$) was measured with a conductivity meter (Seven Easy, Mettler Toledo). It is assumed hereafter that these values are the real resistivities of the solutions.

7.4. Testing the concept of FMIS

7.4.1. Characterization of the double sensor

The goal of this study was to demonstrate the ability to measure two or more signals with one single electrode pair. For this, the frequency dimension was exploited to separate the different signals. The major challenge was to design the sensor such that a maximal frequency separation of the PRFs (figure 7.2) and thus a maximal M (equation 7.4) could be achieved. In the first step, the device was characterized experimentally to verify the validity of our simulations and the consequential chip design. All system specific parameters and the corresponding impedance spectra are presented in figure 7.7. The small deviations in cell constant, resistance and capacitance values were attributed to the flexible PDMS that cannot guarantee very precise fabrication dimensions. In addition, the dimensions of the electrode after fabrication were not exactly $5\mu m$ each ($s_{el2} = 3.4\mu m$ and $w_{el2} = 6.3\mu m$).

Concurrently, the experimental impedance magnitude and phase curves are found to be more flattened than the simulated one (figure 7.7). This is explained by the complex

c(PBS) (ρ_{sol})	0.125x (4.37Ωm)	0.25x (2.24Ωm)	0.5x (1.15Ωm)	1x (0.61Ωm)	2x (0.32Ωm)
Mono sensor 1	748.6±13.3	380.7±7.9	195.8±4.5	103.5±2.4	55.2±1.6
Mono sensor 2	9.1±0.20	4.79±0.06	2.49±0.03	1.32±0.02	0.71±0.01
Double sensor 1	768.3±11.8	393.2±5.5	204.6±1.6	107.1±0.7	57.4±1.0
Double sensor 2	9.30±0.07	4.80±0.03	2.53±0.04	1.37±0.02	0.71±0.01

Table 7.1.: Measured solution resistance values (in kΩ) in channel 1 and 2 in the mono- and double sensor mode as a function of PBS concentration (mean ± SEM, n=5).

nature of the electrode–electrolyte interface (see section 2.2.1 on page 20). Surface roughening and steric effects lead to a multitude of different capacitor–resistor circuits resulting in a descending slope that is inferior to 45° (which is the slope angle of an ideal capacitor). This complex behavior is conventionally described by a constant phase element (De Levie, 1965). However, for the sensor optimization the interface capacitance is considered as a perfect capacitor since the goal here is to simply separate cut-off frequencies. For this purpose, an approximate value for the capacitance is sufficient. A double sensor was fabricated that meets the initial requirement of well frequency-separated PRFs. Small deviations in the cell constant of sensor 1 and the capacitance of sensor 2 were attributed to setup and fabrication. Nevertheless, it has been shown that the double sensor complies with the design specifications.

7.4.2. Validation of the FMIS

In order to validate the FMIS, the similarity of the measurement results of both sub-sensors compared to their corresponding mono sensors was verified on the one hand, and their measurement sensitivity on the other. Channel 1 and 2 were measured individually (mono sensing) and simultaneously (double sensing). The mono sensor measurements were done by leaving one channel filled with air. The double sensor measurements were carried out by varying the PBS concentration in channel 1 and 2 crosswise. The results are shown in table 7.1 and illustrated in figure 7.8. The values for the mono and double sensors match well for both channels with a maximum deviation of less than 4% for sensor 1 at 0.5× PBS (196kΩ vs. 205kΩ). No significant deviation difference from the mono to double sensor is observed between channel 1 and 2 (3.4% vs. 1.5%). Thus, both sensors are considered equally functional. Next, the sensitivity of sub-sensor 1 and 2 was evaluated. Figure 7.8b shows the ratio of the measured resistivity against the real resistivity at different dilutions of PBS. Both sensors show a very high sensitivity with a maximal median deviation of 3.8% for sensor 2 at 1× PBS. Nevertheless, sub-sensor 2 reveals a larger average deviation of the means than sub-sensor 1 (2.2% vs. 0.7%). This is explained by the inherent higher sensitivity of sub-sensor 2, due to its lower resistance compared to sub-sensor 1. In conclusion, no significant value differences between the mono sensors and the FMIS were observed and a high sensitivity was demonstrated.

(a)   (b)
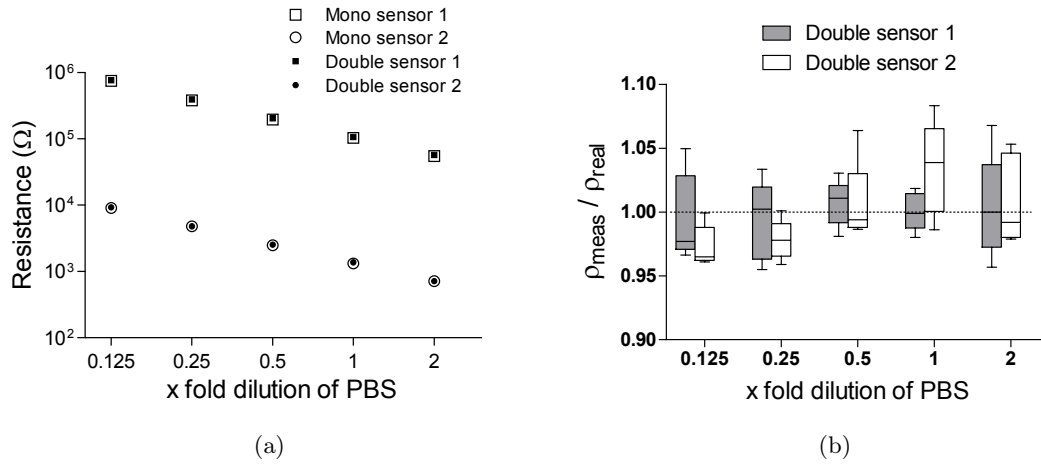
Figure 7.8.: Double sensor validation. (a) Measured solution resistance values in channel 1 and 2 in the mono- and double sensor mode are plotted against the PBS concentration (mono sensor: mean + connecting line; double sensor: mean ± SEM, n=5). Error bars not shown are smaller than the symbol size. The double sensor values correlate well with those from the mono mode. (b) Box plot of the ratio of measured resistivity and real resistivity as a function of PBS concentration (whiskers: min to max). The measured resistivities were calculated dividing the solution resistance by the average experimental cell constant (see figure 7.7). Both sensors show high sensitivity with a maximal median deviation of 3.9 % (sensor 2 at 1x PBS)

7.4.3. Cell toxicity application

The applicability of the FMIS to cell culture experiments was verified. MCF-7 cells were seeded in both microfluidic channels ($10 Mio$ cells/ml) and cultured for a period of $24h$. Then, the cells were treated with $100 \mu M$ doxorubicin in one channel after another with a time delay of 45 min. Accordingly, the sensor selectivity of the FMIS measurement method was investigated for utility in cell toxicity platforms. Figure 7.9 shows the impedance magnitude spectra in the absence and presence of cells (a) as well as the temporal evolution of the cellular impedance for both channels after drug treatment (b). The frequency where the impedance change is largest (following cell–electrode attachment) depends on the sensor geometry. Consequently, different geometrical constants among sensors 1 and 2 lead to two different screening frequencies ($|Z|_{rel}$- maxima in figure 7.9a). Furthermore, it was observed that the relative impedance change is larger for sensor 2 than for sensor 1. This may be explained by the different electrode sizes. One cell is able to cover the entire electrode width of sensor 2, thus insulating this one completely. The electrode of sensor 1, on the other hand, is too large and the current can shunt in between the cells resulting in a leaky insulation and a less strong relative impedance increase. Being treated first with doxorubicin, the resistance of channel 1 dropped by 40% within 30min. The measured resistance in channel 2, on the other hand, remained constant at 100%. Once channel 2 was treated after 45 min, the corresponding resistance decreased as well.

Figure 7.9.: Cell toxicity experiment. a) Impedance magnitude spectra and relative $|Z|$ change ($|Z|_{rel} = (|Z|_{cell} \cdot |Z|_{cell-free})/|Z|_{cell-free}$) due to cell attachment in channel 1 and 2 are shown. Each channel has its specific $|Z|_{rel}$ maxima. b) The cell impedance $|Z|_{cell}$ is shown for both sub-sensors at the $|Z|_{rel}$-maxima-frequencies. MCF-7 cells cultured in both channels were exposed to $100\mu M$ doxorubicin with a time delay of $45min$. '1' and '2' indicate the drug application in channel 1 and 2.

This experiment demonstrates the high selectivity of the FMIS measurement method. Two distinct cell populations have been screened separately with only one electrode pair. Although two identical microfluidic channels have been used, the electrode geometry differed. This might be a problem in cell culture applications where identical conditions are required, e.g. current penetration depth or cell–substrate contact. For those cases, the implementation of an additional electrode–electrolyte capacitor using a simple liquid-filled channel is suggested in order to modify the sub-sensor capacitance value ('capacitive bridge') (an example is provided in appendix D on page 101). In such a case, the final electrode–cell contact region can be identical.

7.4.4. Multi-channel sensing and sensor limitations

The functionality of the double sensor by validation with a cell-based application has been demonstrated. Now, the implementation of more than two sub-sensors is discussed. Instead of using multiple separated electrodes, such a FMIS would not only open the door to very simple multi-channel screening, but also allow the minimization of the total sensor size. A triple sensor has been designed, as illustrated in figure 7.6, according to the simulations presented in figure 7.5. This optimization process aims at both a maximum PRF separation and maximum resistance range. The corresponding impedance spectrum of the fabricated triple sensor is depicted in figure 7.10a. The experimental and the theoretical curve match well, although there are some deviations. These deviations are explained, as already mentioned for the double sensor, by the complex nature of the electrode–electrolyte interface and by the sensor fabrication (see section 2.2.1 on page 20). However, our fabricated triple sensor fulfills the most important requirements, i.e. the
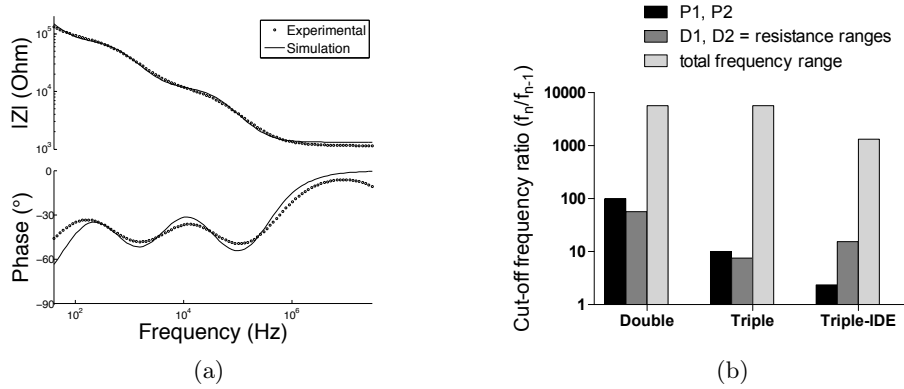
Figure 7.10.: Multi-channel sensing. (a) Simulated and experimental impedance spectrum of the fabricated triple sensor with 1x PBS. Three PRFs are identified indicating three well frequency-separated sub-sensors. The resistance ranges are similar for all sensors ($D_1 = D_2$). (b) The calculated values of $P_{1,2}$, $D_{1,2}$ and frequency range are shown for the double-, triple- and triple-interdigitated sensor. All values correspond to optimized sensors (M_{max}) where $P_1 = P_2$ and $D_1 = D_2$. The resistance ranges of the triple sub-sensors are halved compared to the double sub-sensors while the total frequency range remains constant. In contrary, the resistance ranges of the triple-IDE sub-sensors are increased by the expense of a decreased total frequency range.

distinct separation of the PRFs and equally distributed sub-resistance ranges ($D_1 \approx D_2$), within the total resistance range (D). This total resistance range is predefined by the parameters indexed 1 and 3 and equals the one of the double sensor. As a logical consequence, a common total sensor resistance range for the double and triple sensor results in halved sub-sensor resistance ranges for the triple sensor. This effect is illustrated in figure 7.10b. Hence, the resistance range linearly decreases with an increasing number of sub-sensors. Such a decrease can be opposed by introducing interdigitated electrodes as sub-sensor 3. IDEs decrease the cell constant and thus increase the total resistance range. This effect is shown in figure 7.10b where D is increased by the expense of a decreased P and also a decreased frequency range. In this context, the number of electrode fingers of the IDE can be determined for a desired resistance range (detailed information about this optimization is provided in appendix C on page 99). Despite a decreased frequency range, an increased resistance range can be particularly useful when large resistance changes are measured. In conclusion, a triple sensor using the optimization function M was fabricated. A higher number of sub-sensors at a constant total resistance range is accompanied by a lower measurement resistance range for the individual sub-sensors. This effect may be avoided by selectively increasing D, e.g. by introducing IDEs.

7.5. Future applications of the FMIS

The concept of a FMIS that is capable of screening more than one channel at the same time has been introduced. The simultaneous measurement of these channels was achieved

through frequency multiplexing. The frequency division (FSM) for all sub-sensors required the optimization of the chip design. For this purpose, a simulation model for simple rectangular electrode pairs as well as for interdigitated electrodes was developed. The fabricated chips corresponded well to the model and allowed very precise conductivity measurements in all channels in parallel. The applicability for biological experiments was demonstrated with a cell-based toxicity experiment. It has been shown that two distinct cell populations are monitored separately and simultaneously with only one electrode pair. This technology may also find applications in impedance measurements that are carried out *in vivo*. Micro-probes implanted in tissues to measure the resistivity at different sites can be simplified by reducing the total probe width since parallel electrode traces become unnecessary. Therefore, the invasiveness of a probe using this technology would be decreased. The measurements, as they were carried out in this study, comprised sub-sensors that differed in shape and positioning. When identical experimental conditions are required, e.g. in biological applications, the introduction of "capacitive bridges" is recommended. Capacitive bridges are referred to as capacitors that are placed between the individual sub-sensors, that do not contribute to the resistance measurement, but that modify the capacitance of this sensor. An additional liquid-filled channel, for example, that adds an electrode–electrolyte interface capacitor, may be integrated. On the other hand, the geometry differences may be considered as an advantage since different sensor sizes and geometries lead to different measurement depths. As an application, one FMIS may be used to probe the thickness of a tissue as it has been shown previously with a complex switch system (Linderholm, 2006). Altogether, an easy technique to screen multiple channels at the same time with a simple measurement setup has been developed. In addition to toxicological studies where parallelized screenings are essential, a demand for such devices is also seen in *in vivo* applications where the size of the implanting probes is limited, but multiple sensors are required; as well as in *in vitro* applications where different measurement depths are needed.

8. Conclusions

8.1. Summary of results

This thesis strives to contribute to a more profound understanding on how cellular responses to toxins can be detected using electrical impedance spectroscopy. Important aspects regarding *in vitro* culture and impedimetric analysis of cells in general have been raised and investigated. Several advances contribute to this achievement:

- The frequency domain has been exploited to distinguish toxicity effects on cell populations. Cellular retraction as well as the loss of cell-cell and cell-substrate contacts represent an initial stress response of cells to a toxic compound and precedes severe cellular damage (cell death). Both cell responses (stress and cell death) can be distinguished label-free and continuously by performing impedance measurements at different frequencies. The choice of these frequencies requires the effects from non-biological measurement parameters as well as from the relaxation distribution within a tissue to be taken into account by analyzing the phase angle over frequency. It was further found that the ability to distinguish minor from major cell damage is increased at higher cell densities.

- Acquired resistance of breast cancer cells to doxorubicin has been detected dielectrically. Cells that become resistant possess a higher cell stiffness and were shown to be 175 times more resistive compared to their non-resistant parental cells as was indicated by the low and high frequency impedance signals. In this context, the dependance of the impedance magnitude on the measurement frequency and on the drug concentration resulted in the creation of an impedimetric concentration-response map which distinguishes cellular responses within four concentration ranges.

- Gel electrodes have been designed and fabricated for measuring the three-dimensional impedance of three-dimensional cell populations. In this context, a 2-step soft-lithography fabrication process was developed to mold agarose hydrogel within a PDMS casing. The hydrogel is multipurpose allowing for the creation of three-dimensional gel electrodes and for the gentle perfusion of the cell culture. The specific design of the PDMS-hydrogel chip leads to decreased leak currents, a common problem when performing three-dimensional impedance measurements. In addition, the microfluidic chip is symmetrical with two identical areas where one of them can be used as an internal control.

- A method for multiplexing impedance measurements without the use of a switch nor a multiplexer and with only one electrode was developed. Different parts of

the electrode sensor have different geometries resulting in distinct measurement frequencies. Impedimetric information about each part of the electrode is obtained by screening their specific peak resistance frequency. A"double sensor" and a "triple sensor" have been fabricated and validated with conductivity and cell toxicity experiments.

- With regard to theory, the difference between single cell and cell population impedance characteristics have been expounded. Challenges concerning tissue impedance measurements and their analysis were discussed and design rules for planar bipolar impedance sensors adapted to every tissue's geometry were provided regarding measurement penetration and sensitivity.

8.2. On the control of parameters in bio-impedance measurements

In this thesis, *in vitro* cell cultures have been characterized by performing impedance measurements. An important outcome of this work has been the fact that impedance values and thereto linked biological information can be substantially different for the same biological sample. Non-biological parameters do not only change the practical β-dispersion bandwidth and thus the measurement sensitivity as was described in chapter 2 already, but also determine which properties of the examined biological specimen are primarily recorded. (1) The insulator geometry has a tremendous impact on the preferred current path. For example, an impedance measurement of a tissue within a solution will be less sensitive to para-tissue currents than an insulated tissue and thus mostly informs about the size of this tissue. By adapting the insulation to a specific tissue shape, as was shown in chapter 6, the current passes through the tissue and tissue intrinsic dielectric properties, which inform about density and intercellular spacing, can be extracted. (2) The electrode position impacts the biological information that is gathered. As was shown in chapter 5, when cells are in direct contact with two closely spaced electrodes, adhesive properties and thus the cytoskeleton are represented by the measured impedance since most of the current passes below the cell monolayer between the inner edges of the electrodes and thus indicate the ability of the cells to adhere on the substrate. Considering this, an increased distance between the two electrodes would result in a current path that preferably spreads out into the overlaid solution rather than passing below the cells. Such a configuration would lead to a screening similar to TEER measurements where intercellular junctions mainly contribute to the insulating nature of the overlaid cell layer. Therefore, it is hypothesized that the extracellular resistance difference between MCF-7 WT cells and MCF-7 DOX cells which was observed in figure 5.2 on page 55 would be reversed. In that case, two distinct biological phenomena could be investigated separately on the exact same cell layer with the same measurement method, by changing the electrode dimensions only. (3) The electrode size determines the volume of the tissue that is screened. As was mentioned in chapter 2, a large tissue that is probed with large electrodes can be considered homogenous and the experimentally

determined cell constant using an electrolyte can be employed for tissue calculations. However, when decreasing the size of the electrode, the measurement volume does not only become smaller (localized measurement), but also the impedance becomes more prone to changes at the scale of a cell rather than at the one of a tissue. Impedance scaling laws exist that must be taken into account when designing electrodes for the investigation of specific tissue- or cell-related events. (4) The measurement frequency determines whether the current is blocked by or passes through the cell membrane, ultimately providing information either about extracellular-, intracellular-, cell membrane properties or even about the distribution width of each of them. It was found in chapter 4 that this frequency-dependence of the current path can be exploited to distinguish initial cell stress from major cell damage when exposed to a toxin. In addition, chapter 5 has shown that when studying the concentration dependance of the frequency-dependent impedance, cells experience an increased stiffness when exposed to lower non-toxic drug concentrations and this cell response is expressed through an increased impedance at low frequency only. Such inter-dependance of concentration and frequency on the impedance value shows that this technique is complex, but it is precisely this complexity that renders this method useful. Many different biological phenomena can be detected given the technique is well-understood and well-controlled.

Altogether, the measured impedance of a biological specimen depends on numerous parameters. All these physical phenomena are rather well-known, however, their application to biological samples and consequences on gained biological information was incompletely studied until now. A thorough understanding of their influence on the impedance value and the linked biological information seems necessary for the study of biological processes. This thesis represents an attempt to understand some of them, however a large amount of work is still necessary.

8.3. Significance of impedance technology for toxicology

Although impedance spectroscopy is a non-specific method where the measured impedance changes for the same sample according to a variety of parameters, it remains an attractive technology. This is mainly due to its devoid of sample-interfering substances. Measurements can be recorded continuously on the *in vitro* cell culture. Therefore, the study of treatments with repeated doses becomes highly interesting. In fact, the current animal-based perception of "no observed adverse effect levels"[1] has been challenged by the high sensitivity of emerging techniques such as genomics, proteomics, metabonomics, enabling the detection of responses at very low compound doses (Roggen, 2011). It appears imperative to understand the mechanistic differences between adverse and adaptive responses to a compound, especially with regard to the repeated exposure of cells to a drug (Hsieh et al., 2009; Grotto et al., 2009). In fact, relatively little is known about the differences in mechanisms relevant for repeated dose and acute toxicity. Repeated dose toxicity may be simply a consequence of the prolonged activity of the same toxic pathway that causes

---

[1] NOAEL, denotes the level of exposure of an organism at which there is no biologically significant increase of adverse effects

acute toxicity, however, this is not necessarily the case as has been shown previously (Hengstler et al., 2012). Single administration of high doses of CCl_4 causes cell death to a fraction of hepatocytes. In less than 10 days, the liver regenerates and is functionally and morphologically indistinguishable from control livers. If lower doses of CCl_4 are administered over 6 weeks, liver fibrosis is observed which may be explained by the release of cytokines by stressed or dying hepatocytes (Hengstler et al., 2012). The integration of *in vitro* techniques that allow for the study of proteomic or genomic changes would improve the understanding of the action mechanisms of low and repeated doses of a test compound significantly (Roggen, 2011). However, few studies have been carried out so far (Lee et al., 2011; Tostoes et al., 2012; Mueller et al., 2012; Heussner et al., 2007). In addition to the challenge of maintaining cells viable and functional for long term, most of the employed techniques are end-point assays, rendering them laborious and costly and thus practically unsuitable for continuous measurements on the same sample under repeated drug exposure. Recent tests on hepatocytes, for example, comprised three measurement points (viability and CYP450 activity) during a culture period of 23 days (Mueller et al., 2012). Important information regarding injury and recovery kinetics might have been missed out. Bio-impedance screening, on the contrary, offers a new level for studying toxicity effects.

Impedance-based toxicology is sensitive to electrode positioning, sample geometry and movements as was described above. Therefore, microsystems have the major advantage of representing a controlled environment where highly sensitive and repeatable toxicity tests can be carried out. The miniaturization of such tests is additionally useful for multiplexed systems where a large number of samples are analyzed in parallel for drug screening purposes for example. A further advantage of miniature systems is that portable devices can be built to perform toxicity tests outside the laboratory for water testing for example. This would require the control and measurement apparatus to be downsized and the sample solution to be pretreated (Lichtenberg et al., 2002).

The combined impedimetric analysis of single cells (small electrodes) and of the entire tissue (larger electrodes) from the same culture may allow acquiring new kind of data. Distribution information about the size and intracellular conductivity from various single cells can be compared with distribution information from the tissue (see paper V on page 183) where intercellular interaction is additionally detected. Moreover, the simultaneous measurement of the same tissue with various electrode geometries can provide further biological information. As was outlined above, a thorough understanding of the impedance measurement system potentially offers the integration of multiple impedance sensors for different detection purposes (cell attachment/cytoskeleton, cell-cell contacts/tight junctions), thus rendering this technique more specific.

From a toxicological point of view, the probing of toxic effects of substances on the human organism are ideally performed at the point of care, more precisely within the target organ or tissue itself. *In vivo* toxicity probing of drugs within a patient's liver for example may be a fantasy scenario given the rigorous regulations of biomedical devices and more importantly the readiness of healthy humans to accept an electrical implant for prevention purposes; however, the necessary technology with extremely compact impedance

devices on integrated circuits for example and wireless (telemetry) are available already[2] Overly et al. (2008); Min and Song (2010). In addition, the liver is a very active organ with a strong capability to regenerate where impedimetric changes due to cell stress and cell death seem to be easily detectable. Toxic effects of alcohol or drug ingestion may be monitored live and the corresponding data sent directly to the person's smartphone or treating doctor. The scenario seems fantasy today, but this medical technology might come sooner as one thinks.

---

[2] http://www.analog.com/en/prod/0,2877,AD5933,00.html. Accessed 23 May 2013.

A. Fabrication of "gel electrodes"

A.1. Process flow for the fabrication of hydrogel walls

The fabrication of the PDMS chip, the hydrogel master and the electrode chip were carried out according to standard fabrication procedures that have been employed previously and, therefore, will not be discussed more in detail. The surface treatment of the PDMS chip (1), the hydrogel master (2) and the hydrogel molding (3), on the other hand, are described in this work for the first time and will be explained in detail hereafter. The fabrication protocol has been developed for three different hydrogels, i.e. gelatin (Sigma-Aldrich), PEG-DA ($MW = 575g/mol$, Sigma-Aldrich) and agarose (high gel strength, Sigma-Aldrich).

1. **PDMS surface treatment**: The main goal of the PDMS surface treatment is to reinforce the adhesion of the subsequently molded hydrogel to the PDMS. The surface activation differed depending on the hydrogel that was used:

   a) *Gelatin*: Covalent bonding between PDMS and gelatin can be achieved through the following surface treatment. The PDMS is O_2-plasma treated ($100W$, $0.1min$, $0.6mbar$). This is followed by one hour exposure to vaporized (3-aminopropyl)-triethoxysilane (APTES, Sigma-Aldrich) using a desiccator. The PDMS surface is then put into contact with glutaraldehyde (25%, Sigma-Aldrich), a protein binding promoter, for one hour.

   b) *PEG-DA*: The PDMS surface is O_2-plasma treated ($100W$, $0.1min$, $0.6mbar$), then moistured with a 2,2-dimethoxy-2-phenylacetophenone (DMPA) solution ($0.1g$ DMPA in $1ml$ ethanol) and exposed to $365nm$ UV light for 1min. The PDMS is slightly washed with pure ethanol.

   c) *Agarose*: The PDMS was O_2-plasma treated ($100W$, $0.1min$, $0.6mbar$).

2. **Hydrogel-master surface treatment**: The surface modification of the oxidized silicon-based hydrogel master was common to all hydrogels. The objective is to render the silicon surface hydrophobic to decrease the interaction with the hydrophilic hydrogels. Therefore, the master was exposed to vaporized trichloro(1H,1H,2H,2H-perfluorooctyl)silane (Sigma-Aldrich) in a desiccator for at least one hour.

3. **Hydrogel polymerization**: The different hydrogels have different gelation mechanisms, requiring different protocols.

   a) *Gelatin*: Gelatin gels exist over only a small temperature range with a melting point lying below 37°C. However, gelatin can be enzymatically cross-linked (Paguirigan and Beebe, 2007) making it stable at 37°C. For this, a
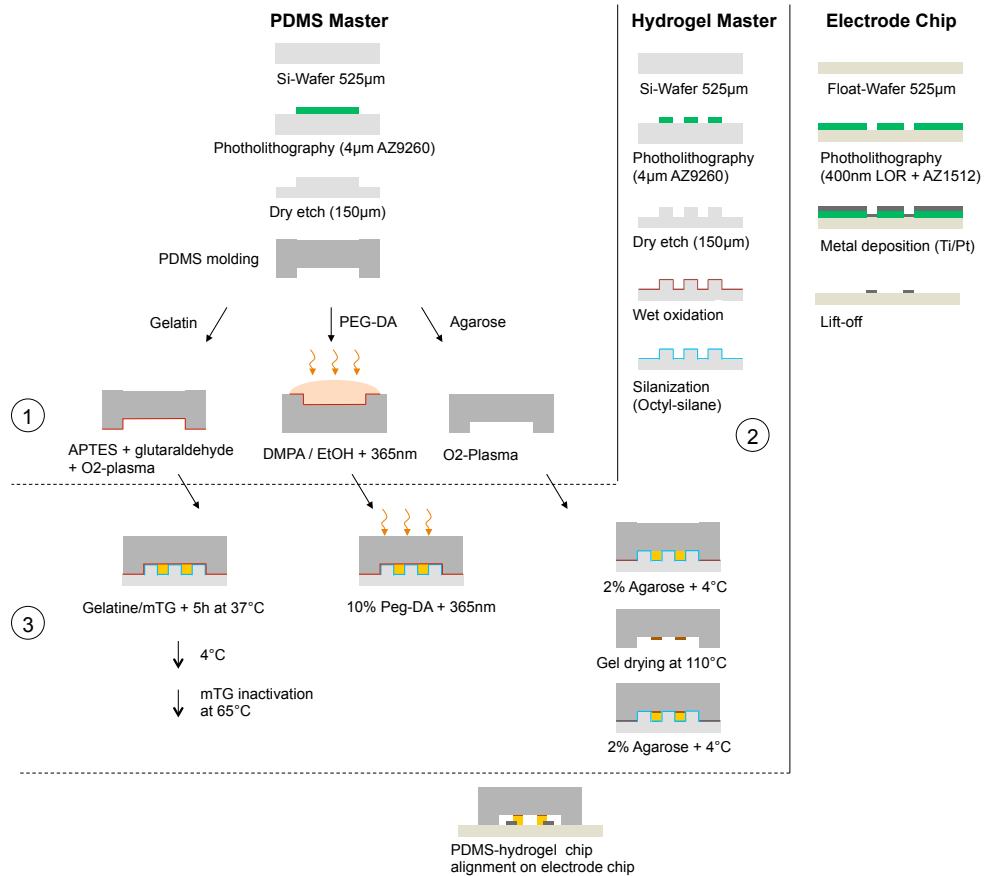
Figure A.1.: Process flow for the fabrication of hydrogel walls and virtual gel electrodes. APTES - (3-aminopropyl)triethoxysilane, PEG-DA - poly(ethylene glycol) diacrylate, DMPA - 2,2-dimethoxy-2-phenylacetophenone, mTG - microbial transglutaminase. (1): surface treatment of PDMS, (2) hydrogel-master surface treatment, (3) hydrogel molding

gelatin/microbial transglutaminase (mTG) mixture using a 12.5wt% gelatin solution in PBS needs to be made. A gelatin/PBS solution is heated to not higher than $70°C$ to solubilize and fully hydrate the gelatin. Then, mTG is dissolved in PBS and added to the hydrated gelatin at $37°C$ to give 10U mTG per gram of gelatin (e.g. $0.1g$ mTG in $1ml$ PBS). The final concentration will be 10wt% gelatin. To avoid too early cross-linking, the gelatin is injected into the device within maximum $5min$. The device is then incubated at $37°C$ for $5h$, subsequently cooled down to $4°C$ and again heated to $65°C$ to heat-inactivate the remaining enzyme.

  b) *PEG-DA*: $0.5g$ liquid PEG-DA is mixed with $15\mu l$ of DMPA solution ($0.1g$ DMPA in $1ml$ ethanol) and vortexed. PBS is added up to $5g$ to obtain a final concentration of 10%.

  c) *Agarose*: 2% agarose in PBS is injected into the chip and cooled down to $4°C$ for $10min$. The PDMS chip with the molded hydrogel is then removed from the hydrogel master and dried at 110°C for $30min$. After that, the agarose molding is repeated. The dried agarose subsequently represents a mechanical anchor between the PDMS and the second agarose mold.

A.2. Cell loading and culture protocol

- The PDMS/hydrogel chip is placed and aligned on the electrode chip within $5min$ to avoid evaporation and shrinking of the hydrogel. The chip is then filled and incubated with ethanol for at least $30min$ to disinfect the chip, and subsequently rinsed with cell medium. $0.5cm$ long teflon tubes ($1.06 \times 1.68mm$, Fisher Scientific) are placed into the perfusion in- and outlets.

- 4% agarose (agarose type VII-A, low gelling temperature, Sigma-Aldrich) is solubilized in PBS at $> 80°C$ and cooled down to 37°C and then mixed with cell medium at 37°C to obtain 2% agarose in PBS/cell medium. (a dry bath was used to maintain a constant temperature of 37°C to avoid gelation of the hydrogel)

- Cells in the flask are trypsinzed and counted. The desired number of cells (in cell medium) is mixed with the agarose solution at 1 : 4 to obtain a final agarose concentration of 0.5%.

- The cell/agarose mixture is injected into the cell channel and an oil droplet (mineral oil, Sigma-Aldrich) is then placed on top of the in- and outlet to avoid evaporation and contamination.

- The chip is placed into the incubator and connected to a syringe pump (using long teflon tubes which reach out of the incubator,$1.06 \times 1.68mm$, Fisher Scientific) (the perfusion channels on the same side were fluidically short-circuited resulting in two syringes por each chip) as well as to the signal cables.

B. Cell constant of distant and large electrodes within a micro-channel

The complete derivation involves the theory of conformal mapping and integral calculation. Here, only the main steps are described. More details can be found in (Braschler, 2009, p.200). Applying the general conformal mapping theory to planar metal electrode within a long access channel, it can be shown that the two-dimensional cell constant is given by

$$\kappa_{2D} = \frac{2K\left(k^2\right)}{K\left(1 - k_2^2\right)} \tag{B.1}$$

where $K(x)$ is the complete elliptic integral of the first kind

$$K\left(x\right) = \int \frac{dt}{\sqrt{\left(1 - t^2\right)\left(1 - x^2 t^2\right)}} \tag{B.2}$$

and the parameter k is given by

$$k \approx 1 - 2\sqrt{\frac{2}{\cosh\left(\pi\frac{r_d}{h}\right)}} \tag{B.3}$$

where h is the channel height and r_d is the channel length. Since $r_d \gg h$, and hence $k_2 \to 1$, one obtains the following approximations

$$k_2^2 \approx 1 - 4\sqrt{\frac{2}{\cosh\left(\pi\frac{r_d}{h}\right)}} \tag{B.4}$$

and

$$\kappa_{2D} = \frac{4}{\pi}\left[2ln\left(2\right) - ln\left(\sqrt{1 - k_2^2}\right)\right] \tag{B.5}$$

By inserting B.3 in B.5 and some simplifications, one obtains

$$\kappa_{2D} \approx \frac{2ln\left(2\right)}{\pi} + \frac{r_d}{h} \tag{B.6}$$

The corresponding three-dimensional cell constant κ is given by

$$\kappa = \frac{1}{w_{ch}}\left(\frac{2ln\left(2\right)}{\pi} + \frac{r_d}{h}\right) \tag{B.7}$$

B. Cell constant of distant and large electrodes within a micro-channel

where w_{ch} is the width of the channel. The first term accounts for the curving of the field lines down towards the metal electrode and the second term corresponds to the resistance due to a channel length equal to r_d.

For two electrodes that are spaced by a distance s_{el} from each other, one consequently obtains

$$\kappa = \frac{1}{w_{ch}} \left(\frac{4ln\,(2)}{\pi} + \frac{s_{el}}{h} \right) \tag{B.8}$$

C. Resistance range extension with interdigitated electrodes

The measured resistance of sub-sensor 3 is decreased by using interdigitated electrodes. This leads to an increased total resistance range D (R_1 is constant). Simultaneously, P decreases because of a decreased $f_{c,5}$. This means that the resistance range can be increased by the expense of a decreased resistance plateau length P. This might be acceptable to the extent where the PRFs and their corresponding R may still be identified. Both, D and P are a function of the number of interdigitated electrode fingers n (Olthuis et al., 1995).

It is now possible to calculate the plateau length for a desired resistance range and thus a given n. For this P calculates as follows

$$P = log\left(\frac{f_3}{f_2}\right) \cdot log\left(\frac{f_5}{f_4}\right) = P_1 \cdot P_2 \tag{C.1}$$

where $P_1 = P_2$ and thus $\frac{f_3}{f_2} = \frac{f_5}{f_4}$ for a maximized M. We summarize the ratio of the frequencies as m

$$m = \frac{f_3}{f_2} = \frac{f_5}{f_4} \tag{C.2}$$

Consequently, for a given n, m can be calculated as follows

$$m = 10^{\sqrt{P_n}} \tag{C.3}$$
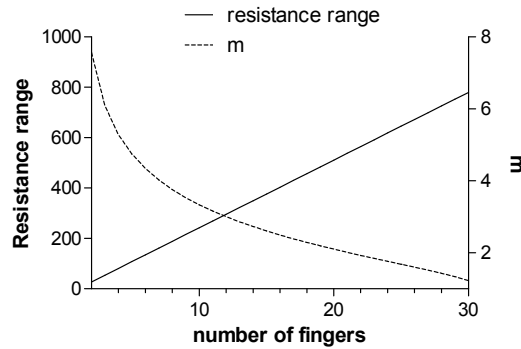
Figure C.1.: The resistance range and the P-specific ratio m are plotted as a function of the number of interdigitated electrode fingers.

C. Resistance range extension with interdigitated electrodes

The resistance range and the frequency ratio m were plotted as a function of n in figure C.1. In conclusion, it is possible to extend the total resistance range and thus the resistance ranges of each sub-sensor by increasing n. This is accompanied by a decreased resistance plateau ratio m which makes the identification of the PRFs more difficult.

D. Capacitive bridge

The value of the low frequency capacitance can be modified by implementing a "bridge capacitor". An additional microfluidic channel is used to create a series electrode-electrolyte capacitor. This one adds up to the double layer capacitor of channel 2 and consequently changes the total capacitor value of sub-sensor 2. The resistance in the bridge channel may be neglected if this one contains a highly concentrated ionic solution. Thus, an identical electrode width for sensor 1 and 2 can be used.
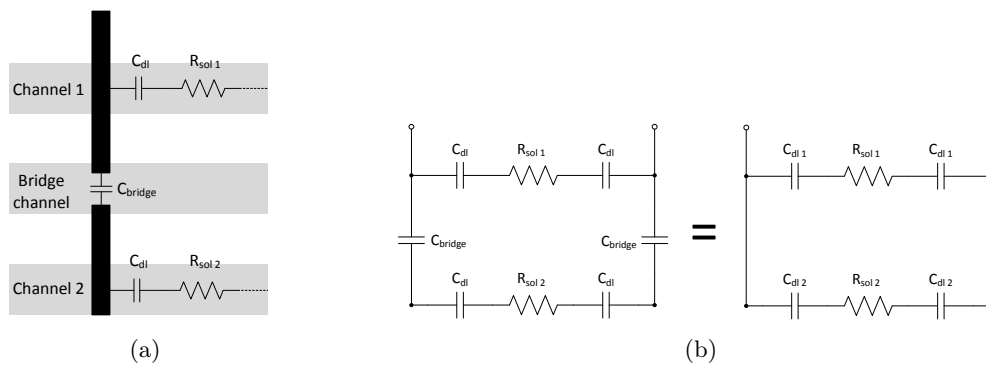
Figure D.1.: Capacitive bridge. a) Scheme of a potential chip design with a capacitive bridge. b) Equivalent electrical circuit of a). ($C_{dl} = C_I$)

E. Microfluidic-based neuronal cell cultures for Alzheimer studies

E.1. Alzheimer's disease - increased mortality rates and still incurable

Alzheimer's disease (AD) is the most common cause of dementia and develops when nerve cells no longer function normally. This process results in memory loss and affects the individual's thinking and behavior. Basic human functions such as walking and swallowing become difficult to carry out. AD is a fatal disease (Alzheimer's Association, 2012).

More than 35 million people worldwide are affected by AD and this number is expected to double every 20 years. Worldwide costs of dementia represent over US$600 billion only in 2010 (Wimo and Prince, 2010). Although death rates decreased significantly for 7 of the 15 leading causes of death in the US Murphy et al. (2010), those from AD experienced a rise of 66% between 2000 and 2008 (Alzheimer's Association, 2012). Despite much effort on the part of academic research and industry the causes of AD are not yet known and no treatment is currently available to slow or stop synaptic and neuronal decline in Alzheimer's disease4. The need for a substantial change with regard to new testing strategies and tools seems to be indispensable. In fact, studies on living animals are difficult to carry out due to a high number of uncontrollable parameters and the difficulty of *in situ* observation. Conventional cell culture, on the other hand, is limited by the inability to precisely control the environment of cells. A comprehensive study of AD requires the highly polarized neurons to be arranged in a complex but well-defined way, a condition that conventional cell culture is not able to fulfill.

To overcome limitations of conventional cell culture assays, microfluidic platforms have been developed for neuroscience applications. Microfluidic systems are capable of regulating fluid flow precisely owing to a laminar flow pattern, structuring cells since many biological species are on the same length scale and manipulating the extracellular environment. This chapter[1] reviews recent developments in microfluidic culture platforms for structured neuronal cell culture and AD research. The first part describes the importance of neuronal networks in AD and how micro-systems may be a key in understanding AD progression in the brain. The second part reviews microfluidic-based *in vitro* Alzheimer models and points out what specific questions may be addressed in future.

---

[1] This chapter will be suject to a review in the book "Microfluidics for medical applications" from the Royal Society of Chemistry
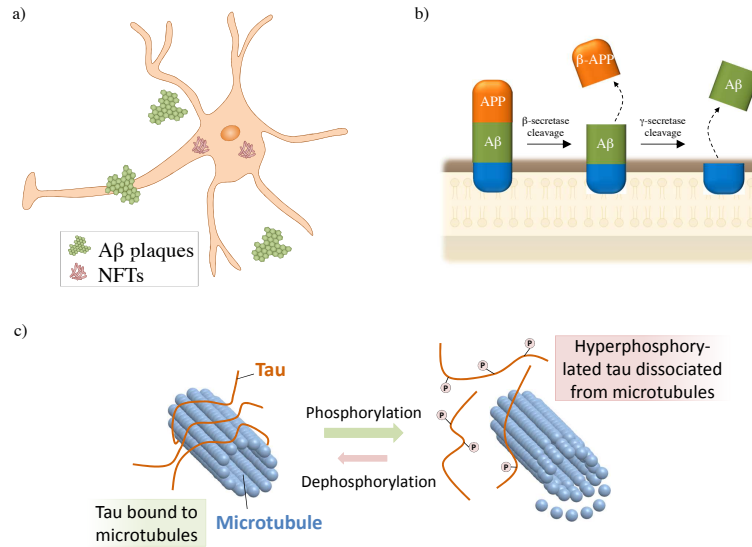
Figure E.1.: Major hallmarks in AD. a) Extracellular deposits of Aβ plaques and intracellular aggregation of pathological Tau to NFTs lead to neuronal decline in AD. b) Aβ plaque production is obtained through cleavage of the precursor protein APP by a γ-secretase and the subsequent cleavage of the left membrane-bound fragment by a γ-secretase. Aβ is released into the extracellular space. c) Balance of Tau-microtubule phosphorylation and dephosphorylation is disturbed in AD leading to hyperphosphorylated Tau proteins that do not bind to the microtubules and that aggregate to NFTs in the cytoplasm (Reprinted by permission from Wiley: Biotechnology and Bioengineering (Kunze et al., 2011b), copyright (2011))

E.2. Unknowns of Alzheimer's disease

E.2.1. Molecular key players of AD

AD is characterized by mainly two abnormalities; extracellular deposits of beta-amyloid (Aβ) (Hardy and Selkoe, 2002) and intracellular aggregates neurofibrillary tangles (NFTs) (Geschwind, 2003) (figure E.1 a). Aβ is a fragment of the amyloid precursor protein (APP), a protein that has been shown to be implicated in synapse formation and transmission (Priller et al., 2006). Arising from the proteolytique cleavage of APP (figure E.1b), Aβ is broken down and eliminated in healthy brains. In Alzheimer diseased brains, however, this process is disrupted and Aβ aggregates to plaques outside the cell. NFTs, on the other hand, are mainly comprised of the microtubule-binding Tau protein. Its major function is to stabilize the microtubules and hence to promote structural support and nutrient transport within neurons. The Tau protein can dissociate from the microtubules when being phosphorylated and re-associate when being dephosphorylated, a dynamic process that is mediated by enzymes called kinases (e.g. GSK) and phosphatases (e.g. PP2A) (figure E.1c). Possessing a multitude of phosphorylation sites, Tau can hence undergo conformational changes that are necessary to carry out its microtubule-supportive function. In diseased brains, however, the process of phosphorylation and dephosphorylation is unbalanced and numerous phosphorylation sites have
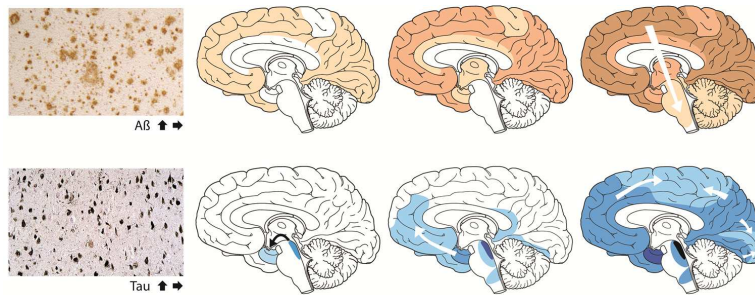
Figure E.2.: Temporo-spatial spreading of Tau-positive neurofibrillary lesions and Aβ plaques in the process of Alzheimer's disease. Aβ-plaques (top) and NFTs (bottom) spread through AD brains in specific patterns. Shading intensities are proportional to the clump density over time. (Reprinted by permission from Wiley: Annals of Neurology (Jucker and Walker, 2011), copyright (2011))

been found to be hyperphosphorylated leading to the complete dissociation of Tau from the microtubules (Bulinski and Gundersen, 2005). As a result, hyperphosphorylated Tau aggregates to NFTs within the cell.

Although many studies have investigated the molecular mechanism of this disease, the reason behind the disrupted Aβ elimination and the increased Tau phosphorylation is still unclear (Ittner and Götz, 2011). Moreover, the sequential order and the cause and effect, especially with regard to the interplay of Aβ and Tau, remain unsolved (Geschwind, 2003).

E.2.2. From molecules to neuronal networks

AD is a progressive disease that spreads throughout the brain according to a predictable pattern (figure E.2). It starts in the entorhinal cortex (EC), where the large projection neurons, that link the cerebral cortex with the hippocampus, are affected first Braak and Braak (1991); Hyman et al. (1984); Hyman and Hoesen (1987); Gomez Isla and West (1996). It then propagates across the limbic system and association cortices (de Calignon et al., 2012). Despite good knowledge about the hierarchical accumulation pattern of Aβ and Tau in the brain, little is known about the mechanism of the initiation and progression of these protein accumulations: why does it start in the EC and why is there a specific spreading pattern (Soto, 2012)?

Recent findings have indicated that Tau aggregates can transfer to neighboring cells and to synaptically connected neurons in distant parts of the brain in a prion-like manner (de Calignon et al., 2012). In fact, a transgenic mouse model with overexpression of human mutant Tau exclusively in layer II of the EC has been established. Several months after lesions in the EC, the Tau pathology appeared in other brain regions with neurons that exhibited no detectable transgene expression; first to neighboring cells and then to neurons downstream in the synaptic circuit. These experiments proved the transfer and progression of misfolded Tau proteins from neuron to neuron in a neuronal circuit-based manner. Moreover, the migrating pathological Tau aggregates were shown to be

endocytosed by healthy neurons (Clavaguera and Bolmont, 2009) where they act as seeds to induce the misfolding of intracellular native Tau proteins and their conversion into NFTs (Frost et al., 2009; Guo and Lee, 2011; Nonaka et al., 2010). In fact, this is a process that was previously reported in other cases where the accumulation of misfolded protein aggregates is mediated by the intercellular spreading of oligomeric seeds. Although the experimental proof of aggregated Tau-spreading may explain the formation of NFTs in a stepwise characteristic pattern Soto (2012), it still remains unclear why only some of the interconnected neurons develop NFTs. There may be conditions that favor or prevent pathological Tau proteins from being transferred and/or from acting as seeds.

In addition to the spreading of pathological Tau, the progression of Aβ deposition was also reported. Experiments where Aβ oligomers were micro-injected into electrophysiologically defined primary hippocampal rat neurons revealed their neuron-to-neuron transfer (Nath et al., 2012). Moreover, a transgenic mice model with spatially restricted overexpression of mutant APP in the EC, demonstrated that Aβ-induced molecular and functional impairments can cross synapses (Harris and Hochhauser, 1992).

All these studies have proven the characteristic spreading of NFTs and Aβ deposits in the brain and have consequently shown the importance of neuronal networks in the progression of AD. Additional elucidation of the detailed mechanism behind the specific spatiotemporal pattern of neuropathology in AD potentially may open new avenues to develop long-awaited strategies to stop the progression of this dreadful disease (Nath et al., 2012).

E.3. Why micro-systems may be a key in understanding the propagation of AD

Although the latest important *in vivo* findings about the transfer of toxic species of Tau and Aβ from transfected brain parts to distinct regions have been a break-through in neurosciences, researchers cannot rule out that a low expression of the transgene Tau (below the level of detection) in other areas than the EC, may have occurred (Soto, 2012) as observed previously (Santacruz et al., 2005). More importantly, detailed investigation at the cellular level is limited: functional and live analysis such as signal recordings or live cell imaging can hardly be performed *in vivo*; stereology and immunocytochemistry are tedious to carry out; too many parameters that cannot be controlled tightly make it difficult to account for a specific phenomenon; and living organisms exhibit a great variability. This section describes how microtechnology-based platforms may provide the essential support for *in vitro* neuronal cell culture and its analysis that may fill the gap between current findings and a thorough understanding of disease progression in AD.

E.3.1. Requirements for *in vitro* studies on AD progression

Experimental models such as animals (e.g. rats, mice) are used for brain studies owing to the preservation of anatomical structures. Different neuronal populations are connected with well-defined topologies and polarities. This directionality exists in devel-

a)

*Conventional
cell culture*

b)

*Compartmentalized
cell culture*

c)

*Orientation /
directionality*

d)

*Three-dimensional
cell culture*

Tissue sophistication

Figure E.3.: Requirements for *in vitro* studies on AD progression. a) Conventional Petri dish cell culture is characterized by intermingled networks with random connections. b) Compartmentalization of different cellular sub-types that are interconnected allows local treatment of specific sub-populations. c) Orientation of neuritic processes leads to well-defined topologies and polarization. d) Three-dimensional, structured and oriented neuronal cultures resemble the most *in vivo* brain tissues.

opmental mechanisms (connection of different neuronal subtypes) (Stiles and Jernigan, 2010) as well as in degeneration of neuronal networks in mature brains (Nath et al., 2012; Peyrin et al., 2011). Conventional cell cultures, on the other hand, are missing the anatomical structure with its highly ordered connectivity of neurons and do not satisfy the requirements of directionality and orientation that are necessary for the study of neuropathology in AD. In fact, conventional cell cultures are characterized by random connections and intermingled networks that vary from one sample to another (Peyrin et al., 2011) (figure E.3). Therefore, in order to study network phenomena and disease progression, (1) different populations of cells need to be separated (spatial compartmentalization) while allowing them to interconnect (connectivity) in (2) a polarized and oriented way (directionality). Moreover, (3) to mimic the *in vivo* tissue structure closely, those interconnected but distinct cell populations need to be dispersed in three dimensions (3D cell culture). Advances in microfluidics and microfabrication have enabled such micro-structuring with the creation of micro-chips as tools for *in vivo*-like anatomically organized neuronal cell cultures on the one hand, and simultaneous cell culture analysis (e.g. signal transmission analysis and on-chip protein analysis) on the other.
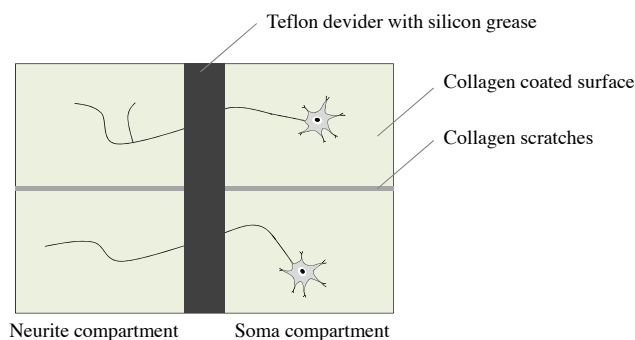
Figure E.4.: Schematic of Campenot chamber. Neurons are cultured in one compartment and neurites can grow through the grease under the Teflon divider into the second chamber allowing the separation of cell soma and neuronal processes. Hence, neurites and soma can be separately exposed to molecules. Scratches on collagen-coated surface were made to hinder neurite outgrowth between neurons within the same compartment

E.3.2. Establishing ordered neuronal cultures with microfluidics

E.3.2.1. Compartmentalization of neuronal cell populations

While continuously striving for a better understanding of AD and simultaneously being limited in the direct observation of living organisms, researchers have made great advances in the last 40 years in reconstructing typical brain patterns *in vitro*. Microtechnology has played the essential role in establishing brain structures that may enable basic neuroscience research as well as pharmaceutical industry to find strategies to counteract AD with its dreadful consequences on people's life.

One of the first steps from random neuronal cell culture towards guided neurite outgrowth was achieved by Robert B. Campenot in 1977 (Campenot, 1977). He was able to compartmentalize somas and their axons by having the processes grow from a soma-containing chamber to a side chamber that contained or not nerve growth factor (NGF). Both chambers were separated by a Teflon divider that adhered on a collagen coated Petri dish by sealing with silicone grease (figure E.4). The seals could be penetrated by growing neurites, but not by the cell soma. He found out that neurites did not only penetrate into the grease, but also grew the full distance under the grease and emerged into the side chamber if a high concentration of NGF was present, but they never appeared in the side chamber if no NGF was added. In this way, he was able to control the local environment of the distal part of the neurites and the one of the somas separately. Interestingly, the method that was used to separate cell soma and distal part of neurites was relatively simple. It was based upon the fact that neurites squeezed themselves between the Teflon and the Petri dish surface through the grease (a gap in the micrometer range). Here, the micro-scale range was exploited to create a mechanical constraint for neuronal processes without the use of any of today's standard microfabrication techniques such as photo-lithography. Nonetheless, these devices were difficult to assemble and hard to image as well as prone to leakage.
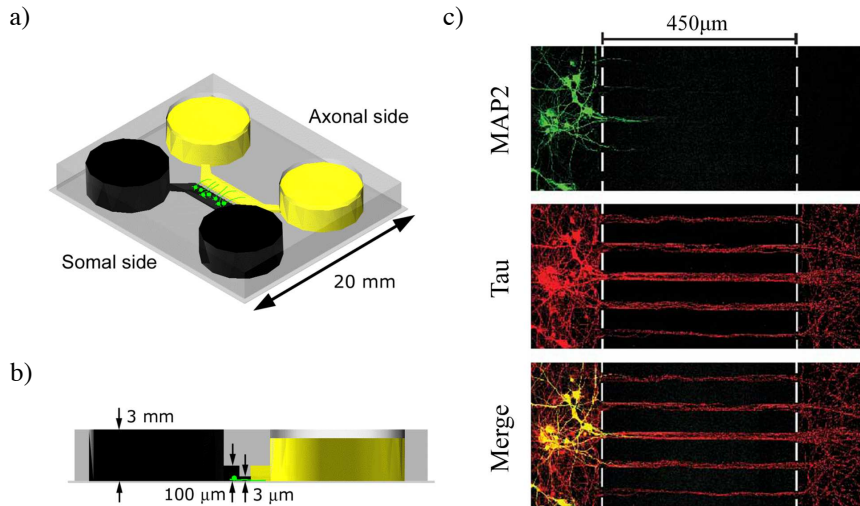
Figure E.5.: Microfluidic-based cell culture platform according to Taylor et al. a) Perspective view of the PDMS culture chamber containing the relief pattern of the soma and axon compartment. Both are connected through microgrooves (10µm wide and 3µm high); b) Side view of the PDMS device. A volume difference between the reservoirs on each site allows chemical environments to be isolated for $20h$ due to the high resistance of the microgrooves c) Axons grew from one chamber to the other one (red: Tau). Dendrites on the other hand did not pass the microgrooves (green: MAP2). (Reprinted with permission from Macmillan Publishers Ltd: Nature methods (Taylor et al., 2005), copyright (2005))

A refinement of this mechanical-constraint-strategy has been achieved by several following studies (Park et al., 2009; Taylor et al., 2005). As an example, Taylor et al. fabricated a microfluidic culture platform consisting of a PDMS mold placed against a coverslip (Figure 5). The design of the device incorporates two culture chambers that are separated by a physical barrier with embedded microgrooves. Those microgrooves are 10µm wide and 3µm high and allowed the neuritic processes, but not the cell bodies, to extent from one chamber to the other. Compared to its predecessor, the major advantages of this device such as reliability, reproducibility and precision are due to its standardized fabrication process (photo-lithography, soft-lithography, replica molding). Furthermore, it was shown that the axonal growth can be polarized without the use of targeting neurotrophins and that the biochemical analysis of pure axonal fractions is facilitated.

Overall, mechanical constraints are a reliable technique to separate cell bodies from each other while allowing neurite connectivity by the means of micro-channels for example. Their fabrication is relatively simple and consistent, especially with standard microfabrication techniques. Also, the cell loading and culturing protocols are straight forward which is why such micro-fabricated microfluidic devices have found repeatedly use in neuroscientific studies (Taylor et al., 2005; Park et al., 2009; Yang et al., 2009; Hayashi et al., 2004; Bertrand et al., 2005; Ishibashi et al., 2006; Campenot, 1982).

A different technique towards reestablishing an ordered arrangement of neuronal cells

in vitro can be achieved through surface patterning. Commonly used procedures include a combination of surface chemistry and photo-lithographic techniques (Kleinfeld, 1988) or soft-lithography. Small organic molecules bind to a surface such as glass or silicon, whose presence promotes (laminin, fibronectin) or inhibits (alkane (Kleinfeld, 1988), untreated silicon (Grattarola et al., 1988) or glass (Schacher and Proshansky, 1983), albumin) neuronal cell attachment. Molecules that promote cell attachment generally have amino acid fragments that interact with specific cell membrane receptors such as integrins. Receptor binding to these sequences can initiate second messenger systems within the cell that promote growth, gene expression and differentiation (Ranieri et al., 1994). Adhesion promoters or inhibitors can be immobilized through simple adsorption. However, the coatings are easily washed off. To avoid this problem, covalent binding may be employed and can be virtually achieved for any molecule. For example, molecules that cannot be formed into silane derivative, such as the glycoproteins fibronectin (Kleinman et al., 1981) or laminin (Timpl et al., 1979), can be patterned by first binding an amine derivative in the desired pattern and then binding the glycoprotein to the amine with chemical cross-linking reagents (Kleinfeld, 1988). Surface patterning with photo-lithography, for example, is attained with a photoresist (e.g. lift-off resist) that protects specific regions from being surface treated. The desired patterning structure on the surface is obtained after the removal of the photoresist (figure E.6a).

Surface patterning through soft-lithography, on the other hand, is a set of techniques that uses elastomeric stamps made of PDMS with patterned relief features in order to immobilize the adhesion molecules onto a surface (figure E.6b) (Kaji et al., 2011; Heller et al., 2005; Franks et al., 2007). Early studies demonstrated the applicability of surface patterning techniques to the patterning of neuronal cell cultures (Heller et al., 2005; Ivanova and Margolis, 1973; Letourneau, 1975) but both the viability and the pattern of outgrowth were not maintained long enough for developing neurons that attain electrical excitability. Later studies showed extended maintenance of viability as well as higher resolution patterns with cells being maintained on lines as fine as 5µm (Kleinfeld, 1988) (see figure E.6c). More recent studies generated more precise micro- and even nanoscale patterns (Kane et al., 1999). Overall, surface patterning allows the separation of cell bodies and cell migration outside the surface patterning area is hindered (which results in a preserved ordered culture). On the other hand, localized chemical treatments of cell bodies and axons separately, for example, is not possible and would require additional mechanical constraints (e.g. for the formation of chemical gradients).

A more recent technique to create patterned neuronal cell cultures is by using hydrogels. Samples of hydrogels are first premixed with different cell populations and are then polymerized in layers that are located in direct contact to each other. Hence cells from different layers can interact through the hydrogel by the diffusion of cellular factors, by neurite outgrowth from one hydrogel layer to the other or by cell migration. Hydrogel layers can be stacked on top of each other (Tan and Desai, 2004) or horizontally side-by-side (Kunze et al., 2011a). As an example, Kunze et al. exploited the laminar flow at microscale to pattern up to four agarose/alginate hydrogel layers (figure E.7a). The device was comprised of four microchannels that were connected to a common main channel. The laminar flow pattern of the hydrogel mixtures resulted in parallel hydrogel
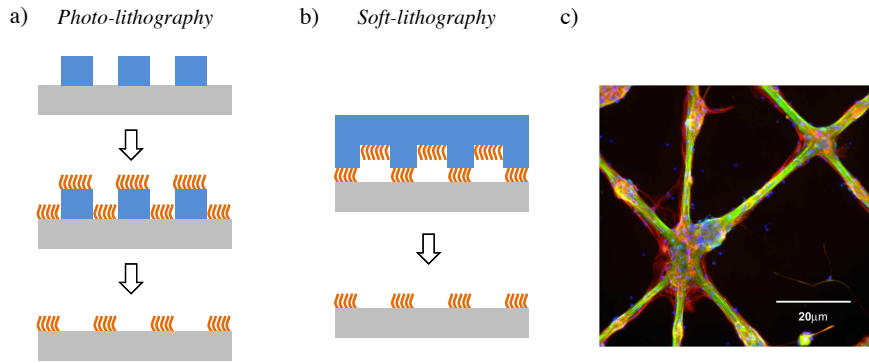
Figure E.6.: Monolayer patterning through surface functionalization. a) Schematic of photolithography-based patterning. Regions protected by the photoresist retain their initial surface when being exposed to the functionalization molecules and subsequently stripped; b) Soft-lithography-based patterning. An elastomeric stamp with patterned relief features is used to print molecules on a surface. First, the stamp is dipped into a solution containing the functionalization molecules and then it is brought into contact with the surface, thus leaving molecules only on the contact area; c) Patterned growth of neurons on a patterned substrate (Reprinted with permission from E. Ujhelyi).

layers flowing side-by-side in the main channel (figure E.7b left). After having thermally-gelled the agarose-alginate hydrogels, their parallel pattern within the main channel was maintained (figure E.7b right). The different hydrogel layers were premixed or not with primary cortical neurons and cultured for up to three weeks. Within that time, cell populations from different layers connected through the outgrowth of neuritic processes (figure E.7c). Furthermore, by pre-mixing specific hydrogel layers with B27 and the subsequent establishment of a timely limited gradient allowed the enhancement of neurite outgrowth into a specific direction.

Overall, hydrogel layers are a very elegant way of patterning cells in 3D (as will be discussed more in detail in section E.3.2.3) and thus of mimicking more closely the native state of neurons within the brain. For this, patterning hydrogels horizontally allows for easier microscopic observation compared to vertically stacked hydrogel with very thick samples. On the other hand, cell loading protocols are more complicated and delicate since all hydrogel-cell mixtures need to be loaded at the same time while establishing more or less identical flows in all microchannels; this technique is still suffering from reproducibility. An automated processing with a cell loader-device that is mostly free of human interaction would potentially enable a very reproducible fabrication of such three-dimensional patterned neuronal cell cultures.

E.3.2.2. Directionality of neurite outgrowth

It has been shown that relatively simple microfabrication tools can be used to spatially isolate the soma of a neuron from its axon. It has furthermore been shown that different cell populations can be separated from each other while maintaining their connectivity. In the brain, however, different neuronal populations are connected with well-defined
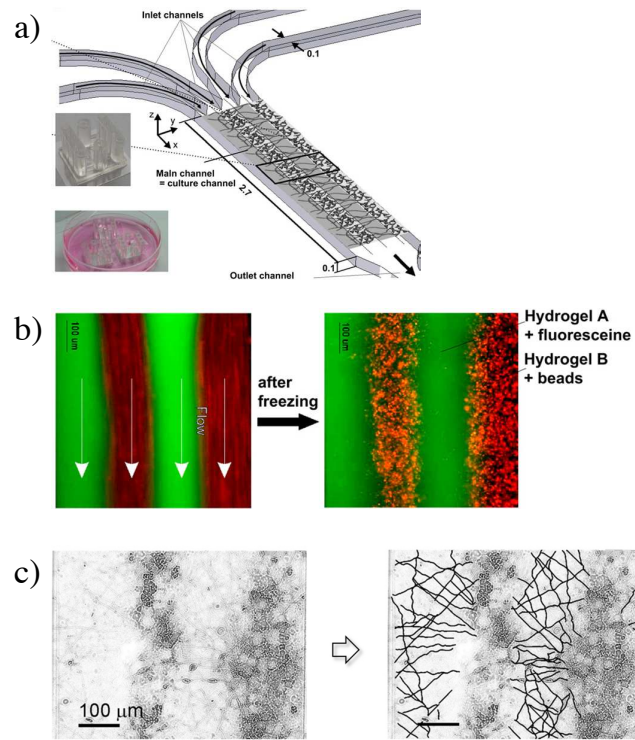
Figure E.7.: Patterned 3D neuronal cell culture in hydrogels. a) Illustration of the layered structure of the 3D neural cell culture. The device is composed of four inlet channels that lead into a main channel with one outlet channel. The two inserts show the final microfluidic device fabricated using PDMS and three devices placed in a Petri dish for incubation during cell culture. b) Fluorescence images taken in the main channel area present the four laminar hydrogel microstructure before (left) and after (right) gelling of the agarose components by cooling down under 26°C. c) DIC images of the main channel at 0 (left) and 5 DIV (right). Single neurites were traced with NeuronJ. (Reprinted from Kunze et al. (2011a), Copyright (2010), with permission from Elsevier)
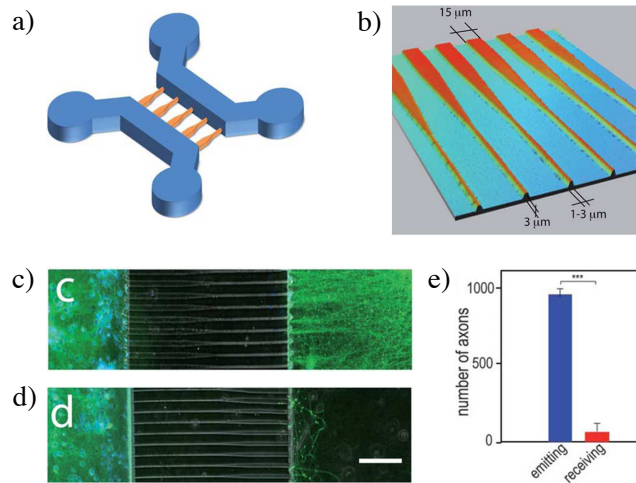
Figure E.8.: Orienting neurite outgrowth with physical constraints. a) 3D view of the microfluidic device used by Peyrin et al. (2011); b) 3D view of the funnel-shaped micro-channels as observed by white-light optical profiling; c) Immunofluorescent images of microfluidic cultures (green: α-tubulin, blue: Hoechst) in which cortical neurons were seeded either on the c) wide (15 µm) or the d) narrow (3 µm) side (bar=50µm). e) Neurite outgrowth to opposite chamber is much higher when seeded on the wide side, bar=50µm (Reproduced from Peyrin et al. (2011)).

polarities (Peyrin et al., 2011), a crucial condition of neuronal networks to guarantee the proper information flow. Hence, the *in vitro* study of polarized neurite outgrowth is essential for the investigation of cellular mechanisms that influence axonal plasticity and response to injury as well as etiology of neurodegenerative diseases. While the study of these phenomena with traditional technologies on a conventional scale is very difficult, axon growth guidance based on microfluidics creates new opportunities for research (Wang et al., 2009).

Peyrin et al. established a microfluidic platform comprising independent cell culture chambers that are connected by an array of asymmetrical micro-channels, so-called "axonal diodes" (figure E.8a and b). The asymmetrical geometry acts as a directional selective filter for axons due to two effects. First, asymmetry imposes directionality by a probabilistic effect easing the entrance of axons on the wide side of the diode compared to the narrow side. Second, axons from neurons, seeded in the receiving chamber, once encountering the diode wall instead of the micro- channels entrance tend to grow perpendicularly to the diode along the chamber wall, without entering to a great extent the narrow side of the diodes; an effect that was correlated to the axonal stiffness that prevents frequent axonal turning. Accordingly, a cortico-striatal oriented network was established, cultured for 3 weeks and proven active through structural (immunostaining of synaptic contacts) and functional analysis (KCl depolarization and electrical recording). The unidirectional axon connectivity was shown to have a very high selectivity of 97% (figure E.8e) (Peyrin et al., 2011).
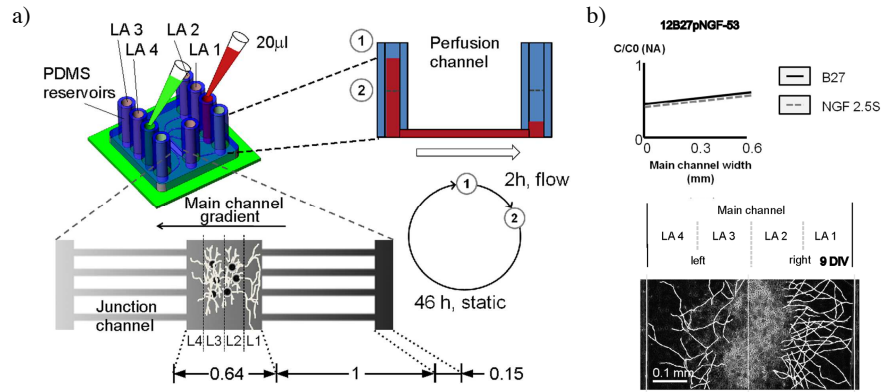
Figure E.9.: Orienting neurite outgrowth using guidance molecules; a) Illustration of experimental setup. Empty polydimethylsiloxane (PDMS) reservoirs are selectively filled with medium (red: enriched NGF/B27 medium, green: pure medium). A 2h perfusion flow due to liquid height differences in the reservoirs establishes a linear gradient of NGF/B27. The long perfusion channels maintain the gradient in the main channel once the perfusion flow stops. Every other day, refilling was repeated. b) Schematic view of synergistic gradient of B27 and NGF and DIC image of neuronal culture with traced neurites at 9DIV, bar = 0.1 mm (Reproduced from Kunze et al. (2011d))

Another very frequently used method for directing neurite outgrowth is by using axon guidance molecules (growth factors, neurotransmitters, netrins, adhesion molecules) or repellents (semaphorins, slits). For this, neuronal cells need to be exposed to biomolecule gradients that are controllable and that mimic those that are present *in vivo* (Keenan and Folch, 2008). Biomolecule gradients can be established either by substrate-bound molecules (Jeon et al., 2002) or by a constant supply and removal of molecules at precise locations Kunze et al. (2011d). Kunze et al. (2011d) reported the use of a microfluidic device to expose a patterned three-dimensional culture of primary neurons to gradients of B27 and nerve growth factor (NGF). The hydrogel-based patterned 3D culture region was separated from two lateral perfusion channels (that acted as a 'source' and 'sink') by small micro-channels that delivered the biomolecules on one side of the hydrogel culture and removed them on the other side (figure E.9a). By this means, it was shown that cortical neurons responded only to synergistic NGF-B27 gradients and that the synaptic density increased proportionally to these gradients (figure E.9b).

Unlike physical constraints as presented by Peyrin et al., directionality obtained through biomolecular gradients enables the creation of directed neurite networks through three-dimensional neuronal cultures. On the other hand, neurite guidance by "axonal diodes" attracts specific attention owing to its ease of fabrication and use as well as to its high efficiency. No complicated setup with a pumping system for long term maintenance of biomolecule gradients is necessary. Moreover, directional efficiency does not depend on the neuronal type that is used since different neuronal cell types may have different responses to various biomolecules (receptor-dependence). Also, the selectivity of physical constraints seems to be higher than the one obtained by the means of biomolecular

cues, apart from the fact that an additional culturing dimension renders high selectivity-efficiency more difficult to achieve. Finally, in view of the study of higher order networks, e.g. to study inter-neuronal transport of pathological Tau species from one neuron to another that is located multiple neuronal connections further, the axonal diode-technique seems being a highly promising approach.

E.3.2.3. Three-dimensional neuronal culture

In vivo tissues have a very complex but well-organized 3D structure. Culturing cells in 3D provides another dimension for external mechanical inputs and for cell adhesion, which dramatically affects integrin ligation, cell contraction and associated intracellular signaling (Griffith and Swartz, 2006; Knight et al., 2000; Roskelley, 1994). Moreover, the diffusion of soluble factors changes dramatically compared to 2D cultures. Hence, culturing cells in a 3D environment seems highly promising since the effect of mechanical and chemical stimuli on 3D neuronal cultures as well as its propagation from one population to the other can be studied.

Establishing patterned 3D cell cultures is a challenging task. It requires a set of biomaterials, scaffold and devices that can support the formation and maintenance of 3D tissue structures and that can be used for specific applications. As already described in section E.3.2.1, Kunze et al. showed that an agarose-alginate mixture can be gelled thermally (figure E.7). It is therefore an excellent candidate for forming horizontal multi-layered scaffolds for micropatterning embedded cells. A further technique, named layer-by-layer deposition, enabled the creation of vertically stacked cell-matrix assemblies (Tan and Desai, 2004). This method involved the stacking of cell-matrix assemblies (collagen, matrigel). The first layer was immobilized on a pre-treated surface using a PDMS stamp; it then contracted and allowed the subsequent overlaying with another cell-matrix assembly. However, vertically stacked cell-hydrogel mixtures make optical observation difficult. Using confocal microscopy, for example, the thickness of the samples may exceed the working distance of the microscope. In addition, images of a specific focal plan observed under standard transmission microscope comprise a wide range of planes that are out of focus, resulting in lower image quality.

A hydrogel-free method to establish 3D neuronal networks was reported by Pautot et al. (2008). This technique involves the culture on silica beads that provide a growth surface for neuronal cells (figure E.10). The use of beads allows moving them without disrupting the neuronal adhesion. They can be assembled to form 3D layered arrays containing distinct subsets of neurons in different layers with constrained connectivity between neurons on different beads. This system could prove very useful for future applications, especially because cell manipulation and culturing is simpler than cell-hydrogel mixture-based protocols. Their future integration into a microfluidic system where different beads (with different neuronal cells) can be patterned and used to build up an oriented neuronal network thanks to biomolecular gradients or physical constraints may allow further refining this technique and obtaining *in vivo*-like orientations of neuronal networks.
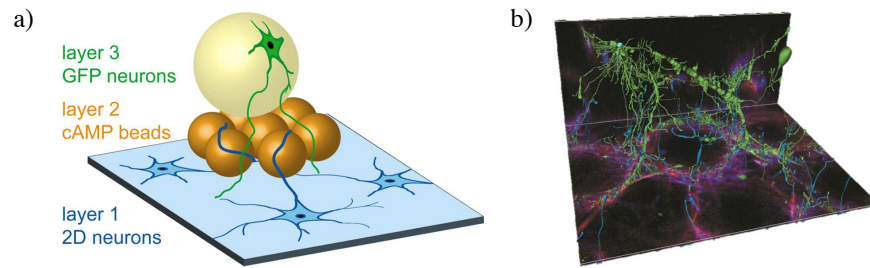
Figure E.10.: Neuronal culture on silica beads. (a) Schematic of the silica beads culture: a 2D culture of neurons was overlayed by cAMP (attractant signaling molecule) coated 45mm beads and a third layer of beads containing GFP-expressing neurons. B) A 3D reconstruction of axons (blue) from neurons on the coverslip (layer 1) growing up into the intermediate layer of cAMP beads (layer 2) and encountering there descending dendrites from bead layer (layer 3) of GFP-expressing cells (green). (Reprinted by permission from Macmillan Publishers Ltd: Nature methods (Pautot et al., 2008), copyright (2008))

Studies	Compartmentalization of cell somas				3D cell culture	Directionality	
	Surface patterning	Mechanical constraints	Gels	Cell migration		Mechanical constraints	Chemical gradients
Campenot 1977		+ [1]					+
Kleinfeld 1988	+						
Taylor 2005		+ [1]					
Kunze 2010			+	+	+		
Pautot 2006		+		+	+		+
Peyrin 2011		+				+	
Ideal	+			-	+	+ (high efficiency)	

[1] only cell soma and axons were compartmentalized

Table E.1.: Categorical chart of prerequisites for studying disease progression in microfluidic devices and how recent studies fit into these categories (only cell soma and axons were compartmentalized)

E.4. Micro-devices-based *in vitro* Alzheimer models

Microtechnology-based devices are the key to structuring neuronal cells *in vitro* such that *in vivo*-like neuronal networks can be reconstructed; i.e. in terms of connected but distinct cell layers, directionality and three-dimensional structures. Although all these prerequisites for establishing an environment similar to the human brain have been achieved individually, no integrated device or technology that is fulfilling all conditions was reported yet (Table E.1). However, avenues for preliminary studies of AD with simplified models are open already and should be pursued in order to obtain important insights into how AD is progressing in the brain and how it can be stopped.

E.4.1. First microtechnology-based experimental models

A first microfluidic approach that allows for the study of axonal biology in AD including transport within neurons was carried out by Poon et al. (2011). Transgenic mouse neurons that overexpressed Aβ (Tg2576) were cultured in a microfluidic device (similar

to the one reported by Taylor et al. (2005)) where cell somas and axons were compartmentalized. Neuritic processes grew from the seeding chamber through >150µm long microgrooves to another chamber that consequently allowed the selective application of a neurotrophin (brain-derived neurotrophic factor (BDNF)) to the axonal terminals. In healthy neurons, BDNF binds to its receptor tropomyosin-related kinase B (TrkB) at the axon terminal; the signal is propagated along the axon to the cell body, where it regulates gene expression and neuronal function. By locally applying BDNF to the axonal terminals, it was shown that the TrkB processing was impaired in transgenic Aβ neurons, but not in non-transgenic mouse neurons (WT). Also, the BDNF vesicle retrograde transport was slower in Tg2576 when compared to WT. Furthermore, it was reported that WT neurons that were exposed to Aβ oligomers prepared *in vitro* exhibited an impaired retrograde transport of axonally applied BDNF and demonstrated a threefold reduction in the accumulation of somal BDNF. Altogether, these findings strongly supported the hypothesis that the presence of either intracellular overexpressed Aβ or extracellular oligomers of Aβ impaired BDNF retrograde transport. More importantly, this study essentially foretasted the potential that underlies studies of compartmentalized neuronal cells and their axons.

A further study on the impact of Aβ was carried out by Kim et al. (2012) where it was shown that Aβ induced rupture of axonal transport can be restored by manipulating the level of α-tubulin acetylation. Axons were separated from their soma by using the Taylor device. Accordingly, the authors were able to examine the mitochondrial movement velocity within axons thanks to their spatial isolation from cell somas in a precise manner. This study demonstrates the utility of structured neuronal cultures for the investigation of transport kinetics within axons after local treatments of cell somas and can therefore provide essential clues for the discovery of potential drug targets.

Kunze and Meissner et al. (2011b, paper II on page 155) reported the culture of two spatially distinct, but interconnected cell populations where one of them was set into a Tau-pathological state. This model represents the first approach for studying disease progression from one cell population to another in a microfluidic device. For this, a microfluidic chip with three compartments was used: two lateral channels where primary cortical neurons were cultured and one main channel where the neuritic processes could interconnect (figure E.11a). Neurites started to grow out after 2 DIV and neurite density in the main channel saturated after 8 DIV (figure E.11b top). That followed, okadaic acid (OA), a protein phosphatase 2A inhibitor, was perfused over one cell culture compartment leading to a linear gradient in the main channel within one minute and a quasi-zero concentration in the second cell compartment. The OA treatment of only one cell population resulted in Tau protein hyperphosphorylation of these cells and hence generated an imbalance of the Tau phosphorylation states between the two connected cell populations (figure E.11b bottom). This controlled generation of two different phosphorylation states within one cell population was referred to as a "co-pathological state". The chemical gradient of okadaic acid induced a Tau phosphorylation gradient throughout the whole cell culture. This metabolic gradient was visualized through immunostaining of the Tau phosphorylation site Ser262. Okadaic acid-exposed cells displayed high intensity Tau aggregates within the cell soma and neurites whereas non-exposed cells exhibited a
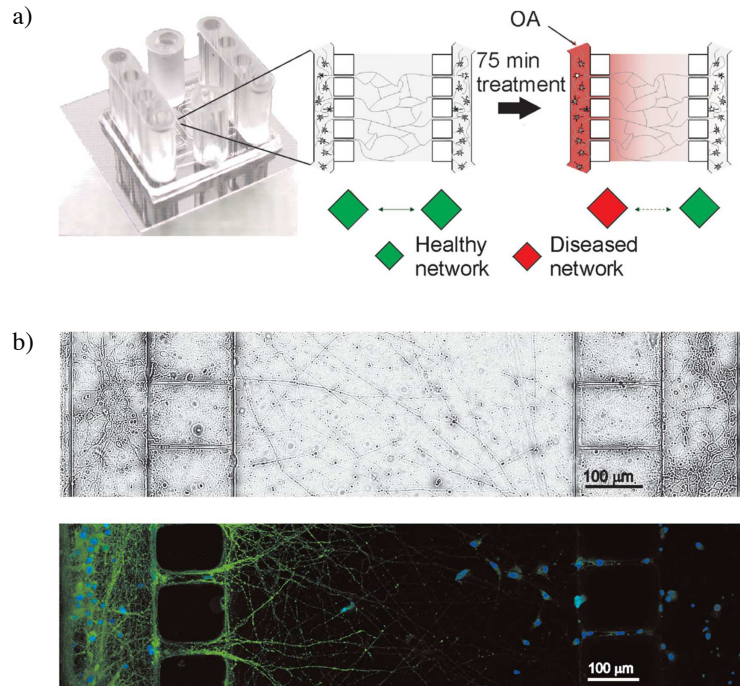
Figure E.11.: Generation of a co-pathological neural cell culture. a) Concept of establishing a co-patholical culture: Two cell populations are spatially separated while being interconnected. Only one of them is treated with okadaic acid (OA), leading to a local hyperphosphorylation of Tau and thus a co-culture of "healthy" and "diseased" neurons; b) Top: DIC image of neuronal culture with two lateral cell soma compartments and a central neurite interconnection chamber. Bottom: Tau phosphorylation imbalance within the entire cell culture is visualized (green: Tau Ser262 – Cy2, blue: DAPI) (Reprinted by permission from Wiley: Biotechnology and Bioengineering Kunze and Meissner et al. (2011), copyright (2011))

much less intense and homogeneous distribution of Tau.

In conclusion, the established model included (1) gradient controlled Tau phosphorylation states and (2) connected diseased and healthy neuronal cell populations and thus illustrated the feasibility of reconstructing typical disease patterns *in vitro*. In addition, Kunze and Meissner et al. demonstrated the application of this concept to a 3D neuronal cell culture (Kunze et al., 2011c). For this, neuronal cells were micropatterend as described in section E.3.2.1 before being exposed to an okadaic acid gradient. Altogether, this new strategy of artificially creating disease states of only precise parts of a neuronal tissue may be an important step towards a thorough understanding of how pathological states of Tau proteins propagate to some cells and not to others. No less important is the question of what effect potential drugs, that counteract the disease progression, have on non-pathological healthy neurons (potential side effects). This is an issue that is especially important in terms of prevention treatment.

E.4.2. Requirements of future microdevice-based studies

Ideally, for reliable *in vitro* studies, experiments should be carried out on tissues that resemble entirely the one of the human brain, but this strategy is thwarted for three reasons. (1) The high complexity of the human brain's macro and micro structure makes it impossible to be artificially reproduced. In addition, reported models that strive for more sophistication are often difficult to fabricate and to use (complicated protocols) and they are lacking in reproducibility, an aspect that is especially important when the application is for drug discovery. (2) Primary cell sources are very limited, even unavailable for human origin. Most of the *in vitro* studies for AD use primary animal cells (e.g. from rats). These sources require costly and time consuming brain tissue extraction protocols and they are controversial due to species differences between animals and humans. Immortal human cell lines (e.g. SHSY-5Y), on the other hand, are abundantly available, but they have undergone genotypic and phenotypic changes and are thus metabolically different from the original primary cells. (3) The observation of disease related phenomena within the tissue is a big challenge in complex tissue samples (especially 3D cell cultures). In fact, visual characterization with fluorescence labeling and confocal microscopy for example is expensive and time consuming. Label-free methods such as impedance spectroscopy, on the other hand, may not provide the deepness of information that is necessary to understand molecular processes. In addition, neuronal signals upon chemical stimulation are difficult to record due to the larger distance between neuronal cells and planar recording electrodes.

Finally, the points mentioned above imply that compromises specific to certain applications may be the key to elucidating disease related questions. Simple detection methods can be used at the expense of decreased tissue sophistication or vice versa. For example, reconstructing complex oriented networks with multiple cellular compartments combined with signal recording electrodes (Linder et al., 2006) and simple microscopic characterization may be acceptable at the expense of three-dimensionality (figure E.12a). Also, the study of disease propagation in a 3D context under confocal microscopy analysis may be tolerable at the cost of decreased neurite orientation efficiency. Furthermore, cell lines may be turned into more neuron-like cells in terms of morphology and biochemistry of human mature neurons by treatment with differentiation promoting chemicals such as retinoic acid (Jones-Villeneuve, 1983) and staurosporine (Shea and Beermann, 1991). Moreover, upcoming suppliers of stem cell- or induced pluripotent stem cell-derived neurons that are reliable and low-priced may represent a further alternative to primary cells.

The possibility to analyze the biological specimen is a fundamental condition for studying disease propagation in microsystems. Representing the ideal case, in situ observation of specific phenomena within the neuronal network may not always be possible depending on the technique that is used. Although fluorescence microscopy and electrical signal recording techniques can be carried out exactly at their experimental location, other methods for protein or RNA quantification require the cells to be isolated from the microsystem. Western blot analysis, for example, may be used to address if pathological Tau or Aβ proteins are spread to downstream synaptically connected neurons. For this, cells from specific compartments or locations need to be removed selectively and efficiently.
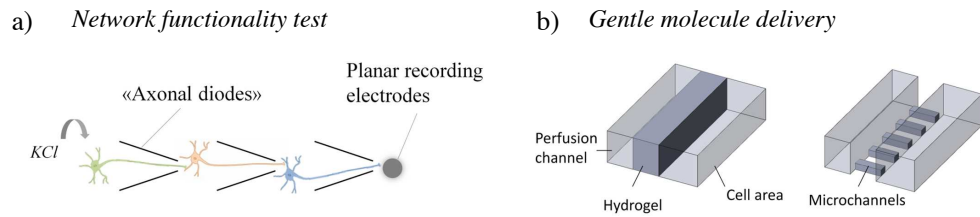
Figure E.12.: Example requirements for future microfluidic-based neuroscience applications. a) Functionality of an oriented neuronal network can be probed as a function of disease progression; b) Molecules can be delivered to the cells in a gentle way, either through a porous hydrogel wall or through small high-resistance microchannels.

Following that, protein lysates are separated on a polyacrylamide gel and visualized on a nitrocellulose membrane with protein-specific antibodies. Due to a decreased number of cells in microfluidic channels in general and thus less total protein amount, it is necessary (1) to extract a maximum number of cells from the microsystem and (2) to guarantee a highly concentrated sample (thus avoiding dilution) in order to obtain a strong signal (coloration).

Moreover, local treatment of specific parts of the neuronal network requires the supply of molecules to each cell sub-population separately. The molecule delivery process needs to be carried out such that the treated cells are not disturbed and do not respond to unwanted stress (flow stress, vibration). For this, special attention is to be paid during pipetting. Alternatively, a molecule injection chamber may be spatially separated from the cell compartment by either high resistance microgrooves or by a permeable hydrogel wall, both allowing the molecule penetration while hindering fluid flow (figure E.12b).

Altogether, complexity and sophistication of artificial neuronal tissues most often stands in contrast to the ease with which the sample is examined and also exposed to stimuli (e.g. molecule delivery). Therefore a compromise for each application specific to a biological question needs to be found. Similarly, metabolically relevant cell models are rare and costly (primary cells, stem cell-derived neuronal cells), while easily available cells lines may be physiologically different than their original cells. Again, the tolerable type of cells used in an experiment strongly depends on the biological question.

E.5. Questions that may be addressed by micro-controlled cultures

Microsystems have shown to be an important tool for studying cell interactions because they allow both, an in vivo-like reconstitution of tissue structures and a more precise functional analysis of neuronal networks. The high potential that underlies microtechnology implies its indispensable use in future neuroscience research. Therefore an interdisciplinary exchange between neuroscientists and microtechnologists seems inevitable.

In fact, local treatment of specific sub-populations of cells within a larger neuronal network requires an accurate control of the cells microenvironment that is reliant on

microfluidics. In addition, in situ and live observation of the sample under investigation necessitates experiments to be carried out on artificial tissues that are reconstituted on thin glass slides. Also, the analysis of electrical functioning of the entire neuronal network depends on the use of signal recording electrodes that share the same size as neuronal cells (i.e. in the micrometer range). Overall, microfabrication techniques can help to elucidate a large number of still open questions:

What factors and mechanisms are responsible for the formation of the first misfolded Tau seeds? This may be due to spontaneous triggers (mutations, transcriptional or translational errors, tissue injury) or exogenous triggers (exposure to preformed aggregates). Misfolded aggregates of an additional protein may promote Tau aggregation (cross-seeding) (Morales et al., 2009). To find an answer to this question, tests may involve the examination of Tau aggregation upon cell exposure to different protein aggregates in order to find out what conditions make healthy cells turn into pathological ones?

How do different stages of Tau aggregation (kinetics, extent) influence the communication between neuronal cells? Following studies may involve the examination of pathological protein transfer to neighboring cells as well as its mechanisms and kinetics. Further questions include how protein aggregates are transferred from one cell to another (secretion, damage of host cell – cell injury) (Guo and Lee, 2011; Nonaka et al., 2010) and what are the mechanisms that lead to the release of those pathological proteins (freely emerged Tau, sequestered within exosomes)? Which species of Tau is specifically responsible for the propagation of NFTs? Also, how are synaptic destruction and neurodegeneration related in time (dying back terminal degeneration, release of Tau is toxic)? Moreover, only some of the interconnected neurons develop NFTs; what conditions prevent the Tau proteins from being transferred? This issue can be investigated by using microsystems where pathologic protein aggregation may be achieved by locally applying exogenous factors or by compartmentalized co-culture of a variety of transgenic diseased cells with healthy cells.

The answers to these questions are of enormous therapeutic interest. Effective drug targets may be developed to counteract not only the symptoms, but the fatal consequences as close as possible at the origin of the pathology. In addition, knowledge about the reason behind individual-dependent progression rates may give rise to personalized treatments (type of medication, doses). Altogether, there is a gap of understanding that may be filled by the means of microtechnology, a tool that has hardly been exploited in AD research with regard to the various studies that can and have to be carried out in order to make head against AD.

Bibliography

A

Abbott, A. (2005). Animal testing: More than a cosmetic change. *Nature*, 438(7065):144–146. (Cited on page 2.)

Abdelghani, A. (2002). Cell-based biosensors for inflammatory agents detection. *Materials Science and Engineering: C*, 22(1):67–72. (Cited on page 39.)

Ackmann, J. and Seitz, M. (1984). Methods of complex impedance measurements in biologic tissue. *Critical reviews in biomedical engineering*, 11(4):281–311. (Cited on page 16.)

Alzheimer's Association (2012). Alzheimer's disease facts and figures. Technical report. (Cited on page 103.)

Astashkina, A., Mann, B., and Grainger, D. (2012). A critical evaluation of in vitro cell culture models for high-throughput drug screening and toxicity. *Pharmacology & Therapeutics*, 134(1):82–106. (Cited on page 2.)

B

Bagnaninchi, P. O. and Drummond, N. (2011). Real-time label-free monitoring of adipose-derived stem cell differentiation with electric cell-substrate impedance sensing. *Proceedings of the National Academy of Sciences of the United States of America*, 108(16):6462–7. (Cited on page 5.)

Banerjee, P., Franz, B., and Bhunia, A. (2010). Mammalian cell-based sensor system. *Whole Cell Sensing Systems I*, 117:21–55. (Cited on page 39.)

Bartholomä, P., Impidjati, Reininger-Mack, A., Zhang, Z., Thielecke, H., and Robitzki, A. (2005). A more aggressive breast cancer spheroid model coupled to an electronic capillary sensor system for a high-content screening of cytotoxic agents in cancer therapy: 3-dimensional in vitro tumor spheroids as a screening model. *Journal of biomolecular screening*, 10(7):705–14. (Cited on page 54.)

BBC (2005). Q&A: Reach chemicals legislation. `http://news.bbc.co.uk/2/hi/europe/4437304.stm`. Accessed: 12/11/2012. (Cited on page 2.)

Bibliography

Bedossa, P. and Paradis, V. (2003). Liver extracellular matrix in health and disease. *The Journal of pathology*, 200(4):504–15. (Cited on page 45.)

Bertrand, J., Winton, M. J., Rodriguez-Hernandez, N., Campenot, R. B., and McKerracher, L. (2005). Application of Rho antagonist to neuronal cell bodies promotes neurite growth in compartmented cultures and regeneration of retinal ganglion cell axons in the optic nerve of adult rats. *The Journal of neuroscience : the official journal of the Society for Neuroscience*, 25(5):1113–21. (Cited on page 109.)

Besser, A. and Schwarz, U. S. (2007). Coupling biochemistry and mechanics in cell adhesion: a model for inhomogeneous stress fiber contraction. *New Journal of Physics*, 9(11):425–425. (Cited on page 47.)

Borkholder, D. A. (1998). *Cell based biosensors using microelectrodes*. Phd thesis, Stanford University. (Cited on page 14.)

Braak, H. and Braak, E. (1991). Demonstration of amyloid deposits and neurofibrillary changes in whole brain sections. *Brain Pathology*, 1(3):213–6. (Cited on page 105.)

Braschler, T. (2009). *Controlled entrapment of cells in hydrogels on chip and cell sorting by dielectrophoresis using liquid electrodes*. PhD thesis, Ecole Polytechnique Fédérale de Lausanne. (Cited on pages 77 and 97.)

Bulinski, J. and Gundersen, G. (2005). Stabilization and post-translational modification of microtubules during cellular morphogenesis. *Bioessays*, 13(6):285–93. (Cited on page 105.)

C

Campenot, R. (1977). Local control of neurite development by nerve growth factor. *Proceedings of the National Academy of Sciences of the United States of America*, 74(10):4516–4519. (Cited on page 108.)

Campenot, R. (1982). Development of sympathetic neurons in compartmentalized cultures:: I. Local control of neurite growth by nerve growth factor. *Developmental biology*, 93(1):13–21. (Cited on page 109.)

Chen, J. S. K., Agarwal, N., and Mehta, K. (2002). Multidrug-resistant MCF-7 breast cancer cells contain deficient intracellular calcium pools. *Breast cancer research and treatment*, 71(3):237–47. (Cited on pages 54 and 60.)

Cho, S., Gorjup, E., and Thielecke, H. (2009). Chip-based time-continuous monitoring of toxic effects on stem cell differentiation. *Annals of anatomy = Anatomischer Anzeiger*, 191(1):145–52. (Cited on page 39.)

Chuang, Y.-H., Chang, Y.-T., Liu, K.-L., Chang, H.-Y., and Yew, T.-R. (2011). Electrical Impedimetric Biosensors for Liver Function Detection. *Biosensors and Bioelectronics*, 28(2010):368–72. (Cited on page 75.)

Clavaguera, F. and Bolmont, T. (2009). Transmission and spreading of tauopathy in transgenic mouse brain. *Nature cell biology*, 11(7):909 – 913. (Cited on page 106.)

Cole, K. (1928). Electric impedance of suspensions of spheres. *The Journal of General Physiology*, 12(1):29–36. (Cited on page 4.)

Cole, K. (1932). Electric phase angle of cell membranes. *The Journal of General Physiology*. (Cited on page 15.)

Cole, K. S. (1940). Permeability and impermeability of cell membranes for ions. *Cold Spring Harbor Symposia on Quantitative Biology*, 8:110–122. (Cited on pages 4 and 16.)

Cole, K. S. and Cole, R. (1941). Dispersion and absorption in dielectrics I. Alternating current characteristics. 9(4):341. (Cited on page 16.)

Conway, B., Bockris, J., and Ammar, I. (1951). The dielectric constant of the solution in the diffuse and Helmholtz double layers at a charged interface in aqueous solution. *Trans. Faraday Soc.*, 47:756–766. (Cited on pages 36 and 77.)

Cornell, B., Braach-Maksvytis, V., King, L., Osman, P., Raguse, B., Wieczorek, L., and Pace, R. (1997). A biosensor that uses ion-channel switches. *Nature*, 387(6633):580–583. (Cited on page 75.)

Cross, S. E., Jin, Y.-S., Lu, Q.-Y., Rao, J., and Gimzewski, J. K. (2011). Green tea extract selectively targets nanomechanics of live metastatic cancer cells. *Nanotechnology*, 22(21):215101. (Cited on page 62.)

Cross, S. E., Jin, Y.-S., Tondre, J., Wong, R., Rao, J., and Gimzewski, J. K. (2008). AFM-based analysis of human metastatic cancer cells. *Nanotechnology*, 19(38):384003. (Cited on page 62.)

D

Davey, C. (1993). *The biomass monitor source book.* Aber Instruments, Aberystwyth. (Cited on page 22.)

de Calignon, A., Polydoro, M., Suárez-Calvet, M., William, C., Adamowicz, D. H., Kopeikina, K. J., Pitstick, R., Sahara, N., Ashe, K. H., Carlson, G. a., Spires-Jones, T. L., and Hyman, B. T. (2012). Propagation of tau pathology in a model of early Alzheimer's disease. *Neuron*, 73(4):685–97. (Cited on page 105.)

De Levie, R. (1965). The influence of surface roughness of solid electrodes on electrochemical measurements. *Electrochimica Acta*, 10(2):113–130. (Cited on pages 21 and 82.)

Bibliography

Debye, P. (1929). *Polar molecules*, volume 8. Dover New York. (Cited on page 4.)

Dellis, J.-L. (2010). ZfitGUI(varargin) fits and simulates impedance data. `http://www.mathworks.com/matlabcentral/fileexchange/26386-zfitguivarargin-fits-and-simulates-impedance-data/content/ZfitGUI.m`. Accessed: 22/11/2012. (Cited on page 34.)

Devarajan, E., Chen, J., and Multani, A. (2002). Human breast cancer MCF-7 cell line contains inherently drug-resistant subclones with distinct genotypic and phenotypic features. *International journal of Oncology*, 20(5):913–20. (Cited on page 54.)

Downward, J. (2003). Targeting RAS signalling pathways in cancer therapy. *Nature reviews. Cancer*, 3(1):11–22. (Cited on page 60.)

E

Eker, B., Meissner, R., Bertsch, A., Mehta, K., and Renaud, P. (2013). Label-free recognition of drug resistance via impedimetric screening of breast cancer cells. *PloS one*, 8(3):e57423. (Cited on page 54.)

El-Hassan, H. (2003). Involvement of mitochondria in acetaminophen-induced apoptosis and hepatic injury Roles of cytochrome c, Bax, Bid, and caspases. *Toxicology and Applied Pharmacology*, 191(2):118–129. (Cited on page 48.)

European Commission (2006). Regulation (EC) No 1907/2006 of the European Parliament and of the Council of 18 December 2006 concerning the Registration, Evaluation, Authorisation and Restriction of Chemicals (REACH). (Cited on page 2.)

European Medecines Agency (2008). Non-Clinical Guideline on Drug-induced hepatotoxicity. Technical report. (Cited on page 2.)

European Medicines Agency (2009). Guidance on Nonclinical Safety Studies for the Conduct of Human Clinical Trials and Marketing Authorization for Pharmaceuticals M3(R2). Technical report. (Cited on page 2.)

F

Frampton, J. P. and al., E. (2007). Three-dimensional hydrogel cultures for modeling changes in tissue impedance around microfabricated neural probes. *Journal of Neural Engineering*, 4(4):399. (Cited on page 7.)

Franks, W., Schenker, I., Schmutz, P., and Hierlemann, A. (2005). Impedance characterization and modeling of electrodes for biomedical applications. *IEEE transactions on bio-medical engineering*, 52(7):1295–302. (Cited on page 23.)

Franks, W., Tosatti, S., Heer, F., Seif, P.and Textor, M., and Hierlemann, A. (2007). Patterned cell adhesion by self-assembled structures for use with a CMOS cell-based biosensor. *Biosensors and Bioelectronics*, 22(7):1426–33. (Cited on page 110.)

Fricke, H. (1924). A mathematical treatment of the electrical conductivity of colloids and cell suspensions. *The Journal of General Physiology*, 6(4):375–384. (Cited on page 4.)

Friedrich, J., Seidel, C., Ebner, R., and Kunz-Schughart, L. A. (2009). Spheroid-based drug screen: considerations and practical approach. *Nat. Protocols*, 4(3):309–324. (Cited on page 7.)

Frost, B., Jacks, R., and Diamond, M. (2009). Propagation of tau misfolding from the outside to the inside of a cell. *Journal of Biological Chemistry*, 284(19):12845–12852. (Cited on page 106.)

G

Garagorri, N., Fermanian, S., Thibault, R., Ambrose, W. M., Schein, O. D., Chakravarti, S., and Elisseeff, J. (2008). Keratocyte behavior in three-dimensional photopolymerizable poly(ethylene glycol) hydrogels. *Acta biomaterialia*, 4(5):1139–47. (Cited on page 67.)

Gawad, S. (2004). *Dielectric spectroscopy in a microfabricated flow cytometer*. Phd thesis, Ecole Polytechnique Fédérale de Lausanne (EPFL). (Cited on pages 6, 39, 46, and 48.)

Geschwind, D. H. (2003). Tau phosphorylation, tangles, and neurodegeneration: the chicken or the egg? *Neuron*, 40(3):457–460. (Cited on pages 104 and 105.)

Giaever, I. and Keese, C. R. (1984). Monitoring fibroblast behavior in tissue culture with an applied electric field. *Proceedings of the National Academy of Sciences of the United States of America*, 81(12):3761–4. (Cited on page 5.)

Giaever, I. and Keese, C. R. (1991). Micromotion of mammalian cells measured electrically. *Proceedings of the National Academy of Sciences of the United States of America*, 88(17):7896–900. (Cited on page 5.)

Gomez Isla, T. and West, H. (1996). Clinical and pathological correlates of apolipoprotein E epsilon 4 in Alzheimer's disease. *Annals of Neurology*, 39(1):62–70. (Cited on page 105.)

Grattarola, M., Tedesco, M., Cambiaso, a., Perlo, G., Giannetti, G., and Sanguineti, a. (1988). Cell adhesion to silicon substrata: characterization by means of optical and acoustic cytometric techniques. *Biomaterials*, 9(1):101–6. (Cited on page 110.)

Griffith, L. G. and Swartz, M. A. (2006). Capturing complex 3D tissue physiology in vitro. *Nature reviews. Molecular cell biology*, 7(3):211–24. (Cited on pages 6 and 115.)

Grimnes, S. and Martinsen, O. (2008). *Bioimpedance and bioelectricity basics.* Academic press. (Cited on page 4.)

Grimnes, S. and Martinsen, O. G. (2005). Cole electrical impedance model–a critique and an alternative. *IEEE transactions on bio-medical engineering*, 52(1):132–5. (Cited on page 16.)

Grotto, D., de Castro, M. M., Barcelos, G. R., Garcia, S. C., and Barbosa Jr, F. (2009). Low level and sub-chronic exposure to methylmercury induces hypertension in rats: nitric oxide depletion and oxidative damage as possible mechanisms. *Archives of toxicology*, 83(7):653–662. (Cited on page 89.)

Guck, J., Schinkinger, S., Lincoln, B., Wottawah, F., Ebert, S., Romeyke, M., Lenz, D., Erickson, H. M., Ananthakrishnan, R., Mitchell, D., Käs, J., Ulvick, S., and Bilby, C. (2005). Optical deformability as an inherent cell marker for testing malignant transformation and metastatic competence. *Biophysical journal*, 88(5):3689–98. (Cited on page 62.)

Guo, J. L. and Lee, V. M.-Y. (2011). Seeding of normal Tau by pathological Tau conformers drives pathogenesis of Alzheimer-like tangles. *The Journal of biological chemistry*, 286(17):15317–31. (Cited on pages 106 and 121.)

H

Haas, S., Jahnke, H.-G., Glass, M., Azendorf, R., Schmidt, S., and Robitzki, A. A. (2010). Real-time monitoring of relaxation and contractility of smooth muscle cells on a novel biohybrid chip. *Lab on a chip*, 10(21):2965–71. (Cited on page 5.)

Haessler, U., Kalinin, Y., Swartz, M. a., and Wu, M. (2009). An agarose-based microfluidic platform with a gradient buffer for 3D chemotaxis studies. *Biomedical microdevices*, 11(4):827–35. (Cited on page 8.)

Halter, R. J., Hartov, A., Heaney, J. A., Paulsen, K. D., and Schned, A. R. (2007). Electrical impedance spectroscopy of the human prostate. *Biomedical Engineering, IEEE Transactions on*, 54(7):1321–1327. (Cited on page 16.)

Hardy, J. and Selkoe, D. J. (2002). The amyloid hypothesis of Alzheimer's disease: progress and problems on the road to therapeutics. *Science*, 297(5580):353–356. (Cited on page 104.)

Harris, a. L. and Hochhauser, D. (1992). Mechanisms of multidrug resistance in cancer treatment. *Acta oncologica (Stockholm, Sweden)*, 31(2):205–13. (Cited on pages 54 and 106.)

Hayashi, H., Campenot, R. B., Vance, D. E., and Vance, J. E. (2004). Glial lipoproteins stimulate axon growth of central nervous system neurons in compartmented cultures. *The Journal of biological chemistry*, 279(14):14009–15. (Cited on page 109.)

Heller, D., Garga, V., Kelleher, K., and Lee, T. (2005). Patterned networks of mouse hippocampal neurons on peptide-coated gold surfaces. *Biomaterials*, 26(8):883889. (Cited on page 110.)

Hengstler, J. G., Marchan, R., and Leist, M. (2012). Highlight report: towards the replacement of in vivo repeated dose systemic toxicity testing. *Archives of toxicology*, 86(1):13–5. (Cited on page 90.)

Heussner, A., O'Brien, E., and Dietrich, D. (2007). Effects of repeated ochratoxin exposure on renal cells in vitro. *Toxicology in vitro*, 21(1):72–80. (Cited on page 90.)

Höber, R. (1910). Eine methode, die elektrische leitfähigkeit im innern von zellen zu messen. *Pflüger's Archiv für die gesamte Physiologie des Menschen und der Tiere*, 133(4-6):237–253. (Cited on page 4.)

Hsieh, C.-Y., Miaw, C.-L., Hsieh, C.-C., Tseng, H.-C., Yang, Y.-H., and Yen, C.-H. (2009). Effects of chronic 4-n-nonylphenol treatment on aortic vasoconstriction and vasorelaxation in rats. *Archives of toxicology*, 83(10):941–946. (Cited on page 89.)

Hug, T. S. (2003). Biophysical methods for monitoring cell-substrate interactions in drug discovery. *Assay and drug development technologies*, 1(3):479–88. (Cited on pages 39 and 75.)

Hyman, B. and Hoesen, G. V. (1987). Neuron numbers in Alzheimer's disease: Cell-specific pathology. *Neurobiology of Aging*, 8(6):555–556. (Cited on page 105.)

Hyman, B. T., Van Hoesen, G. W., Damasio, A. R., and Barnes, C. L. (1984). Alzheimer's disease: cell-specific pathology isolates the hippocampal formation. *Science*, 225(4667):1168–1170. (Cited on page 105.)

I

Isambert, H. (1998). Understanding the electroporation of cells and artificial bilayer membranes. *Physical review letters*, 80(15):3404–3407. (Cited on page 13.)

Ishibashi, T., Dakin, K. A., Stevens, B., Lee, P. R., Kozlov, S. V., Stewart, C. L., and Fields, R. D. (2006). Astrocytes promote myelination in response to electrical impulses. *Neuron*, 49(6):823–32. (Cited on page 109.)

Itakura, Y., Tajima, T., Ohoke, S., Matsuzawa, J., Sudo, H., and Yamamoto, S. (1989). Osteocompatibility of platinum-plated titanium assessed in vitro. *Biomaterials*, 10(7):489–93. (Cited on pages 19 and 29.)

Ittner, L. M. and Götz, J. (2011). Amyloid-β and tau–a toxic pas de deux in Alzheimer's disease. *Nature reviews. Neuroscience*, 12(2):65–72. (Cited on page 105.)

Bibliography

Ivanova, O. and Margolis, L. (1973). The use of phospholipid film for shaping cell cultures. *Nature*, 242(5394):200–201. (Cited on page 110.)

Ivorra, A., Genescà, M., Sola, A., Palacios, L., Villa, R., Hotter, G., and Aguiló, J. (2005). Bioimpedance dispersion width as a parameter to monitor living tissues. *Physiological Measurement*, 26(2):S165–S173. (Cited on pages 16, 20, and 21.)

J

Jacobs, P., Varlan, A., and Sansen, W. (1995). Design optimisation of planar electrolytic conductivity sensors. *Medical and Biological Engineering and Computing*, 33(6):802–810. (Cited on page 22.)

Jahnke, H.-G., Rothermel, A., Sternberger, I., Mack, T. G., Kurz, R. G., Pänke, O., Striggow, F., and Robitzki, A. A. (2009). An impedimetric microelectrode-based array sensor for label-free detection of tau hyperphosphorylation in human cells. *Lab on a Chip*, 9(10):1422–1428. (Cited on pages 5 and 39.)

Janmey, P. A., Euteneuer, U., Traub, P., and Schliwa, M. (1991). Viscoelastic properties of vimentin compared with other filamentous biopolymer networks. *The Journal of cell biology*, 113(1):155–60. (Cited on page 62.)

Jeon, N. L., Baskaran, H., Dertinger, S. K., Whitesides, G. M., Van De Water, L., and Toner, M. (2002). Neutrophil chemotaxis in linear and complex gradients of interleukin-8 formed in a microfabricated device. *Nature biotechnology*, 20(8):826–830. (Cited on page 114.)

Jones-Villeneuve, E. (1983). Retinoic acid-induced neural differentiation of embryonal carcinoma cells. *Molecular and cellular biology*, 3(12):2271–2279. (Cited on page 119.)

Jucker, M. and Walker, L. C. (2011). Pathogenic protein seeding in Alzheimer disease and other neurodegenerative disorders. *Annals of neurology*, 70(4):532–40. (Cited on page 105.)

K

Kaji, H., Camci-Unal, G., Langer, R., and Khademhosseini, A. (2011). Engineering systems for the generation of patterned co-cultures for controlling cell-cell interactions. *Biochimica et biophysica acta*, 1810(3):239–50. (Cited on page 110.)

Kane, R. S., Takayama, S., Ostuni, E., Ingber, D., and Whitesides, G. M. (1999). Patterning proteins and cells using soft lithography. *Biomaterials*, 20(23-24):2363–2376. (Cited on page 110.)

Kasi, H., Meissner, R., Babalian, A., van Lintel, H., Bertsch, A., and Renaud, P. (2011). Direct localised measurement of electrical resistivity profile in rat and embryonic chick retinas using a microprobe. *Journal of Electrical Bioimpedance*, 1(26471):84. (Cited on pages 29 and 75.)

Kaufmann, S. H. and Vaux, D. L. (2003). Alterations in the apoptotic machinery and their potential role in anticancer drug resistance. *Oncogene*, 22(47):7414–30. (Cited on page 54.)

Keenan, T. M. and Folch, A. (2008). Biomolecular gradients in cell culture systems. *Lab Chip*, 8(1):34–57. (Cited on page 114.)

Kerner, T. E., Paulsen, K. D., Hartov, A., Soho, S. K., and Poplack, S. P. (2002). Electrical impedance spectroscopy of the breast: clinical imaging results in 26 subjects. *Medical Imaging, IEEE Transactions on*, 21(6):638–645. (Cited on page 16.)

Khetani, S. R. and Bhatia, S. N. (2008). Microscale culture of human liver cells for drug development. *Nature biotechnology*, 26(1):120–6. (Cited on page 45.)

Kim, C., Choi, H., Jung, E. S., Lee, W., Oh, S., Jeon, N. L., and Mook-Jung, I. (2012). HDAC6 Inhibitor Blocks Amyloid Beta-Induced Impairment of Mitochondrial Transport in Hippocampal Neurons. *PloS one*, 7(8):e42983. (Cited on page 117.)

Kleinfeld, D. (1988). Controlled outgrowth of dissociated neurons on patterned substrates. *The Journal of neuroscience*, 8(11):4098–4120. (Cited on page 110.)

Kleinman, H., Klebe, R., and Martin, G. (1981). Role of collagenous matrices in the adhesion and growth of cells. *The Journal of cell biology*, 88(3):473–485. (Cited on page 110.)

Kloss, D., Fischer, M., Rothermel, A., Simon, J. C., and Robitzki, A. A. (2008). Drug testing on 3D in vitro tissues trapped on a microcavity chip. *Lab on a chip*, 8(6):879–84. (Cited on pages 7, 8, 69, and 75.)

Knight, B., Laukaitis, C., Akhtar, N., and Hotchin, N. (2000). Visualizing muscle cell migration in situ. *Current Biology*, 10(10):576–585. (Cited on pages 6 and 115.)

Kols, A. (2002). Breast cancer: increasing incidence, limited options. *Outlook*, 19(4). (Cited on page 53.)

Kon, K., Ikejima, K., Okumura, K., Aoyama, T., Arai, K., Takei, Y., Lemasters, J. J., and Sato, N. (2007). Role of apoptosis in acetaminophen hepatotoxicity. *Journal of gastroenterology and hepatology*, 22(s1):S49–S52. (Cited on page 47.)

Kovacs, G. (1994). Introduction to the theory, design, and modeling of thin-film microelectrodes for neural interfaces. In *Enabling technologies for cultured neural networks*, pages 121–165. Academic Press, San Diego. (Cited on pages 19, 20, 21, 22, and 77.)

Bibliography

Krinke, D., Jahnke, H.-G., Mack, T. G. a., Hirche, A., Striggow, F., and Robitzki, A. A. (2010). A novel organotypic tauopathy model on a new microcavity chip for bioelectronic label-free and real time monitoring. *Biosensors & bioelectronics*, 26(1):162–8. (Cited on pages 5 and 39.)

Kroemer, G. (2009). Classification of cell death:. 16(1):3–11. (Cited on page 40.)

Kunze, A., Giugliano, M., Valero, A., and Renaud, P. (2011a). Micropatterning neural cell cultures in 3D with a multi-layered scaffold. *Biomaterials*, 32(8):2088–98. (Cited on pages 110 and 112.)

Kunze, A., Meissner, R., Brando, S., and Renaud, P. (2011b). Co-pathological connected primary neurons in a microfluidic device for Alzheimer studies. *Biotechnology and bioengineering*, 108(9):2241–5. (Cited on pages 104 and 117.)

Kunze, A., Meissner, R., Brando, S., and Renaud, P. (2011c). Co-pathological states of tau proteins in a 3D micropatterned neural cell culture. *15th International Conference on Miniaturized Systems for Chemistry and Life Sciences*, 1:696–698. (Cited on page 118.)

Kunze, A., Valero, A., Zosso, D., and Renaud, P. (2011d). Synergistic NGF/B27 gradients position synapses heterogeneously in 3D micropatterned neural cultures. *PloS one*, 6(10):e26187. (Cited on page 114.)

L

Leclerc, E. (2004). Perfusion culture of fetal human hepatocytes in microfluidic environments. *Biochemical Engineering Journal*, 20(2-3):143–148. (Cited on page 8.)

Lee, S., Poet, T. S., Smith, J. N., Hjerpe, A. L., Gunawan, R., and Timchalk, C. (2011). Impact of repeated nicotine and alcohol coexposure on in vitro and in vivo chlorpyrifos dosimetry and cholinesterase inhibition. *Journal of toxicology and environmental health. Part A*, 74(20):1334–50. (Cited on page 90.)

Letourneau, P. (1975). Cell-to-substratum adhesion and guidance of axonal elongation. *Developmental biology*, 44(1):92–101. (Cited on page 110.)

Lichtenberg, J., de Rooij, N. F., and Verpoorte, E. (2002). A microchip electrophoresis system with integrated in-plane electrodes for contactless conductivity detection. *Electrophoresis*, 23(21):3769–3780. (Cited on page 90.)

Lin, S.-P., Kyriakides, T. R., and Chen, J.-J. J. (2009). On-line observation of cell growth in a three-dimensional matrix on surface-modified microelectrode arrays. *Biomaterials*, 30(17):3110–7. (Cited on page 7.)

Linder, V., Koster, S., Franks, W., Kraus, T., Verpoorte, E., Heer, F., Hierlemann, A., and de Rooij, N. F. (2006). Microfluidics/cmos orthogonal capabilities for cell biology. *Biomedical microdevices*, 8(2):159–166. (Cited on page 119.)

Linderholm, P. (2006). *Two-dimensional microimpedance imaging for cell culture monitoring*. PhD thesis, Ecole Polytechnique Federale de Lausanne (EPFL). (Cited on pages 6, 7, 9, 19, 22, 24, 29, 35, 46, and 86.)

Linderholm, P., Braschler, T., Vannod, J., Barrandon, Y., Brouard, M., and Renaud, P. (2006). Two-dimensional impedance imaging of cell migration and epithelial stratification. *Lab on a chip*, 6(9):1155–62. (Cited on page 5.)

Liu, W., Deng, Y., Liu, Y., Gong, W., and Deng, W. (2013). Stem cell models for drug discovery and toxicology studies. *Journal of biochemical and molecular toxicology*, 27(1):17–27. (Cited on page 3.)

Liu, Y. and Vrana, N. (2009). Physically crosslinked composite hydrogels of PVA with natural macromolecules: structure, mechanical properties, and endothelial cell compatibility. *Journal of biomedical materials research. Part B, Applied biomaterials*, 90b(2):492–502. (Cited on page 67.)

Lo, C.-M., Keese, C. R., and Giaever, I. (1993). Monitoring Motion of Confluent Cells in Tissue Culture. *Experimental Cell Research*, 204(1):102–109. (Cited on page 5.)

M

Macdonald, R. (2005). LEVM/LEVMW Manual. `http://scholar.google.com/scholar?hl=en&btnG=Search&q=intitle:LEVM+/+LEVMW+Manual#0`. Accessed: 05/04/2011. (Cited on page 34.)

McAdams, E. T. and Jossinet, J. (1995). Tissue impedance: a historical overview. *Physiological measurement*, 16(3 Suppl A):A1–13. (Cited on page 16.)

McHardy, L. M., Warabi, K., Andersen, R. J., Roskelley, C. D., and Roberge, M. (2005). Strongylophorine-26, a Rho-dependent inhibitor of tumor cell invasion that reduces actin stress fibers and induces nonpolarized lamellipodial extensions. *Molecular cancer therapeutics*, 4(5):772–8. (Cited on page 48.)

Meissner, A., Wernig, M., and Jaenisch, R. (2007). Direct reprogramming of genetically unmodified fibroblasts into pluripotent stem cells. *Nature biotechnology*, 25(10):1177–1181. (Cited on page 3.)

Meissner, R., Eker, B., Kasi, H., Bertsch, A., and Renaud, P. (2011). Distinguishing drug-induced minor morphological changes from major cellular damage via label-free impedimetric toxicity screening. *Lab on a chip*, 11(14):2352–61. (Cited on pages 16, 39, and 75.)

Bibliography

Meissner, R., Joris, P., Eker, B., Bertsch, A., and Renaud, P. (2012). A microfluidic-based frequency-multiplexing impedance sensor (FMIS). *Lab on a chip*, 12(15):2712–8. (Cited on page 76.)

Mercanzini, A., Colin, P., Bensadoun, J.-C., Bertsch, A., and Renaud, P. (2009). In vivo electrical impedance spectroscopy of tissue reaction to microelectrode arrays. *IEEE transactions on bio-medical engineering*, 56(7):1909–18. (Cited on pages 33 and 75.)

Min, J., P. S. Y. C. and Song, B. (2010). Development of a low-cost multifunctional wireless impedance sensor node. *Smart Struct. Syst*, 6(5):689–709. (Cited on page 91.)

Morales, R., Green, K., and Soto, C. (2009). Cross currents in protein misfolding disorders: interactions and therapy. *CNS & neurological disorders drug targets*, 8(5):363–371. (Cited on page 121.)

Moscow, J. A. and Dixon, K. H. (1993). Glutathione-related enzymes, glutathione and multidrug resistance. *Cytotechnology*, 12(1-3):155–70. (Cited on page 54.)

Mueller, D., Müller-Vieira, U., Biemel, K. M., Tascher, G., Nüssler, A. K., and Noor, F. (2012). Biotransformation of diclofenac and effects on the metabolome of primary human hepatocytes upon repeated dose exposure. *European journal of pharmaceutical sciences : official journal of the European Federation for Pharmaceutical Sciences*, 45(5):716–24. (Cited on page 90.)

Murphy, S. L., Xu, J., , and Kochanek, K. D. (2010). National Vital Statistics Reports Deaths : Preliminary Data for 2010. *National Vital Statistics Reports*, 60(4). (Cited on page 103.)

N

Nath, S., Agholme, L., Kurudenkandy, F. R., Granseth, B., Marcusson, J., and Hallbeck, M. (2012). Spreading of Neurodegenerative Pathology via Neuron-to-Neuron Transmission of β-Amyloid. *The Journal of neuroscience : the official journal of the Society for Neuroscience*, 32(26):8767–77. (Cited on pages 106 and 107.)

Nonaka, T., Watanabe, S. T., Iwatsubo, T., and Hasegawa, M. (2010). Seeded aggregation and toxicity of {alpha}-synuclein and tau: cellular models of neurodegenerative diseases. *The Journal of biological chemistry*, 285(45):34885–98. (Cited on pages 106 and 121.)

North-Lewis, P. (2008). *Drugs and the liver*. Pharmaceutical Press. (Cited on pages 40 and 45.)

O

Okita, K., Ichisaka, T., and Yamanaka, S. (2007). Generation of germline-competent induced pluripotent stem cells. *Nature*, 448(7151):313–317. (Cited on page 3.)

Olson, H., Betton, G., Robinson, D., Thomas, K., Monro, A., Kolaja, G., Lilly, P., Sanders, J., Sipes, G., Bracken, W., Dorato, M., Van Deun, K., Smith, P., Berger, B., and Heller, A. (2000). Concordance of the toxicity of pharmaceuticals in humans and in animals. *Regulatory toxicology and pharmacology : RTP*, 32(1):56–67. (Cited on page 2.)

Olson, M. F. and Sahai, E. (2009). The actin cytoskeleton in cancer cell motility. *Clinical & experimental metastasis*, 26(4):273–87. (Cited on page 59.)

Olthuis, W., Streekstra, W., and Bergveld, P. (1995). Theoretical and experimental determination of cell constants of planar-interdigitated electrolyte conductivity sensors. *Sensors and Actuators B: Chemical*, 24(1-3):252–256. (Cited on pages 22, 78, and 99.)

Opp, D., Wafula, B., Lim, J., Huang, E., Lo, J.-C. C., and Lo, C.-M. M. (2009). Use of electric cell-substrate impedance sensing to assess in vitro cytotoxicity. *Biosens Bioelectron*, 24(8):2625–2629. (Cited on page 2.)

Otero-González, L., Sierra-Alvarez, R., Boitano, S., and Field, J. A. (2012). Application and validation of an impedance-based real time cell analyzer to measure the toxicity of nanoparticles impacting human bronchial epithelial cells. *Environmental science & technology*, 46(18):10271–8. (Cited on pages 5 and 32.)

Overly, T. G., Park, G., Farinholt, K. M., and Farrar, C. R. (2008). Development of an extremely compact impedance-based wireless sensing device. *Smart Materials and Structures*, 17(6):065011. (Cited on page 91.)

P

Paguirigan, A. L. and Beebe, D. J. (2007). Protocol for the fabrication of enzymatically crosslinked gelatin microchannels for microfluidic cell culture. *Nature protocols*, 2(7):1782–8. (Cited on page 93.)

Pampaloni, F., Reynaud, E. G., and Stelzer, E. H. K. (2007). The third dimension bridges the gap between cell culture and live tissue. *Nature reviews. Molecular cell biology*, 8(10):839–45. (Cited on page 8.)

Park, J., Koito, H., Li, J., and Han, A. (2009). Microfluidic compartmentalized co-culture platform for CNS axon myelination research. *Biomedical microdevices*, 11(6):1145–53. (Cited on page 109.)

Bibliography

Pauly, H. and Schwan, H. (1959). Impendance of a suspension of ball-shaped particles with a shell; a model for the dielectric behavior of cell suspensions and protein solutions. *Zeitschrift für Naturforschung. Teil B: Chemie, Biochemie, Biophysik, Biologie*, 14B(2):125–31. (Cited on pages 6 and 39.)

Pautot, S., Wyart, C., and Isacoff, E. (2008). Colloid-guided assembly of oriented 3D neuronal networks. *Nature methods*, 5(8):735–740. (Cited on pages 115 and 116.)

Perl, A. K., Wilgenbus, P., Dahl, U., Semb, H., and Christofori, G. (1998). A causal role for E-cadherin in the transition from adenoma to carcinoma. *Nature*, 392(6672):190–3. (Cited on page 60.)

Pessina, A. (1993). Topoisomerase I in multiple drug resistance. *Cytotechnology*, 12(1-3):127–35. (Cited on page 54.)

Peyrin, J.-M., Deleglise, B., Saias, L., Vignes, M., Gougis, P., Magnifico, S., Betuing, S., Pietri, M., Caboche, J., Vanhoutte, P., Viovy, J.-L., and Brugg, B. (2011). Axon diodes for the reconstruction of oriented neuronal networks in microfluidic chambers. *Lab on a chip*, 11(21):3663–73. (Cited on pages 107 and 113.)

Pierce, R. H., Franklin, C. C., Campbell, J. S., Tonge, R. P., Chen, W., Fausto, N., Nelson, S. D., and Bruschi, S. a. (2002). Cell culture model for acetaminophen-induced hepatocyte death in vivo. *Biochemical pharmacology*, 64(3):413–24. (Cited on page 47.)

Pluen, A., Netti, P. A., Jain, R. K., and Berk, D. A. (1999). Diffusion of macromolecules in agarose gels: comparison of linear and globular configurations. *Biophysical journal*, 77(1):542–52. (Cited on page 67.)

Pollard, T. D. and Cooper, J. A. (2009). Actin, a central player in cell shape and movement. *Science*, 326(5957):1208–12. (Cited on page 59.)

Poon, W. W., Blurton-Jones, M., Tu, C. H., Feinberg, L. M., Chabrier, M. A., Harris, J. W., Jeon, N. L., and Cotman, C. W. (2011). β-Amyloid impairs axonal BDNF retrograde trafficking. *Neurobiology of aging*, 32(5):821–33. (Cited on page 116.)

Priller, C., Bauer, T., Mitteregger, G., Krebs, B., Kretzschmar, H. a., and Herms, J. (2006). Synapse formation and function is modulated by the amyloid precursor protein. *The Journal of neuroscience : the official journal of the Society for Neuroscience*, 26(27):7212–21. (Cited on page 104.)

Prot, J. M., Aninat, C., Griscom, L., Razan, F., Brochot, C., Guillouzo, C. G., Legallais, C., Corlu, A., and Leclerc, E. (2011). Improvement of hepg2/c3a cell functions in a microfluidic biochip. *Biotechnology and bioengineering*, 108(7):1704–1715. (Cited on page 45.)

Prot, J.-M., Bunescu, A., Elena-Herrmann, B., Aninat, C., Snouber, L. C., Griscom, L., Razan, F., Bois, F. Y., Legallais, C., Brochot, C., et al. (2012). Predictive toxicology

using systemic biology and liver microfluidic on chip approaches: Application to acetaminophen injury. *Toxicology and applied pharmacology*, 259(3):270–280. (Cited on page 45.)

R

Ranieri, J. P., Bellamkonda, R., Bekos, E. J., Gardella, J. A., Mathieu, H. J., Ruiz, L., and Aebischer, P. (1994). Spatial control of neuronal cell attachment and differentiation on covalently patterned laminin oligopeptide substrates. *International journal of developmental neuroscience : the official journal of the International Society for Developmental Neuroscience*, 12(8):725–35. (Cited on page 110.)

Rao, J. and Li, N. (2004). Microfilament actin remodeling as a potential target for cancer drug development. *Current cancer drug targets*, 4(4):345–354. (Cited on page 60.)

Rickert, J., Göpel, W., Beck, W., Jung, G., and Heiduschka, P. (1996). A 'mixed' self-assembled monolayer for an impedimetric immunosensor. *Biosensors and Bioelectronics*, 11(8):757–768. (Cited on page 75.)

Roggen, E. L. (2011). In vitro toxicity testing in the twenty-first century. *Frontiers in pharmacology*, 2. (Cited on pages 89 and 90.)

Roskelley, C. (1994). Extracellular matrix-dependent tissue-specific gene expression in mammary epithelial cells requires both physical and biochemical signal transduction. *Proceedings of the National Academy of Sciences of the United States of America*, 91(26):12378–12382. (Cited on pages 6 and 115.)

S

Santacruz, K., Lewis, J., Spires, T., and Paulson, J. (2005). Tau suppression in a neurodegenerative mouse model improves memory function. *Science*, 309(5733):476–481. (Cited on page 106.)

Satcher, R. L. and Dewey, C. F. (1996). Theoretical estimates of mechanical properties of the endothelial cell cytoskeleton. *Biophysical journal*, 71(1):109–18. (Cited on page 62.)

Schacher, S. and Proshansky, E. (1983). Neurite regeneration by Aplysia neurons in dissociated cell culture: modulation by Aplysia hemolymph and the presence of the initial axonal segment. *The Journal of neuroscience*, 3(12):2403–2413. (Cited on page 110.)

Schmitz, S. (2007). *Der Experimentator: Zellkultur*. Spektrum Akademischer Verlag. (Cited on page 45.)

Schwan, H. (1954). Die elektrischen eigenschaften von muskelgewebe bei Niederfrequenz. *Z. Naturforsch*, 96:245–251. (Cited on page 4.)

Bibliography

Schwan, H. (1994). Electrical properties of tissues and cell suspensions: mechanisms and models. *Engineering in Medicine and Biology Society*, 1:A70–A71. (Cited on page 4.)

Schwan, H. P. (1999). The practical success of impedance techniques from an historical perspective. *Annals of the New York Academy of Sciences*, 873(1):1–12. (Cited on page 4.)

Sharma, S., Santiskulvong, C., Bentolila, L. A., Rao, J., Dorigo, O., and Gimzewski, J. K. (2012). Correlative nanomechanical profiling with super-resolution f-actin imaging reveals novel insights into mechanisms of cisplatin resistance in ovarian cancer cells. *Nanomedicine: Nanotechnology, Biology and Medicine*, 8(5):757–766. (Cited on pages 60 and 62.)

Shea, T. and Beermann, M. (1991). Staurosporine-induced morphological differentiation of human neuroblastoma cells. *Cell biology international reports*, 15(2):161–168. (Cited on page 119.)

Shin, Y., Han, S., Jeon, J. S., Yamamoto, K., Zervantonakis, I. K., Sudo, R., Kamm, R. D., and Chung, S. (2012). Microfluidic assay for simultaneous culture of multiple cell types on surfaces or within hydrogels. *Nature protocols*, 7(7):1247–59. (Cited on page 8.)

Shrivastava, S., Chung, B., and Khademhosseini, A. (2008). A microwell array system for stem cell culture. *Biomaterials*, 29(6):752–763. (Cited on page 67.)

Simstein, R., Burow, M., Parker, A., Weldon, C., and Beckman, B. (2003). Apoptosis, chemoresistance, and breast cancer: insights from the mcf-7 cell model system. *Experimental biology and medicine*, 228(9):995–1003. (Cited on page 54.)

Smith, D. A. (1991). Species differences in metabolism and pharmacokinetics: are we close to an understanding? *Drug metabolism reviews*, 23(3-4):355–373. (Cited on page 2.)

Snouber, L. C., Bunescu, A., Naudot, M., Legallais, C., Brochot, C., Dumas, M. E., Elena-Herrmann, B., and Leclerc, E. (2013). Metabolomics-on-a-chip of hepatotoxicity induced by anticancer drug flutamide and its active metabolite hydroxyflutamide using hepg2/c3a microfluidic biochips. *Toxicological Sciences*, 132(1):8–20. (Cited on page 45.)

Soto, C. (2012). In vivo spreading of tau pathology. *Neuron*, 73(4):621–3. (Cited on pages 105 and 106.)

Souteyrand, E., Cloarec, J., Martin, J., Wilson, C., Lawrence, I., Mikkelsen, S., and Lawrence, M. (1997). Direct detection of the hybridization of synthetic homo-oligomer DNA sequences by field effect. *The Journal of Physical Chemistry B*, 101(15):2980–2985. (Cited on page 75.)

Steude, A., Schmidt, S., Robitzki, A. A., and Pänke, O. (2011). An electrode array for electrochemical immuno-sensing using the example of impedimetric tenascin C detection. *Lab on a chip*, 11(17):2884–92. (Cited on page 75.)

Stieglitz, T. (2004). Electrode materials for recording and stimulation. *Neuroprosthetics: Theory and Practice*, pages 475–516. (Cited on pages 21 and 45.)

Stiles, J. and Jernigan, T. L. (2010). The basics of brain development. *Neuropsychology review*, 20(4):327–48. (Cited on page 107.)

Stolwijk, J. A., Hartmann, C., Balani, P., Albermann, S., Keese, C. R., Giaever, I., and Wegener, J. (2011). Impedance analysis of adherent cells after in situ electroporation: non-invasive monitoring during intracellular manipulations. *Biosensors & bioelectronics*, 26(12):4720–7. (Cited on page 75.)

Suresh, S. (2007). Biomechanics and biophysics of cancer cells. *Acta biomaterialia*, 3(4):413–38. (Cited on page 62.)

Suresh, S., Spatz, J., Mills, J. P., Micoulet, A., Dao, M., Lim, C. T., Beil, M., and Seufferlein, T. (2005). Connections between single-cell biomechanics and human disease states: gastrointestinal cancer and malaria. *Acta biomaterialia*, 1(1):15–30. (Cited on page 62.)

T

Takahashi, K. and Yamanaka, S. (2006). Induction of pluripotent stem cells from mouse embryonic and adult fibroblast cultures by defined factors. *cell*, 126(4):663–676. (Cited on page 3.)

Tan, W. and Desai, T. A. (2004). Layer-by-layer microfluidics for biomimetic three-dimensional structures. *Biomaterials*, 25(7-8):1355–1364. (Cited on pages 110 and 115.)

Tarantola, M., Pietuch, A., Schneider, D., Rother, J., Sunnick, E., Rosman, C., Pierrat, S., Sönnichsen, C., Wegener, J., and Janshoff, A. (2010). Toxicity of gold-nanoparticles: Synergistic effects of shape and surface functionalization on micromotility of epithelial cells. *Nanotoxicology*, pages 1–15. (Cited on page 75.)

Taylor, A., Blurton-Jones, M., and Rhee, S. (2005). A microfluidic culture platform for CNS axonal injury, regeneration and transport. *Nature methods*, 2(8):599–605. (Cited on pages 109 and 117.)

Thielecke, H., Mack, A., and Robitzki, A. (2001). Biohybrid microarrays Impedimetric biosensors with 3D in vitro tissues for toxicological and biomedical screening. *Fresenius' Journal of Analytical Chemistry*, 369(1):23–29. (Cited on page 7.)

Tijero, M., Gabriel, G., Caro, J., Altuna, A., Hernández, R., Villa, R., Berganzo, J., Blanco, F. J., Salido, R., and Fernández, L. J. (2009). SU-8 microprobe with microelectrodes for monitoring electrical impedance in living tissues. *Biosensors & bioelectronics*, 24(8):2410–6. (Cited on page 75.)

Timpl, R., Rohde, H., and Robey, P. (1979). Laminin-a glycoprotein from basement membranes. *Journal of Biological Chemistry*, 254(19):9933–9937. (Cited on page 110.)

Toh, Y.-C., Zhang, C., Zhang, J., Khong, Y. M., Chang, S., Samper, V. D., van Noort, D., Hutmacher, D. W., and Yu, H. (2007). A novel 3D mammalian cell perfusion-culture system in microfluidic channels. *Lab on a chip*, 7(3):302–9. (Cited on page 8.)

Tostoes, R. M., Leite, S. B., Serra, M., Jensen, J., Björquist, P., Carrondo, M. J. T., Brito, C., and Alves, P. M. (2012). Human liver cell spheroids in extended perfusion bioreactor culture for repeated-dose drug testing. *Hepatology (Baltimore, Md.)*, 55(4):1227–36. (Cited on page 90.)

Tu, Y., Xu, F. H., Liu, J., Vescio, R., Berenson, J., Fady, C., and Lichtenstein, a. (1996). Upregulated expression of BCL-2 in multiple myeloma cells induced by exposure to doxorubicin, etoposide, and hydrogen peroxide. *Blood*, 88(5):1805–12. (Cited on page 54.)

U

Ueda, K., Clark, D., Chen, C., Roninson, I., Gottesman, M., and Pastan, I. (1987). The human multidrug resistance (mdr1) gene. cdna cloning and transcription initiation. *Journal of Biological Chemistry*, 262(2):505–508. (Cited on page 54.)

Ussing, H. H. and Zerahn, K. (1951). Active transport of sodium as the source of electric current in the short-circuited isolated frog skin. *Acta Physiologica Scandinavica*, 23(2-3):110–127. (Cited on pages 4 and 5.)

V

Van Gerwen, P., Laureys, W., Huyberechts, G., De Baeck, M., Baert, K., Suis, J., Varlan, a., Sansen, W., Hermans, L., and Mertens, R. (1998). Nanoscaled interdigitated electrode arrays for biochemical sensors. *Proceedings of International Solid State Sensors and Actuators Conference (Transducers '97)*, 49:907–910. (Cited on page 22.)

van Grinsven, B., Vanden Bon, N., Grieten, L., Murib, M., Janssens, S. D., Haenen, K., Schneider, E., Ingebrandt, S., Schöning, M. J., Vermeeren, V., Ameloot, M., Michiels, L., Thoelen, R., De Ceuninck, W., and Wagner, P. (2011). Rapid assessment of the stability of DNA duplexes by impedimetric real-time monitoring of chemically induced denaturation. *Lab on a chip*, 11(9):1656–63. (Cited on page 75.)

W

Wang, J., Ren, L., Li, L., Liu, W., Zhou, J., Yu, W., Tong, D., and Chen, S. (2009). Microfluidics: a new cosset for neurobiology. *Lab on a chip*, 9(5):644–52. (Cited on page 113.)

Ward, S. (2008). Cell-based Assays and their Role in the Future of Toxicity Testing: Part I. `http://alttox.org/spotlight/013/`. Accessed: 06/12/2012. (Cited on page 3.)

Wegener, J., Keese, C. R., and Giaever, I. (2000). Electric cell-substrate impedance sensing (ECIS) as a noninvasive means to monitor the kinetics of cell spreading to artificial surfaces. *Experimental cell research*, 259(1):158–66. (Cited on page 5.)

Wheelock, M. J., Shintani, Y., Maeda, M., Fukumoto, Y., and Johnson, K. R. (2008). Cadherin switching. *Journal of cell science*, 121(Pt 6):727–35. (Cited on page 60.)

Wimo, A. and Prince, M. (2010). World Alzheimer Report. *Alzheimer's Disease International*. (Cited on page 103.)

Winograd-Katz, S. E., Brunner, M. C., Mirlas, N., and Geiger, B. (2011). Analysis of the signaling pathways regulating Src-dependent remodeling of the actin cytoskeleton. *European journal of cell biology*, 90(2-3):143–56. (Cited on page 60.)

X

Xia, L., Ng, S., Han, R., Tuo, X., Xiao, G., Leo, H. L., Cheng, T., and Yu, H. (2009). Laminar-flow immediate-overlay hepatocyte sandwich perfusion system for drug hepatotoxicity testing. *Biomaterials*, 30(30):5927–5936. (Cited on pages 8 and 45.)

Y

Yang, L., G. V. and Mishra, A. (2007). Synthetic antimicrobial oligomers induce a composition-dependent topological transition in membranes. *Journal of the american chemical society*, 129(40):12141–12147. (Cited on page 67.)

Yang, I. H., Siddique, R., Hosmane, S., Thakor, N., and Höke, A. (2009). Compartmentalized microfluidic culture platform to study mechanism of paclitaxel-induced axonal degeneration. *Experimental neurology*, 218(1):124–8. (Cited on page 109.)

Z

Zhang, M., Lee, P., Hung, P., Johnson, T., Lee, L., and Mofrad, M. (2008). Microfluidic environment for high density hepatocyte culture. *Biomedical Microdevices*, 10(1):117–121. (Cited on page 8.)

Zhao, J. and Guan, J.-L. (2009). Signal transduction by focal adhesion kinase in cancer. *Cancer metastasis reviews*, 28(1-2):35–49. (Cited on page 59.)

Paper I

Distinguishing drug-induced minor morphological changes from major cellular damage
via label-free impedimetric toxicity screening

Lab on a Chip

PAPER

Distinguishing drug-induced minor morphological changes from major cellular damage *via* label-free impedimetric toxicity screening†

Robert Meissner,* Bilge Eker, Harsha Kasi, Arnaud Bertsch and Philippe Renaud

We present a novel perfusion-based microfluidic platform for label-free drug toxicity screening which can single out non-lethal morphological changes from cellular death using electrical impedance spectroscopy. Minor cellular changes such as cell–cell contacts and major cell injury were identified *via* impedance phase angle analysis and follow-up of impedance magnitude at different frequencies. Having exposed HepG2/C3A cells to acetaminophen (AP), we showed that continuous drug perfusion caused a time and concentration-dependent impedance decrease. Moreover, perfusion of repeated doses revealed altered dielectric properties of the cell culture after recovery from AP exposure. This study highlights the possibility to sense cellular changes long before cellular death takes place, pointing out the remarkable sensitivity advantage of this technique over standard endpoint viability tests and its interest for toxicology.

1 Introduction

During the last decade, liver toxicity has been one of the most frequent reasons for pharmacovigilance safety reports and drug withdrawal from the market.[1–3] Around one million animals are used every year in Europe in toxicology tests causing ethical problems as well as enormous costs.[4] Moreover, in a large number of cases, animal studies cannot be used to perform human liver toxicity testing because of species differences[5] indicating that preclinical evaluation of new drugs is of high importance.[1] Issues related to the animal use in the safety evaluation of pharmaceuticals and chemicals have directed the researchers to investigate alternative testing methods.

Miniaturized bioanalytical tools fulfill many conditions required by modern diagnostics such as low consumption of reagents and analytes, reduced transport time, simultaneous and fast monitoring of multiple signals.[6] In addition, they allow very precise control of fluid flows creating new methods for tissue engineering.[7] The culture of hepatocytes in microsystems has been described previously. Microsystems have shown to offer more suitable environments than traditional cell culture flasks owing to the optimized perfusion flow,[8] shear stress protection,[9,10] 3D culture[11–13] and co-culture of parenchymal and non-parenchymal cells.[14] Nonetheless, most functional and morphological characterization of on chip hepatocyte cell cultures have been evaluated by biochemical analysis of the perfused cell-culture medium (albumin and ammonia production, glucose and glutamine consumption, CYP450 enzyme activity assays[9,10,14–16]). This results in substantial time costs as well as human and material resources evoking the demand for alternative, economical and automatized screening methods.

Cell-based impedance spectroscopy is a label-free and non-destructive method to measure dielectric properties of biological samples. Electric signals are convenient parameters for recording and processing compared to other techniques such as optical detection, *e.g.* no light source and detectors are required. Impedance screening has previously been employed to measure a wide range of cell culture dependent parameters such as cell growth and cell adhesion,[17–19] epithelial layer thickness,[20] fibroblast motion,[21] muscle cell contractility,[22] stem cell migration,[23] transient receptor channel activity[24] and cell viability.[25] Moreover, it has become a convenient tool to estimate toxicity kinetics.[26,27] In all these studies, the temporal evolution of a given cellular parameter was monitored by impedance measurements performed at one frequency only where the cellular contribution appeared maximal. Considering a single cell as a shell-covered sphere,[28,29] it is further necessary to distinguish cellular events within frequency ranges. At low frequency (LF), cells act as insulators due to the capacitive nature of the cell membrane. At high frequency (HF), the cell membrane capacitor is short-circuited and intracellular matter has an effect on the impedance. Hence, frequency dependent impedance screening offers plethora of information on intra- and extracellular properties.

Herein, we developed a microelectronics-based microfluidic perfusion system for hepatocyte culture and real-time monitoring of drug toxicity-induced effects. To our knowledge, this is the first study that investigates hepatocyte culture dependent changes as a function of impedance changes over a wide frequency range. We were able to distinguish between

Laboratoire de Microsystèmes LMIS4, Ecole Polytechnique Fédérale de Lausanne, Station 17, CH-1015 Lausanne, Switzerland. E-mail: robert. meissner@epfl.ch; Tel: +41 216936752

morphological changes and cell viability by studying the impedance with phase angle analysis and introducing a novel low frequency correction method based on bipolar (two-point) measurements. In order to study drug induced cytotoxicity, acetaminophen (AP), one of the widely used analgesic with a well-known severe hepatotoxicity, was perfused continuously and in repeated doses in our microfluidic system.

2 Materials and methods

2.1 Microfluidic chip design and fabrication

A microfluidic chip with filters inducing mechanical trapping and perfusion for cell culture was designed (Fig. 1). Hepatocytes are versatile cells having high energy demands. *In vivo*, hepatocytes are located close or in direct contact to the fenestrated sinusoid endothelium providing efficient nutrient and oxygen supply.[30] In our device, a low hepatocyte-perfusion distance was guaranteed by introducing four relatively thin filters (100×500 μm), separated by 50 μm gaps. The filters were defined by arrays of PDMS pillars (Ø 40 μm). The total channel height was 60 μm. Cell-filled filters cause high flow resistance, resulting in the perfusion medium to flow between the filters rather than through them. 5 μm spacing between neighboring micropillars allowed efficient diffusion and exchange of nutrients and waste. In addition, cells are not directly exposed to the main flow which potentially hinders cell proliferation.

The device fabrication was performed as described previously.[31] Briefly, a silicon wafer with oxidized surface (1 μm) was structured by photolithography and deep reactive ion etching. The obtained silicon master was then used to mold PDMS with a molding tool. The PDMS block is further placed on top of a glass slide with microfabricated electrodes.

2.2 Electrode design and fabrication

Electrodes are implemented in the device for impedance measurements of the hepatic cell population. We designed interdigitated electrodes (IDEs) so that the larger total electrode surface area contributes to higher measurement sensitivity. IDEs were adapted to the microfluidic four-filter configuration such that the sensing area is limited to the region where cells are trapped in filters (Fig. 2). Thus, each electrode trace carries four arms (each 20 μm wide) with nine fingers (10 μm wide, spaced
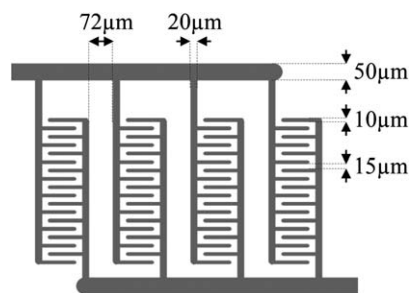
Fig. 2 Electrode design. A bipolar interdigitated electrode (IDE) pair has been adapted to the microfluidic four-filter configuration to maximize electrode surface coverage for high-sensitivity impedance measurement of the cell culture area. Total of 36 electrode fingers are provided for each electrode ($w = 10$ μm, $l = 100$ μm) separated by a gap of 15 μm.

15 μm apart). Electrode edges are rounded up to reduce fringing effects and local current concentration.[32] We used platinum as electrode material since it is biocompatible[33] and highly polarizable, thus minimizing faradaic currents and reducing the risk of generation of cytotoxic compounds.[34] A 20 nm thick titanium adhesion layer and a 200 nm thick platinum layer were evaporated in that order and structured on a 4 inch glass substrate using standard photolithographic lift-off technique.

2.3 Microfluidic cell culture and experimental setup

HepG2/C3A cells were cultured in a 75 cm² flask before loading them in the microfluidic chip. Cells were incubated in Dulbecco's Modified Eagle's Medium (DMEM) (Invitrogen, Switzerland), containing 10% fetal calf serum (Invitrogen, Switzerland), at 37 °C and 5% CO_2. Medium was changed every three days. Once cell confluency was reached, cells were detached with 0.25% trypsin/EDTA (Invitrogen, Switzerland) and used for microfluidic cell culture.

All materials were autoclaved before use except poly(methyl methacrylate) (PMMA) holders which were disinfected with 70% ethanol. The glass chip with electrodes and the PDMS chip were surface treated (50 W, 0.6 min, 0.6 bar) using oxygen plasma (Femto SLS, Diener electronic, Germany). Glass chip, printed circuit board, PDMS chip and PMMA holder were assembled and ∼20 000 cells in medium were injected in the inlet reservoir of the PDMS chip. Tubing was used to connect the PDMS chip to the medium reservoir. The device was placed into the CO_2-
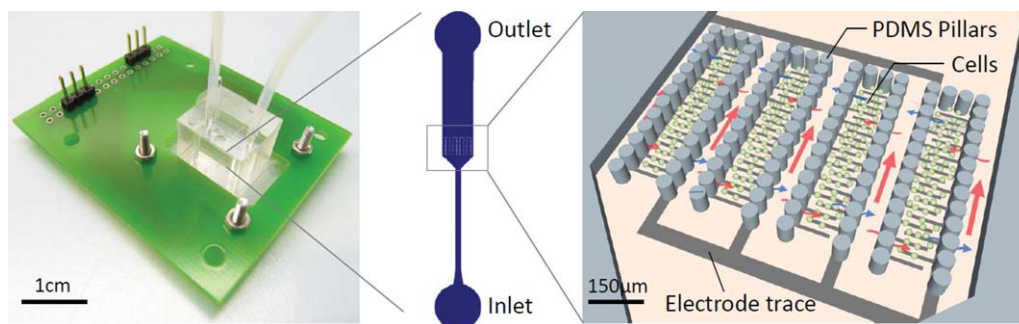
Fig. 1 Microfluidic device and electrical interface. (Left) Photograph of the printed circuit board with polydimethylsiloxane (PDMS) chip. (Middle) Design of the microfluidic channel. (Right) Schematic of cell culture area involving PDMS pillars for cell immobilization and flow stress protection. The main flow is passing between the filters (large red arrows), and efficient nutrient supply and waste removal are provided by gentle diffusion (curved red and blue arrows). Electrodes are implemented for impedance recording.

incubator on top of a microscope with a humidity-protected objective (Precise Eye, Navitar, USA) connected to a C-mount camera (uEye, IDS Imaging, Germany) and an optical light fiber attached to a light source. The tube from the outlet reservoir of the PDMS chip was then connected to a syringe pump (NE-300, TSE-Systems, USA). Coaxial cables were used to connect the device to an impedance analyzer (Agilent 4294A, Agilent technologies, USA). A small hole at the back of the incubator connects the inside equipment with the humidity sensitive outside equipment. The impedance analyzer was connected to a PC *via* a GPIB controller (Universal Serial Bus (USB)-GPIB-HS, National Instruments, USA).

Cell culture was performed in the microchip for 5 days in order to make sure the cells proliferated and were healthy inside the filters. The cell medium was perfused continuously during the cell culture at the flow rate of 10 nl s^{-1}. Acetaminophen (Sigma-Aldrich, Switzerland) was dissolved in cell medium and added to the perfusion medium at different concentrations (5, 10 and 20 mM). The treatment time was 48 h for continuous and 72 h for repeated dose perfusion. Impedance spectra were recorded every minute from 100 Hz to 4 MHz (10 mV amplitude, 0 mV bias) using Matlab software.[35] 10 mV was chosen since it results in an electric field of ~5 V cm^{-1} (data not shown) close to the electrode surface. This is three orders of magnitude lower than the membrane permeation limit of 1–4 kV cm^{-1} (for 1 μs to a few ms)[36] and can be considered as safe. Simultaneously, the objective inside the incubator allowed visual follow-up of the microfluidic culture.

2.4 Fluorescence microscopy

For immunocytochemical staining, cultures were fixed with 4% paraformaldehyde in phosphate buffered saline (PBS) (Invitrogen, Switzerland) for 20 min. After washing, cells were dried and stored at −20 °C until use. After thawing, HepG2/C3A cells were treated with 3% BSA/0.1% Triton X-100 (both Sigma-Aldrich, Switzerland) for 45 min. For tight junction staining, cells were first incubated with the primary antibody monoclonal rabbit-anti-occludin (1 : 200, Invitrogen, Switzerland) for 90 min and subsequently with the Cy-2 coupled secondary antibody (1 : 150, Dianova GmbH, Germany) for 2 h. For actin staining, cells were incubated with FITC coupled phalloidin (Sigma-Aldrich, Switzerland) for 2 h. Subsequently; samples were incubated with 0.1 μg ml^{-1} DAPI in PBS (Sigma-Aldrich, Switzerland) for 30 min. After repeated washing, cells were observed with a confocal laser scanning microscope (LSM 700 inverted, Zeiss, Germany). 3D Images were obtained from z-stack acquisition mode by using the 3D image processor Imaris (Switzerland).

For live/dead staining, cells were washed with PBS and incubated with staining solution of fluorescein diacetate and propidium iodide (1 : 1000, Sigma-Aldrich, Switzerland) for 10 min. Samples were examined with a fluorescence microscope (LSM 700 inverted, Zeiss, Germany).

2.5 Cell viability assay

3-(4,5-Dimethylthiazol-2-yl)-2,5-diphenyltetrazolium bromide (MTT) stock solution was prepared by dissolving 2.5 mg MTT

ml^{-1} in PBS without Ca Mg^{-1}. Cells were seeded into a 96-well plate and incubated for 2 days. Cell medium was removed and cells were incubated in 200 μl AP solution (20 mM) at different times (2 h, 6 h, 8 h, 24 h). After drug exposure, cytotoxicity was determined by removing the drug solution and adding 200 μl of fresh medium + 50 μl of MTT stock solution. Following 3 h incubation at 37 °C, MTT-DMEM medium solution was removed and 150 μl of DMSO was added. After shaking well for 30 min, absorbance was analyzed at 590 nm using a microplate reader.

2.6 Electrode-cell population model

The electrical properties of a cell can be described with an equivalent circuit made of a membrane capacitor C_m with a series intracellular resistance R_{intra} and a parallel extracellular resistance R_{extra}.[37] However, a cell population comprises many cells with different microenvironments implying a multitude of such equivalent circuits with different time constants.[38] Consequently, C_m is replaced by a constant phase element (eqn (1)) which attributes a resistive component to the observed cell population relaxation.[39]

$$CPE_{cells} = \frac{1}{\beta_{cells}(j\omega)^{\alpha_{cells}}} \qquad (1)$$

where β_{cells} is the CPE_{cells}-magnitude, α_{cells} the CPE_{cells}-exponent, ω the circular frequency and j the imaginary number. The electrode–electrolyte interface is represented by an electrode constant phase element CPE_{el}. It accounts for the non-ideal capacitive behavior due to surface roughness[40] and protein adsorption[41] on the metal surface. C_{par} is the parasitic capacitance between the electrodes. This model is presented in Fig. 3a and is shown to be in accordance with a typical measured impedance spectrum (Fig. 3b).

In this study we have utilized different analysis methods to evaluate recorded impedance data. Cell growth in the microchip was first plotted as a single frequency time scan at 100 kHz. We specifically chose 100 kHz since the maximum difference was obtained between the impedance profile in the presence of cell population and that in the absence of cells, thus providing highest sensitivity in the impedance measurements. In addition, drug toxicity effects were examined at low frequency (LF) and high frequency (HF). LF is defined as the frequency before membrane relaxation‡ takes place (high impedance of CPE_{cells}) and gives information about extracellular properties. Low frequency signals are generally affected by electrode–electrolyte interface contribution in the bipolar measurement method, resulting in higher impedance magnitudes as shown in Fig. 4. Although the absolute electrode-interface impedance Z_{CPE_el} value is considered constant at a specific frequency, its relative contribution to measured impedance magnitude $|Z|$ varies with

‡ Membrane relaxation terms the shortening of the membrane capacitor and thus its frequency dependency. With increasing frequency, polarization of charges and permittivity will decrease because the direction of the applied electric field varies more quickly than the displacement and accumulation of charges. Cell membrane is not a barrier to current anymore above membrane relaxation and information regarding heterogeneous structure and dielectric properties of cell interior can be obtained.

a)

b)
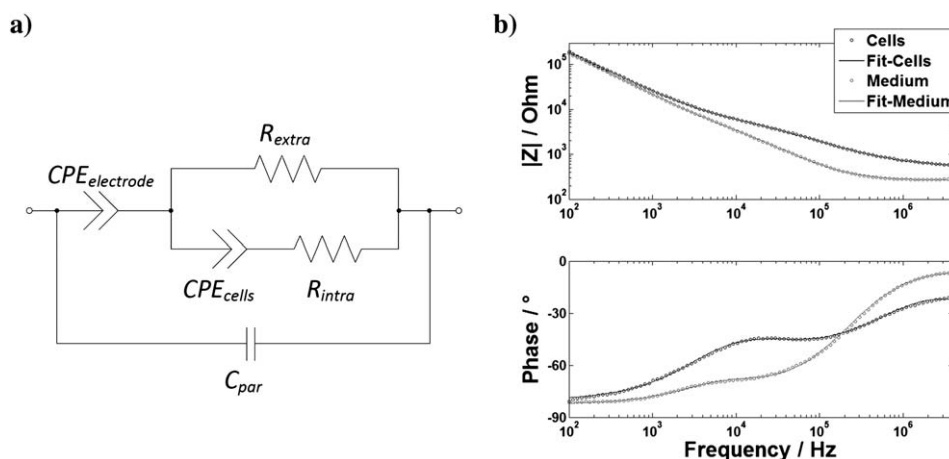
Fig. 3 Equivalent circuit modeling. (a) The cell population is represented by the Cole model with an extracellular resistance (R_{extra}) in parallel to the tissue constant phase element (CPE_{cells}) and a high frequency intracellular current pathway (R_{intra}). The electrode/electrolyte interface is modeled by a CPE (CPE_{el}). A parallel capacitance (C_{par}) characterizes parasitic current shunts at high frequency. (b) Impedance plot of a high density cell culture. The equivalent circuit was used to fit the plot. Chi-squared $= 1.9 \times 10^{-4}$, sum of squares $= 3.4 \times 10^{-2}$.
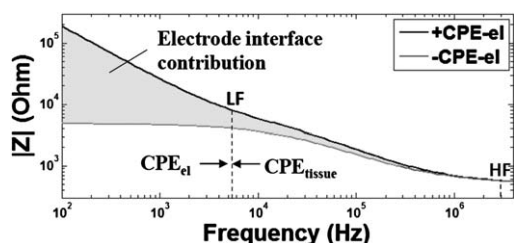
Fig. 4 Low frequency signal correction. Exemplary impedance magnitude–frequency spectrum for cell covered electrodes and simulated spectrum without CPE_{el}. The simulated curve was obtained through fitting of the experimental curve to the equivalent circuit (Fig. 3a) and redrawing without the CPE_{el}. The low frequency (LF) signal is influenced by the electrode capacitance, while the high frequency (HF) signal remains unaffected. The choice of a suitable frequency to screen extracellular events is a compromise between low CPE_{el}, low CPE_{cells} and high resolution.

changing R_{extra} (see Fig. S1 in the ESI† for detailed explanation). This leads to imprecision and misinterpretation of measurement results.

Here, we introduce a new electrode correction method for bipolar measurements. In this corrected method, we remove the electrode–electrolyte interface contribution from the measured impedance magnitude by subtraction. In order to determine Z_{CPE_el}, a control experiment was performed by monitoring the impedance in only cell medium without the cells for the whole experimental period (β_{el} was found to be $1.5 \times 10^{-8}\ \Omega^{\alpha-1}\ F^{\alpha}$ and 0.91 for α_{el}). The choice of LF depends mainly on two parameters. LF is ideally chosen very low to eliminate the influence of the cell membrane capacitance. However, Z_{CPE_el} dominates the measured impedance magnitude at very low frequencies, making the $|Z|$ relatively insensitive to cellular parameters, even after correction.

In our experiments, LF was chosen between ~1 kHz and ~30 kHz to mediate between these two factors. In order to achieve highest measurement sensitivity, 10 kHz was selected

since the corresponding phase angle variation with changing extracellular environment was nearly maximal while aiming less influence from the membrane capacitance (Fig. 6a and S2 in the ESI†). Meanwhile, the choice of HF is less tedious. HF is defined as the frequency where the membrane capacitor is short-circuited and provides information about the cell interior. At HF, electrode contributions are negligible as shown in Fig. 4 and C_{par} can be ignored since the measured phase angle is close to $0°$ and reveals an almost purely resistive behavior. Thus, we have chosen HF as 3 MHz.

2.7 Statistical analysis

Impedance magnitude values and absorbance at 590 nm (MTT viability assay) at different time points after AP addition were expressed as means with 95% confidence interval. Statistical analysis of each time point was performed compared to the initial value at 0 h using two-way ANOVA and Bonferroni post-test. The observed importance level (p-value) of the difference between two means was considered significant when $p < 0.05$, very significant when $p < 0.01$ and extremely significant when $p < 0.001$.

3 Results

3.1 An artificial sinusoid-like hepatocyte culture

The goal of this study was to develop a microfluidic biosensing platform on which the culture and toxicity screening of HepG2/C3A cells can be performed. The first step involved immobilizing the cells within the four filters as shown in Fig. 5a and c. Cells, injected in the microfluidic device, get trapped within the micropillar array with some cells escaping through the gaps between the filters. It was observed that the amount of cells finally immobilized strongly depends on the flow rate during cell loading. Flow rates in the range of 20 nl s^{-1} were the most suitable for an efficient cell loading, resulting in a trapping of up to 90% of the injected cells in the filter.
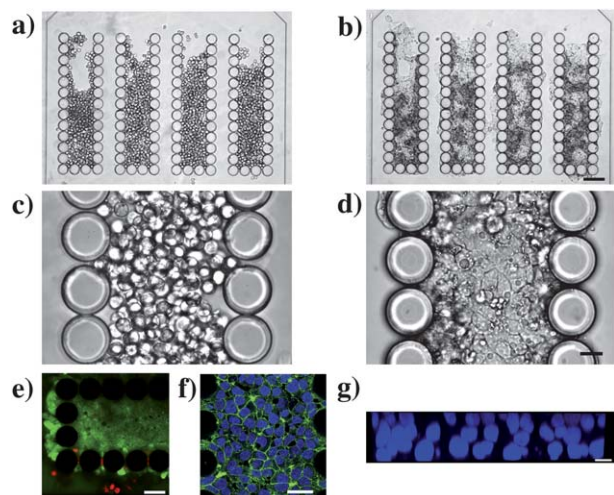
Fig. 5 Imaging of cell culture within the microfluidic device. (a) and (c) show nearly full filters after cell loading. (b) and (d) show cells after 3 days of culture. The high density culture is characterized by direct cell–cell contact (arrow 2) and multiple cell layers (arrows 1 and 3) (bar = 80 μm at the top and 20 μm at the bottom). (e) Viability of cells within filters is shown in green and some cells in perfusion regions undergo cell death (red) (green: fluorescein diacetate, red: propidium iodide). (f) Immuno-cytochemical staining of occludin indicates the presence of cellular tight junctions (bar = 40 μm, green = Cy-2). (g) Three cell layers are identified in the z direction (blue: DAPI) (bar = 10 μm).

Cell culture in the microchip was performed for 5 days. Cells attached to the surfaces and to each other during this period (Fig. 5b). This high cell density culture was characterized by close cell–cell contacts (Fig. 5d and f) and multiple cell layers in the z-direction (Fig. 5b, dark regions). A confocal image showing the xz-plane in Fig. 5g revealed the presence of three cell layers stacked on top of each other, indicating a 3D cell culture. In addition, as shown in Fig. 5e, despite high cell density, cell viability was maintained within the filters with some dead cells in the perfusion region only.

3.2 Impedimetric characterization of cell growth

We examined the hepatic cell population with impedance spectroscopy during the entire cell culture. The impedance spectra as a function of cell culture time are shown in Fig. 6a. We observed an increase of |Z| within a frequency range from 5 kHz to 3 MHz. Lower frequencies (<5 kHz) are not affected by the growing cell population. The phase angle increased within a frequency window of 1 kHz to 100 kHz and decreased at HF.

Phase angles obtained at 3 MHz are much closer to 0° compared to those at lower frequencies, indicating more resistive characteristics at higher frequencies. The largest difference between the impedance profile in the presence of cells and that without the cells was observed at 100 kHz. Fig. 6b shows |Z| at 100 kHz, and the cell growth profile measured by the impedance was confirmed with the cell growth observed under the microscope (see Fig. S3 in the ESI†). A typical growth curve with initial lag phase and exponential growth was obtained by the impedance measurement as seen in Fig. 6b. The stationary phase was reached at the end of seven days once the electrode area was
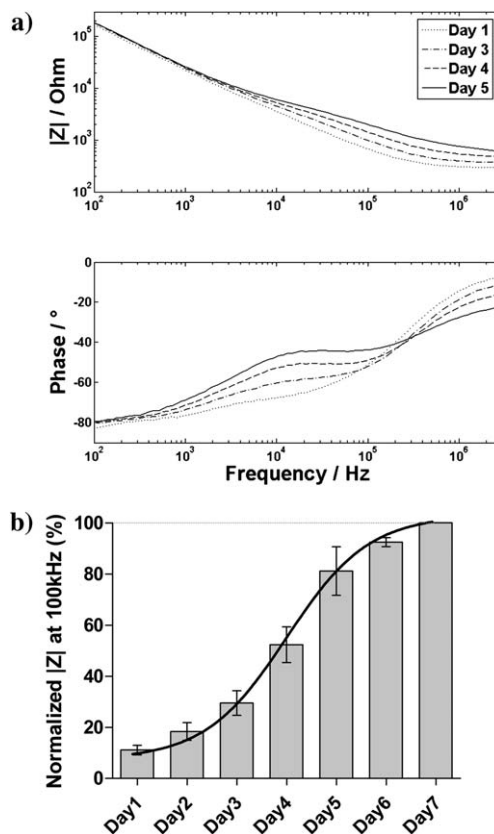
Fig. 6 Impedimetric characterization of cell growth. (a) Bode plot of spectra recorded on different days of culture. (b) Normalized impedance magnitude at 100 kHz for 7 days of culture (n = 5). We normalized each value to their final (day 7) value. The solid line presents a fit of the data.

fully covered with cells. Hence, we have shown that impedance changes due to the cell growth are strongly frequency-dependent.

3.3 Label-free monitoring of AP-induced toxicity

We studied the effect of AP on the microscale culture using impedance spectroscopy. In order to analyze AP toxicity-induced effects, we examined the LF and HF signals separately. The LF signal provides information about extracellular properties whereas HF signal reflects intracellular characteristics. The phase angle indicates if the system behaves like a resistor (→ 0°) or a capacitor (→ −90°). As already shown in Fig. 6a, a LF phase angle of −40° (10 kHz) at high cell density indicated both resistive and capacitive effects. To reliably analyze cell dependent extracellular changes and their kinetics, all impedance analyses involve correction of |Z| values by subtracting the electrode interface effect from measured impedance magnitudes at 10 kHz (see Fig. S1 in the ESI† for detailed information). Such correction provides the approximation of experimental values to the ideal linear profile of a simple resistance circuit and permits to eliminate the effect of the electrode-interface capacitance.

We performed AP treatment with different concentrations under continuous perfusion exposure. Fig. 7a shows impedance magnitude changes at 10 kHz and 3 MHz for different time points. The long-term impedance magnitude is similar for measurements at 10 kHz and 3 MHz, but its evolution has
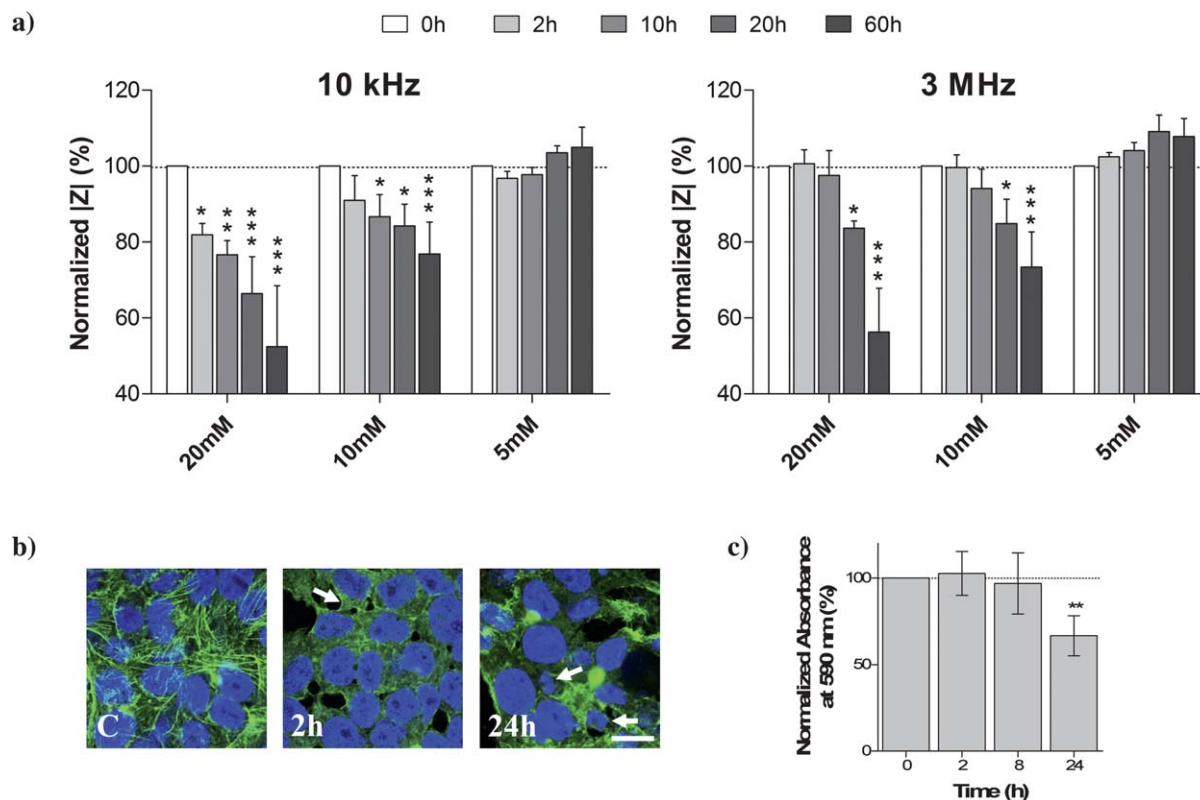
Fig. 7 Effect of AP treatment. (a) Normalized impedance in the microchip as a function of AP concentration under different drug treatment times. We normalized each value to their initial (0 h) value. Impedance magnitude changes (mean ± 95% CI) at 10 kHz and 3 MHz after application of three different concentrations (5 mM, 10 mM, 20 mM) are shown. Kinetics of the decrease in |Z| was found to be frequency-dependent. (b) Cytoskeletal changes after AP exposure. Immunocytochemical staining of actin cytoskeleton revealed structural changes as early as 2 h after 20 mM AP treatment. C: actin forms a fiber-like network in the untreated sample. 2 h: actin is less organized and dispersed throughout the cytoplasm and displays slightly higher fluorescence intensity at the cell periphery (arrow). 24 h: actin is heterogeneously dispersed in the cell. Apoptosis is observed as indicated by arrows (bar = 10 μm, green = Cy-2, blue = DAPI). (c) MTT viability assay. % cell viability *vs.* time. Mean ± 95% CI of absorbance at 590 nm is shown. Statistical analysis of each time point in (a) and (c) was performed compared to the initial value at 0 h ($n = 4$; *$p < 0.05$, **$p < 0.01$, ***$p < 0.001$).

different profiles for both frequencies. LF signal drops as early as 2 h of drug exposure, whereas the HF signal does not change significantly. For AP concentrations above 5 mM, longer exposure results in lower impedance magnitude. Furthermore, increasing concentrations of AP lead to a larger change in impedance magnitude for treatments of similar durations. The impedance magnitude for an exposure of the cells to a 5 mM AP concentration follows a different evolution than that for higher concentrations and actually increases with exposure time.

In order to make sure that the impedance magnitude changes originate from the AP-induced cellular changes and not from the presence of AP in the cell medium itself, we have recorded the spectra of cell medium with and without AP in the absence of cells as a control experiment. We observed an impedance change of only 10 Ω after AP addition (see Fig. S4 in the ESI†). Such small resistance changes can be neglected when the observed variation in the impedance is more than 1000 Ω in the presence of cells.

Immunocytochemical staining of actin was performed on cultured cells exposed to a 20 mM concentration and revealed structural changes as early as 2 h after AP treatment as shown in Fig. 7b. Non-treated cells exhibit a fiberlike network of actin filaments, providing attachment between cells and the substrate

and also neighboring cells. This organizational structure disappeared after 2 h of AP exposure. Instead, an even distribution of actin was observed in the cells with a slightly higher presence at the cell periphery (Fig. 7b, 2 h arrow). Cells that were treated for 24 h showed heterogeneous dispersion of actin. Also, nuclear fragmentation indicated apoptosis in some cells (Fig. 7b, 24 h arrows). The cell viability, on the other hand, decreased significantly after 24 h, and no cell death was observed up to 8 h as shown in Fig. 7c.

We examined the ability of HepG2/C3A cells to recover from AP induced cell injury. Five days after the cells were seeded in the microfluidic device, 10 mM AP was perfused for 3 h. The cell culture was then washed with clean medium for 21 h. A second AP perfusion was performed for 24 h before perfusing the cells again with fresh medium. Fig. 8a shows the normalized impedance magnitude *vs.* time at 10 kHz and 3 MHz. During the first AP treatment, $|Z|_{10 \text{ kHz}}$ dropped by 13% whereas $|Z|_{3 \text{ MHz}}$ remained constant. After flushing with fresh medium, we observed complete recovery of the 10 kHz signal and no change was observed at 3 MHz. During the second AP treatment, the LF signal dropped sharply by 20% within 3.5 h, followed by a slower decrease around 21% in the next 21.5 h. At HF, the signal decreased only 20% in 24 h. When the AP was rinsed away with
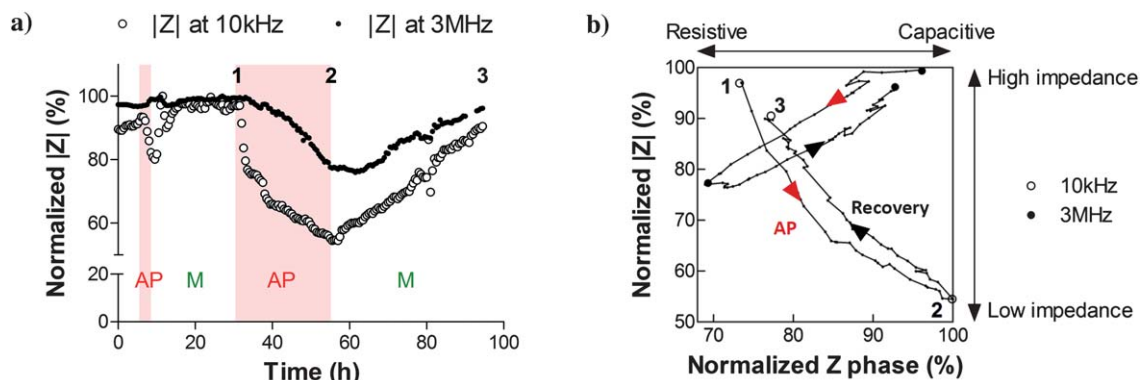
Fig. 8 Perfusion of repeated AP doses. (a) Temporal evolution of $|Z|_{10\ kHz}$ and $|Z|_{3\ MHz}$ shows different decay profiles with time after AP exposure as well as signal recovery once perfused with clean medium (b) $|Z|$ is plotted *vs.* phase angle. A more capacitive response at both LF and HF is observed during recovery.

cell medium one more time, $|Z|_{10\ kHz}$ increased again and almost full recovery was obtained after 40 h. The full recovery of $|Z|_{3\ MHz}$ was also obtained after showing no change for around 8 h in the impedance when the drug was removed from cells. The relative change of phase angle during the AP exposure and cell recovery with impedance magnitude is shown in Fig. 8b. The signal at 10 kHz measured during the cell recovery is more capacitive than that before AP treatment. The same applies to the HF signal, having a more capacitive signal than that before drug inducement. In conclusion, 10 mM treatment of HepG2/C3A cells results in frequency-dependent impedance changes and kinetics. LF and HF signals both show that the recovery signal is inherently more capacitive after AP exposure.

4 Discussion

In the current study, we have shown that impedance spectroscopy is a useful non-end point technique that distinguishes between extracellular phenomena and cell viability. We demonstrated that our microfluidic device is a suitable environment for HepG2/C3A cell growth. The possibility to perform impedance spectroscopy on-chip is an easy and fast screening technique of cell growth and concentration-dependent drug induced changes on the intracellular and extracellular environment. We further demonstrated that cell recovery can be monitored when cells are treated with doses of AP. Moreover, we have shown that non-drug treated and recovered cell populations possess different dielectric properties (Fig. 8b).

4.1 The microfluidic perfusion culture

We designed a microfluidic device in which cell culture can be performed with continuous perfusion of medium and without shear stress applied on the cells because of the implemented filter design. Our experiments showed higher cell viability and cell growth inside the filters than that of outside potentially owing to the protection of cells from the effect of shear stress caused by the direct flow. In addition, sterile conditions can easily be maintained when using a perfusion system (non-loop) and a PDMS microbioreactor. This reduces the need for the use of antibiotics that have potential long term effects on cells.[42] Our microfluidic cell culture showed very high cell density in the filters with

a maximum distance of 50 μm for diffusion of nutrients as determined by the filter width. These specifications meet *in vivo* conditions since extracellular matrix constitutes a small portion of the normal liver (around 3%)[43] and tight junctions are important for firm cellular attachment permitting cell-to-cell signaling across communication junctions.[30] Although the presented cell culture may not be considered as 3D (due to the absence of extracellular matrix), formation of multi-layer stack of cells is still important[44] since most of the cell surface is in direct contact with adjacent cells. This is not true for standard cell culture in 2D Petri dish, where cells are cultured on a hard surface and with abundant amount of cell medium. Based on cell growth and high cell viability, we consider our device and culture conditions to be effective for drug cytotoxicity studies, although a complete biochemical analysis (quantification of albumin and CYP450 activity[9,14]) was not our focus and hence was not conducted in the framework of this study.

4.2 Impedimetric characterization of the hepatic cell population

We investigated dielectric properties of HepG2/C3A cells with our system. Although the maximum cellular contribution to the impedance magnitude was observed at around ~100 kHz, the phase angle did not change at this frequency but varied significantly at ~10 kHz and ~3 MHz. On the one hand, this difference originates in the impedance being dominated by the electrode impedance at LF, thus making the LF impedance magnitude less sensitive to the presence of cells. On the other hand, the extracellular resistance is shorted by the cell membrane capacitor above 10 kHz as indicated by the phase angle. Hence, if one wants to measure predominantly extracellular events, 10 kHz appears to be the most sensitive frequency (phase angle is most resistive before membrane relaxation). At ~100 kHz phase angles are constant during the cell culture due to the balance between an increasing extracellular resistance and membrane capacitance. Moreover, intracellular properties can be investigated at HF as mentioned earlier. The impedance at HF increases with the increasing number of cells because intracellular matter is less conductive than the surrounding medium.[29] Nevertheless, the corresponding phase angle decreases due to the increasing tissue capacitance that was observed up to 3 MHz (Fig. 6a).

Thus, our experiments provide information about extracellular, intracellular and cell membrane properties. Such cell specific characteristics can only be distinguished with the interpretation of the impedance spectra with corresponding phase angle profile, thus making phase angle analysis an indispensable tool for understanding cellular phenomena.

The phase-component of the impedance has a typical angle of $\sim-45°$ at 10 kHz and of $\sim-15°$ at 3 MHz. This indicates stronger capacitive behavior of the cell population at LF, originating from the electrode and the tissue capacitance. We introduced a new correction method to eliminate the effect of the electrode–electrolyte interface and to offer the possibility to theoretically counteract the inherent drawback of bipolar measurement. This technique assumes that electrode characteristics do not change throughout the whole experiment time. Practical alternatives to eliminate the electrode interface contribution are multipolar measurements such as tetrapolar configuration.[23] However, these techniques have a limited practical bandwidth, at least when using microelectrodes, as described previously.[23] On the contrary, it is currently not possible to apply such a correction method for tissue capacitance since it changes with the tissue resistance.

4.3 Impedimetrical detection of AP-induced cellular changes

We observed that impedance changes after AP treatment were time and dose-dependent. Significant changes on the impedance spectra after 2 h at 10 kHz confirm that impedance screening is a very sensitive method. Continuous monitoring up to 60 h revealed the high potential to obtain real-time information. When comparing low and high frequency measurements, we found that $|Z|_{3\ MHz}$ decreases later than $|Z|_{10\ kHz}$. This shows that different information can be obtained when investigating different frequency ranges as presented in Fig. 9. At LF, cell membranes act as capacitors and block the current flow through the cells. Protein channels embedded in the cell membrane are negligible as their resistance is in the $M\Omega$ range.[45] This leads to a high extracellular resistance, considering a densely packed insulating cell layer. If cell–substrate and cell–cell contacts are loosened and cells start to retract, current shunts through the intercellular space which results in an abrupt resistance drop (due to the inverse quadratic relationship between R_{extra} and intercellular distance). This phenomenon explains the signal decrease at LF. Such rapid impedance decrease is correlated with cytoskeletal actin and subsequent morphological changes after AP exposure (Fig. 7b). In cell culture on stiff substrates and dense cell–cell contacts, the actin cytoskeleton tends to organize in stress fibers.[46] AP treatment disrupts such fiberlike organization by mechanisms involving glutathione depletion, oxidative stress and mitochondrial dysfunction.[47] This leads to cell–substrate and cell–cell detachment as described in former studies where cytoplasmic retraction and cell lifting have been observed.[48] Previous studies also indicated that AP mediated metabolism can cause the deactivation of the Rho protein which in turn is responsible for the formation of actin stress fibers.[49] In long-term drug exposure, cells start dying either through apoptosis or necrosis[50,51] which again leads to signal decrease. This is consistent with the changes observed in the cell morphology inside the microchip such as cell retraction and increase in the intercellular space after 2 h and cell
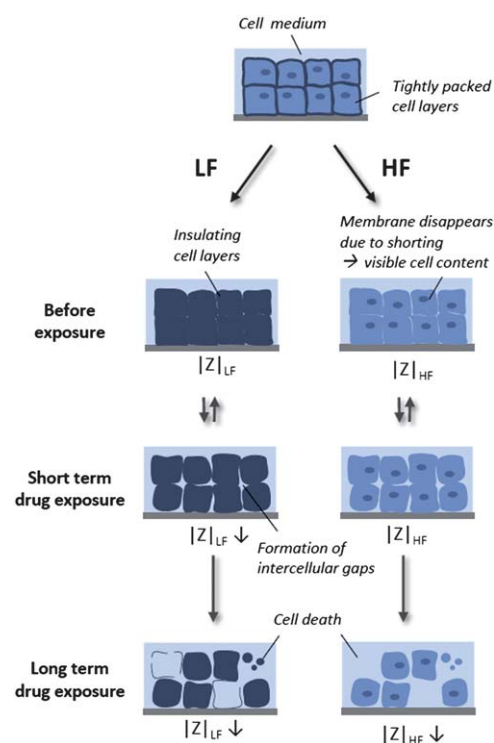
Fig. 9 Hypothesized correlation between frequency-dependent impedance changes and cell culture morphology. After short term drug exposure, cell–cell contacts are loosened and the formation of intercellular gaps causes current shunting at low frequency (LF), but no significant impedance change at high frequency (HF) due to their low volume fraction. Low conductivity cytosol (high volume fraction) is eliminated through continuous perfusion following cell death after long term drug exposure. This leads to decrease in the impedance at HF.

death after 24 h AP exposure as seen in Fig. S5b and c in the ESI†. On the other hand, at HF, the membrane capacitor is considered shorted and both extracellular and intracellular matter contribute to the measured impedance. Intercellular gaps formed after AP exposure barely contribute to the decrease in HF impedance due to their low volume fraction compared to the large intracellular volume at high cell density. When cells start dying, ion pumps embedded in the membrane cease functioning and small pores are formed during cell death, leading to exchange of intra- and extracellular matter. Considering continuous perfusion of the cell sample, cell cytosol is replaced by fresh medium, which has two to three times higher conductivity than the cytosol.[29] Our results on HF kinetics indicate that the conductivity change in such large volume contributes to the impedance decrease. Indeed, the measured HF values in Fig. 7a follow the same trend as the profile obtained in the MTT viability test (Fig. 7c) and other reported conventional viability data on HepG2 cells.[52,53] The present data strongly suggest that, in combination with very high cell density and continuous perfusion flow, HF measurements report serious cell injury, while LF measurements inform about intercellular and morphological phenomena.

Furthermore, we measured that $|Z|_{10\ kHz}$ was higher at 20 h and 60 h than initially when 5 mM AP was applied. This is due to the continuously growing liver carcinoma cell line used in our experiments. Cell growth is disrupted after AP exposure, and cell

cycle reentry occurred after a certain 'adaptation time'. 5 mM AP concentration was too low to cause serious HepG2 cell population damage within 60 h.

The perfusion of repeated AP doses revealed the ability of HepG2 cells to recover from drug-induced cell injury. The signal recovery was obtained within 5 h as seen in Fig. 8a after 3 h exposure to 10 mM AP solution and flushing with medium stimulated the reestablishment of cell–cell and cell–substrate contacts. Longer AP treatment caused major cell injury, indicated by the HF signal. During the following medium perfusion, cells reattach to each other and to the substrate, characterized by constant HF- and increasing LF signal. Subsequently, cell proliferation starts and reestablishes an impedance value of 90% after 40 h of medium perfusion, showing an increase in both high and low frequency magnitudes. Even though, impedance values were regained, we showed that the recovered cell population showed a more capacitive behavior compared to non-treated cells, which could be attributed to remaining cell membrane blebbing, membrane asymmetry and cell debris from apoptotic and necrotic events. These results indicate the advantage of electrical characterization over standard end-point assays when using doses that are sublethal but still cause toxic effects.

Conclusions

In conclusion, we have developed a microfluidic-based sensing platform for hepatocyte culture using dielectric screening. It enables direct, continuous, label-free and non-invasive measurements of cell dependent parameters. We demonstrated that phase angle analysis is an indispensable tool to understand cellular phenomena when impedance spectroscopy is used. We were able to distinguish between morphological changes and severe cell injury within a cell population owing to the combination of high-density culture, perfusion flow and whole impedance-frequency spectrum analysis. More importantly, cellular changes can be sensed long before cellular death, offering a very high sensitive technique over standard expensive and time consuming viability assays. Future improvements of the technique will include on-chip controls, real-time normalization and the use of multiple assays run in parallel to increase the statistical strength. Therefore, the use of an electrode switch might be considered for high-throughput cytotoxicity screening that can meet the needs of pharmaceutical industry more closely.

Therefore, as a novel demonstration of drug induced cytotoxicity screening with impedance spectroscopy within a wide frequency range, this study offers a highly sensitive detection platform for cellular behavior during cell culture and drug exposure. From this point of view, this cell-based impedimetric sensing system inside microfluidic filters opens new avenues to develop new classes of detection devices for cellular phenomena upon toxicant intake. Real-time imaging and continuous monitoring of cell dependent changes using microfluidics combined with the detection of cellular events using phase angle and impedance analysis allow developing new designs of microscale cytotoxicity-based sensing systems for different cell types under various physiological conditions. Overall, this system exemplifies the significance of microfluidics and cell dielectric properties to create a miniaturized detection device for cell toxicology studies.

Acknowledgements

Notes and references

1 *Non-Clinical Guideline on Drug-Induced Hepatotoxicity*, European Medecines Agency, 2008.
2 K. E. Lasser, *JAMA, J. Am. Med. Assoc.*, 2002, **287**, 2215–2220.
3 R. J. Temple, *JAMA, J. Am. Med. Assoc.*, 2002, **287**, 2273–2275.
4 A. Abbott, *Nature*, 2005, **438**, 144–146.
5 H. Olson, G. Betton, D. Robinson, K. Thomas, A. Monro, G. Kolaja, P. Lilly, J. Sanders, G. Sipes, W. Bracken, M. Dorato, V. D. Koen, P. Smith, B. Berger and A. Heller, *Regul. Toxicol. Pharmacol.*, 2000, **32**, 56–67.
6 S. J. Maerkl, *Integrative Biology: Quantitative Biosciences from Nano to Macro*, 2009, vol. 1, pp. 19–29.
7 L. G. Griffith and M. A. Swartz, *Nat. Rev. Mol. Cell Biol.*, 2006, **7**, 211–224.
8 E. Leclerc, *Biochem. Eng. J.*, 2004, **20**, 143–148.
9 L. Xia, S. Ng, R. Han, X. Tuo, G. Xiao, H. L. Leo, T. Cheng and H. Yu, *Biomaterials*, 2009, **30**, 5927–5936.
10 C. Zhang, Z. Zhao, N. Aida, D. van Noort and H. Yu, *Lab Chip*, 2009, **9**, 3185–3192.
11 F. Pampaloni, E. G. Reynaud and E. H. K. Stelzer, *Nat. Rev. Mol. Cell Biol.*, 2007, **8**, 839–845.
12 F. Pampaloni, E. H. K. Stelzer and A. Masotti, *Recent Pat. Biotechnol.*, 2009, **3**, 103–117.
13 J. H. Sung, C. Kam and M. L. Shuler, *Lab Chip*, 2010, **10**, 446–455.
14 S. R. Khetani and S. N. Bhatia, *Nat. Biotechnol.*, 2008, **26**, 120–126.
15 R. Baudoin, PhD thesis, Université de Technologie de Compiègne (UTC), 2008.
16 Y.-C. Toh, C. Zhang, J. Zhang, Y. M. Khong, S. Chang, V. D. Samper, D. van Noort, D. W. Hutmacher and H. Yu, *Lab Chip*, 2007, **7**, 302–309.
17 P. Mitra, C. R. Keese and I. Giaever, *BioTechniques*, 1991, **11**, 504–510.
18 J. Wegener, C. R. Keese and I. Giaever, *Exp. Cell Res.*, 2000, **259**, 158–166.
19 S.-P. Lin, T. R. Kyriakides and J.-J. J. Chen, *Biomaterials*, 2009, **30**, 3110–3117.
20 P. Linderholm, J. Vannod, Y. Barrandon and P. Renaud, *Biosens. Bioelectron.*, 2007, **22**, 789–796.
21 I. Giaever and C. R. Keese, *Proc. Natl. Acad. Sci. U. S. A.*, 1991, **88**, 7896–7900.
22 S. Haas, H.-G. Jahnke, M. Glass, R. Azendorf, S. Schmidt and A. A. Robitzki, *Lab Chip*, 2010, **10**, 2965–2971.
23 P. Linderholm, T. Braschler, J. Vannod, Y. Barrandon, M. Brouard and P. Renaud, *Lab Chip*, 2006, **6**, 1155–1162.
24 O. Pänke, W. Weigel, S. Schmidt, A. Steude and A. A. Robitzki, *Biosens. Bioelectron.*, 2011, **26**, 2376–2382.
25 G. Mernier, W. Hasenkamp, N. Piacentini and P. Renaud, *Sens. Actuators, B*, 2010, DOI: 10.1016/j.snb.2010.10.050, in press.
26 H.-G. Jahnke, A. Rothermel, I. Sternberger, T. G. A. Mack, R. G. Kurz, O. Pänke, F. Striggow and A. A. Robitzki, *Lab Chip*, 2009, **9**, 1422–1428.
27 D. Krinke, H.-G. Jahnke, T. G. A. Mack, A. Hirche, F. Striggow and A. A. Robitzki, *Biosens. Bioelectron.*, 2010, **26**, 162–168.
28 H. Pauly and H. P. Schwan, *Z. Naturforsch., B: Anorg. Chem., Org. Chem., Biochem., Biophys., Biol.*, 1959, **14B**, 125–131.
29 S. Gawad, PhD thesis (no 3011), Ecole Polytechnique Fédérale de Lausanne (EPFL), 2004.
30 P. North-Lewis, *Drugs Liver*, 2008, 12.
31 A. Kunze, M. Giugliano, A. Valero and P. Renaud, *Biomaterials*, 2010, **32**, 2088–2098.

32 H. Kasi, R. Meissner, A. Babalian, H. van Lintel, A. Bertsch and P. Renaud, *Journal of Electrical Bioimpedance*, 2011, **1**, 84.

33 Y. Itakura, T. Tajima, S. Ohoke, J. Matsuzawa, H. Sudo and S. Yamamoto, *Biomaterials*, 1989, **10**, 489–493.

34 P. Linderholm, PhD thesis (no 3604), Ecole Polytechnique Fédérale de Lausanne (EPFL), 2006.

35 A. Mercanzini, P. Colin, J.-C. Bensadoun, A. Bertsch and P. Renaud, *IEEE Trans. Biomed. Eng.*, 2009, **56**, 1909–1918.

36 H. Isambert, *Phys. Rev. Lett.*, 1998, **80**, 3404–3407.

37 P. J. W. Debye, *Polar Molecules*, Dover New York, 1929.

38 H. P. Schwan, *IEEE Trans. Electr. Insul.*, 1985, **EI-20**, 913–922.

39 K. S. Cole and R. H. Cole, *Dispersion and Absorption in Dielectrics I. Alternating Current Characteristics*, 1941.

40 R. DeLevie, *Electrochim. Acta*, 1965, **10**, 113–130.

41 T. Stieglitz, *Neuroprosthetics: Theory and Practice*, 2004, pp. 475–516.

42 S. Schmitz, *Der Experimentator: Zellkultur*, 2007.

43 P. Bedossa and V. Paradis, *J. Pathol.*, 2003, **200**, 504–515.

44 T. Tokiwa and M. Kodama, *In vitro* cellular & developmental biology, *Animal*, 1997, **33**, 150–151.

45 G. B. Ermentrout, *Electrical Properties of a Membrane*, http://www.cnbc.cmu.edu/~bard/passive2/node5.html, accessed 2010.

46 A. Besser and U. S. Schwarz, *New J. Phys.*, 2007, **9**, 425.

47 K. Kon, K. Ikejima, K. Okumura, T. Aoyama, K. Arai, Y. Takei, J. J. Lemasters and N. Sato, *J. Gastroenterol. Hepatol.*, 2007, **22** (Suppl. 1), S49–S52.

48 R. H. Pierce, C. C. Franklin, J. S. Campbell, R. P. Tonge, W. Chen, N. Fausto, S. D. Nelson and S. A. Bruschi, *Biochem. Pharmacol.*, 2002, **64**, 413–424.

49 L. M. McHardy, K. Warabi, R. J. Andersen, C. D. Roskelley and M. Roberge, *Mol. Cancer Ther.*, 2005, **4**, 772–778.

50 H. El-Hassan, *Toxicol. Appl. Pharmacol.*, 2003, **191**, 118–129.

51 A. H. Boulares and T. Ren, *Basic Clin. Pharmacol. Toxicol.*, 2004, **94**, 19–29.

52 I. Manov, Y. Bashenko, M. Hirsh and T. C. Iancu, *Basic Clin. Pharmacol. Toxicol.*, 2006, **99**, 213–224.

53 N. H. Shear, I. M. Malkiewicz, D. Klein, G. Koren, S. Randor and M. G. Neuman, *Skin Pharmacol. Appl. Skin Physiol.*, 1995, **8**, 279–291.

154

Paper II

Co-pathological connected primary neurons in a microfluidic device for Alzheimer studies

Kunze, A., Meissner, R., S. Brando, and P. Renaud, Bertsch, A., Renaud, P. (2011),
Biotechnology and Bioengineering, 108(9), 2241-2245

Co-Pathological Connected Primary Neurons in a Microfluidic Device for Alzheimer Studies

Anja Kunze, Robert Meissner, Serena Brando, Philippe Renaud

Laboratoire de Microsystèmes LMIS4, Ecole Polytechnique Fédérale de Lausanne, Station 17, CH-1015 Lausanne, Switzerland; telephone: +41-216936839; fax: +41-216935950; e-mail: anja.kunze@epfl.ch

ABSTRACT: This communication presents a novel experimental model for Alzheimer studies, where connected primary neurons were set into subtend, co-pathological states. Cortical neurons were cultured in two separated cell compartments in a microfluidic device. A neurite network was generated in a main channel through the neurite outgrowth from both cell compartments. A gradient of okadaic acid (OA) is generated over this neurite network by perfusion. OA is a phosphatase inhibitor that induces hyperphosphorylation of Tau proteins, a major hallmark in Alzheimer disease. The local OA treatment resulted in a connected "diseased" and "healthy" cell population. Anti-phosphorylated tau (Ser262) staining confirmed different states of phosphorylated Tau proteins, and synapthophysin staining the connection of "healthy" and "diseased" cells. Here, we present a novel in vitro model that opens the possibility to study cellular and molecular propagation mechanisms in neurodegeneration, in Tauopathies (as e.g., in Alzheimer), as well as simultaneous drug effects on connected healthy and diseased cell populations.

Biotechnol. Bioeng. 2011;108: 2241–2245.

© 2011 Wiley Periodicals, Inc.

KEYWORDS: primary neural cell culture; co-pathology; hyperphosphorylated Tau; microfluidic device; chemical gradient; okadaic acid

Alzheimer's disease (AD) is the most common cause of dementia and affects more than 35.6 million people worldwide representing over US $604 billion in 2010 (Wimo and Prince, 2010). The disease starts from a very precise brain area, the limbic system, and spreads out in distinct brain regions, indicating the contribution of neural networks in disease propagation (Delacourte, 2008; Savioz et al., 2009). While most Alzheimer studies are focused on biochemical mechanisms (Brandt et al., 2005; Small, 2008),

interactions between neurons have been shown to be important as well (Horn et al., 1996; Palop et al., 2006; Pariente et al., 2005). In vivo, however, studies of interactions between co-localized Alzheimer affected and non-affected neurons are very difficult to reproduce, and also, traditional in vitro techniques are limited so far. Microfluidic devices have come up in the last 5 years to enhance neuronal cultures, where cell placement can be locally controlled and neurites guided along microchannels (Millet et al., 2010; Pearce and Williams, 2006; Taylor and Jeon, 2010; Wang et al., 2009). Also, perfusion of neurites has been used to change transport mechanism in the axon to the soma (Taylor et al., 2010). All these examples have in common that they study cell effects on one homogeneous cell population, only. But to study interactions between healthy and diseased neuronal cells, two-cell populations have to be connected to each other by generating an active neurite network.

Here, we present a novel experimental model to generate two distinct co-pathological states within two separated primary cortical cell compartments that are connected through a neurite network. A special chosen microfluidic design (Fig. 1a), adapted from literature (Shamloo and Heilshorn, 2010), guarantees the local pattern of primary cortical neurons as well as their connectivity and communication through a neuronal network after cell culture. The cell metabolism of one compartment can be changed locally. Okadaic acid (OA), a protein phosphatase 2A (PP2A) inhibitor (Fig. 1c), was perfused over one-cell culture compartment, as shown in Figure 1b. The OA results in protein hyperphosphorylation, namely Tau proteins, which are known to be a major hallmark of AD (Arias et al., 1993; Krinke et al., 2010; Wang et al., 2001; Zhang and Simpkins, 2010). Local inhibition of dephosphorylation generates an imbalance of the Tau phosphorylation states between the two connected cell populations. We called the controlled generation of two different phosphorylation states between connected neuronal cell compartments a co-pathological state. Furthermore, neural cells showing
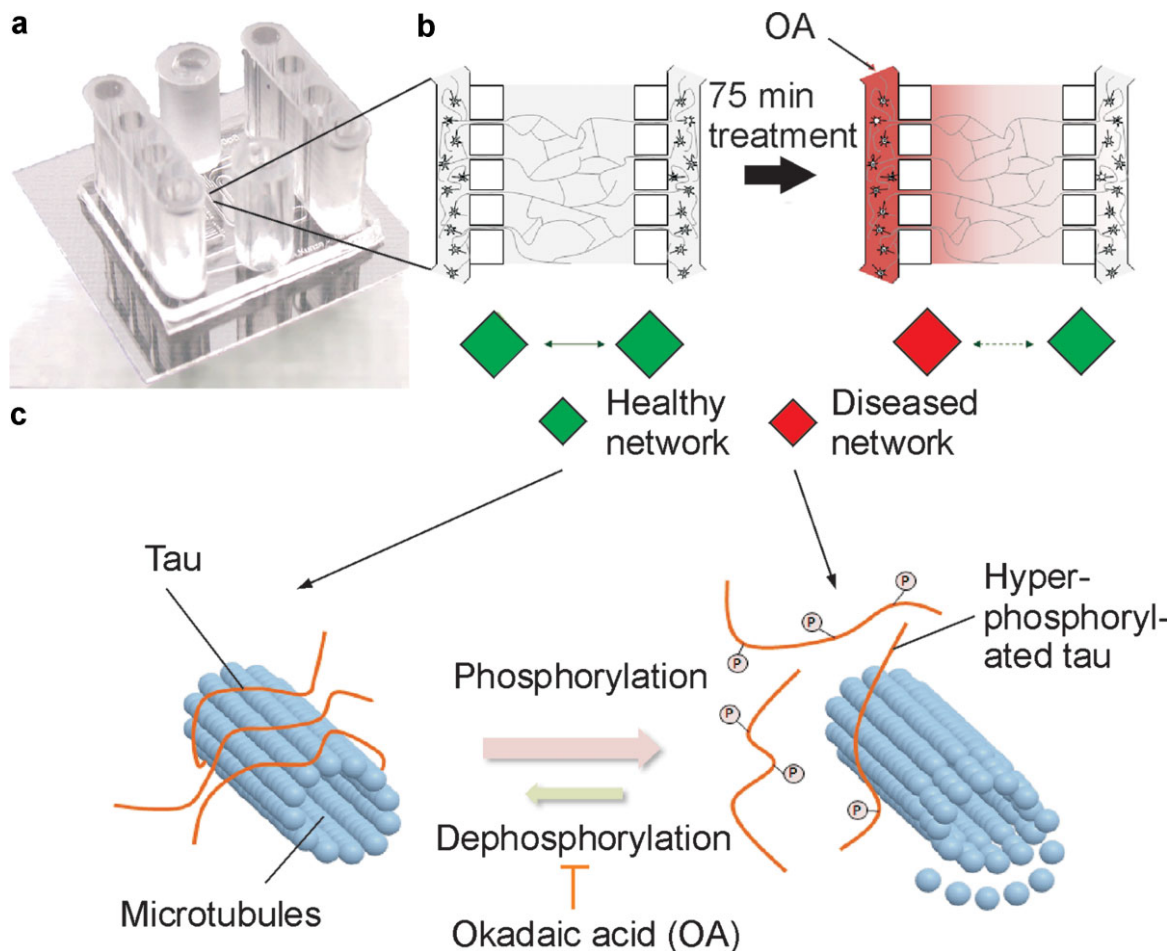
Figure 1. Generation of a co-pathological neural cell culture. **a**: Photograph image of the PDMS microfluidic device. **b**: Schematic of experimental procedure to achieve a co-existence of diseased and healthy neurons after 8 days in vitro: Step 1: Neuronal cells cultured in two lateral channels; Step 2: Local injection of okadaic acid in the left culture channel, generating a concentration gradient in the main channel. Cells are treated for 75 min, leading to a local diseased neuronal cell culture due to Tau-hyperphosphorylation. **c**: Disequilibrium of Tau-microtubule-binding induced by inhibition of dephosphorylation through okadaic acid.

Tau-hyperphosporylation states after OA treatment are defined as diseased neurons, while neurons with normal Tau phosporylation states are called healthy neurons.

To achieve the co-pathological culture, a microfluidic-based cell culture device in poly(dimethylsiloxane) (PDMS) was fabricated. The microfluidic design has three compartments: two lateral cell culture channels (3 mm long, 200 μm wide, and 100 μm high), 24 junction channels (150 μm long, 10 μm high, and 20 μm wide) and a main channel (3 mm long $\times$ 640 μm wide $\times$ 100 μm high). The two different heights of the microfluidic channels required a two-step fabrication process of the silicon master used for PDMS molding. We developed a two-step dry etching process to fabricate the two different heights in silicon. We chose the two-step dry etching process, because of the longer life span of silicon structures compared to photoresist structures for PDMS molding. The detailed process flow for fabricating the silicon master is described in Additional supporting information (Fig. 1). After PDMS molding the microfluidic

device has 7 mm high PDMS reservoirs on the top of the PDMS body to generate perfusion flow through the cell culture channels. When only one reservoir is filled up to 7 mm, the pressure difference between the full and the empty reservoir causes a perfusion flow for at least 75 min. Applying perfusion flow in the two-cell culture channels, while one fluid is enriched with OA, will lead to linear concentration gradients through the junction channels and across the main channel. The special design of the main channel favored the formation of complex neurite structures between the two-cell compartments. The junction channels function as neurite navigators and as injection channels to generate a chemical gradient in the main channel. Dissociated cortical neurons (E19) were obtained from embryonic rats (Wistar; a detailed description of the cell culture protocol can be found in the Materials and Methods Section and in additional supporting information). The surface of microfluidic channels was pre-treated with 0.01% (v/v) poly(ethylenimine) in borate buffer to enhance neural

cell attachment and to avoid air bubble entrapment. All channels were filled with Neurobasal/B27 prior cell injection. Twenty microliters of cell suspension was loaded in each of the two PDMS reservoirs of the cell culture channels. The microfluidic devices were placed in Petri dishes, surrounded by Neurobasal/PenStrep and incubated for 8 days (95% air, 5% CO_2, 65% R.H.).

After 2 days in vitro (DIV) we observed neurite outgrowth through the junction channels and into the main channel. From 5 DIV, neurite length saturated in the microfluidic device (Fig. 2; in Additional supporting information). Figure 2a shows the two neuronal cell compartments after 8 DIV with neurites grown into the main channel. We observed that most cell bodies were located in the cell culture channels. In addition we found that roughly one-third of cells had migrated from the cell compartments through the junction channels into the main channel (Fig. 3; in Additional supporting information). Functional neurite connectivity in the main channel was shown through synapthophysin immunostaining (Fig. 4; in Additional supporting information).

After 8 DIV, 600 nM OA in Neurobasal was injected in one of the reservoirs for the left cell culture channel; only Neurobasal was filled in the right reservoir. In this way, the left neuronal cell population was exposed to OA for 75 min. During perfusion the OA diffused from the cell culture channel through the junction channels across the main channel. An experiment with fluoresceine showed the
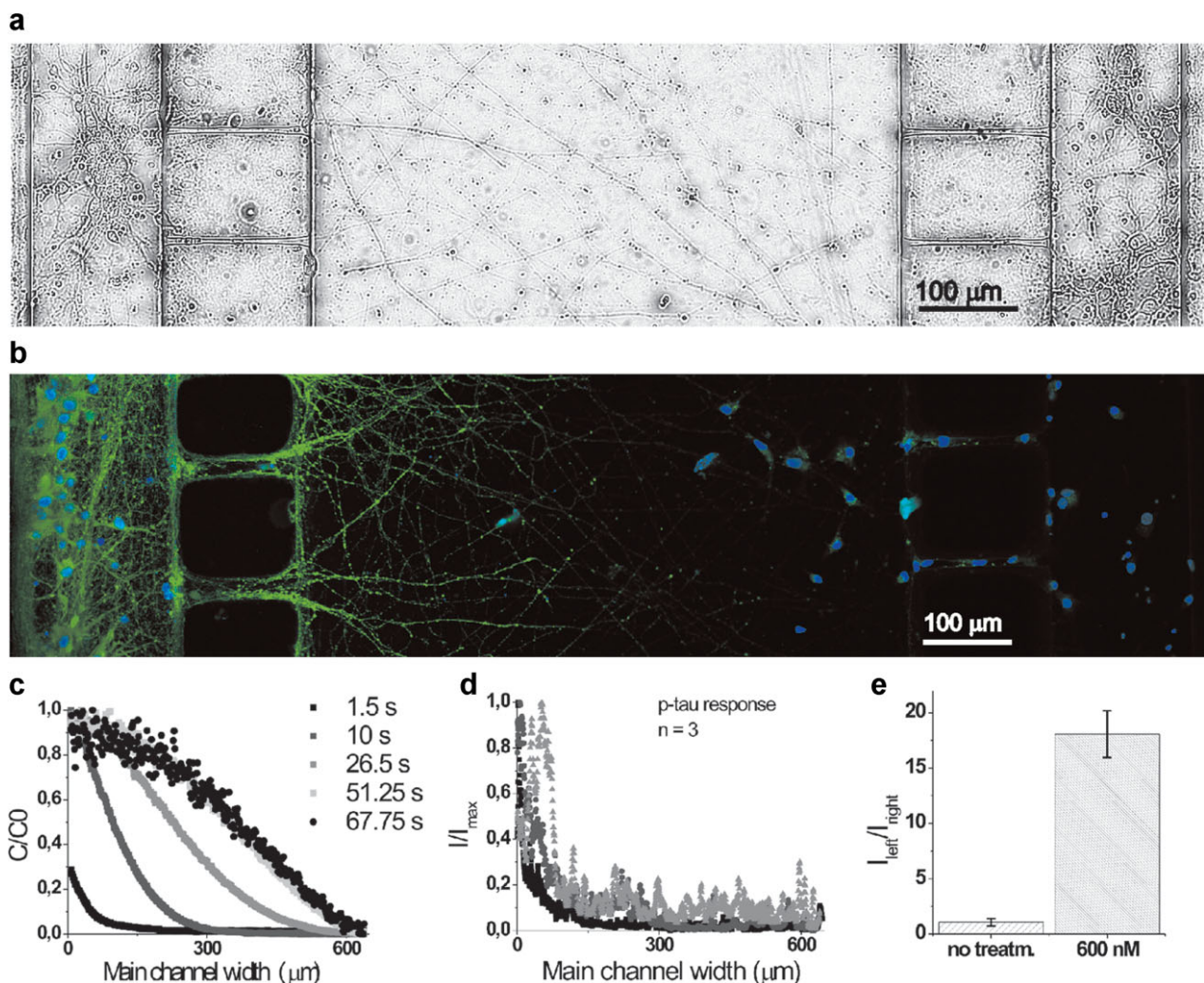
Figure 2. Co-pathological cell compartments of primary cortical neurons after treatment. **a**: Differential interference contrast (DIC) image of the primary cell culture in the microfluidic device before OA treatment. **b**: Immunocytochemical staining of Ser262-phosphorylated Tau proteins after OA treatment (600 nM) for 75 min (green: CY-2, blue: DAPI). **c**: Transient chemical gradients in the main channel, characterized with 20 μmol fluoresceine, stabilized after 1 min (time in s). **d**: Mean fluorescence intensity across the main channel corresponding to the presence of immunostained phospho-Tau-Ser262 gradient generated through OA treatment in three different devices. **e**: Fluorescence intensity ratio of left to right cell compartment representing the phosphorylated Tau imbalance, $n = 4$. t-Test showed significant different phosphorylated Tau states, $P < 0.001$.

generation of transient chemical gradients across the main channel and the establishment of linear gradients after 1 min (Fig. 2c and Additional supporting information). For a diffusion coefficient of 200 μm^2/s for OA, the linear gradient can be assumed after approx. 30 min.

After OA treatment, PP2A inhibition leads to hyperphosphorylation of Tau proteins and dissociates microtubules, as already shown in Figure 1c, a main indicator for AD (Ballatore et al., 2007; Brandt et al., 2005; Wang et al., 2001). Different phosphorylation states in neurites in the main channel were visualized with Ser262-Tau immunostaining. Figure 2b shows a confocal image from the microfluidic device after OA perfusion and immunostaining. On the left, hyperphosphorylated Tau proteins are present, while in the main channel the effect decreases in correlation with the chemical gradient of OA. The different phosphorylation states are represented in Figure 2d by their fluorescence intensity. In non-treated experiments, no significant intensity differences can be observed between left and right cell populations (Fig. 2e). On the other hand, there is a striking 19:1 ratio between the left and right phosphorylated Tau imbalance.

Now, we discuss the effect of local phosphorylated Tau after OA treatment on primary cortical neurons in the two-cell compartments. Diseased neurons in the left cell compartment exhibit phosphorylated Tau aggregates in neurites (Fig. 3a, arrow 1) and accumulation in the soma (Fig. 3a, arrow 2). Both effects are in correlation with previous studies, where phosphorylated Tau unbinds from microtubules and forms aggregates causing axon swelling (Yoon et al., 2006) and filament formation in somata (Togo et al., 2004). In contrast to the diseased neuron, a homogeneous Tau-distribution can be seen in Figure 3b, a healthy neuron, as indicated by a non-textured, lower fluorescence intensity, without aggregates and accumulations. The counting of cell numbers and neurites per cell in both cell populations (Fig. 3c and d) yields no significant decrease of cells after the OA perfusion, while neurites per cells reduced about 32% in the left perfusion channel. Our results confirm that the cell response is independent on sheer stress that can also be induced during perfusion. The staining of synapses with synaptophysin after the OA treatment (Fig. 3 in Supplementary data) confirms the connection between the healthy and the diseased cell population. In addition to Tau hyperphosphorylation, OA treatment has previously been linked to oxidative stress (Zhang and Simpkins, 2010) and increased intracellular amyloid β (Sun et al., 2002), two further characteristics in AD brains (Baig et al., 2009; Nunomura et al., 2006). All these data indicate the relevance of OA treatment for AD.

In conclusion, we have developed a novel experimental model to generate two distinct co-pathological states in connected neural cell culture in vitro. In a PDMS microfluidic device, neuronal cells have been cultured up to 8 days in two separate cell compartments and formed neurite connections to each other. A local perfusion of OA caused a local hyperphosphorylation of Tau, a characteristic
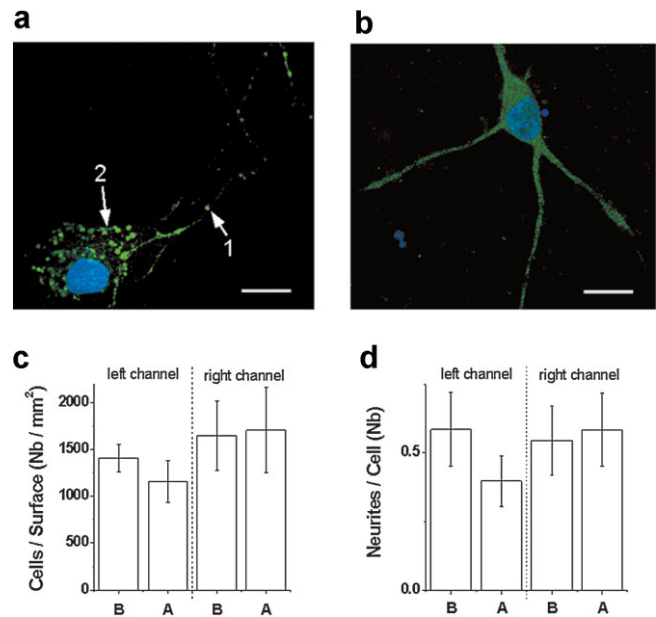
Figure 3. OA perfusion generates co-pathological states of phosphorylated Tau without significant influence on neuronal integrity of healthy and diseased cells. **a,b**: Fluorescent images of neuronal cells show staining of phosphorylated Tau in green and DAPI in blue. (a) Diseased cell from left compartment and (b) healthy cell from right compartment in the same microfluidic device. Diseased neurons demonstrated accumulation of phosphorylated Tau clusters in neurites (1) and soma (2). Healthy neurons showed homogeneous distribution of Tau within neurites. Bars = 10 μm. **c**: Cell number counted in cell culture channels, B = before treatment, A = after treatment, $n = 5$. **d**: Neurites per cell before and after OA treatment, $n = 5$. In the left perfusion channel a significant decrease of neurites was detected (t-test, $P < 0.05$), whereas the number of cells did not differ significant.

feature of AD. By immunostaining, we confirmed in the microfluidic device: (1) gradient controlled Tau phosphorylation states and (2) diseased and healthy neuronal cell population. The different phosphorylation states resulted in a co-pathological state of equilibrated versus disequilibriated phosphorylated Tau metabolism within the same neural cell culture. Our novel microfluidic-based experimental model generated co-pathological states of phosphorylated Tau proteins within a connected cell culture of primary cortical neurons. This new model allows in future the study of neurodegenerative propagation processes or the performing of drug efficiency tests while evaluating side effects between healthy and diseased cell compartments.

Materials and Methods

Microfluidic Device Fabrication

Microfluidic devices were fabricated by PDMS injection molding over silicon masters at 80°C for 1 h. The microfluidic channels are cast in the bottom of a PDMS body through two-step structured silicon masters. Silicon masters were fabricated in the clean room (for more details

see Additional supporting information, Fig. 1). PDMS microfluidic channels were sealed with 18 mm × 18 mm glass slides using oxygen plasma bonding (50 W, 0.5 sccr, 0.3 mtorr, 45 s).

Primary Cortical Cell Culture in the Microfluidic Device

Dissociated cortical neurons (E19) were obtained from embryonic rats (Wistar) in accordance to all state and federal regulations. Cortical tissues were extracted from the embryonic brain and digested for 15 min in an enzyme solution at 37°C according to standard protocols previously described (Kunze et al., 2010). For the 2D neural cell culture until network formation, the microfluidic device was pre-filled with culture medium. We added 20 µL cell suspension of 10×10^6 neurons/mL into the PDMS reservoirs of the perfusion channels. Neurobasal medium, 2% (v/v) B27, 1% (v/v) PenStrep was filled to all other reservoirs. Neuronal cells were cultured in microfluidic devices in an incubator at 37°C (95% air, 5% CO_2, 65% relative humidity). To prevent evaporation, microfluidic devices were placed in petri dishes and surrounded with Neurobasal medium. Medium change has been conducted every 3 days.

Immunocytochemistry and Imaging

Neural cells in the microfluidic devices were incubated with a 3% BSA solution (in 0.1% Triton/PBS) for 45 min before immunostaining. Phospho-Tau Ser262 primary antibody (1:150 in PBST) was injected into all reservoirs and incubated for 2 h at 4°C. The samples were washed three times with PBST and treated in dark with a CY-2 coupled secondary antibody (1:150 in PBST) over night at 4°C. The microfluidic channels were again washed three times with PBS followed by a cell nuclei staining with DAPI (1:7,000 in PBS) for 20 min at room temperature. A confocal microscope was used to quantify Tau phosphorylation states.

References

Arias C, Sharma N, Davies P, Shafit-Zagardo B. 1993. Okadaic acid induces early changes in microtubule-associated protein 2 and tau phosphorylation prior to neurodegeneration in cultured cortical neurons. J Neurochem 61(2):673–682.

Baig S, van Helmond Z, Love S. 2009. Tau hyperphosphorylation affects Smad 2/3 translocation. Neuroscience 163(2):561–570.

Ballatore C, Lee VM, Trojanowski JQ. 2007. Tau-mediated neurodegeneration in Alzheimer's disease and related disorders. Nat Rev Neurosci 8(9):663–672.

Brandt R, Hundelt M, Shahani N. 2005. Tau alteration and neuronal degeneration in tauopathies: Mechanisms and models. Biochim Biophys Acta (BBA)—Mol Basis Dis 1739(2–3):331–354.

Delacourte A. 2008. Tau pathology and neurodegeneration: An obvious but misunderstood link. J Alzheimers Dis 14(4):437–440.

Horn D, Levy N, Ruppin E. 1996. Neuronal-based synaptic compensation: A computational study in Alzheimer's disease. Neural Comput 8(6):1227–1243.

Krinke D, Jahnke H-G, Mack TGA, Hirche A, Striggow F, Robitzki AA. 2010. A novel organotypic tauopathy model on a new microcavity chip for bioelectronic label-free and real time monitoring. Biosens Bioelectron 26(1):162–168.

Kunze A, Giugliano M, Valero A, Renaud P. 2010. Micropatterning neural cell cultures in 3D with a multi-layered scaffold. Biomaterials 32(8):2088–2098.

Millet LJ, Stewart ME, Nuzzo RG, Gillette MU. 2010. Guiding neuron development with planar surface gradients of substrate cues deposited using microfluidic devices. Lab Chip 10(12):1525–1535.

Nunomura A, Castellani RJ, Zhu X, Moreira PI, Perry G, Smith MA. 2006. Involvement of oxidative stress in Alzheimer disease. J Neuropathol Exp Neurol 65(7):631–641.

Palop JJ, Chin L, Mucke L. 2006. A network dysfunction perspective on neurodegenerative diseases. Nature 443(7113):768–773.

Pariente J, Cole S, Henson R, Clare L, Kennedy A, Rossor M, Cipoloti L, Puel M, Demonet J, Chollet F, Frackowiak RS. 2005. Alzheimer's patients engage an alternative network during a memory task. Ann Neurol 58(6):870–879.

Pearce TM, Williams JC. 2006. Microtechnology: Meet neurobiology. Lab Chip 7:30–40.

Savioz A, Leuba G, Vallet PG, Walzer C. 2009. Contribution of neural networks to Alzheimer disease's progression. Brain Res Bull 80(4–5):309–314.

Shamloo A, Heilshorn SC. 2010. Matrix density mediates polarization and lumen formation of endothelial sprouts in VEGF gradients. Lab Chip 10(22):3061–3068.

Small DH. 2008. Network dysfunction in Alzheimer's disease: Does synaptic scaling drive disease progression? Trend Mol Med 14(3):103–108.

Sun X, Cole GM, Chu T, Xia W, Galasko D, Yamaguchi H, Tanemura K, Frautschy SA, Takashima A. 2002. Intracellular A[beta] is increased by okadaic acid exposure in transfected neuronal and non-neuronal cell lines. Neurobiol Aging 23(2):195–203.

Taylor AM, Jeon NL. 2010. Micro-scale and microfluidic devices for neurobiology. Curr Opin Neurobiol 20(5):640–647.

Taylor AM, Dieterich DC, Ito HT, Kim SA, Schuman EM. 2010. Microfluidic local perfusion chambers for the visualization and manipulation of synapses. Neuron 66(1):57–68.

Togo T, Akiyama H, Iseki E, Uchikado H, Kondo H, Ikeda K, Tsuchiya K, de Silva R, Lees A, Kosaka K. 2004. Immunohistochemical study of Tau accumulation in early stages of Alzheimer-type neurofibrillary lesions. Acta Neuropathol 107(6):504–508.

Wang J-z, Tung YC, Wang Y, Li XT, Iqbal K, Grundke-Iqbal I. 2001. Hyperphosphorylation and accumulation of neurofilament proteins in Alzheimer disease brain and in okadaic acid-treated SY5Y cells. FEBS Lett 507(1):81–87.

Wang J, Ren L, Li L, Liu W, Zhou J, Yu W, Tong D, Chen S. 2009. Microfluidics: A new cosset for neurobiology. Lab Chip 9:644–652.

Wimo A, Prince M. 2010. Alzheimer's Disease International, World Alzheimer Report 2010, The global economic impact of dementia. Karolinska Institutet, Stockholm, Sweden and Institute of Psychiatry, King's College London, UK.

Yoon SY, Choi JE, Yoon JH, Huh JW, Kim DH. 2006. BACE inhibitor reduces APP-beta-C-terminal fragment accumulation in axonal swellings of okadaic acid-induced neurodegeneration. Neurobiol Dis 22(2):435–444.

Zhang Z, Simpkins JW. 2010. An okadaic acid-induced model of tauopathy and cognitive deficiency. Brain Res 1359:233–246.

Paper III

Microfluidic-based frequency-multiplexing impedance sensor (FMIS)

Meissner, R. , Joris, P., Eker, B., Bertsch, A., Renaud, P. (2012), *Lab Chip*, 12(15), 2712-2718

Lab on a Chip

PAPER

A microfluidic-based frequency-multiplexing impedance sensor (FMIS)†‡

Robert Meissner,‡* Pierre Joris,‡ Bilge Eker, Arnaud Bertsch and Philippe Renaud

We present a novel technology for the simultaneous and simple impedimetric screening of multiple microfluidic channels with only one electrode pair. We have exploited the frequency dimension to distinguish between up to three channels. Each 'sub-sensor' possesses its corresponding measurement frequency where the sample-specific dielectric properties can be probed. We have shown the validity of our frequency-multiplexing impedance sensor (FMIS) by comparison with conventional 'single sensors'. Our highly sensitive FMIS was proven suitable for life science applications through usage as a cell-based toxicology platform. We are confident that our technology might find great utility in parallelized cell-based analysis systems as well as in biomedical devices where size limitations and spatially distributed probing are important parameters.

1 Introduction

Impedance spectroscopy is widely used in analytical chemistry (*e.g.* in conductivity measurements) as well as in biosensing. Many cell-based assays rely on the impedance as a cell status indicator for drug response and toxicity.[1–5] A great variety of applications have also been demonstrated with small biological components such as proteins,[6,7] antibodies[8,9] and nucleic acids.[10,11] In all these cases, one electrode pair is used to screen one specific sample only. The automatized measurement of the dielectric properties of various samples results in a multitude of electrodes, each of them additionally connected to a common multiplexing switch that is controlled by multiplexing software. These setups are not only complex, but also add noise to the recorded biological signals.

Similarly, impedance spectroscopy has been used for biomedical purposes where micro-probes are implanted in a tissue *in vivo* to measure their resistivity at different sites.[12–14] To access these sites, the micro-probe had to be either displaced within the tissue leading to cellular damage, or be equipped with an array of separate micro-electrodes along the probe. Separate electrodes require corresponding electrode traces that are placed in parallel on the shaft. This increases the size of the entire micro probe and potentially leads to tissue damage and inflammatory reaction. Thus, there is a great need for very small devices that are, nevertheless, equipped with a multitude of spatially dispersed sensors.

In this study, we report the development of a frequency-multiplexing impedance sensor (FMIS). Our novel technology allows the screening of multiple sites or channels with one single electrode pair only. We have developed a theoretical model for designing a FMIS and fabricated devices with up to three sub-sensors. Subsequently, we have demonstrated the functionality of a FMIS system that records two signals simultaneously. Cell-based toxicity screening is applied and demonstrates the great impact that the FMIS technology might have in future applications.

2 Theory

2.1 The concept of microfluidic-based frequency multiplexing

The purpose of this device is to screen the bulk resistance in multiple microfluidic channels with a single electrode pair (Fig. 1). Instead of using individual sensors that are accessed through a switch, we are aiming at a "switch-free" simultaneous
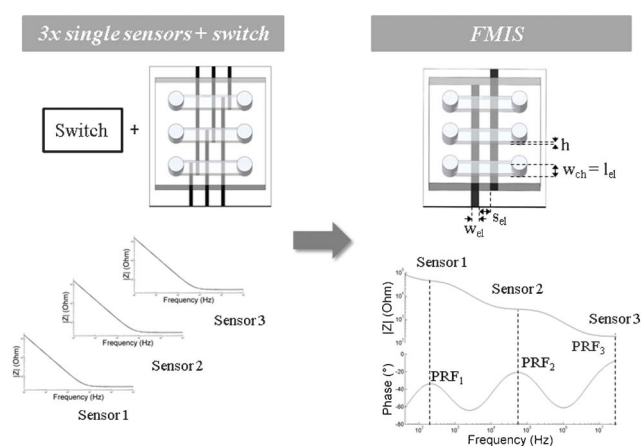
Laboratoire de Microsystèmes LMIS4, Ecole Polytechnique Fédérale de Lausanne, Station 17, CH-1015, Lausanne, Switzerland.
E-mail: robert.meissner@epfl.ch; Tel: +41 216936752
† Electronic Supplementary Information (ESI) available: See DOI: 10.1039/c2lc40236j
‡ These authors contributed equally to this work.

Fig. 1 Concept of microfluidic-based frequency multiplexing. Left: standard measurements of three samples in different channels with three electrode pairs and a switch system. Right: the same measurements using one single frequency-multiplexing impedance sensor (FMIS).

recording with one FMIS. This can be achieved by connecting a single electrode pair to different parallelized channels. All channels with their embedded electrode segment define one "sub-sensor" respectively. Due to different geometries of the electrode segments, each sub-sensor has a specific peak resistance frequency[13] (PRF)§ where the sample resistance from the corresponding micro channel can be probed.

Accordingly, the impedimetric information is obtained by choosing the corresponding measurement frequency. In conclusion, frequency-dependent current pathways are created where the interface capacitors act as gates.

2.2 Modeling of a simple electrode–electrolyte sensor

Hereafter, the equivalent circuit model of a sub-sensor is discussed in more detail. An electrical double layer is built up at the electrode–electrolyte interface when an electrode is in contact with a solution. This double layer can be modelled as a capacitor (C_{dl}) and adds up in series to the solution resistance (R_{sol}). The cross-section of the sensor that was used in this study is illustrated in Fig. 2.

The electrical double layer capacitance can be calculated with the simple mathematical Helmholtz–Perrin model ($V < 50$ mV)[15]:

$$C_H = \frac{1}{2} \varepsilon_0 \varepsilon_r \frac{A}{d_{OHP}} = \frac{1}{2} \varepsilon_0 \varepsilon_r \frac{w_{el} \cdot l_{el}}{d_{OHP}} \quad (1)$$

where $\varepsilon_0 = 8.85 \times 10^{-12}$ Fm^{-2} is the vacuum permittivity, $\varepsilon_r = 12.4$¶ is the relative permittivity of water,[16] A is the surface area of the electrode, w_{el} is the width of the electrode, l_{el} is the electrode length (= channel width w_{ch}) and $d_{OHP} = 5$ Å is the outer Helmholtz plane distance.[16] The capacitance is divided by 2 to account for both measurement electrodes (in series).

It has been described earlier that the double layer capacitance is potential dependant[15] (Gouy–Chapman capacitance). For simplicity, we did not consider the effect of voltage-dependant space charge because its effect on the sensor design optimization is negligible.


Fig. 2 Cross-section of the planar bipolar sensor with corresponding equivalent circuit and dimension parameters.

The solution resistance can be calculated as follows

$$R_{sol} = \rho \kappa \quad (2)$$

where ρ is the resistivity of the solution and κ is the cell constant, a geometrical factor. The cell constant depends on the shape of the sample and the electrodes. Two cases have been employed in this study. For the case where large electrodes are spaced far from each other, the cell constant calculates as follows[17] (a derivation is provided in the ESI†)

$$\kappa = \frac{1}{w_{ch}} \left(\frac{s_{el}}{h} + \frac{4\ln(2)}{\pi} \right) \quad (3)$$

where s_{el} is the interelectrode spacing, w_{ch} is the channel width and h is the channel height. The first term can be interpreted as the resistance through the channel and the second term as the series resistance due to the curving of the field lines down towards the metal electrode. For the case where small electrodes are placed in proximity, the cell constant calculates as follows[18]

$$\kappa = \frac{1}{l_{el}} \frac{K(k)}{K\left(\sqrt{1-k^2}\right)} \quad (4)$$

where $K(k)$ is the complete elliptic integral of the first kind and $k = s_{el}/(s_{el} + 2w_{el})$.

2.3 Optimization of frequency-multiplexing

For the FMIS, several sub-sensors characterized by different geometries are connected in parallel. In order to perform reliable impedance measurements in the different channels, a number of parameters need to be optimized. Two factors influencing the measurement sensitivity have to be taken into account. First, the PRF of the different sub-sensors needs to be well-defined and well-separated for good identification of all sensor-specific measurement frequencies. Second, the total resistance range needs to be maximal in order to avoid cross-talk between the sensors and to guarantee a large resistance measurement window (ΔR). It is obvious, however, that these two conditions are guaranteed by separating the different cut-off frequencies. We call this process the frequency separation method (FSM). All relevant frequencies for the FSM are illustrated in Fig. 3.

As a specific case, all the following considerations apply to a triple-sensor (a similar reasoning is valid for any number of sensors). A maximal separation of the PRFs requires the differences of all cut-off frequencies (Δf_{1-4}) to be as large as possible. This is guaranteed by maximizing the product of all the Δf. We further refer to this product as M:

---

§ The peak resistance frequency is the frequency of $1/Z = 1/X_1 + 1/(R + X_2)$ where the impedance is most resistive, i.e. the phase angle is close to $0°$. The corresponding impedance magnitude indicates the value of R. X_1 and X_2 are the reactances of two capacitances (in our case: electrical double layer capacitances or the parasitic capacitance at high frequency).

¶ The relative permittivity at an outer Helmholtz distance of 5 Å corresponds to 24.8 (and $\varepsilon_r = 0$ at $d_{OHP} = 0$) according to Conway et al.[16] An average value of 12.4 for the entire electrical double layer was used in this study. This is valid because of the linear relationship between d and ε_r.
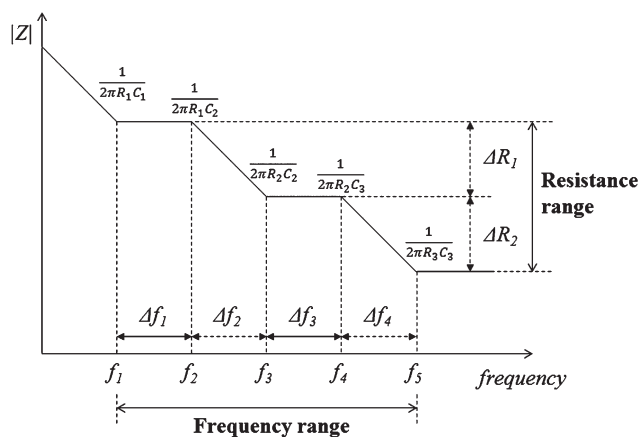
Fig. 3 A simplified impedance magnitude-frequency spectrum according to a triple sensor. All cut-off frequencies necessary for the optimization process are shown. C_n is the double layer capacitance and R_n is the bulk resistance of the nth electrode-channel segment.

$$M = \underbrace{(\Delta f_1 \cdot \Delta f_3)}_{P} \cdot \underbrace{(\Delta f_2 \cdot \Delta f_4)}_{D}$$
$$= \left(\log\left(\frac{f_2}{f_1}\right) \cdot \log\left(\frac{f_4}{f_3}\right)\right) \cdot \left(\log\left(\frac{f_3}{2}\right) \cdot \log\left(\frac{f_5}{f_4}\right)\right) \quad (5)$$

where $\Delta f_n = \log(f_{n+1}/f_n)$ is defined as the cut-off frequency difference, P as the plateau length parameter and $D = \Delta R_1 \times \Delta R_2$ as the total resistance range.

In Fig. 3 the different cut-off frequencies are given by $f_c = 1/(2\pi RC)$, where R is the solution resistance R_{sol} (eqn (2)) and C is the Helmholtz double layer capacitance C_H (eqn (1)). Consequently, the maximization of M has implications on all the experimental parameters from eqn (1–4). It becomes nevertheless apparent that only w_{el} and s_{el} are relevant for the optimization process since l_{el} is cancelled out (if kept the same for all channels) and ρ cannot differ in cell culture applications. Finally, M can be simplified as

$$M = \log\left(\frac{w_{el,1}}{w_{el,2}}\right) \times \log\left(\frac{w_{el,2}}{w_{el,3}}\right) \times \log\left(\frac{\kappa_1}{\kappa_2}\right) \times \log\left(\frac{\kappa_2}{\kappa_3}\right) \quad (6)$$

where κ is calculated according to the electrode size by using eqn (3) and eqn (4).

We have simulated M for all three sensors as a function of w_{el} and s_{el} as shown in Fig. 4. According to Fig. 4a, both electrode spacing and width have to be as large as possible for sub-sensor 1. In this case, the main size limitations are given by the available space on chip and by the lowest AC measurement frequency. Similarly, according to Fig. 4c, the geometrical dimensions have to be as small as possible for sub-sensor 3, the main limitation being now given by the microfabrication process. Once the dimensions of sub-sensors 1 and 3 are set, the electrode spacing and width of sub-sensor 2 can be optimized by maximizing the function M (Fig. 4b).

Note that the dimensions of sub-sensors 1 and 3 determine respectively the lowest and highest cut-off frequencies of the FMIS, and consequently its total frequency range (= f_1/f_5) and

total resistance range (= R_3/R_1). The optimization of the dimensions of sub-sensor 2 determines the other cut-off frequencies such that they are distributed as equally as possible over the total frequency range, especially $P_1 = P_2$ ($\Delta f_1 = \Delta f_3$) and $D_1 = D_2$ ($\Delta f_2 = \Delta f_4$).

Moreover, the total resistance range D can be further increased by introducing interdigitated electrodes (IDE), simultaneously decreasing the plateau lengths (P). We have developed a model that provides the number of interdigitated electrode fingers for a desired resistance range (see Fig. S1 in the ESI† for detailed information).

3 Materials and methods

3.1 Electrode chip design and fabrication

The electrode dimensions were based on the simulations presented in Fig. 4. We have chosen large $s_{el,1}$ and $w_{el,1}$ (8000 μm and 500 μm) as indicated by Fig. 4a. The parameters of the third sensor, $s_{el,3}$ and $w_{el,3}$, were chosen small (both 5 μm). In the case of the triple sensor, the additional parameters $s_{el,2}$ and $w_{el,2}$ were chosen according to the resulting optimum as demonstrated in Fig. 4b ($w_{el,2} = 51$ μm and $s_{el,2} = 1150$ μm). The FMIS is shown in Fig. 5 (double sensor: only the upper and lower channel was used; triple sensor: all channels).

For the electrode microfabrication, a 20 nm thick titanium adhesion layer and a 200 nm thick platinum layer were successively evaporated and structured on a 4-inch glass substrate using the standard photolithographic lift-off technique.

3.2 Microfluidic chip design and fabrication

A microfluidic chip made of PDMS (polydimethylsiloxane) was used to separate the sensing areas. Two (double sensor) or three (triple sensor) microfluidic channels were embedded, all with a channel width of $w_{ch}(l_{el}) = 500$ μm and a channel height of $h = 120$ μm. The channel height was defined by the fabrication process. For this, a cutter plotter was used to cut and structure a 120 μm thick tape that was adhered onto a transparent foil. The resulting structure was used to mold the PDMS microfluidic chip. Holes punched through the PDMS served as injection reservoirs.

3.3 Conductivity and cell culture experiments

The assembled PDMS and electrode chip were connected to a printed circuit board (PCB) for electrical measurements. The microfluidic channels were filled with different concentrations of PBS (phosphate buffered saline) ($0.125\times$, $0.25\times$, $0.5\times$, $1\times$, $2\times$). First, only one channel was filled with liquid while the other ones contained air (mono sensor). Second, all channels were filled with PBS and the concentration was varied crosswise (double/triple sensor). The impedance was measured with an impedance analyser (Agilent 4294, Agilent technologies, USA) from 40 Hz to 30 MHz (10 mV amplitude, 0 mV bias) and recorded using Matlab software. The solution resistances were consequently obtained through equivalent circuit fitting. All values are presented as mean ± standard error of the mean (SEM). For sensitivity determination (ρ_{meas}/ρ_{real}), the measured resistivity was obtained by dividing the mean resistance by the average experimental cell constant. The resistivity of the different

Fig. 4 Simulation of M as a function of w_{el} and s_{el}. (a) Sub-sensor 1 indicates a large M with larger values for $w_{el,1}$ and $s_{el,1}$, (b) sub-sensor 2 indicates an optimum of M at $w_{el,2} \approx 50$ μm and $s_{el,2} \approx 1000$ μm; (c) sub-sensor 3 maximizes M for small values of $w_{el,3}$ and $s_{el,3}$. All simulations were carried out with the fabrication values ($w_{el,1} = 500$ μm, $w_{el,2} = 51$ μm, $w_{el,3} = 5$ μm, $s_{el,1} = 800$ μm, $s_{el,2} = 1150$ μm, $s_{el,3} = 5$ μm).

Fig. 5 Electrode (black) and channel (grey) design. The bipolar electrode pair is characterized by three sub-regions that differ in electrode width and spacing. Three microfluidic channels are implemented to create a sample separation aligned onto the three sub-sensors. Four PCB connection pads are used since the shortening of the current injection and the voltage pick-up electrodes are done on-chip (higher sensitivity).

solutions was measured with a conductivity meter (SevenEasy, Mettler Toledo). We assume hereafter that these values are the real resistivities of the solutions.

MCF-7 cells were cultured in a 75 cm^2 flask before loading them in the microfluidic chip. The cells were incubated in Dulbecco's Modified Eagle's Medium (DMEM) (Invitrogen, Switzerland), containing 10% fetal calf serum (Invitrogen, Switzerland), at 37 °C and 5% CO$_2$. The cells were loaded into the microfluidic channels at a density of 10 Mio cells ml^{-1}. They were cultured for 24 h before 100 mM doxorubicin treatment was started. The drug treatment initiation was shifted by 45 min for the two channels so that the functionality of the double sensor could be demonstrated. All materials were autoclaved for the cell culture experiments.

4 Results and discussion

4.1 Characterization of the double sensor

The goal of this study was to demonstrate the ability to measure two or more signals with one single electrode pair. For this, we have exploited the frequency dimension to separate the different signals. The major challenge was to design the sensor such that a maximal frequency separation of the PRFs (Fig. 1) and thus a maximal M (eqn (5)) could be achieved.

In the first step, we have characterized our device experimentally to verify the validity of our simulations and the consequential chip design. All system specific parameters are presented in Table 1 and the corresponding impedance spectra are depicted in Fig. 6.

The small deviations in cell constant, resistance and capacitance values were attributed to the flexible PDMS that cannot guarantee very precise fabrication dimensions. In addition, the dimensions of the electrode after fabrication were not exactly 5 μm each ($s_{el2} = 3.4$ μm and $w_{el2} = 6.3$ μm).

Table 1 Theoretical and experimental values for equivalent circuit parameters for the double sensor. Calculated data was obtained by eqn (1)–(4). Experimental data was extracted through equivalent circuit fitting (mean, n = 5)

Parameters	Calculated data	Experimental data
R_1	82 kΩ	104 kΩ
R_2	1.2 kΩ	1.5 kΩ
C_1	27.4 nF	28.4 nF
C_2	0.35 nF	0.29 nF
f_1	70 Hz	40 Hz
f_2	5.6 kHz	5.6 kHz
f_3	383 kHz	357 kHz
κ_1	139 × 10^3 m^{-1}	169 × 10^3 m^{-1}
κ_2	2026 m^{-1}	2156 m^{-1}

Fig. 6 Simulated and experimental impedance spectra of the double sensor.

Concurrently, the experimental impedance magnitude and phase curves are found to be more flattened than the simulated one (Fig. 6). This is explained by the complex nature of the electrode–electrolyte interface. Surface roughening and steric effects lead to a multitude of different capacitor–resistor circuits resulting in a descending slope that is inferior to 45° (which is the slope angle of an ideal capacitor). This complex behaviour is conventionally described by a constant phase element.[19] However, for the sensor optimization we consider the interface capacitance as a perfect capacitor since the goal here is to simply separate cut-off frequencies. For this purpose, an approximate value for the capacitance is sufficient.

We fabricated a double sensor that meets the initial requirement of well frequency-separated PRFs. Small deviations in the cell constant of sensor 1 and the capacitance of sensor 2 were attributed to setup and fabrication. Nevertheless, it has been shown that the double sensor complies with the design specifications.

4.2 Validation of the FMIS

In order to validate our FMIS, we checked the similarity of the measurement results of both sub-sensors compared to their corresponding mono sensors on the one hand, and their measurement sensitivity on the other. We have measured channel 1 and 2 individually (mono sensing) and simultaneously (double sensing). The mono sensor measurements were done by leaving one channel filled with air. The double sensor measurements were carried out by varying the PBS concentration in channel 1 and 2 crosswise. The results are shown in Table 2 and illustrated in Fig. 7. The values for the mono and double sensors match well for both channels with a maximum deviation of less than 4% for sensor 1 at $0.5\times$ PBS (196 kΩ vs. 205 kΩ). No significant

deviation difference from the mono to double sensor is observed between channel 1 and 2 (3.4% vs. 1.5%). Thus, both sensors are considered equally functional. Next, we have evaluated the sensitivity of sub-sensor 1 and 2. Fig. 7b shows the ratio of the measured resistivity against the real resistivity at different dilutions of PBS. Both sensors show a very high sensitivity with a maximal median deviation of 3.8% for sensor 2 at $1\times$ PBS. Nevertheless, sub-sensor 2 reveals a larger average deviation of the means than sub-sensor 1 (2.2% vs. 0.7%). This is explained by the inherent higher sensitivity of sub-sensor 2, due to its lower resistance compared to sub-sensor 1. In conclusion, no significant value differences between the mono sensors and the FMIS were observed and a high sensitivity was demonstrated.

4.3 Cell toxicity application

The applicability of the FMIS to cell culture experiments was verified. We seeded MCF-7 cells, a human breast cancer cell line, in both microfluidic channels and cultured them for a period of 24 h. We then treated the cells with 100 µM doxorubicin in one channel after another with a time delay of 45 min. Accordingly, the sensor selectivity of the FMIS measurement method was investigated for utility in cell toxicity platforms. Fig. 8 shows the impedance magnitude spectra in the absence and presence of cells (a) as well as the temporal evolution of the cellular impedance for both channels after drug treatment (b). The frequency where the impedance change is largest (following cell–electrode attachment) depends on the sensor geometry. Consequently, different geometrical constants among sensors 1 and 2 lead to two different screening frequencies (relative |Z|-maxima in Fig. 8a). Furthermore, we observed that the relative impedance change is larger for sensor 2 than for sensor 1. This may be explained by the different electrode sizes. One cell is able

Table 2 Measured solution resistance values (in kΩ) in channel 1 and 2 in the mono- and double sensor mode as a function of PBS concentration (mean $\pm$ SEM, n = 5)

PBS conc. (resistivity)	$0.125\times$ (4.37 Ωm)	$0.25\times$ (2.24 Ωm)	$0.5\times$ (1.15 Ωm)	$1\times$ (0.61 Ωm)	$2\times$ (0.32 Ωm)
Mono sensor 1	748.6 $\pm$ 13.3	380.7 $\pm$ 7.9	195.8 $\pm$ 4.5	103.5 $\pm$ 2.4	55.2 $\pm$ 1.6
Mono sensor 2	9.12 $\pm$ 0.19	4.79 $\pm$ 0.06	2.49 $\pm$ 0.03	1.32 $\pm$ 0.02	0.71 $\pm$ 0.01
Double sensor 1	768.3 $\pm$ 11.8	393.2 $\pm$ 5.5	204.6 $\pm$ 1.6	107.1 $\pm$ 0.7	57.4 $\pm$ 1.0
Double sensor 2	9.30 $\pm$ 0.07	4.80 $\pm$ 0.03	2.53 $\pm$ 0.04	1.37 $\pm$ 0.02	0.71 $\pm$ 0.01
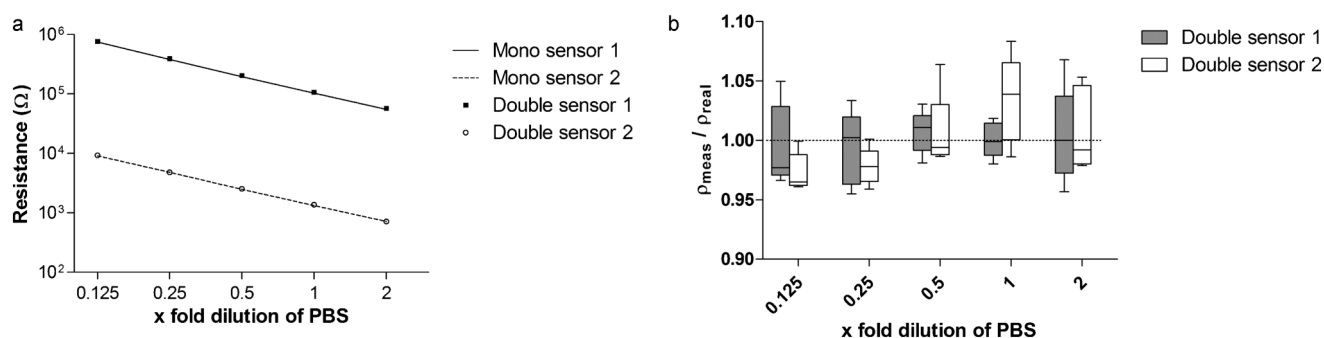
Fig. 7 Double sensor validation. (a) Measured solution resistance values in channel 1 and 2 in the mono and double sensor mode are plotted against the PBS concentration (mono sensor: mean + connecting line; double sensor: mean $\pm$ SEM, n = 5). Error bars not shown are smaller than the symbol size. The double sensor values correlate well with those from the mono mode. (b) Box plot of the ratio of the measured resistivity and the real resistivity as a function of the PBS concentration (whiskers: min to max). The measured resistivities were calculated by dividing the solution resistance by the average experimental cell constant (see Table 1). Both sensors show a high sensitivity with a maximal median deviation of 3.9% (sensor 2 at $1\times$ PBS).
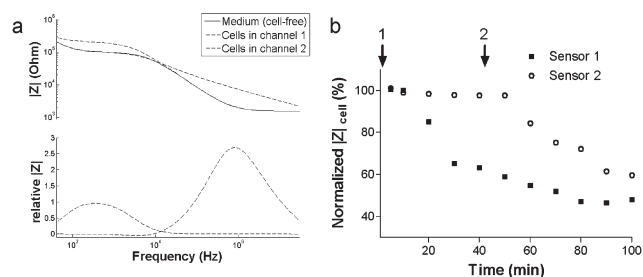
Fig. 8 Cell toxicity experiment. (a) Impedance magnitude spectra and relative |Z| change (*rel.* |Z| = (|Z|$_{cell}$·|Z|$_{cell-free}$)/|Z|$_{cell-free}$) due to cell attachment in channel 1 and 2 are shown. Each channel has its specific rel. |Z| maxima. (b) The cell impedance Z_{cell} is shown for both sub-sensors at the rel. |Z|-maxima-frequencies. MCF-7 cells cultured in both channels were exposed to 100 μM doxorubicin with a time delay of 45 min. '1' and '2' indicate the drug application in channel 1 and 2.

to cover the entire electrode width of sensor 2, thus insulating this one completely. The electrode of sensor 1, on the other hand, is too large and the current can shunt in between the cells resulting in a leaky insulation and a less strong relative impedance increase.

Being treated first with doxorubicin, the resistance of channel 1 dropped by 40% within 30 min. The measured resistance in channel 2, on the other hand, remained constant at 100%. Once channel 2 was treated after 45 min, the corresponding resistance decreased as well.

This experiment demonstrates the high selectivity of the FMIS measurement method. Two distinct cell populations have been screened separately with only one electrode pair. Although two identical microfluidic channels have been used, the electrode geometry differed. This might be a problem in cell culture applications where identical conditions are required, *e.g.* current penetration depth or cell–substrate contact. For those cases, we suggest implementing an additional electrode–electrolyte capacitor using a simple liquid-filled channel in order to modify the sub-sensor capacitance value ('capacitive bridge') (an example is provided in Fig. S2 in the ESI†). In such a case, the final electrode–cell contact region can be identical.

4.4 Multi-channel sensing and sensor limitations

We have demonstrated the functionality of the double sensor by validation with a cell-based application. We will now discuss the implementation of more than two sub-sensors. Instead of using multiple separated electrodes, such a FMIS would not only open the door to very simple multi-channel screening, but also allow the minimization of the total sensor size.

A triple sensor has been designed, as illustrated in Fig. 5, according to the simulations presented in Fig. 4. This optimization process aims at both a maximum PRF separation and maximum resistance range. The corresponding impedance spectrum of the fabricated triple sensor is depicted in Fig. 9a. The experimental and the theoretical curve match well, although there are some deviations. These deviations are explained, as already mentioned for the double sensor, by the complex nature of the electrode–electrolyte interface and by the sensor fabrication (see section 4.1). However, our fabricated triple sensor fulfils the most important requirements, *i.e.* the distinct separation of

the PRFs and equally distributed sub-resistance ranges ($D_1 \approx D_2$), within the total resistance range (D). This total resistance range is predefined by the parameters indexed 1 and 3 and equals the one of the double sensor. As a logical consequence, a common total sensor resistance range for the double and triple sensor results in halved sub-sensor resistance ranges for the triple sensor. This effect is illustrated in Fig. 9b. Hence, the resistance range linearly decreases with an increasing number of sub-sensors. Such a decrease can be opposed by introducing interdigitated electrodes (IDEs) as sub-sensor 3. IDEs decrease the cell constant and thus increase the total resistance range. This effect is shown in Fig. 9b where D is increased by the expense of a decreased P and also a decreased frequency range. In this context, the number of electrode fingers of the IDE can be determined for a desired resistance range (detailed information about this optimization is provided in Fig. S1 in the ESI†). Despite a decreased frequency range, an increased resistance range can be particularly useful when large resistance changes are measured.

In conclusion, we have been able to fabricate a triple sensor using the optimization function M. A higher number of sub-sensors at a constant total resistance range is accompanied by a lower measurement resistance range for the individual sub-sensors. This effect may be avoided by selectively increasing D, *e.g.* by introducing IDEs.

5 Conclusions

We have introduced the concept of a FMIS that is capable of screening more than one channel at the same time. The simultaneous measurement of these channels was achieved through frequency multiplexing. The frequency division (FSM) for all sub-sensors required the optimization of the chip design. For this purpose, we have developed a simulation model for simple rectangular electrode pairs as well as for interdigitated electrodes. Our fabricated chips corresponded well to the model and allowed very precise conductivity measurements in all channels in parallel. The applicability for biological experiments was demonstrated with a cell-based toxicity experiment. It has been shown that two distinct cell populations are monitored separately and simultaneously with only one electrode pair.

Our technology may find applications in impedance measurements that are carried out *in vivo*. Microprobes implanted in tissues to measure the resistivity at different sites can be simplified by reducing the total probe width since parallel electrode traces become unnecessary. Therefore, the invasiveness of a probe using our technology would be decreased.

The measurements, as they were done in this study, comprised of sub-sensors that differed in shape and positioning. When identical experimental conditions are required, *e.g.* in biological applications, we recommend the introduction of "capacitive bridges". We refer to capacitive bridges as capacitors that are placed between the individual sub-sensors, that do not contribute to the resistance measurement, but that modify the capacitance of this sensor. An additional liquid-filled channel, for example, that adds an electrode–electrolyte interface capacitor, is currently being developed. On the other hand, the geometry differences may be considered as an advantage since different sensor sizes and geometries lead to different measurement
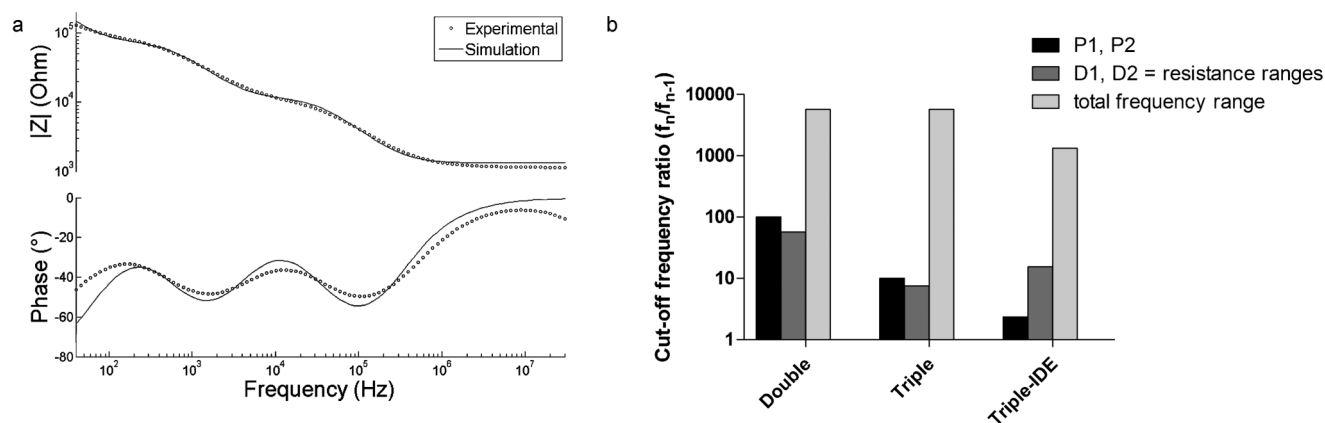
Fig. 9 Multi-channel sensing. (a) Simulated and experimental impedance spectra of the fabricated triple sensor with $1\times$ PBS. Three PRFs are identified indicating three well frequency-separated sub-sensors. The resistance ranges are similar for all sensors ($D_1 \approx D_2$). (b) The calculated values of $P_{1,2}$, $D_{1,2}$ and the frequency range are shown for the double, triple and triple-interdigitated sensor. All values correspond to optimized sensors (M_{max}) where $P_1 = P_2$ and $D_1 = D_2$. The resistance ranges of the triple sub-sensors are halved compared to the double sub-sensors while the total frequency range remains constant. In contrary, the resistance ranges of the triple-IDE sub-sensors are increased by the expense of a decreased total frequency range.

depths. As an application, one FMIS may be used to probe the thickness of a tissue as it has been shown previously with a complex switch system.[20]

Altogether, we have introduced an easy technique to screen multiple channels at the same time with a simple measurement setup. We see a high demand for such devices in *in vivo* applications where the size of the implanting probes is limited, but multiple sensors are required; as well as in *in vitro* applications where different measurement depths are needed.

References

1 R. Meissner, B. Eker, H. Kasi, A. Bertsch and P. Renaud, *Lab Chip*, 2011, **11**, 2352–61.
2 T. S. Hug, *Assay Drug Dev. Technol.*, 2003, **1**, 479–88.
3 D. Kloss, M. Fischer, A. Rothermel, J. C. Simon and A. Robitzki, *Lab Chip*, 2008, **8**, 879–84.
4 M. Tarantola, A. Pietuch, D. Schneider, J. Rother, E. Sunnick, C. Rosman, C. Pierrat, C. Sönnichsen, J. Wegener and A. Janshoff, *Nanotoxicology*, 2011, **2**, 254–268.
5 J. A. Stolwijk, C. Hartmann, P. Balani, S. Albermann, C. R. Keese, I. Giaever and J. Wegener, *Biosens. Bioelectron.*, 2011, **26**, 4720–7.
6 B. A. Cornell, V. Braach-Maksvytis, L. King, P. Osman, B. Raguse, L. Wieczorek and R. Pace, *Nature*, 1997, **387**, 580–583.
7 Y.-H. Chuang, Y.-T. Chang, K.-L. Liu, H.-Y. Chang and T.-R. Yew, *Biosens. Bioelectron.*, 2011, **28**, 368–72.
8 J. Rickert, W. Göpel, W. Beck, G. Jung and P. Heiduschka, *Biosens. Bioelectron.*, 1996, **11**, 757–768.
9 A. Steude, S. Schmidt, A. A. Robitzki and O. Pänke, *Lab Chip*, 2011, **11**, 2884–92.
10 E. Souteyrand, J. Cloarec, J. Martin, C. Wilson, I. Lawrence, S. Mikkelsen and M. Lawrence, *J. Phys. Chem. B*, 1997, **101**, 2980–2985.
11 B. van Grinsven, N. Vanden Bon, L. Grieten, M. Murib, S. D. Janssens, K. Haenen, E. Schneider, S. Ingebrandt, M. J. Schöning, V. Vermeeren, M. Ameloot, L. Michiels, R. Thoelen, W. De Ceuninck and P. Wagner, *Lab Chip*, 2011, **11**, 1656–63.
12 H. Kasi, R. Meissner, A. Babalian, H. van Lintel, A. Bertsch and P. Renaud, *Journal of Electrical Bioimpedance*, 2011, **1**, 84.
13 A. Mercanzini, P. Colin, J.-C. Bensadoun, A. Bertsch and P. Renaud, *IEEE Trans. Biomed. Eng.*, 2009, **56**, 1909–18.
14 M. Tijero, G. Gabriel, J. Caro, A. Altuna, R. Hernández, R. Villa, J. Berganzo, F. J. Blanco, R. Salido and L. J. Fernández, *Biosens. Bioelectron.*, 2009, **24**, 2410–6.
15 G. T. A. Kovacs, in *Enabling technologies for cultured neural networks*, ed. T. M. Stenger, D. A. and McKenna, Academic Press, San Diego, 1994, pp. 121–165..
16 B. Conway, J. O. M. Bockris and I. Ammar, *Trans. Faraday Soc.*, 1951, **47**, 756–766.
17 T. Braschler, PhD thesis, Ecole Polytechnique Fédérale de Lausanne, 2009, p. 200.
18 W. Olthuis, W. Streekstra and P. Bergveld, *Sens. Actuators, B*, 1995, **24**, 252–256.
19 R. De Levie, *Electrochim. Acta*, 1965, **10**, 113–130.
20 P. Linderholm, J. Vannod, Y. Barrandon and P. Renaud, *Biosens. Bioelectron.*, 2007, **22**, 789–96.

Paper IV

Label-free recognition of drug resistance via impedimetric screening of breast cancer cells

Eker, B., Meissner, R., Bertsch, A., Mehta, K., Renaud, P. (2013), *PLoS ONE*, 8(3), e57423.1-12

⦿ **PLOS** | ONE

Label-Free Recognition of Drug Resistance *via* Impedimetric Screening of Breast Cancer Cells

Bilge Eker[1]*⁹, **Robert Meissner**[1]⁹, **Arnaud Bertsch**[1], **Kapil Mehta**[2], **Philippe Renaud**[1]

1 Laboratory of Microsystems (LMIS4), École polytechnique fédérale de Lausanne, Station 17, CH-1015 Lausanne, Switzerland, 2 Department of Experimental Therapeutics, Cancer Medicine (Biochemistry), The University of Texas MD Anderson Cancer Center, Houston, Texas, United States of America

Abstract

We present a novel study on label-free recognition and distinction of drug resistant breast cancer cells (MCF-7 DOX) from their parental cells (MCF-7 WT) *via* impedimetric measurements. Drug resistant cells exhibited significant differences in their dielectric properties compared to wild-type cells, exerting much higher extracellular resistance (R_{extra}). Immunostaining revealed that MCF-7 DOX cells gained a much denser F-actin network upon acquiring drug resistance indicating that remodeling of actin cytoskeleton is probably the reason behind higher R_{extra}, providing stronger cell architecture. Moreover, having exposed both cell types to doxorubicin, we were able to distinguish these two phenotypes based on their substantially different drug response. Interestingly, impedimetric measurements identified a concentration-dependent and reversible increase in cell stiffness in the presence of low non-lethal drug doses. Combined with a profound frequency analysis, these findings enabled distinguishing distinct cellular responses during drug exposure within four concentration ranges without using any labeling. Overall, this study highlights the possibility to differentiate drug resistant phenotypes from their parental cells and to assess their drug response by using microelectrodes, offering direct, real-time and noninvasive measurements of cell dependent parameters under drug exposure, hence providing a promising step for personalized medicine applications such as evaluation of the disease progress and optimization of the drug treatment of a patient during chemotherapy.

Competing Interests: One of the authors in the submitted paper, Kapil Mehta, is a PLOS ONE Editorial Board member. This does not alter the authors' adherence to all the PLOS ONE policies on sharing data and materials.

* E-mail: bilge.eker@epfl.ch

⑨ These authors contributed equally to this work.

Introduction

Breast cancer is the most common cancer type in women and one of the leading causes of female mortality worldwide [1]. Chemotherapy is still one of the main treatment methods in clinic, causing cell death in breast tumors treated with various anti-cancer drugs. Despite the fact that many tumors initially respond to chemotherapy, cells can gain resistance and they can adapt to survive. Drug resistance often involves the transition of cancer cells from an anti-estrogen-sensitive, non-metastatic, hormone dependent phenotype to an anti-estrogen-insensitive, metastatic and hormone independent phenotype [2]. Despite the fact that there have been a plethora of studies addressing the mechanism behind drug resistance [3–11], a comprehensive answer to such a complex problem still remains elusive. Hence, a pressing demand has directed researchers towards the development of rapid and simple techniques for the investigation of interactions of cancer cells with drugs [12] at different stages of the disease.

Cell-based impedance spectroscopy has attracted significant attention as a label-free and non-invasive tool to study cellular properties such as cell adhesion and cell growth [13–15], cell migration [16,17], stem cell differentiation [18] and the effect of anti-cancer drugs on cancer cells [19–21]. Although, there have been some efforts on dielectric characterization of drug resistant cells with impedance spectroscopy [22,23] and also with dielectrophoresis technique [24], there has been no detailed study that distinguishes cell models of acquired drug resistance without genetic manipulation from their parental cells, nor investigation of drug interaction with such cells. Still substantial work needs to be done to demonstrate a comprehensive explanation why dielectric properties of cancer cells change when they gain drug resistance and how drug resistant cells interact with drugs compared to their parental wild type cells.

In addition, most of the toxicity studies demonstrated only the temporal evolution of cellular changes at one frequency where the contribution of cells to the measurement is at its maximum (cell index). As was pointed out previously [25,26], it is possible to distinguish cellular events by measuring the impedance spectra at distinct frequencies assuming that a single cell can be described as a shell-covered sphere [27,28]. At low frequencies (LF), the cell membrane capacitor functions as an insulator and extracellular events can be probed with impedance. At high frequencies (HF), the cell membrane capacitor is short-circuited, and the impedance changes correlate with intracellular events. Thus, impedance measurements within a wide frequency range (from Hz to MHz) allow the differentiation between the extracellular environment and the cell interior, and their changes can be probed simultaneously.

Herein, we performed real-time monitoring of drug induced cellular changes for MCF-7 breast cancer cells using impedance spectroscopy. We were able to distinguish drug resistant breast cancer cells (MCF-7 DOX) from their parental cells (MCF-7 WT) by studying their inherent dielectric properties. The effect of doxorubicin, one of the most widely used anti-tumor antibiotics, was investigated over a wide frequency range and revealed sharp differences in the temporal evolution of cellular changes between the two phenotypes. To our knowledge, this is the first study that differentiates drug resistant breast cancer cells from their parental cells based on their dielectric properties and investigates their drug response at different stages of the disease using impedance screening at different frequencies.

Materials and Methods

Electrode Design and Fabrication

Interdigitated (IDEs) electrodes as shown in Figure S1 were implemented in a well-based device for impedance measurements of MCF-7 cell populations. IDEs offer highly sensitive measurement owing to having large total electrode surface area. Platinum was used for electrode material since it is biocompatible [29], and highly polarizable offering mild conditions such as minimum faradaic currents and lower risk of generation of cytotoxic compounds [30]. Following evaporation of 20 nm thick titanium adhesion layer, 200 nm thick platinum layer was evaporated and patterned on a 4-inch glass substrate using standard photolithographic lift-off technique.

Cell Lines and Cell Culture on Microelectrodes

MCF-7 cells; wild-type (MCF-7 WT) and doxorubicin resistant (MCF-7 DOX) cells (resistant to 1 µg/ml doxorubicin) were kindly provided by Prof. Kapil Mehta (Department of Bioimmunotherapy, The University of Texas M. D. Anderson Cancer Center, Houston) [31]. MCF-7 DOX are a subclone of MCF-7 WT cells that was selected by continuous exposure to doxorubicin and they are functionally and phenotypically distinct from the parental MCF-7 cells [32]. Both cell lines were maintained at 37°C and 5% CO2/95% air in RPMI 1640 culture medium (Sigma-Aldrich, Switzerland) supplemented with 10% heat-inactivated fetal calf serum (Invitrogen, Switzerland), 2 mM glutamine and antibiotics (100 U/ml penicillin and 100 µg/ml streptomycin) (Invitrogen, Switzerland). MCF-7 DOX cells were cultured in the presence of 1 µg/ml doxorubicin (LC Laboratories, USA) in order to maintain the drug-resistance phenotype. When cells are confluent inside 75 cm^2 cell culture flasks, cells were detached with 0.25% trypsin/EDTA (Invitrogen, Switzerland), counted with hemacytometer (Sigma-Aldrich, Switzerland), and loaded inside the wells.

Glass chips (electrodes) were autoclaved and poly(methylmethacrylate) (PMMA) wells (inner diameter = 10 mm and height = 8 mm) were disinfected with 70% ethanol before use. For each electrode chip, one PMMA well was attached on it with polydimethylsiloxane (PDMS) (Figure 1). 400 µl of cell suspension with 1 million.ml^{-1} cell density was seeded inside the well. 400000 cells on each electrode chip were sufficient enough to cover the inside part of the wells (5095 cells/mm2). The device was placed into the CO$_2$ incubator and connected to an impedance analyzer (Agilent 4294A, Agilent technologies, USA) via coaxial cables, which pass through a small hole at the back of the incubator, connecting the inside of the incubator to the outside equipment.

After seeding the cells, both cell lines attached on the electrodes within 10 h as was monitored by impedance spectroscopy (Figure S2). Cells reached confluency resulting in a constant impedance
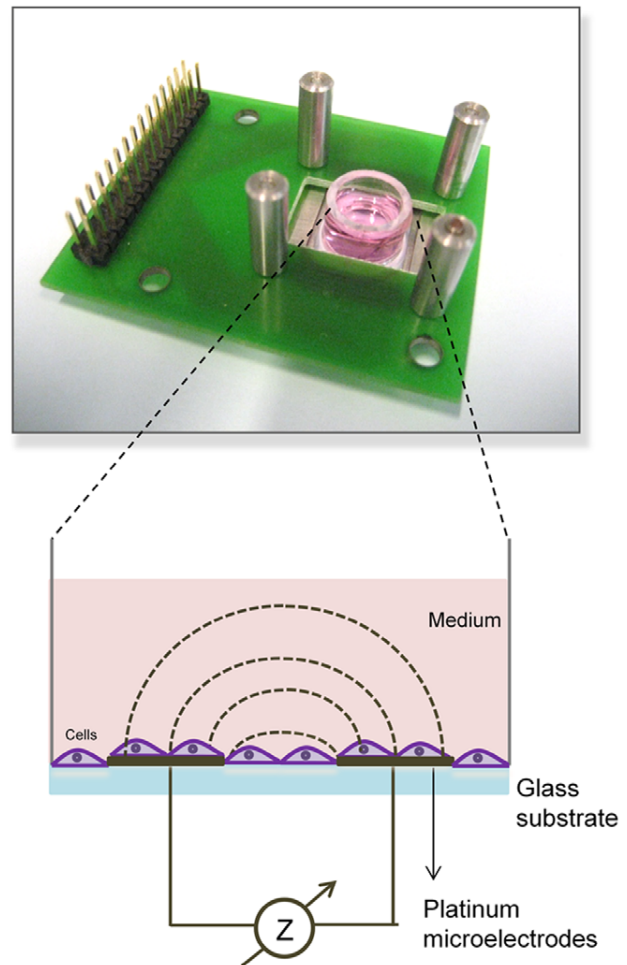
Figure 1. Cell culture well platform and electrical interface (top). Schematic of cell culture on microelectrodes (bottom). doi:10.1371/journal.pone.0057423.g001

signal. Potential cell proliferation in z-direction (multilayer) did not lead to further impedance increase since the current density of the electric field is not strong enough to impact the impedance signal (larger distance from electrodes). Then, doxorubicin was dissolved in cell medium and added to the wells at different concentrations (from 0.005 µM to 40 µM for MCF-7 WT and from 2 µM to 100 µM for MCF-7 DOX). The drug treatment for both cell lines was performed for 48 h. Impedance spectra were recorded from 100 Hz to 30 MHz (10 mV amplitude, 0 mV bias) using Matlab software [33]. The impedance measurements were performed at 10 mV since it corresponds to an electric field of 5 V cm^{-1} close to the electrode surface, which is three orders of magnitude lower than the membrane permeation limit of 1–4 kV cm^{-1} [34] and can be considered as safe.

Equivalent Electrical Circuit Modeling for Cell Type Characterization

The electrical properties of a cell can be described with an electrical circuit, which has a membrane capacitor C_m with a series intracellular resistance R_{intra} and a parallel extracellular resistance R_{extra} [35]. C_m is replaced by a constant phase element (equation (1)) since a cell population might have variations in their properties and those of their microenvironments exerting heterogeneity

within the same cell population and might result in a number of equivalent circuits with different time constants [36–38].

$$CPE_{cells} = \frac{1}{\beta_{cells}(j\omega)^{\alpha_{cells}}} \qquad (1)$$

where β_{cells} is the magnitude and α_{cells} is the exponent component of CPE_{cells}, ω is the circular frequency and j the imaginary number. The electrode–electrolyte interface is represented by an electrode constant phase element CPE_{el}, which describes the non-ideal capacitive behavior of the electrode due to surface roughness [39] and protein adsorption [40] on the metal surface. C_{par} is the parasitic capacitance between the electrodes. This equivalent circuit model (Figure 2a) was shown to have a good correlation with measured impedance spectrum (Figure 2b). The weighted sum of squares (WSS) was calculated as 0.2247 based on the following equation (2).

$$WSS = \sum \frac{\left((\text{Re,Im})_{model} - (\text{Re,Im})_{observation}\right)^2}{|Z|_{observation}} \qquad (2)$$

Cell-dependent circuit components such as R_{extra}, R_{intra}, CPE_{cells} (α_{cells} and β_{cells}) were obtained based on the fitting of the impedance data to the equivalent circuit model. First, the impedance spectra of the medium without cells were fitted and CPE_{el} and C_{par} were obtained as $5.5 \pm 0.9 \times 10^{-8}$ $\Omega^{\alpha-1}F^{\alpha}$ and $(9.7 \pm 0.9) \times 10^{-12}$ F respectively. Then, the impedance spectra of both cell lines were fitted and their specific circuit components were compared.

Equivalent circuit fitting is convenient since it allows attributing values to all elements of a specific circuit model and comparing these between different cells. However, for cultures exerting low impedances (such as after drug exposure or low cell density), the fitting process becomes less reliable since more than one solution with low error becomes possible considering the number of free parameters and the less characteristic impedance curves. Therefore, we have chosen to follow-up the raw data at specific frequencies for drug effect analysis as will be described in the next section.

Choice of Measurement Frequencies for Drug Response Studies

For drug response studies, we have recorded impedance data both at low frequency (LF) and high frequency (HF). LF is defined as the frequency before the membrane capacitor is shorted and gives information about the cell exterior. Once the membrane capacitor is short-circuited, the cell membrane is not a barrier to current anymore, the current can pass through the cell interior and information regarding the intracellular resistance can be obtained. Based on this information, the drug response studies for both cell lines were performed to extract both extra- and intracellular properties of cells.

The choice of the two frequencies is based on a whole spectrum analysis as follows. LF is ideally chosen at $f = 0$ Hz in order to avoid the impedance drop caused by the shortening of the membrane capacitor at higher frequencies. However, this is not possible at least for bipolar measurements since the impedance owing to the capacitive double layer at the electrode/electrolyte interface decreases the sensitivity for extracellular effects. Therefore, an intermediate frequency compromising both effects (interface and cell membrane capacitances) needs to be chosen. For this, we have defined LF as the frequency where the difference between the phase angle in the presence and that in the absence of

cells is maximal (ϕ_{LF}) (equation 3).

$$\phi_{LF} = \max_{i=1,\dots,n} \left(\frac{\phi_{cells}(f_i) - \phi_0(f_i)}{\phi_0(f_i)} \right) \qquad (3)$$

where $\phi_{cells}(f_i)$ is the frequency-dependent impedance phase in the presence of cells and $\phi_0(f_i)$ is the one in the absence of cells. n is the total number of frequency points at which the impedance was measured. The impedance magnitude at this maximum phase difference frequency was found to be most sensitive to extracellular resistance changes. In our case, LF was determined as 10 kHz (Figure 2b).

HF, on the other hand, needs to be chosen high enough to avoid the impact of the membrane capacitor. HF was chosen as 2 MHz since at this frequency the phase angle was closest to 0° before being impacted by the parasitic capacitance (Figure 2b).

Half Maximal Inhibitory Concentration (IC_{50}) Calculation

In order to calculate the half maximal inhibitory concentrations (IC_{50}) of MCF-7 WT and MCF-7 DOX cell lines, the normalized $|\mathcal{Z}|_{cells}$ at 2 MHz were plotted *vs.* logarithm of different concentrations of doxorubicin. These inhibitory concentration-response curves were fitted with nonlinear regression by using equation (4) (GraphPad Software, USA) and IC_{50} values were extracted.

$$Y = Y_{bottom} + \frac{Y_{top} - Y_{bottom}}{1 + 10^{(\log(IC_{50}) - X) \cdot m}} \qquad (4)$$

where Y_{bottom} and Y_{top} are the values of the y-axis that correspond to the bottom and the top part of fitting curve repsectively, IC_{50} is half maximal inhibitory concentration, and m is the steepness of the curve (a m of -1 is standard).

Fluorescence Microscopy

For immunohistochemistry staining cells were fixed with 4% paraformaldehyde in phosphate buffer saline (PBS) (Invitrogen, Switzerland) for 20 min. After fixation, cells were treated with 3% BSA/0.1% Triton X-100 (Sigma-Aldrich, Switzerland) for 50 min. For tight junction staining, cells were first incubated with the primary antibody monoclonal rabbit-anti-occludin (1:200, Invitrogen, Switzerland) for 2 h and subsequently with the Cy-2 coupled secondary antibody (1:150, Dianova GmbH, Germany) for 2 h. For E-cadherin staining cells were incubated with the primary antibody monoclonal mouse-anti-E-cadherin (1:150, Invitrogen, Switzerland) for 2 h and followed by the incubation of rhodamine coupled secondary antibody (1:200, Dianova GmbH, Germany) for 2 h. For actin staining, cells were incubated with FITC coupled phalloidin (Sigma- Aldrich, Switzerland) for 2 h. Thereafter; all samples were incubated with 0.1 µg ml^{-1} DAPI in PBS (Sigma-Aldrich, Switzerland) for 30 min. After repeated washing, cells were observed with a confocal laser-scanning microscope (LSM 700 inverted, Zeiss, Germany).

Time-Lapse Microscopy

Both cell lines were cultured in glass bottom culture dishes (MatTek Corporation, USA). After all the cells adhered on the glass bottom, the effect of doxorubicin at different concentrations (from 0.02 to 20 µM) on cells were monitored with time-lapse microscopy (Olympus CellR inverted, Japan) at 37°C and 5% CO_2 during 2 days, taking measurements every 30 min. The cell morphology during drug exposure was investigated with 60× objective and phase contrast mode.
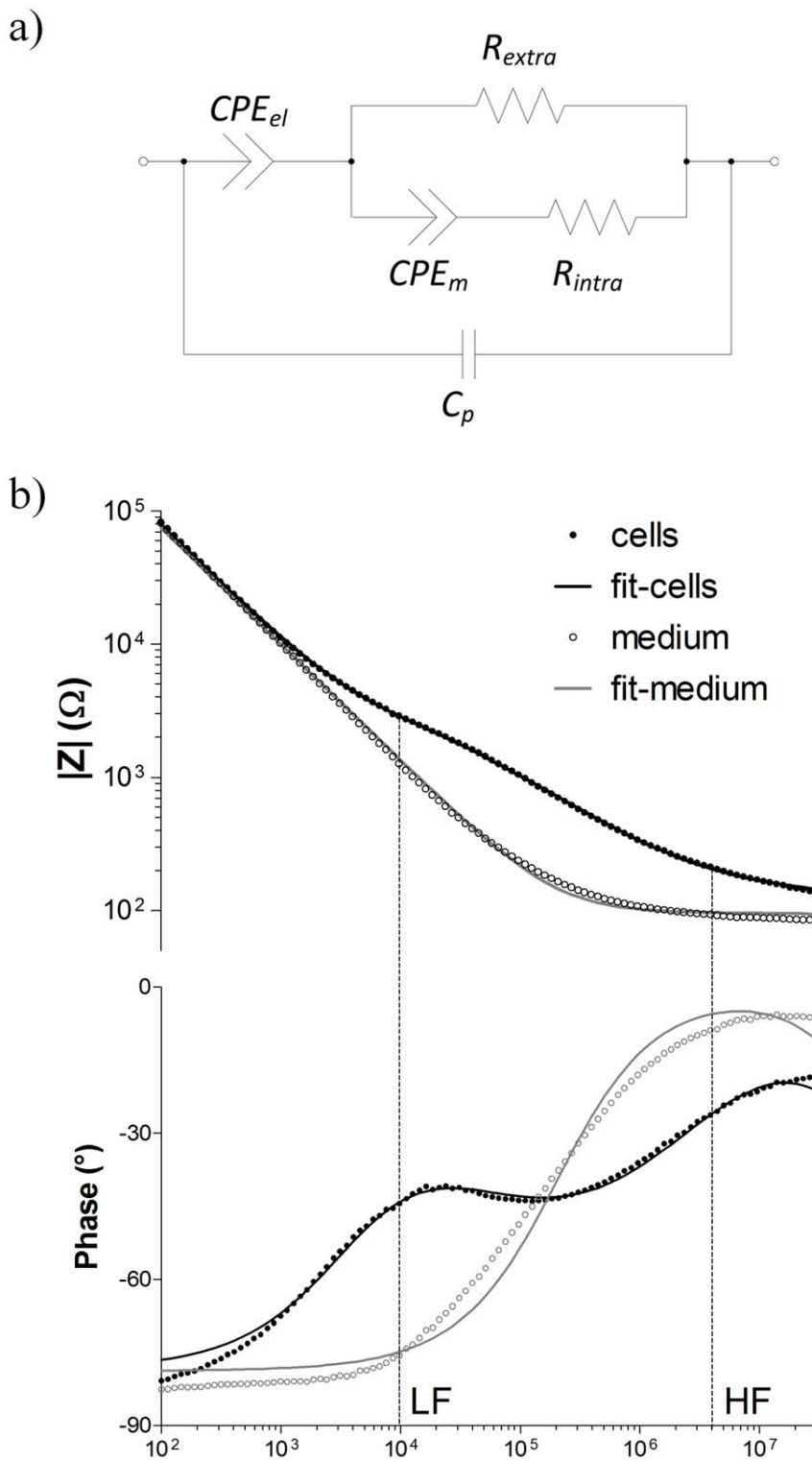
Figure 2. Equivalent circuit modeling. a) The cell population is represented by the Cole-Cole model with an extracellular resistance (R_{extra}) in parallel to the tissue constant phase element (CPE_{cells}) and a high frequency intracellular current pathway (R_{intra}). The electrode/electrolyte interface is modeled by a constant phase element ($CPE_{electrode}$). A parallel capacitance (C_{par}) characterizes parasitic current shunts at high frequency. b) Impedance plot of MCF-7 cell culture. LF and HF refer to the low and high frequency respectively that were followed-up in this study. The equivalent circuit was used to fit the impedance and phase angle plots. (Weighted Sum of squares = 0.2247).
doi:10.1371/journal.pone.0057423.g002

Statistical Analysis

Dielectric components of cells such as R_{extra} obtained for MCF-7 WT cells in 35 different chips and MCF-7 DOX cells in 20 different chips were expressed as means with 95% confidence interval. Statistical analysis of R_{extra} was compared between MCF-7 WT and MCF-7 DOX cell populations using unpaired t-test. The observed importance level (p-value) of the difference between two means was considered significant when p<0.001.

Results

MCF-7 DOX and MCF-7 WT Cells Possessed Different Extracellular Properties

We investigated whether doxorubicin resistant MCF-7 cells (MCF-7 DOX) can be singled out from their parental cells (MCF-7 WT) or not based on their dielectric properties. In order to reach this goal, the impedance spectra of MCF-7 WT and MCF-7 DOX cells with equal cell density were fitted in the absence of drug. Figure 3 shows the values of the fitted circuit components (R_{extra}, R_{intra}, magnitude β of CPE_{cells}) for both wild type and drug resistant cells. Although R_{intra}, and β showed negligible change when the cells gained resistance to doxorubicin, we observed a significant difference in R_{extra} between these two. MCF-7 DOX cells exhibited 50% increase in R_{extra} compared to MCF-7 WT cells when both were cultured at confluency on platinum electrodes.

In order to find out the reason behind the increase of R_{extra} when the MCF-7 WT cells gain drug resistance, we investigated the nature of MCF-7 cellular tight junctions, adhesive junctions and cytoskeleton structure by occludin staining, E-cadherin staining and actin labeling respectively (Figure 4). The presence of tight and adhesive junctions was confirmed for MCF-7 WT cells. Occludin and E-Cadherin labeling was intense and formed a continuous line at the cell contacts. No E-Cadherin could be identified for MCF-7 DOX cells and tight-junctions were very rare. Immunocytochemical staining of actin cytoskeleton revealed significant structural changes between MCF-7 WT and MCF-7 DOX cells. Drug resistant cells exhibited a highly dense fiber-like network of actin filaments while MCF-7 WT cells showed much less labeling for F-actin protein.

MCF-7 DOX and MCF-7 WT Cells Displayed Different Impedance Response to Doxorubicin at Low and High Frequency

The effect of doxorubicin on MCF-7 WT and MCF-7 DOX was studied separately at LF and HF. First, MCF-7 WT and MCF-7 DOX cells were exposed to a 20 μM concentration of doxorubicin during one day of continuous exposure. Figure 5 shows time dependent impedance magnitude changes at 10 kHz. The impedance response to doxorubicin of both cell lines is substantially different. While MCF-7 WT cells were severely affected by the drug at this concentration, MCF-7 DOX cells showed increasing impedance magnitudes under drug exposure within 24 h. Control experiments showed that both MCF-7 DOX and MCF-7 WT cells were healthy in the absence of drug and displayed relatively unchanged impedance profiles within 24 h. In order to make sure the impedance magnitude changes originate from doxorubicin-induced cellular changes, not from the presence of doxorubicin in the cell medium itself, the spectra of cell medium with and without drug were recorded as a control experiment. Only a 5% increase was observed in the impedance when 20 μM doxorubicin was introduced to the cell medium (Figure S3). This is negligible compared to the observed increase of the impedance in the presence of cells. In addition, the temporal evolution of $|Z|$ of 20 μM doxorubicin in cell medium also did not show any change when there are no cells inside the wells (Figure S3).

Doxorubicin treatment with different concentrations was performed with MCF-7 WT cells but one-day drug exposure was enough to obtain significant cellular changes for highly sensitive MCF-7 WT cells. Doxorubicin was dissolved in cell medium and added to the cells at different concentrations (from 0.005 μM to 40 μM for MCF-7 WT and from 2 μM to 100 μM for MCF-7 DOX). As seen in Figure 6a, The LF signal exhibited an increase in the presence of low drug concentrations when HF signal was unaltered. When cells were exposed to higher drug concentrations, the LF signal reversed its direction and started decreasing after 0.02 μM drug intake, while HF signal did not change significantly up to 2 μM drug exposure and decreased much later than LF signal. Figure S4 also supports the correlation between LF and HF signals and the drug induced morphological changes of MCF-7 WT as a function of drug concentrations.

On the other hand, since MCF-7 DOX cells are highly resistant; their temporal evolution was monitored during drug
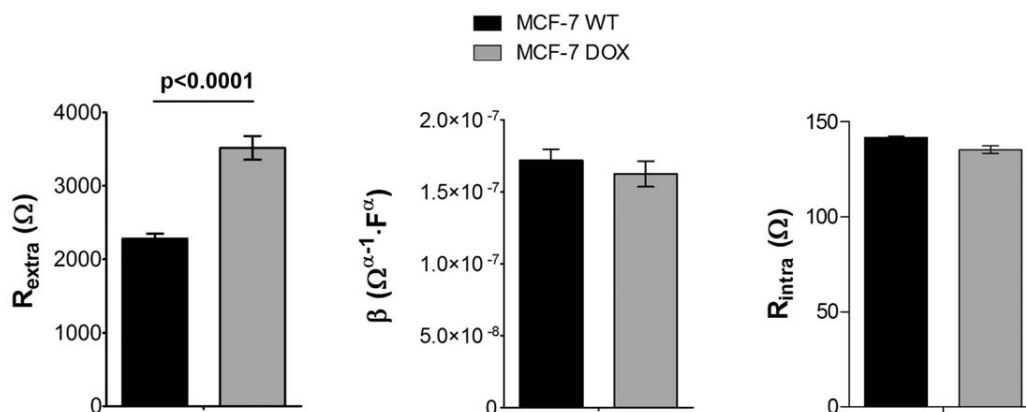
Figure 3. Comparison of the dielectric components of MCF-7 WT and MCF-7 DOX cells (mean ± SEM). a) The resistant cells display a significant increase in R_{extra} compared to the wild type cells (p<0.0001). b) and c) The magnitude β of CPE_{cells} and R_{intra} do not show significant alterations when the cells gain drug resistance. (n=35 for MCF-7 WT and n=21 for MCF-7 DOX cells, cell constant=3660±50 m^{-1} and σ_{medium}=361 mS.cm^{-1}, substrate: platinum).
doi:10.1371/journal.pone.0057423.g003
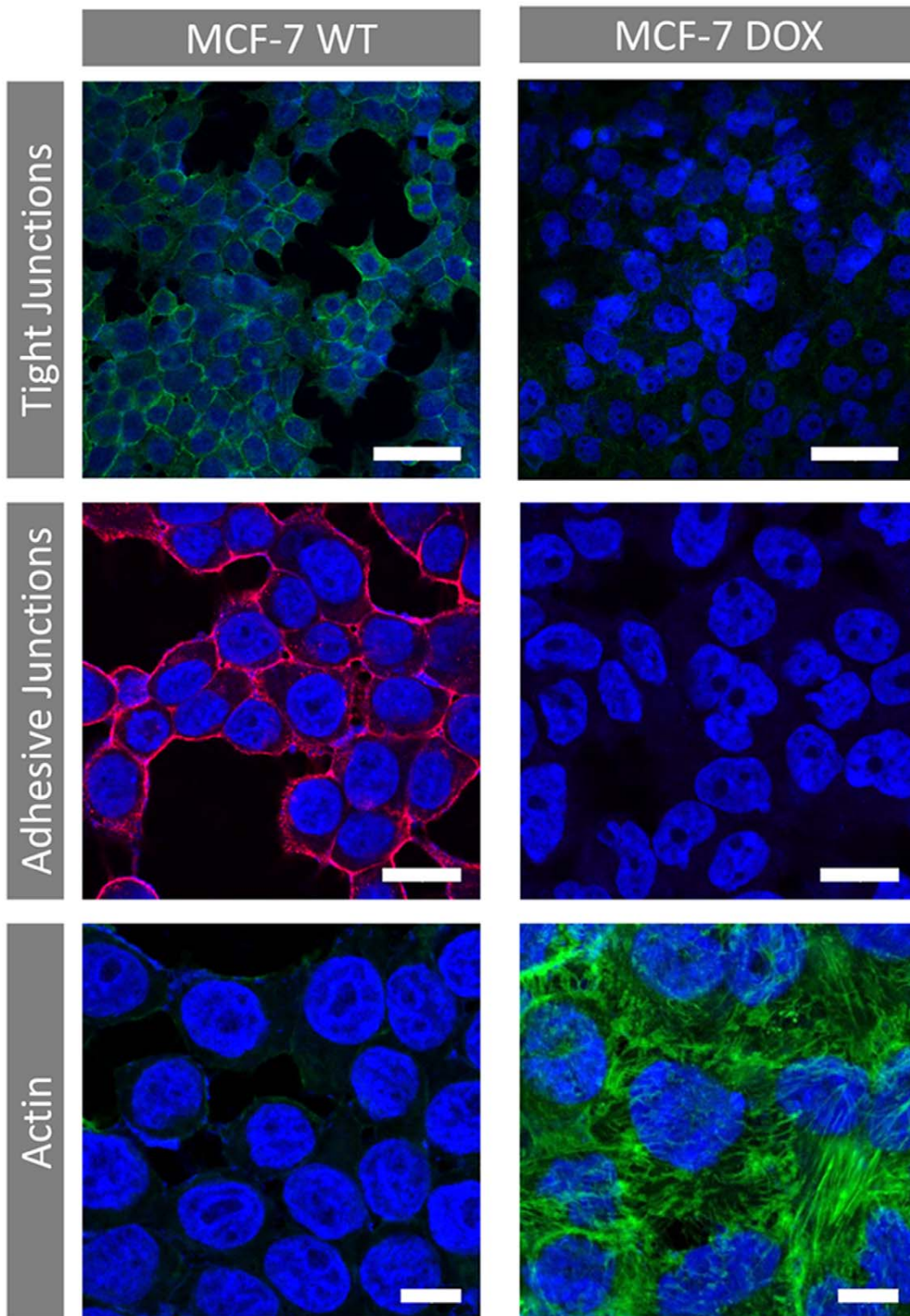
Figure 4. Immunocytochemical staining of cellular tight junctions (bar = 50 μm, green: occludin-Cy-2, blue: DAPI), adhesive junctions (bar = 20 μm Red: E-cadherin - Rhodamine, blue: DAPI) and actin (bar = 10 μm, green: Phalloidin-FITC, blue: DAPI) for MCF-7 WT and MCF-7 DOX cells. Loss of tight junctions and adhesive junctions is observed upon gaining drug resistance. No E-cadherin was identified for MCF-7 DOX cells. Drug resistant cells displayed a highly dense fiber-like network of actin filaments and more cell-to-cell contact compared to MCF-7 WT cells.
doi:10.1371/journal.pone.0057423.g004
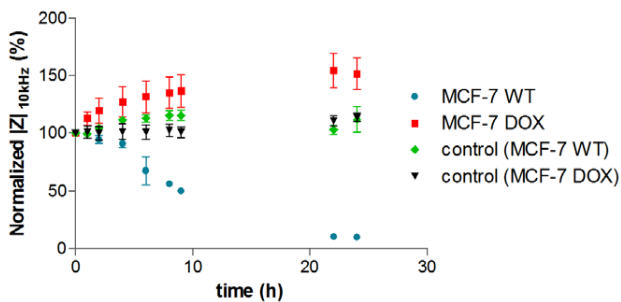
Figure 5. Drug response of MCF-7 WT cells and MCF-7 DOX cells to 20 μM doxorubicin during 24 h at LF (10 kHz). Data points (mean ± SEM, n = 5) were normalized to the magnitude value at t = 0 h. The impedance drops sharply at LF for MCF-7 WT cells, indicating that 20 μM doxorubicin is strong enough to induce toxic effects, while cells in the absence of drug (control) were healthy and LF signal was relatively unchanged. On the other hand, MCF-7 DOX cells displayed increasing impedance compared to their control indicating resistance to this drug concentration and demonstrating the substantial differences in the drug response of MCF-7 WT cells and their drug resistant phenotypes.
doi:10.1371/journal.pone.0057423.g005

exposure for a longer period of time (48 h). LF signal showed considerable increase up to 20 μM drug exposures while HF signal displayed a slight increase up to the same drug concentration (Figure 6b). Figure S5 also confirms that MCF-7 DOX cells were healthy and dense, all adhered on the platinum electrodes after 24 h of 20 μM drug exposure. High concentrations of doxorubicin (from 40 μM to 100 μM) lead to an impedance drop at both LF and HF, revealing similar kinetics and decreasing sharply at both frequencies.

In addition, concentration-response curves were obtained by plotting $|\mathcal{Z}|$ at 2 MHz after 48 h of drug exposure vs. different drug concentrations. The half maximal inhibitory concentrations (IC_{50}) for both MCF-7 WT and MCF-7 DOX cells were extracted from the fit to sigmoid concentration-response curves as shown in Figure 7. IC_{50} values were obtained as 0.4 μM and 70 μM for wild-type cells and drug resistant cells respectively.

MCF-7 DOX and MCF-7 WT Cells Showed Remarkable LF Impedance Increase at Nontoxic Drug Doses

MCF-7 DOX cells showed a concentration-dependent impedance increase when they were exposed to drug concentrations between 2 μM and 20 μM and such impedance increase with respect to the control was more pronounced at LF with very little difference obtained at HF (Figure 6b and 8a). When the drug was replaced with medium after MCF-7 DOX cells were exposed to such concentrations of doxorubicin for 48 h, the impedance signals retrieved back to their initial magnitudes (Figure 8b). In addition, a step-wise increase of the drug concentration also leads to a sequential increase of $|\mathcal{Z}|$ (Figure 8c). The subsequent exposure of the resistant cells to first 5 μM and then 20 μM doxorubicin concentrations (each for 24 h) resulted in a step-wise increase of $|\mathcal{Z}|$; finally the signal dropped back to its initial value after incubating the cells in medium for 1 h.

Such an impedance increase at nontoxic drug concentrations was also observed for MCF-7 WT cells (Figure 6a). MCF-7 WT cells displayed higher impedance when they were exposed to the nonlethal drug concentrations such as 2 and 5 nM compared to the same cells in the absence of drug (control). Such an increase was observed only at LF while HF signal showed negligible change in the presence of non-lethal drug concentrations.
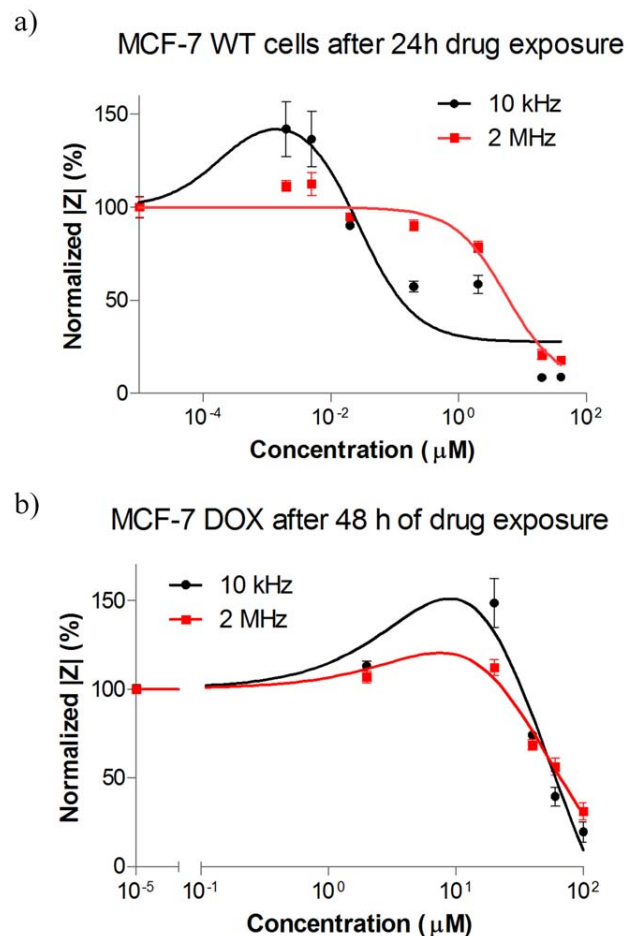
Figure 6. Normalized |Z| vs. different concentrations of doxorubicin at LF (10 kHz) and HF (2 MHz) for a) MCF-7 WT: the LF and HF signals exhibit different profiles with respect to different drug concentrations. At low drug concentrations, the LF signal increased when HF signal was unaltered. At mild drug concentrations such as 0.2 μM doxorubicin, the LF signal decreased with no change in HF signal. At high drug concentrations such as 20 μM and 40 μM doxorubicin both LF and HF signal decreased sharply, showing similar kinetics. b) MCF-7 DOX: the LF signal increases at non-lethal drug concentrations when HF signal exhibited a slight increase. At high drug concentrations such as 40 μM and higher, the LF and HF signal displayed similar impedance profiles and dropped sharply. The plots were fitted by nonlinear regression based on the equation for bell-shaped concentration response only for visual presentation. Data points (mean ± SEM, n = 5) were normalized to the magnitude value at t = 0 h.
doi:10.1371/journal.pone.0057423.g006

Discussion

In the present study, we have demonstrated that impedance spectroscopy is a simple and useful technique that distinguishes drug resistant cells from their parental cells based on their dielectric properties. Drug resistant variants were shown to exert higher extracellular resistance. It was found that actin cytoskeletal remodeling might play an important part in higher extracellular resistant behavior of MCF-7 DOX cells, providing stronger cellular architecture. Moreover, we have screened concentration and time dependent effects of doxorubicin on cell interior and exterior of breast cancer cells at earlier and later stages of the disease. Our experiments indicate four distinct drug concentration
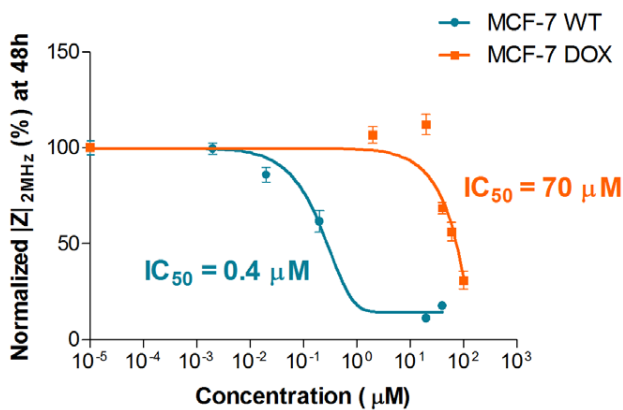
Figure 7. Concentration-response curves are obtained by plotting $|Z|$ at 2 MHz after exposing the cells to various concentrations of doxorubicin. The data was fitted to a sigmoid model. Based on the resulting fit, IC_{50} values were obtained as 0.4 µM and 70 µM for MCF-7 WT and MCF-7 DOX respectively. Data points (mean ± SEM, n = 5) were normalized to the magnitude value at t = 0 h. doi:10.1371/journal.pone.0057423.g007

ranges that display particular dielectric responses of the cells under drug exposure.

Distinction of Drug Resistant Cells with their Cell Dielectric Properties

We investigated the dielectric properties of MCF-7 DOX cells and MCF-7 WT cells. Based on fitting their impedance profiles with the equivalent circuit model, both cell lines exhibited similar R_{intra} and β indicating that there were no measurable alterations in the electrical properties of the cell membrane and cytosol when MCF-7 cells gain drug resistance. However, drug resistant cells displayed 50% increase in R_{extra}, implying significant changes in the cell morphology and structure upon drug resistance. The finding with R_{extra} is a novel result, however quite unexpected. R_{extra} for drug resistant cells was expected to be lower since loss of tight junctions and absence of E-cadherin in MCF-7 DOX cells (Figure 4) should have resulted in shunting of the current flow through the intercellular space and thereby lowering the R_{extra}. On the other hand, actin staining shows that MCF-7 DOX cells possessed highly dense F-actin network and had elongated form of

actin fibers in cytoplasm up to cell peripheral region, while MCF-7 WT cells had peripheral actin, which is much less dense in their cellular structure. These results suggest that remodeling of the actin cytoskeleton might probably be the reason behind the higher extracellular resistance when MCF-7 cells become resistant to doxorubicin and when seeded at confluence on platinum electrodes. In fact, in cell culture on stiff substrates, the actin cytoskeleton tends to organize in stress fibers [41]. Doxorubicin treatment disrupts such fiber-like organization [42,43] leading to cell–substrate detachment [44].

Hence, the actin network is a crucial and complex system that provides base and support to retain cell morphology and mechanical structure [45]. The extracellular and phenotypical events of a metastatic carcinoma are mainly governed by structural reorganization of actin [46,47]. If the MCF-7 cells use the reorganization of the actin cytoskeleton to become resistant to doxorubicin, then a question may arise about the role of dynamic actin remodeling on transformation of a cancer cell to a drug resistant phenotype. Some studies showed that actin remodeling may play a part in inactivation of some actin binding proteins such as E-cadherins [48,49] and gelsolin [50] that have tumor-suppressor functions, and activation of actin signaling pathways that leads to malignant phenotypes such as pathways involving Ras [51] and Src [52] proteins. A recent study showed lower cell stiffness upon disrupting the actin cytoskeleton with an inhibitor of actin polymerization, implying the importance of actin remodeling in drug-mediated cell stiffness modulation and drug resistance [53]. However, it is still unclear if such highly dense F-actin network participates in drug efflux by limiting the drug intake by drug resistant cells or if such organization of F-actin filaments participates in drug efficacy through influencing the cell membrane physical properties. In addition, such actin reorganization might be a consequence of drug-induced phenotypic events of a signaling pathway that leads to drug resistance. The exact effect of actin remodeling on the drug resistance remain to be elucidated and was not our focus here, thereby was not conducted in the framework of this study.

Overall, the drug resistant cells were distinguished from their parental cells based on their higher extracellular resistance. Such detection of drug resistant cells based on their dielectric properties might allow assessing the stage of the disease by selective recognition of certain phenotypes and designing the optimum personalized treatment based on the disease progress.

Figure 8. Effect of stimulatory non-toxic drug concentrations on MCF-7 DOX. a) MCF-7 DOX exhibits a concentration-dependent increase in impedance magnitudes during drug treatment with nontoxic concentrations. The plot was fitted by nonlinear regression using exponential decay equation only for visual presentation. b) Impedance magnitudes vs. time plots of MCF-7 DOX cells when 20 µM doxorubicin was applied for 48 h and followed by medium washing for 24 h. This shows that the impedance increase is reversible when the drug is removed. c) Temporal evolution of $|Z|$ when resistant cells were exposed to 5 µM doxorubicin for 24 h, followed by 20 µM drug concentration for 24 h, then medium washing as a last step for 1 h. This shows that the impedance increase can be sequentially added up; once the stress on cells is removed, the initial state of extracellular environment is reobtained. Data points (mean ± SEM, n = 5) were normalized to the magnitude value at t = 0 h. doi:10.1371/journal.pone.0057423.g008

MCF-7 DOX Displayed a 175 Times Higher Drug Resistance

The drug response of MCF-7 DOX cells was compared with the one of MCF-7 WT cells. It was observed that only strong doxorubicin concentrations such as 40 μM and higher could decrease the LF and HF impedance signal of MCF-7 DOX within 48 h (Figure 6b). MCF-7 WT cells, on the other hand, already displayed an impedance decrease at much lower concentration such as 0.2 μM after 24 h (Figure 6a), showing that MCF-7 DOX cells are more resistant to doxorubicin.

Based on the concentration response curves of these two cell lines (Figure 7), MCF-7 DOX cells exhibited a 175 times higher IC_{50} value than that of MCF-7 WT cells, which is consistent with the findings of Mehta et al. who obtained more than 150 times more resistance with MCF-7 DOX cells compared to their parental cells by applying conventional viability assay to the same cell lines [11]. This shows that impedance screening offers a highly sensitive label-free technique that can assess the effect of a drug on the different phenotypes of the same cell type with high accuracy.

Impedance Profiles Revealed Four Distinct Drug Responses within Specific Ranges of Drug Concentrations

We already showed in our previous study that LF and HF impedance signals exhibited different kinetics when cells were exposed to drug, revealing different information about cell properties [25]. In this study, we also observed different temporal evolutions at LF and HF when MCF-7 WT cells were exposed to 0.2 μM and higher doses of doxorubicin (Figure 6a). At LF cell membranes block the current from flowing inside the cells, acting as capacitors. Such densely packed insulating cell layer exerts a high extracellular resistance and this resistance is prone to change when stress is applied on cells. The extracellular resistance drops when cell-substrate and cell-cell contacts are weaker due to the contraction of cells in the presence of drug and current flows through the intercellular space more easily. This phenomenon is the reason why the LF signal decreases upon interaction with drug [25] and renders this method much more sensitive to toxic effects compared to traditional viability assays since drug toxicity can be sensed long before cell death takes place (see Figure 4 in [10]). On the other hand, the cell membrane capacitor shortcuts at HF and cell interior contribute to the measured impedance more significantly. As we already discussed in our earlier study [25] when cells are dying, the intra- and extracellular matters exchange due to the pore formation during cell death, resulting in more conductive cytosol with the influx of more conductive cell medium [28], and thus lower HF impedance signal.

In addition to the difference between LF and HF profiles, we have observed two more distinct responses at LF within specific concentration ranges (Figure 9). First, the drug has no effect, resulting in unaltered LF and HF signal. Second, at higher nontoxic drug concentrations, an increase in impedance at LF is observed. The cell morphology might adapt itself in a way that cells show stimulatory response upon drug interaction and impede the current more with enhanced cell-substrate contact, resulting in higher impedance at LF while HF signal remains the same. When the drug is toxic at higher concentrations, there are two circumstances that need to be taken into account. At mild inhibitory drug doses, there might be an intermediate phase where drug induced morphological changes might result in lower LF while cell interior is unaffected with no change in HF signal. At higher toxic concentrations, drug might induce substantial changes in the extracellular and intracellular environment, reflecting in

sharp and simultaneous decrease in both LF and HF signal. These findings indicate that impedance spectroscopy not only distinguishes minor morphological changes from major cellular damage based on different kinetics of LF and HF signal, but also provides useful information when applying non-toxic drug concentrations, i.e. distinguishing concentrations that induce a stimulatory response from the concentrations that result in no measurable effect.

Impedimetric Measurements Revealed Enhanced Cell Stiffness at Non-toxic Drug Concentrations

When low concentrations of doxorubicin (2–5 nM for MCF-7 WT and 2–20 μM for MCF-7 DOX) were added to the cell medium, $|\mathcal{Z}|$ showed remarkable increase, especially at LF, compared to that of cells in the absence of drug (Figure 6). The HF signal was relatively unchanged. In addition, there was no impedance change when such drug concentrations were added to the cell medium itself in the absence of cells. These results imply that drug at low and non-toxic concentrations might influence the biophysical and biomechanical properties of cells as hypothesized in Figure 9 and the cellular structure might adapt its organization in a way to fight against the drug by gaining cell stiffness. In fact, while a disease state causes biological and functional changes in cells, it also leads to the significant changes in the morphological properties of cells [54]. Cytoskeletal actin has a crucial role in governing mechanical properties of cells [55,56] and it is prone to dynamic changes during progression of cancer in all forms [54]. Some studies showed increased cell stiffness when normal cells evolve to be cancerous cells [57] and some showed reduced cell stiffness upon metastasis using different biomechanical assays [58,59]. Moreover, it was revealed that chemotherapy drugs such as taxol and cisplatin resulted in the increase in cell stiffness of metastatic cancer cells [60] and increased cell stiffness of drug
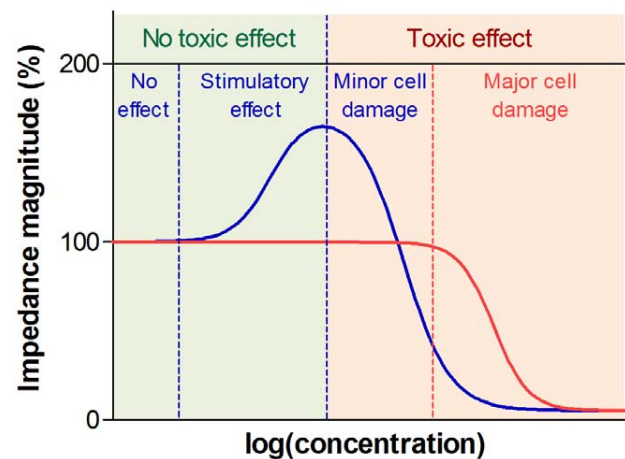
Figure 9. Hypothesized impedimetric concentration response map. (1) At low nontoxic drug concentrations, the drug has no effect on cells, which results in unchanged LF and HF signal. (2) There is a drug concentration range where stimulatory effect takes place and reflects in higher impedance owing to the changes in the cellular structure and cell-cell interaction. (3) At toxic drug concentrations, there are two different circumstances that need to be taken into account. (3) At mild drug concentrations, the drug induces minor morphological changes while cell interior is intact, reflecting in lower LF with HF remaining the same. (4) At high inhibitory concentrations, the LF and HF signal drop sharply due to the substantial morphological changes and major cell damage.
doi:10.1371/journal.pone.0057423.g009

sensitive ovarian cancer cells upon sublethal concentrations of cisplatin was shown by using atomic force microscopy (AFM) [53]. Here, we also observed pronounced and intense changes in the actin cytoskeleton structure and organization when cells gain drug resistance. This indicates that cell stiffness might play an important part behind the 50% increase of $|\mathcal{Z}|$ in the presence of non-toxic concentrations of doxorubicin, but possibly other factors regarding drug-induced extracellular events might also contribute to such an impedance increase at LF.

In addition, it was shown that the drug-induced impedance increase is concentration-dependent (Figure 8a) and reversible (Figure 8b and 8c). This implies that the drug itself might induce a direct effect on cellular structure, and/or cells might temporarily adopt a protection mechanism against the drug effects by their structural reorganization *via* actin remodeling. Overall, potential stimulatory drug effects such as cell stiffness were measured during the continuous exposure of cells to the nontoxic drug concentrations. These findings suggest that impedance spectroscopy is suitable for detecting and quantifying the increasing cell stiffness of drug sensitive cancer cells upon drug exposure and sensing the alterations of biomechanical properties of cancer cells on the onset of drug resistance.

Conclusions

In conclusion, we demonstrated that drug resistant breast cancer cells could be distinguished from their parental cell population based on the differences in their dielectric properties such as R_{extra}. It was also shown that these two cell lines demonstrate a sharply different impedance response to doxorubicin. Moreover, a reversible increase in the cell stiffness in the presence of nontoxic drug concentrations could be measured using impedimetric measurements, indicating that structural reorganization of F-actin due to the drug could play a significant role on the onset of gaining drug resistance. Such stimulatory response with simultaneous LF and HF analysis enabled the creation of an impedimetric cellular drug response map. Future investigations might include testing heterogeneous tissue samples from patients and the use of multiple assays running in parallel within an automatic system in order to develop a high-throughput platform that meets the needs of laboratory diagnostics and pharmaceutical industry more comprehensively.

Overall, impedance screening is a trendsetting technique owing to a number of striking advantages including label-free, non-destructive, cost-effective and continuous cell characterization. From this point of view, cell-based impedimetric sensing opens new avenues in personalized medicine to create new classes of detection devices for drug induced cellular events. Such sensing of cellular phenomena using impedance analysis combined with real-time imaging might represent a useful technique for identification of cancer cells at different stages and their interaction with drug during the disease. Thus, such miniaturized devices could be useful for personalized medicine applications to identify the disease progress and optimize the drug treatment of a patient during chemotherapy.

References

1. Adrienne K (2002) Breast Cancer: Increasing Incidence, Limited Options. OutLook 19: 1–8.
2. Simstein R, Burow M, Parker A, Weldon C (2012) Experimental Biology and Medicine Cancer: Insights From the MCF-7 Cell.
3. Kaufmann SH, Vaux DL (2003) Alterations in the apoptotic machinery and their potential role in anticancer drug resistance. Oncogene 22: 7414–7430. Available: http://www.ncbi.nlm.nih.gov/pubmed/14576849. Accessed 2012 Nov 11.
4. Tu Y, Xu FH, Liu J, Vescio R, Berenson J, et al. (1996) Upregulated expression of BCL-2 in multiple myeloma cells induced by exposure to doxorubicin,

Supporting Information

Figure S1 Electrode design; a bipolar interdigitated electrode (IDE) pair were adapted to six-filter configuration to maximize electrode surface coverage for high-sensitivity impedance measurement of the cell culture area. Total of 54 electrode fingers are provided for each electrode (w = 10 µm, l = 100 µm) separated by a gap of 15 µm.
(TIF)

Figure S2 Cell adherence on microelectrodes monitored as a function of time by impedance spectroscopy at 10 kHz for a) MCF-7 WT b) MCF-7 DOX. Imaging of cell culture on microelectrodes before drug treatment for c) MCF-7 WT and d) MCF-7 DOX.
(TIF)

Figure S3 a) The impedance profile of cell medium with and without doxorubicin in the absence of cells at 10 kHz as a control experiment. 5% increase in the impedance magnitude was observed when 20 µM drug was introduced to the cell medium; b) The temporal evolution of |Z| of 20 µM doxorubicin in cell medium in the absence of cells, no change was observed in the impedance as a function of time at 10 kHz.
(TIF)

Figure S4 Imaging of MCF-7 WT cells on microelectrodes before and after drug treatment of a) 0.2 µM doxorubicin b) 2 µM doxorubicin c) 20 µM doxorubicin. (a) 8 h and 24 h of 0.2 µM drug treatment caused morphological changes such as cell retraction (blue arrow) but no cell death was observed (b) Cell retraction (blue arrow) and formation of wider intercellular gaps (red arrow) were observed after 8 drug treatment and some cell death occurred (black arrow) after 24 h of 2 µM drug treatment. (c) Severe morphological changes (red arrow) and cell death (black arrow) took place both after 8 h and 24 h treatment of 20 µM doxorubicin.
(TIF)

Figure S5 Imaging of MCF-7 DOX cells on microelectrodes before and after drug treatment of a) 20 µM doxorubicin; no cell death was observed after 24 h and cells were healthy and highly densely packed on the microelectrodes. b) No doxorubicin (control); cells were healthy and densely packed after 24 h.
(TIF)

Acknowledgments

Author Contributions

Obtained permission for use of cell line: KM. Review of the manuscript: AB. Conceived and designed the experiments: BE RM PR. Performed the experiments: BE RM. Analyzed the data: BE RM PR. Contributed reagents/materials/analysis tools: KM AB PR. Wrote the paper: BE RM.

    etoposide, and hydrogen peroxide. Blood 88: 1805–1812. Available: http://www.ncbi.nlm.nih.gov/pubmed/8781438.
5. Kitada S, Pedersen IM, Schimmer AD, Reed JC (2002) Dysregulation of apoptosis genes in hematopoietic malignancies: 3459–3474. doi:10.1038/sj/onc/1205327.
6. Moscow JA, Dixon KH (1993) Glutathione-related enzymes, glutathione and multidrug resistance. Cytotechnology 12: 155–170. Available: http://www.ncbi.nlm.nih.gov/pubmed/7765324.

7. Ueda K, Clark D, Chen C, Roninson IR, Gottesman MM, et al. (1987) The human multidrug resistance (mdr1) gene. cDNA cloning and transcription initiation. Journal of Biological Chemistry 262: 505–508.

8. Blobe GC, Khan WA, Halpern AE, Obeid LM, Hannun YA (1993) Selective regulation of expression of protein kinase C beta isoenzymes occurs via alternative splicing. The Journal of biological chemistry 268: 10627–10635. Available: http://www.ncbi.nlm.nih.gov/pubmed/7683684.

9. Pessina A (1993) Topoisomerase I in multiple drug resistance. Cytotechnology 12: 127–135. Available: http://www.ncbi.nlm.nih.gov/pubmed/7764454.

10. Chen JSK, Konopleva M, Andreeff M, Multani AS, Pathak S, et al. (2004) Drug-resistant breast carcinoma (MCF-7) cells are paradoxically sensitive to apoptosis. Journal of cellular physiology 200: 223–234. Available: http://www. ncbi.nlm.nih.gov/pubmed/15174092. Accessed 10 Nov 2012.

11. Chen JSK, Agarwal N, Mehta K (2002) Multidrug-resistant MCF-7 breast cancer cells contain deficient intracellular calcium pools. Breast cancer research and treatment 71: 237–247. Available: http://www.ncbi.nlm.nih.gov/pubmed/ 12002342.

12. Liu Q, Yu J, Xiao L, Tang J, Zhang Y (2009) Impedance studies of bio-behavior and chemosensitivity of cancer cells by micro-electrode arrays. Biosensors and …. Available: http://www.sciencedirect.com/science/article/pii/ S0956566308003989. Accessed 16 Nov 2012.

13. Wegener J, Keese CR, Giaever I (2000) Electric cell-substrate impedance sensing (ECIS) as a noninvasive means to monitor the kinetics of cell spreading to artificial surfaces. Experimental cell research 259: 158–166. Available: http:// www.ncbi.nlm.nih.gov/pubmed/10942588. Accessed 18 Jan 2011.

14. Lin S-P, Kyriakides TR, Chen J-JJ (2009) On-line observation of cell growth in a three-dimensional matrix on surface-modified microelectrode arrays. Biomaterials 30: 3110–3117. Available: http://www.ncbi.nlm.nih.gov/pubmed/ 19344948. Accessed 18 Jan 2011.

15. Mitra P, Keese CR, Giaever I (1991) Electric measurements can be used to monitor the attachment and spreading of cells in tissue culture. BioTechniques 11: 504–510. Available: http://www.ncbi.nlm.nih.gov/pubmed/1793585. Accessed 18 Jan 2011.

16. Giaever I, Keese CR (1991) Micromotion of mammalian cells measured electrically. Proceedings of the National Academy of Sciences of the United States of America 88: 7896–7900. Available: http://www.pubmedcentral.nih. gov/articlerender.fcgi?artid = 52411&tool = pmcentrez&rendertype = abstract. Accessed 18 Jan 2011.

17. Keese C, Wegener J (2004) Electrical wound-healing assay for cells in vitro. Proceedings of the …. Available: http://www.pnas.org/content/101/6/1554. short. Accessed 16 Nov 2012.

18. Bagnaninchi PO, Drummond N (2011) Real-time label-free monitoring of adipose-derived stem cell differentiation with electric cell-substrate impedance sensing. Proceedings of the National Academy of Sciences of the United States of America 108: 6462–6467. Available: http://www.pubmedcentral.nih.gov/ articlerender.fcgi?artid = 3080969&tool = pmcentrez&rendertype = abstract. Accessed 26 October 2012.

19. Liu Q, Yu J, Xiao L, Tang J, Zhang Y (2009) Impedance studies of bio-behavior and chemosensitivity of cancer cells by micro-electrode arrays. Biosensors and …. Available: http://www.sciencedirect.com/science/article/pii/ S0956566308003989. Accessed 14 January 2013.

20. Arias L, Perry C, Yang L (2010) Real-time electrical impedance detection of cellular activities of oral cancer cells. Biosensors and Bioelectronics. Available: http://www.sciencedirect.com/science/article/pii/S0956566310001144. Accessed 14 January 2013.

21. Susloparova A, Koppenhöfer D, Vu X (2012) Impedance spectroscopy with field-effect transistor arrays for the analysis of anti-cancer drug action on individual cells. Biosensors and …. Available: http://www.sciencedirect.com/ science/article/pii/S095656631200365X. Accessed 14 January 2013.

22. Bartholomä P, Impidjati, Reininger-Mack a, Zhang Z, Thielecke H, et al. (2005) A more aggressive breast cancer spheroid model coupled to an electronic capillary sensor system for a high-content screening of cytotoxic agents in cancer therapy: 3-dimensional in vitro tumor spheroids as a screening model. Journal of biomolecular screening 10: 705–714. Available: http://www.ncbi.nlm.nih.gov/ pubmed/16131482. Accessed 11 November 2012.

23. Chen J, Zheng Y, Tan Q, Shojaei-Baghini E, Zhang YL, et al. (2011) Classification of cell types using a microfluidic device for mechanical and electrical measurement on single cells. Lab on a chip 11: 3174–3181. doi:10.1039/c1lc20473d.

24. Coley HM, Labeed FH, Thomas H, Hughes MP (2007) Biophysical characterization of MDR breast cancer cell lines reveals the cytoplasm is critical in determining drug sensitivity. Biochimica et biophysica acta 1770: 601– 608. doi:10.1016/j.bbagen.2006.12.002.

25. Meissner R, Eker B, Kasi H, Bertsch A, Renaud P (2011) Distinguishing drug-induced minor morphological changes from major cellular damage via label-free impedimetric toxicity screening. Lab on a chip 11: 2352–2361. Available: http://www.ncbi.nlm.nih.gov/pubmed/21647498. Accessed 21 February 2012.

26. Seoane F, Lindecrantz K (2004) Brain electrical impedance at various frequencies: the effect of hypoxia. … in Medicine and …. Available: http:// ieeexplore.ieee.org/xpls/abs_all.jsp?arnumber = 1403674. Accessed 14 Jan 2013.

27. Pauly H, Schwan HP (1959) Uber die Impedanz einer Suspension von kugelförmigen Teilchen mit einer Schale; Ein Modell fur das dielektrische Verhalten von Zellsuspensionen und von Proteinlösungen. Z Naturforsch B 14B: 125–131.

28. Gawad S (2004) PhD thesis (no 3011), École polytechnique fédérale de Lausanne École polytechnique fédérale de Lausanne.

29. Itakura Y, Tajima T, Ohoke S, Matsuzawa J, Sudo H, et al. (1989) Osteocompatibility of platinum-plated titanium assessed in vitro. Biomaterials 10: 489–493. Available: http://www.ncbi.nlm.nih.gov/pubmed/2804237. Accessed 18 Jan 2011.

30. Linderholm P (PhD thesis) (2006) Two-dimensional Microimpedance Imaging for Cell Culture Monitoring École polytechnique fédérale de Lausanne.

31. Mehta K (1994) High Levels of transglutaminase expression in doxorubicin-resistant human breast carcinoma cells. International Journal of Cancer: 400– 406.

32. Devarajan E, Chen J, Multani AS, Pathak S, Sahin A a, et al. (2002) Human breast cancer MCF-7 cell line contains inherently drug-resistant subclones with distinct genotypic and phenotypic features. International journal of oncology 20: 913–920.

33. Mercanzini A, Colin P, Bensadoun J-C, Bertsch A, Renaud P (2009) In vivo electrical impedance spectroscopy of tissue reaction to microelectrode arrays. IEEE transactions on bio-medical engineering 56: 1909–1918. Available: http://www.ncbi.nlm.nih.gov/pubmed/19362904.

34. Isambert H (1998) Understanding the electroporation of cells and artificial bilayer membranes. Physical review letters 80: 3404–3407. Available: http:// link.aps.org/doi/10.1103/PhysRevLett.80.3404. Accessed 28 April 2011.

35. Debye PJW (1929) Polar molecules. Dover New York. Available: http://www. citeulike.org/user/weeks/article/1931205. Accessed 18 Jan 2011.

36. Schwan HP (1985) Analysis of Dielectric Data: Experience gained withbiological materials: 913–922.

37. Grimnes S, Martinsen OG (2005) Cole electrical impedance model–a critique and an alternative. IEEE transactions on bio-medical engineering 52: 132–135. Available: http://www.ncbi.nlm.nih.gov/pubmed/15651574.

38. Cole KS (1940) Permeability and impermeability of cell membranes for ions. Cold Spring Harbor Symposia on Quantitative Biology 8: 110–122. Available: http://symposium.cshlp.org/content/8/110.short.

39. Acta E, Ireland N (1965) The Influence of surface roughness of solid electrodes on electrochemical measurements. 10: 113–130.

40. Stieglitz T (2004) Electrode materials for recording and stimulation. Neuroprosthetics: Theory and Practice: 475–516. Available: http://en.scientificcommons. org/20349729. Accessed 15 Dec 2010.

41. Besser A, Schwarz US (2007) Coupling biochemistry and mechanics in cell adhesion: a model for inhomogeneous stress fiber contraction. New Journal of Physics 9: 425–425. Available: http://stacks.iop.org/1367-2630/9/i = 11/ a = 425?key = crossref.ecbea7e76b72769c1d0b28e0c4ab3e38.

42. Bijman M (2006) agents inhibit angiogenesis at subtoxic concentrations, a process associated with inhibition of Rac1 and Cdc42 activity and changes in the endothelial cytoskeleton. Molecular cancer …. Available: http://mct. aacrjournals.org/content/5/9/2348.short. Accessed 14 Jan 2013.

43. Grzanka D, Domaniewski J, Grzanka A (2005) Effect of doxorubicin on actin reorganization in Chinese hamster ovary cells. Neoplasma. Available: http:// ukpmc.ac.uk/abstract/MED/15739026. Accessed 14 Jan 2013.

44. Pierce RH, Franklin CC, Campbell JS, Tonge RP, Chen W, et al. (2002) Cell culture model for acetaminophen-induced hepatocyte death in vivo. Biochemical pharmacology 64: 413–424. Available: http://www.ncbi.nlm.nih.gov/ pubmed/12147292.

45. Pollard TD, Cooper J a (2009) Actin, a central player in cell shape and movement. Science (New York, NY) 326: 1208–1212. Available: http://www. ncbi.nlm.nih.gov/pubmed/19965462. Accessed 26 Oct 2012.

46. Zhao J, Guan J-L (2009) Signal transduction by focal adhesion kinase in cancer. Cancer metastasis reviews 28: 35–49. Available: http://www.ncbi.nlm.nih.gov/ pubmed/19169797. Accessed 26 Oct 2012.

47. Olson MF, Sahai E (2009) The actin cytoskeleton in cancer cell motility. Clinical & experimental metastasis 26: 273–287. Available: http://www.ncbi.nlm.nih. gov/pubmed/18498004. Accessed 11 Nov 2012.

48. Perl a K, Wilgenbus P, Dahl U, Semb H, Christofori G (1998) A causal role for E-cadherin in the transition from adenoma to carcinoma. Nature 392: 190–193. Available: http://www.ncbi.nlm.nih.gov/pubmed/9515965.

49. Wheelock MJ, Shintani Y, Maeda M, Fukumoto Y, Johnson KR (2008) Cadherin switching. Journal of cell science 121: 727–735. Available: http:// www.ncbi.nlm.nih.gov/pubmed/18322269. Accessed 2 Nov 2012.

50. Rao J (2004) Microfilament actin remodeling as a potential target for cancer drug development. Current cancer drug targets.

51. Downward J (2003) Targeting RAS signalling pathways in cancer therapy. Nature reviews Cancer 3: 11–22. Available: http://www.ncbi.nlm.nih.gov/ pubmed/12509763. Accessed 5 Nov 2012.

52. Winograd-Katz SE, Brunner MC, Mirlas N, Geiger B (2011) Analysis of the signaling pathways regulating Src-dependent remodeling of the actin cytoskeleton. European journal of cell biology 90: 143–156. Available: http://www. p u b m e d c e n t r a l . n i h . g o v / a r t i c l e r e n d e r . fcgi?artid = 3005982&tool = pmcentrez&rendertype = abstract. Accessed 11 Nov 2012.

53. Sharma S, Santiskulvong C, Bentolila L a, Rao J, Dorigo O, et al. (2011) Correlative nanomechanical profiling with super-resolution F-actin imaging reveals novel insights into mechanisms of cisplatin resistance in ovarian cancer

cells. Nanomedicine: nanotechnology, biology, and medicine: 1–10. Available: http://www.ncbi.nlm.nih.gov/pubmed/22024198. Accessed 10 May 2012.

54. Suresh S (2007) Biomechanics and biophysics of cancer cells. Acta biomaterialia 3: 413–438. Available: http://www.pubmedcentral.nih.gov/articlerender.fcgi?artid = 2917191&tool = pmcentrez&rendertype = abstract. Accessed 4 Nov 2012.

55. Satcher RL, Dewey CF (1996) Theoretical estimates of mechanical properties of the endothelial cell cytoskeleton. Biophysical journal 71: 109–118. Available: h t t p : / / w w w . p u b m e d c e n t r a l . n i h . g o v / a r t i c l e r e n d e r . fcgi?artid = 1233462&tool = pmcentrez&rendertype = abstract. Accessed 11 Nov 2012.

56. Janmey P a, Euteneuer U, Traub P, Schliwa M (1991) Viscoelastic properties of vimentin compared with other filamentous biopolymer networks. The Journal of cell biology 113: 155–160. Available: http://www.pubmedcentral.nih.gov/articlerender.fcgi?artid = 2288924&tool = pmcentrez&rendertype = abstract.

57. Cross SE, Jin Y-S, Tondre J, Wong R, Rao J, et al. (2008) AFM-based analysis of human metastatic cancer cells. Nanotechnology 19: 384003. Available: http://www.ncbi.nlm.nih.gov/pubmed/21832563. Accessed 8 Nov 2012.

58. Suresh S, Spatz J, Mills JP, Micoulet A, Dao M, et al. (2005) Connections between single-cell biomechanics and human disease states: gastrointestinal cancer and malaria. Acta biomaterialia 1: 15–30. Available: http://www.ncbi.nlm.nih.gov/pubmed/16701777. Accessed 6 Nov 2012.

59. Guck J, Schinkinger S, Lincoln B, Wottawah F, Ebert S, et al. (2005) Optical deformability as an inherent cell marker for testing malignant transformation and metastatic competence. Biophysical journal 88: 3689–3698. Available: h t t p : / / w w w . p u b m e d c e n t r a l . n i h . g o v / a r t i c l e r e n d e r . fcgi?artid = 1305515&tool = pmcentrez&rendertype = abstract. Accessed 11 Nov 2012.

60. Cross SE, Jin Y-S, Lu Q-Y, Rao J, Gimzewski JK (2011) Green tea extract selectively targets nanomechanics of live metastatic cancer cells. Nanotechnology 22: 215101. Available: http://www.pubmedcentral.nih.gov/articlerender.fcgi?artid = 3151463&tool = pmcentrez&rendertype = abstract. Accessed 10 Nov 2012.

Paper V

On the relationship between tissue structure and dielectric β-dispersion

Joris, P., Meissner, R., van Lintel, H., Bertsch, A., Renaud, P. (2013), *submitted*

On the relationship between tissue structure and dielectric β-dispersion

We present a method that enables estimating parameters linked to the cellular structure of biological tissues using impedance spectroscopy. We defined a parameter that allows drawing conclusions about the distribution of cell membrane capacitances as well as extra- and intracellular resistances within tissues. This method is based on an accurate description of the fundamental difference in dielectric dispersion properties between tissues and single cells, a phenomenon that has remained incompletely explained since its observation by K. Cole in 1932 (K. Cole, J Gen Physiol. 15, 6 (1932)).

Introduction - Biological tissues are heterogeneous compositions of cells, each of them being described by specific properties (e.g. cell-cell distance, cell size, amount of intracellular organelles). Those properties differ from one cell to another resulting in a natural distribution within the tissue. Information about these distributions has not been exploited until now. In fact, optical microscopy does not allow the analysis of a large number of cells with their microenvironments due to low throughput and the inability to image large 3D environments of biological tissues. Moreover, when primary cells are biopsied and isolated from their tissue either for single cell flow cytometry analysis [1], [2] or for *in vitro* cell culture, their natural microenvironment is dramatically changed regarding intercellular distances, cell shape and cellular metabolism. However, the knowledge of cellular distributions may be a highly valuable asset in characterizing tissues and diagnosing their pathological states. For example, intercellular communication distances are an important parameter for cell-to-cell signaling [3] which in turn is sensitive to cancerous alterations [4], [5]. Distribution changes of such distances may therefore indicate early, localized pathological changes within a tissue.

A biological cell behaves like an equivalent electrical circuit as shown in figure 1a where the cell membrane is represented by a capacitor, the intra- and extracellular matter by resistors. Information about the nature of this circuit and the value of each element can be obtained by measuring the impedance over a wide frequency range (impedance spectroscopy) as illustrated in figure 1b. However, it has been shown by K. Cole in 1932 that when measuring tissues, the impedance spectrum deviates from the one that is hypothesized for a single cell (figure 1b, Nyquist plot) [6]. Although an element named constant phase element (CPE) was suggested by Cole in 1940 [7] and used instead of a capacitance for almost a century to describe this particular β-dispersion[1] behavior of cells in tissues [8], [9], [10], the physical meaning of its parameters (CPE exponent α and magnitude β) has been unclear and for this reason the parameters themselves have been rarely used [11], [12], [13]. Several studies interpreted the α as an indicator of tissue heterogeneity in cell sizes and shapes [14], [15] as well as of heterogeneity in the extracellular space [16], but no precise explanation has been provided. H.P. Schwan rightly stated in 1957 that a distribution of such microenvironments, each with a specific time constant, leads to such CPE-like behavior [17] but again no more detail about the dispersion mechanism of tissues was given. An intrinsic electrical property of biological tissues has been incompletely explained for more than 80 years now.

In this article we provide new insight into how the β-dispersion of tissues is related to the electrical circuit of a single cell in medium. We show that the CPE exponent α does not directly correlate with tissue heterogeneity as was claimed before. Based on our findings, we demonstrate how impedance

---

[1] β-dispersion describes the ability of cell membranes to act like a capacitance which filters out currents at low frequency and allows high frequency currents to pass through. This phenomenon is centered between 0.1 and 10 MHz.

spectroscopy allows obtaining qualitative data about distributions of cell membrane capacitances as well as of extra- and intracellular resistances and accordingly how distribution information about cellular parameters such as extracellular spacing, cell sizes and shapes can be extracted.
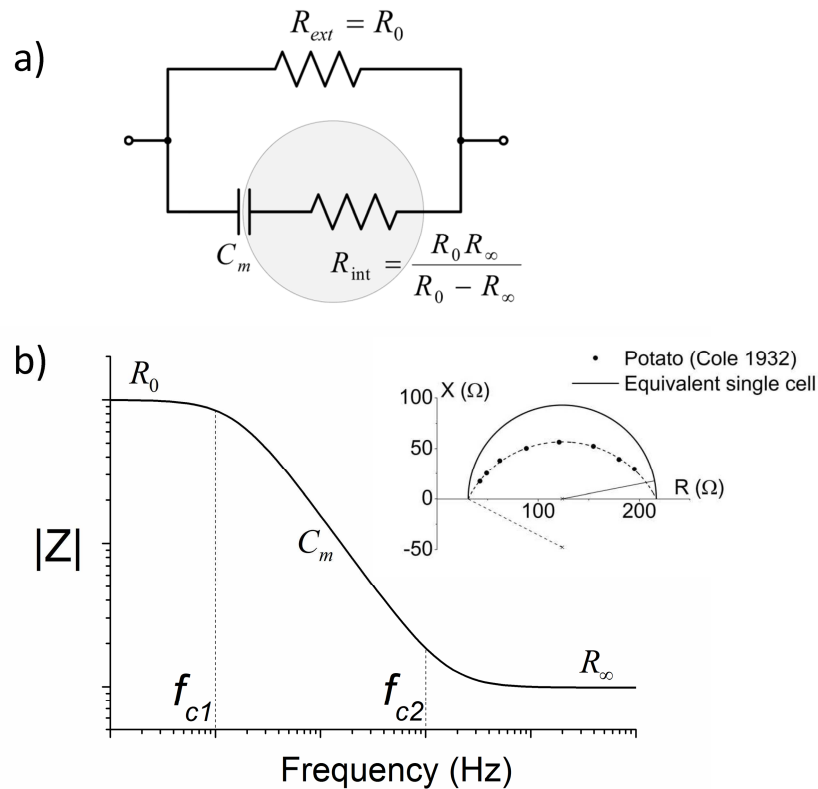
Figure 1: Single cell impedance. a) Equivalent electrical circuit of a single cell with a cell membrane capacitance C_m, a series intracellular resistance R_{int} and a parallel extracellular resistance R_{ext}; b) Impedance spectrum corresponding to the equivalent circuit of a single cell (big: Bode plot, small: Nyquist plot)

Equivalent electrical circuit of biological tissues - In order to better understand the effect of tissue structures on impedance measurements, an overall equivalent electrical circuit model was built. A tissue is generally composed of a large number of cells. One single cell in a tissue is modeled by a capacitance C_m representing the lipid bilayer membrane, a resistance R_{int} representing the inner media of the cell and a resistance R_{ext} representing the extracellular microenvironment (figure 1a). By connecting a large number of these single cell elementary circuits, a complex three-dimensional model of a tissue is obtained as illustrated in figure 2. Although this model is simplified, e.g. neglecting ion channels embedded in the cell membrane [18] and intracellular organelles [19], it is complex enough to provide insight in the main characteristics of tissue-specific impedance spectra in the β-dispersion frequency range. Within a tissue, different cell sizes, shapes and distances result in different resistance and capacitance values for each single elementary circuit. For each of the three elements (R_{ext}, R_{int} and C_m) these values give rise to a distribution providing the probability for every element in a random single cell circuit to take a certain value. We assumed a homogeneous tissue, i.e. the distribution is the same for the whole circuit and we simulated impedance spectra by first determining the mean and the width of the distribution for the three single cell circuit elements. The values for every element were then allocated randomly. We used lognormal distribution as a distribution function for the different elements since it is a good description of size distributions in nature [20] (see supplemental material for distribution and simulation details).
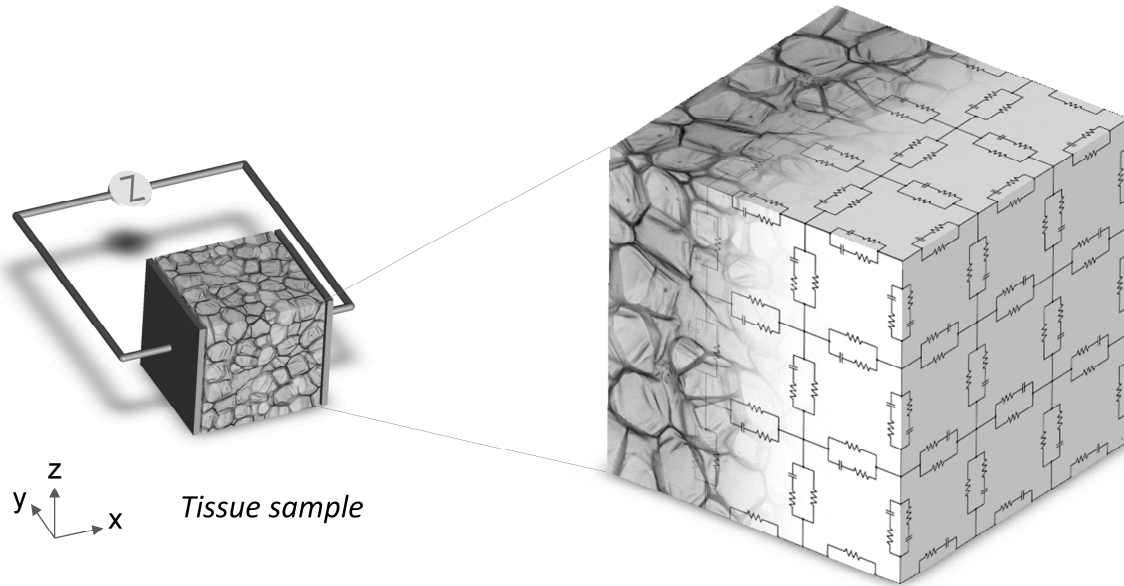
Figure 2: Complex tissue circuit with distributed single elements. The tissue model is made of a 3D-matrix of connected single cell equivalent circuits. Carrot cell picture is adapted from Gibson et al. [21] **(image: Don Galler), with kind permission from Cambridge University Press.**

Influences of distribution width on impedance spectra - The different elements of a single cell circuit have an effect on distinct parts of the impedance spectrum. To study the effect of their distribution within the complex tissue circuit from figure 2, we simulated tissues with only one of the three elements being distributed, the two others being uniform and we compared the obtained graphs with the one of a circuit with no distribution at all (figure 3). It is noted that each cell in the circuit has two cut-off frequencies $f_{c1} = 1/(2\pi R_0 C_m)$ and $f_{c2} = 1/(2\pi R_0 C_m)$ where the part of the spectrum at which the impedance is dominated by the membrane capacitance is separated from the parts at which the impedance is dominated by the resistance at zero frequency R_0 (f_{c1}) and by the resistance at infinite frequency R_∞ (f_{c2}) (see figure 1b, these frequencies are precisely defined by the phase being equal to 45°). When all three elements are the same in every cell of the whole tissue circuit, they also have the same cut-off frequencies resulting in an impedance behavior that is equivalent to the one of a single cell circuit (clear dots in figures 3a, b and c). On the contrary, when R_{ext}, R_{int} and C_m are distributed, this also affects the distribution of f_{c1} and f_{c2}, albeit to a different extent: a deviation from the single cell spectrum occurs around f_{c1} when R_{ext} is distributed (figure 3a), around f_{c2} when R_{int} is distributed (figure 3b) and around both cut-off frequencies when C_m is distributed (figure 3c). In all cases, the transition from resistive to capacitive regime and vice versa is shifted between the single cell circuits. As a consequence, the slope of the impedance modulus |Z| is becoming smaller at these frequencies. When R_{ext} is distributed, f_{c2} should also be slightly distributed since R_∞ also depends on the external resistances. Nevertheless this effect can be neglected in a first approximation; especially if the ratio between R_0 and R_∞ is large and thus the dependency of R_∞ on R_{ext} is negligible. Regarding a distribution of C_m, both cut-off frequency distributions overlap if they are wide enough and almost no part of the impedance modulus has a slope of one anymore (figure 3c).

By examining the effect of the distribution of every element individually, we discovered that each of them acts on a specific part of the spectrum. More importantly, if only one element is distributed, the resulting impedance is not showing a constant slope during the dispersion (see FigS1 in the supplemental material), unlike generally assumed in past bio-impedance spectroscopy studies. A very specific combination of element distributions might lead to such a constant phase but this is not the general case as will be shown later in this study. For this reason, we introduce hereafter a dispersion

element. This new element will allow us to acquire a better understanding of the dispersion curve and to gather more information about tissue specific distributions from the impedance measurements.
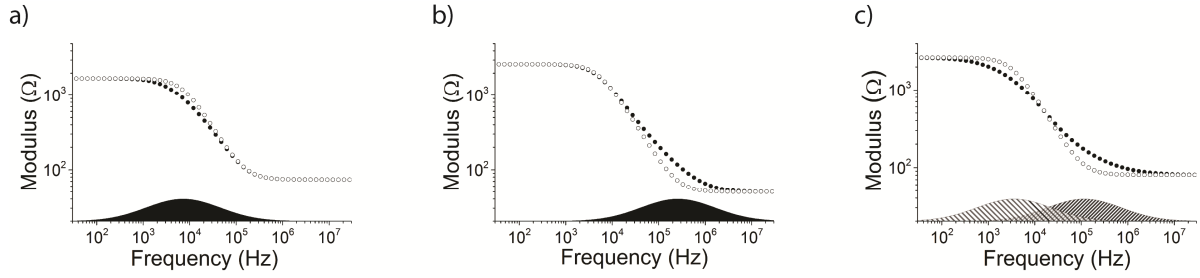

Figure 3: Impedance modulus with a distribution of $\sigma = 0.8$ for a) R_{ext}, b) R_{int} and c) C_m. The resulting curves are compared with the non-distributed curves (clear dots). The distribution curves on the x-axis represent the distribution of cut-off frequencies.

Distribution element - The method presented here to extract information about the distribution of the different elements from the tissue impedance spectrum is based on a new circuit element called dispersion element (DE) with an impedance

$$Z_{DE}(f) = \frac{1}{\beta(f)\left(i \cdot 2\pi f\right)^{\alpha(f)}}$$

This element is simply a capacitance if $\alpha = 1$ for all f and β is frequency-independent; it is a constant phase element (CPE) if both α and β are frequency-independent. Owing to the frequency dependence of the parameters α and β, the resulting general tissue circuit (figure 4b) allows describing every β-dispersion behavior of any tissue model of figure 2. In fact, the DE, in contrary to the commonly used capacitance or CPE, accounts exactly for the distribution effect of the three single cell circuit elements in the tissue. Thus the DE-based circuit is not a *fitting* model of the measured data but its impedance is set *equal* to the data thanks to the freedom given by $\alpha(f)$ and $\beta(f)$. Since $\beta(f)$ depends only on $\alpha(f)$ and on a constant parameter β_0 (see the supplemental material for detailed information on how to extract $\alpha(f)$ and $\beta(f)$), most of the relevant information concerning the distribution of the different elements is stored in $\alpha(f)$.

As depicted in figure 4, the value of $\alpha(f)$ is 1 at very high and very low frequencies since none or all of the membrane capacitances are shorted. In the frequency range of the β-dispersion, $\alpha(f)$ is characterized by two troughs corresponding to the distribution of the cut-off frequencies (f_{c1} for R_{ext} and C_m, f_{c2} for R_{int} and C_m, see supplemental information for a more detailed explanation). Consequently, the commonly used model of the CPE with a constant α over the dispersion frequency range is an imprecise description of the general β-dispersion and contains less information than the complete curve of $a(f)$.
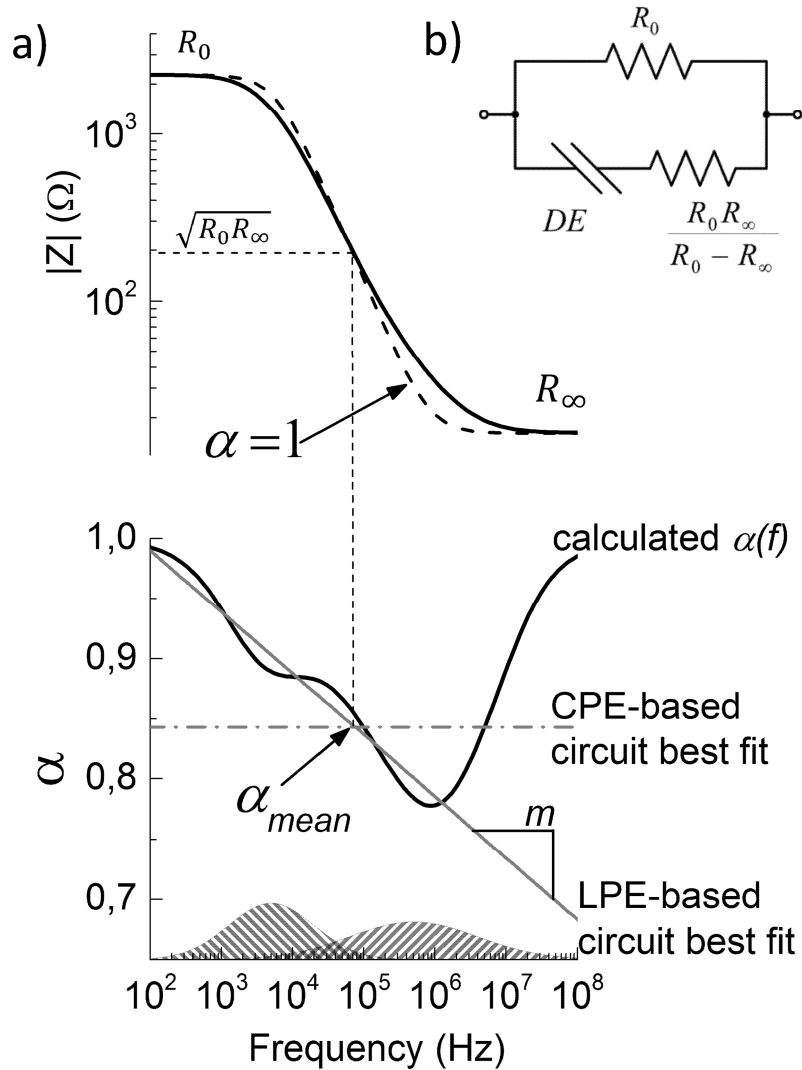
Figure 4: a) The parameter $\alpha(f)$ for a lognormal distribution of the elements R_{ext} ($\sigma = 0.4$), R_{int} ($\sigma = 0.7$) and C_m ($\sigma = 0.2$) is shown. The real tissue $\alpha(f)$ (calculated) cannot be known for experimental data (due to imprecise values for R_0 and R_∞) and is therefore approximated by a capacitance ($\alpha=1$), a constant phase element (CPE) or a logarithmic phase element (LPE). In contrast to capacitance and CPE, LPE carries additional information about the distribution of the circuit elements. The corresponding α_{mean} is extracted at the frequency where $|Z| = \sqrt{R_0 R_\infty}$ b) General equivalent tissue circuit that models the complex tissue circuit from figure 2.

Logarithmic phase element - The curve of $\alpha(f)$ is directly related to the distributions of the different elements and therefore offers useful information about the tissue structure. However the computation of $\alpha(f)$ is only possible as long as R_0 and R_∞ are precisely known. Experimental measurements do not allow obtaining such precise values due to the limited frequency measurement range (defined by the apparatus) and more importantly due to other system-related circuit elements (electrode capacitance at low frequency and the parasitic effects at high frequency). We circumvent this problem by fitting the impedance curve using a tissue circuit with a specific case of the DE that we refer to as logarithmic phase element (LPE), whose frequency exponent $\alpha(f)$ is growing or decreasing logarithmically with the frequency:

$$\alpha(f)_{LPE} = m \cdot log\left(\frac{f}{f_{mean}}\right) + \alpha_{mean}$$

where α_{mean} is the value of $\alpha(f)_{LPE}$ at the frequency f_{mean} and m is the slope of $\alpha(f)_{LPE}$ on a logarithmic scale of the frequencies. The frequency f_{mean} is defined as the frequency where the impedance modulus is the geometric mean $\sqrt{R_0 R_\infty}$ of R_0 and R_∞ (figure 4a). By fitting the impedance data to the LPE-based tissue circuit, we obtain R_0, R_∞, slope, α_{mean} and β_0 as fit results where slope and α_{mean} carry tissue-related distribution information that has been unavailable until now. Note that $\alpha(f)_{LPE}$ is not a fit to the calculated $\alpha(f)$, but it results from the fit of the measurement data to the LPE-based tissue circuit (figure 4b where the DE is replaced by a LPE).

In conclusion, the DE is a general element that, placed into the tissue circuit, completely describes the β–dispersion behavior of every tissue as shown in figure 2, owing to the frequency-dependence of its parameters. Different approximations of the DE have been considered in the past (Table 1). Both the capacitance and the CPE are dispersion elements that possess a constant α and thus a constant phase over frequency. The LPE is a more sophisticated element that takes into account the distribution weighting of the elements of a single cell circuit. More advanced elements are imaginable in order to describe the real tissue dispersion behavior; however, such models would be prone to overfitting due to their increased number of free parameters.

Dispersion elements	$\alpha(f) = 1$	$\beta(f) = C$	C	constant phase	by Debye
	$\alpha(f) = 0...1$	$\beta(f) = \beta$	CPE		by Cole
	$\alpha(f) = \alpha_{mean} + m \cdot log\left(\dfrac{f}{f_{mean}}\right)$	$\beta(f) = \beta_{mean}\left(\dfrac{f}{f_{mean}}\right)^{-mlog\left(2\pi\sqrt{ff_{mean}}\right)}$	LPE	variable phase	
	$\alpha(f) = $ any function	$\beta(f) = \beta_0 e^{-\int_{\alpha_i}^{\alpha(f)} log(2\pi f(x))dx}$	other VPE		
	$\alpha(f) = \alpha(f)_{real}$	$\beta(f) = \beta(f)_{real}$	real dispersion		

Table 1: The dispersion element describes a tissue's dispersion behavior completely. The corresponding $\alpha(f)$ and $\beta(f)$ can be found only as long as R_0 and R_∞ are precisely known. Since this is not possible in practice, approximations can be made and these are subdivided into two groups. A simple capacitance and a CPE both have constant phases. More sophisticated models have variable phases with a frequency-dependence closer to the real one. The LPE represents a good compromise between frequency-dependence and few model parameters, but in theory any more complex equation is possible. Derivation of the formulas for $\beta(f)$ is available in the supplemental information.

Correlation between LPE and distribution width - In order to correlate tissue structure with the results of the LPE fit, the lognormal distribution width σ of the different elements was varied by keeping the mean value of each element constant. We extracted the values of α_{mean} and slope, which determine uniquely $\alpha(f)_{LPE}$ (figure 5).

Simulations were carried out with a cubic circuit where x, y, $z = 12$ cells (1728 cells). The value of $\Delta logR = log(R_0/R_\infty)$ was kept at 1.5. α_{mean} decreases for an increasing σ of any of the three elements, this effect being stronger for the membrane capacitances. The slope is dependent on which element is distributed: positive for the external resistance, slightly negative for the membrane capacitance and strongly negative for the internal resistance.

In a tissue, all three elements are distributed, which leads to a combination of their effects on α_{mean} and on the slope. Based on our simulations, we created a distribution map that distinguishes different cases according to specific pairs of alpha and slope as illustrated in figure 5b. The slope gives insight into

which of the distributions is stronger (external resistance if the slope is within the dark gray area, internal resistance if the slope is within the light gray area). In addition, the lower the value of α_{mean} is, the higher is the probability that C_m is distributed (patterned gradient). Moreover, we are able to detect relative differences between tissues based on the directional influences of each element's distribution (arrows). Although the knowledge of α_{mean} and slope does not provide enough information to uniquely determine the distribution width values of the different elements, it does enable determining the range in which they are included.
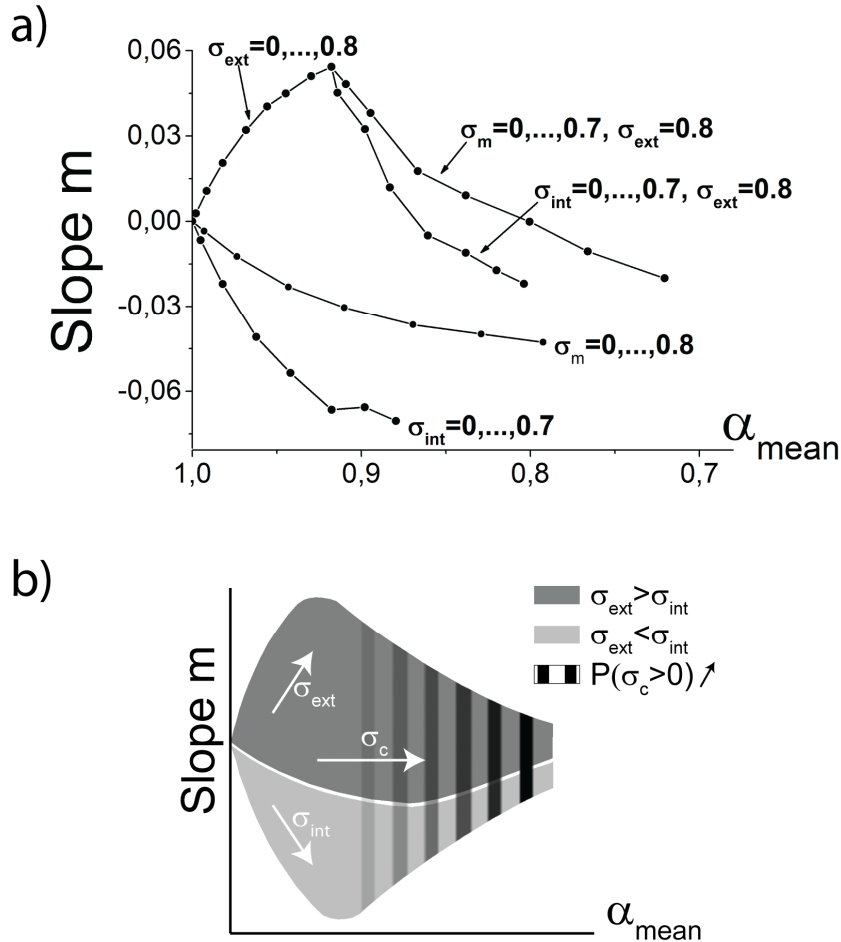

Figure 5: The parameters α_{mean} versus slope of the dispersion corresponding to different distributions of the elements R_{ext}, R_{int} and C_m a) Simulations of a selection of different distribution combinations with $\Delta log R = 1.5$. σ=0 when not mentioned b) Simplified distribution map where specific combinations of α_{mean} and slope provide information about distribution weighting among the three elements. This map is based on simulations run for all combinations of distribution widths between 0 and 1 with a mesh of 0.1.

Validation with plant tissue - For validation of our method, we chose carrots (*Docus carota*) as tissue samples because of their availability and ease of handling. α_{mean} and slope were extracted from impedance measurements on the three different parts of the carrot as depicted in figure 6a and compared to the tissue structures as observed under the microscope (figures 6b-d).

The parameter α_{mean} alone ($\approx \alpha_{CPE}$) does not allow differentiating all tissue samples but thanks to the additional slope value, the different parts of the carrot can be distinguished unequivocally and their cellular structures estimated as follows : the lower α_{mean} (wider distribution of membrane capacitances) and the lower slope (wider distribution of internal resistances with respect to external resistances) of part 2 correlate with the cell sizes being visibly more distributed in part 2 than in parts

1 and 3. According to the difference in slope between part 1 and part 3, the external resistances are more distributed in part 1.

Finally, it is noted that although cell sizes can be estimated using optical microscopy, this is hardly possible for intercellular spaces, which are in the micro to nanometer range. Therefore, our technique enables qualifying a tissue characteristic that has been inaccessible until now.
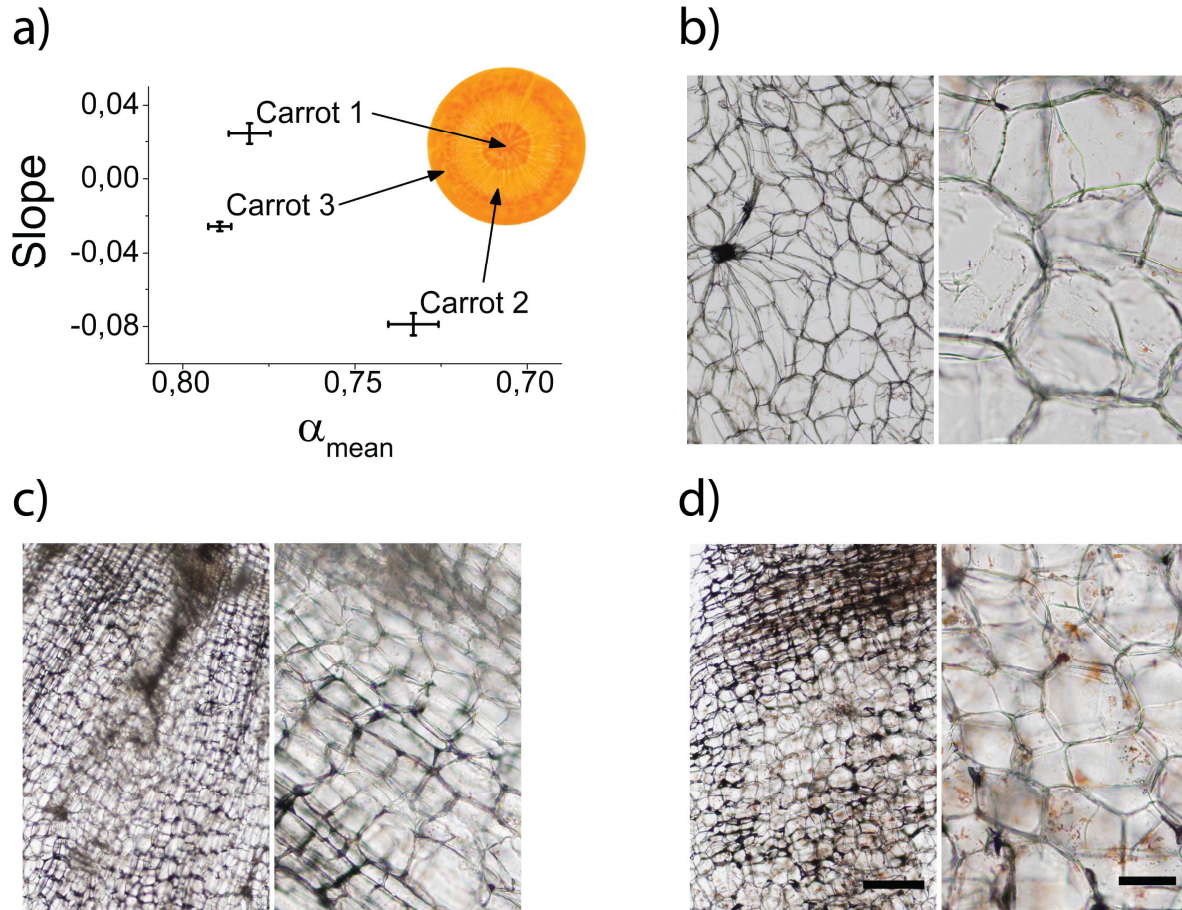
Figure 6: (a) α_{mean} and slope from LPE-based tissue circuit best fits of measurements on carrots (mean±SEM, n=8) (b-d) Bright field images of three different parts of a carrot slice as depicted in (a). (b) Center part (1), (c) Intermediate part (2), (d) external part (3). The scale bar corresponds to 200 μm on the right side and 50μm on the left side.

Conclusion - This article explains the deviation of tissue dispersions from hypothesized single cell circuits. Although K. Cole introduced a so called *constant phase element* which more closely described the observed curves; the physical meaning of its parameters was unclear and therefore mostly unexploited. Tissue-specific information that is related to cellular distributions was missed.

The study of tissue dispersion effects revealed that the distribution of each of the three basic elements of a single cell circuit (intra- and extracellular resistance as well as cell membrane capacitance) throughout the whole tissue circuit has a distinct impact on the impedance curves. We introduced a new element named *logarithmic phase element* that allows drawing conclusions about distributions within a tissue. Our distribution results on plant tissues correlated with cellular structures that were observed under the microscope, pointing out the potential this method might have on human disease diagnostics where fast, label-free and above all objective analysis methods are of high interest.

The variations of different tissue-specific parameters such as cell sizes, intracellular properties and above all intercellular distances may be compared and such gained knowledge might help understand

fundamental disease-related phenomena within tissues. Considering the wide use of electrical impedance spectroscopy, our new technique may have strong implications on tissue characterization, in particular in the field of cancer diagnostics, but also in the study and characterization of *in vitro* cell populations for tissue engineering.

References

[1] K. Goda, A. Ayazi, D. R. Gossett, J. Sadasivam, C. K. Lonappan, E. Sollier, A. M. Fard, S. C. Hur, J. Adam, C. Murray, C. Wang, N. Brackbill, D. Di Carlo, et B. Jalali, « High-throughput single-microparticle imaging flow analyzer », *Proc. Natl. Acad. Sci. U. S. A.*, vol. 109, n° 29, p. 11630-11635, juill. 2012.

[2] A. Tzur, J. K. Moore, P. Jorgensen, H. M. Shapiro, et M. W. Kirschner, « Optimizing Optical Flow Cytometry for Cell Volume-Based Sorting and   Analysis », *PLoS One*, vol. 6, n° 1, janv. 2011.

[3] K. Francis et B. O. Palsson, « Effective intercellular communication distances are determined by the   relative time constants for cyto/chemokine secretion and diffusion », *Proc. Natl. Acad. Sci. U. S. A.*, vol. 94, n° 23, p. 12258-12262, nov. 1997.

[4] J. M. Levsky, S. M. Shenoy, J. R. Chubb, C. B. Hall, P. Capodieci, et R. H. Singer, « The spatial order of transcription in mammalian cells », *Journal of Cellular Biochemistry*, vol. 102, n° 3, p. 609–617, 2007.

[5] G. S. Martin, « Cell signaling and cancer », *Cancer Cell*, vol. 4, n° 3, p. 167-174, sept. 2003.

[6] K. Cole, « Electric phase angle of cell membranes », *The Journal of General Physiology*, vol. 15, n° 6, p. 641-649, 1932.

[7] K. S. Cole, « Permeability and impermeability of cell membranes for ions », *Cold Spring Harbor Symposia on Quantitative Biology*, vol. 8, p. 110-122, janv. 1940.

[8] R. J. Halter, A. Hartov, J. A. Heaney, K. D. Paulsen, et A. R. Schned, « Electrical impedance spectroscopy of the human prostate », *IEEE Trans Biomed Eng*, vol. 54, n° 7, p. 1321-1327, juill. 2007.

[9] T. E. Kerner, K. D. Paulsen, A. Hartov, S. K. Soho, et S. P. Poplack, « Electrical impedance spectroscopy of the breast: clinical imaging results in 26 subjects », *IEEE Transactions on Medical Imaging*, vol. 21, n° 6, p. 638 -645, juin 2002.

[10] R. Meissner, B. Eker, H. Kasi, A. Bertsch, et P. Renaud, « Distinguishing drug-induced minor morphological changes from major cellular damage via label-free impedimetric toxicity screening », *Lab Chip*, vol. 11, n° 14, p. 2352-2361, juin 2011.

[11] S. Grimnes et O. G. Martinsen, « Cole electrical impedance model--a critique and an alternative. », *IEEE transactions on bio-medical engineering*, vol. 52, n° 1, p. 132-5, janv. 2005.

[12] E. T. McAdams et J. Jossinet, « Tissue impedance: a historical overview. », *Physiological measurement*, vol. 16, n° 3 Suppl A, p. A1-13, août 1995.

[13] K. S. Cole et R. H. Cole, « Dispersion and Absorption in Dielectrics I. Alternating Current Characteristics », *The Journal of Chemical Physics*, vol. 9, n° 4, p. 341-351, avr. 1941.

[14] J. J. Ackmann et M. A. Seitz, « Methods of complex impedance measurements in biologic tissue », *Crit Rev Biomed Eng*, vol. 11, n° 4, p. 281-311, 1984.

[15] R. S. Foster, R. Bihrle, N. T. Sanghvi, F. J. Fry, et J. P. Donohue, « High-intensity focused ultrasound in the treatment of prostatic disease », *Eur. Urol.*, vol. 23 Suppl 1, p. 29-33, 1993.

[16] A. Ivorra, M. Genescà, A. Sola, L. Palacios, R. Villa, G. Hotter, et J. Aguiló, « Bioimpedance dispersion width as a parameter to monitor living tissues », *Physiological Measurement*, vol. 26, n° 2, p. S165-S173, avr. 2005.

[17] H. P. Schwan, « Electrical properties of tissue and cell suspensions », *Adv Biol Med Phys*, vol. 5, p. 147-209, 1957.

[18] K. S. Cole, *Membranes, Ions, and Impulses: A Chapter of Classical Biophysics*. University of California Press, 1968.

[19] H. P. Schwan, « Electrical properties of tissues and cell suspensions: mechanisms and models »,
in *Proceedings of the 16th Annual International Conference of the IEEE Engineering in Medicine
and Biology Society, 1994. Engineering Advances: New Opportunities for Biomedical Engineers*,
1994, p. A70 -A71 vol.1.

[20] A. Giometto, F. Altermatt, F. Carrara, A. Maritan, et A. Rinaldo, « Scaling body size
fluctuations », *PNAS*, mars 2013.

[21] L. J. Gibson, M. F. Ashby, et B. A. Harley, *Cellular Materials in Nature and Medicine*, 1re éd.
Cambridge University Press, 2010.

Acknowledgements

Curriculum Vitae

Robert Meissner

Route du Tirage 11,
1806 St. Légier
rob.meissner@gmail.com
+41 76 378 53 31
Age: 28
German (B permit)
Married

- Trilingual and international experience
- Expertise in pharmaceutical industry, biosensors and biomedical devices
- Hard working, persistent and innovative

PRACTICAL EXPERIENCE

Ph.D. candidate   6/2009-07/2013
Ecole Polytechnique Fédéral de Lausanne (EPFL) with Prof. Renaud

I am building solutions to the various needs of modern in vitro cell-based analysis systems as well as of biomedical devices by the means of microtechnology.

- 6 journal papers, 5 conference proceedings, Featured spotlight paper in "Biotechnology and Bioengineering"
- Winner of Bioalps best-poster award, EPFL featured my study on Alzheimer's disease with a main article
- Invited plenary speaker at IBCA conference in Regensburg

Research assistant   10/2008-4/2009
Universität Leipzig, Germany

I genetically modified and characterized neuroblastoma cells for neurodegenerative studies.

- This model has been used for bioelectronics-based drug screening (Krinke et al, 2010)

Industrial Internship   2/2008-8/2008
Sanofi Pasteur, France

I developed a logistics tool that calculates the fabrication lead times of bacterial and viral seed lots up to 12 months in advance, taking into account the need for vaccine production, R&D, quality control and quality assurance.

- This tool is now being used on four production sites in France, USA and Canada.
- Guidance of international conference meetings

Research Assistant   6/2007-9/2007
California State University, Los Angeles, USA

I investigated the role of singlet oxygen in the active sites of enzymes.

- I have established a protocol to synthesize quantum dots for the production of singlet oxygen.
- I received a grant by the "Deutscher Akademischer Austauschdienst" for this work

Founder and Self Employed   6/2006-12/2008
Dederon® Service, Erfurt, Germany

I have founded and managed an individual enterprise dedicated to patent research on behalf of Jenoptik AG, Germany.

German Civilian Service   4/2003-6/2004
Yarra School, Melbourne, Australia

I was an assistant teacher for German lessons and organized the setup of the new school library.

EDUCATION HISTORY

Doctor of Philosophy (Ph.D.) dissertation
7/2009 – early 2013
Ecole Polytechnique Fédérale de Lausanne (EPFL), Lausanne, Switzerland

M.Sc. & M.Eng (Diplôme d'Ingénieur) in Biochemistry & Biotechnology
10/2004-4/2009
Double Diploma at the Universität of Leipzig and l'Institut National des Sciences Appliquées (INSA), Lyon

LANGUAGES

- German - mother tongue
- English - fluent (spoken and written) – C2
- French - fluent (spoken and written) – C2
- Italian - basic knowledge – A2

EXTRACURRICULAR ACTIVITIES

I have played in several soccer teams in five countries (1994-2012) and I have lead the Rudolstadt soccer team in Germany as their team captain (1998-2001)

TECHNICAL SKILLS

Software
Matlab, SolidWorks, ImageJ, Comsol, MS Word, MS Excel, MS PowerPoint, MS Access, MS Project, Adobe Photoshop, Mendeley
HTML, JavaScript, Turbo Pascal, Visual Basic

Life sciences
cell culture, immunocytochemistry, ELISA, confocal microscopy, microbiology, DNA cloning, RNA & DNA purification, western plot, polymerase chain reaction (PCR), optical spectroscopy (UV/VIS), impedance spectroscopy

Pharmaceutical
good laboratory practices (GLP), good manufacturing practices (GMP), risk assessment (EMEA), production and storage procedures for biotech drug industry

Microtechnology
microfluidics, PDMS, hydrogels, clean room microfabrication (lithography, lift-off, etching), surface functionalization, scanning electron microscopy (SEM)